TU Delft

Delft University of Technology

Understanding the Fundament of Virus Inactivation via Modeling

Tan, C.

DOI
10.4233/uuid:14351363-b5d1-41ec-ac32-8efb4817481b

Publication date
2023

Document Version
Final published version

Citation (APA)
Tan, C. (2023). *Understanding the Fundament of Virus Inactivation via Modeling*. [Dissertation (TU Delft), Delft University of Technology]. https://doi.org/10.4233/uuid:14351363-b5d1-41ec-ac32-8efb4817481b

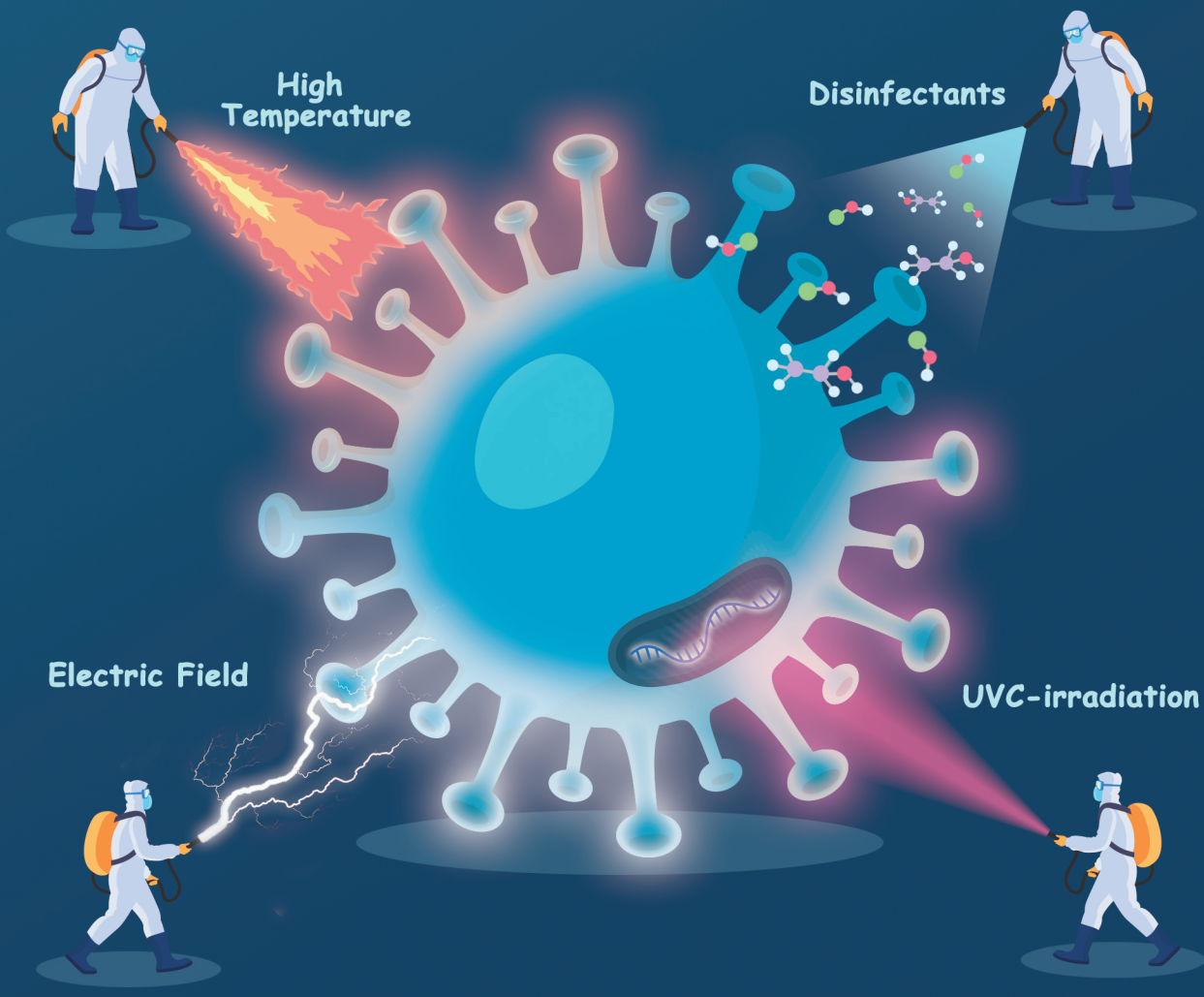
Important note
To cite this publication, please use the final published version (if applicable).
Please check the document version above.

Copyright
Other than for strictly personal use, it is not permitted to download, forward or distribute the text or part of it, without the consent of the author(s) and/or copyright holder(s), unless the work is under an open content license such as Creative Commons.

Takedown policy
Please contact us and provide details if you believe this document breaches copyrights.
We will remove access to the work immediately and investigate your claim.

This work is downloaded from Delft University of Technology.
For technical reasons the number of authors shown on this cover page is limited to a maximum of 10.

Understanding the Fundament of Virus Inactivation Via Modeling



CHUNJIAN TAN

Understanding the Fundament of Virus Inactivation Via Modeling

UNDERSTANDING THE FUNDAMENT OF VIRUS INACTIVATION VIA MODELING

Dissertation

for the purpose of obtaining the degree of doctor
at Delft University ofTechnology
by the authority of the Rector Magnificus Prof.dr.ir. T.H.J.J. van der Hagen
chair of the Board for Doctorates
to be defended publicly on
Monday, 24 April 2023 at 15:00 o'clock

by

Chunjian TAN

Master of Engineering in Mechanical Engineering,
Guilin University of Electronic Technology, Guilin, China,
born in Guangxi, China.

This dissertation has been approved by

Promotor: Prof. dr. G.Q. Zhang

Composition of the doctoral committee:

Rector Magnificus,	Chairperson
Prof. dr. G.Q. Zhang,	Delft University of Technology, promotor
Prof. dr. H.Y. Ye,	Southern University of Science and Technology, copromotor

Independent members:

Prof. dr. L. Wang,	Peking University
Prof. dr. D.A. Pijnappels,	Leiden University Medical Center
Prof. dr. X.J. Fan,	Lamar University
Prof. dr. ir. W.D. van Driel,	Delft University of Technology
Prof. dr. ir. P.M. Sarro,	Delft University of Technology

Keywords: Molecular-level inactivation mechanism; Density functional theory; Molecular dynamics; Quantum chemical calculation; SARS-CoV-2; Heating inactivation; Chemical disinfectants; UVC irradiation; Electric field treatment

Printed by: Ipskamp Printing

Front & Back: Cover art work of all elements, including viruses, cartoon characters, and lightning, and so on, by Chunjian Tan and Ruqin Wang.

Copyright © 2023 by Chunjian Tan

ISBN 978-94-6473-098-2

An electronic version of this dissertation is available at
http://repository.tudelft.nl/.

To my Father and Mother

CONTENTS

Summary xi

Samenvatting xv

1 Introduction 1
- 1.1 Background . . . 2
- 1.2 Overview of coronaviruses . . . 2
  - 1.2.1 Coronaviruses . . . 2
  - 1.2.2 Structural proteins and their function in CoVs . . . 3
  - 1.2.3 Genetic structure in CoVs . . . 5
  - 1.2.4 Pathogenic mechanism of CoVs . . . 5
  - 1.2.5 Transmission modes of CoVs . . . 8
- 1.3 Inactivation approaches for CoVs . . . 9
  - 1.3.1 Chemical inactivation approaches . . . 9
  - 1.3.2 Physical inactivation approaches . . . 10
- 1.4 Inactivation mechanisms for pathogens . . . 11
- 1.5 Problems in the methods and mechanisms of viral inactivation . . . 12
- 1.6 The layout of this dissertation . . . 14

References . . . 15

2 Unrevealing the possible impact of high temperature on SARS-CoV-2: A computational study 25
- 2.1 Molecular dynamics theory . . . 26
- 2.2 The stability of SARS-CoV-2 in different environmental conditions . . . 28
- 2.3 Effect of temperature on the spike protein of SARS-CoV-2 . . . 29
- 2.4 The possible impact of temperature on the phospholipid membrane of SARS-CoV-2 . . . 31
  - 2.4.1 Phospholipid membrane of SARS-CoV-2 . . . 31
  - 2.4.2 Construction of the initial model . . . 32
  - 2.4.3 Computational methodologies . . . 33
  - 2.4.4 Results and discussion . . . 35
- 2.5 Conclusions . . . 44

References . . . 44

3 The inactivation mechanism of chemical disinfectants against SARS-CoV-2: From the molecular-level perspective 49
- 3.1 Density functional theory . . . 50
- 3.2 Inactivation of SARS-CoV-2 virions by commonly available disinfectants . . . 51
- 3.3 The interaction mechanisms of chemical disinfectants with 3CL hydrolase . . . 54
  - 3.3.1 3CL hydrolase of SARS-CoV-2 . . . 54

3.3.2 Construction of the initial models . . . 55
3.3.3 Computational methods . . . 56
3.3.4 Molecular dynamics simulations . . . 57
3.3.5 First principles simulations . . . 62
3.3.6 Comparison of inactivation mechanisms . . . 65
3.4 The interaction mechanisms of chemical disinfectants with the phospholipid membrane . . . 65
3.4.1 Construction of the initial models . . . 65
3.4.2 Computational methods . . . 67
3.4.3 Molecular dynamics calculations . . . 67
3.5 Conclusions . . . 77
References . . . 78

4 Ultraviolet C inactivation of infectious viruses with multifunctional UVC-LED platform: Virucidal performance and mechanism 87
4.1 Introduction . . . 88
4.2 Virus inactivation experiments based on the customized UVC-LED platform . . . 89
4.2.1 Experimental preparation . . . 89
4.2.2 Experimental design . . . 90
4.2.3 Experimental result . . . 93
4.3 Molecular-level study on the inactivation mechanism of UVC irradiation . . . 95
4.3.1 Theoretical foundations of computational chemistry . . . 95
4.3.2 Evaluation of basis sets . . . 98
4.3.3 Evaluation of DFT functionals . . . 100
4.3.4 Computational methods and nucleotide models . . . 102
4.3.5 UV-vis absorption spectrums of four RNA nucleotides . . . 102
4.3.6 Electron excitation characteristics of four RNA nucleotides . . . 104
4.3.7 Transition state of dual uracil reaction . . . 109
4.3.8 Reaction rate constant of dual uracil molecules . . . 120
4.4 Conclusions . . . 122
References . . . 122

5 Inactivation of pathogens using electric fields on a microchip platform: An experimental and computational study 129
5.1 Introduction . . . 130
5.2 Electrical inactivation of bacteriophage phi-6 on microelectrodes . . . 132
5.2.1 Design and modeling of three microelectrodes . . . 132
5.2.2 Experimental material and methods . . . 134
5.2.3 Experimental results and discussion . . . 134
5.3 Electrical inactivation of Escherichia coli on microelectrodes . . . 139
5.3.1 Experimental material and methods . . . 139
5.3.2 Experimental results and discussion . . . 141
5.4 Dynamics of viral lipid bilayer induced by electric fields . . . 145
5.4.1 Modeling and computational methods . . . 145
5.4.2 Results and discussion . . . 146

5.5 Conclusions . . . 155
References . . . 155

6 Conclusion and Future Perspective **161**
6.1 Conclusions . . . 162
6.2 Future Perspective . . . 164

Acknowledgements **167**

A Supporting Information Chapter 2 **169**
A.1 Analytical details of the bilayer membrane . . . 169
A.2 Deformation of the bilayer membrane . . . 169
References . . . 171

B Supporting Information Chapter 3 **173**
B.1 The structure of spike protein and the protein-ethanol system . . . 173
B.2 Radial distribution function . . . 173
B.3 Deformation of the bilayer membrane . . . 175
References . . . 175

C Supporting Information Chapter 4 **177**
C.1 UVC-LED platform design for virus inactivation . . . 177
C.1.1 Irradiance modeling . . . 177
C.1.2 Requirement and design of UVC-LED platform . . . 178
C.1.3 Characterization of UVC-LEDs . . . 182
C.2 The atom-to-atom charge transfer matrix of four RNA nucleotides . . . 185

D Supporting Information Chapter 5 **189**
D.1 Material parameters for microeletrode models . . . 189
D.2 Structural parameters for three microeletrodes . . . 189
D.3 Electric field distribution of microelectrodes . . . 190
D.4 Fabrication of the microelectrodes . . . 195

Curriculum Vitæ **203**

List of Publications **205**

SUMMARY

Historically, viruses have always been the causative agent of most human diseases. As one of the most devastating pandemics in human history, the COVID-19 pandemic, associated with SARS-CoV-2, is responsible for tens of millions of casualties in the world since the end of 2019. Meanwhile, it also has destabilized global economics. Therefore, in the absence of vaccines and particular drugs, exploring effective disinfection methods for lethal viruses is critical to prevent the spread of pandemics. At present, many scientific studies have demonstrated a variety of inactivation methods for bacteria and viruses, including conventional and advanced ones. Those methods show high antiviral activity for viruses such as human CoVs. However, most research focuses on the effectiveness and efficiency of viral inactivation. Besides benefiting from the development of semiconductor technology, it is possible for viral inactivation by utilizing multi UVC-LEDs (UVC irradiation) or microelectrodes (electric field). Most importantly, the molecular-level mechanisms of virus inactivation are still unclear and debated. Therefore, it is meaningful to uncover the molecular-level mechanism of virus disinfection methods and explore more effective antiviral schemes for preventing viral diseases. In this thesis, the research works mainly focus on the following contents.

Study on the inactivation mechanism of high temperature. Using the molecular dynamics method, the dynamics behavior of the bilayer membrane without structural proteins is theoretically revealed at varying temperatures. The dynamics could be reflected by the total APL, membrane thickness, mass density, electron density, lateral diffusion, and radial distribution function. The simulation results suggest that the total APL of the bilayer increases gradually with temperatures, while the membrane thickness is inversely related to temperatures. No water molecules can be found in the interior of the membrane, regardless of temperature. This result means that more than the spacing between lipid molecules is required to allow water molecules to enter the interior of the lipid membrane. As a result, high temperatures do not disrupt of the bilayer structure, which is confirmed by the published experimental results. Moreover, the mass and electron densities clearly show that the lipids' head-groups are susceptible to the effect of temperature compared to the fatty acid tail. Upon heating, the bilayer membrane transitions into the liquid-disordered phase, where lipid molecules become more active and intensely diffuse in the membrane plane. Meanwhile, the lipid molecules' fatty acid tails are considerably flexing and bending. Eventually, 2D RDFs further demonstrate the lateral expansion of the lipid membrane.

Study on the inactivation mechanism of chemical disinfectants. The interaction mechanism of chemical agents with SARS-CoV-2 is theoretically investigated by utilizing MD and DFT calculations. For the case of 3CL hydrolase, the results show that the biocidal ingredients prefer to bind to the unsaturated oxygen atoms of 3CL hydrolase. The interaction is dependent on the concentration of biocidal ingredients. Among anchored structures, the ingredient-S1 conformations are more favorable than other con-

formations in that the active ingredients are anchored to S2 or S3. Their binding energies and charge transfer are more prominent than 0.5 eV and 0.1 *e*, respectively. In the case of the lipid membrane, the structural parameters of the bilayer membrane demonstrate that the presence of biocidal ingredients would alter the bilayer structure of SARS-CoV-2, such as lateral swelling and progressive thinning, and HClO in particular. With increasing concentration, more ingredient molecules are at the bilayer center. Similar to the case of 3CL hydrolase, ingredient molecules prefer to bind to the unsaturated oxygen atoms of the lipid molecules. 2D RDFs of P-P and N-N atomic pairs directly suggest that the lateral spacing between two P or N atoms of the lipid head-groups increases, illustrating the cause of lateral swelling of the bilayer membrane.

Study on the inactivation recipe and mechanism of UVC irradiation. The inactivation experiments for Influenza A PR8 are carried out on the designed UVC-LEDs platform to explore the optimal inactivation recipe. The available results show that the dual-wavelength scheme has no obvious advantage over the single-wavelength scheme. The wavelength of 259 nm exhibits the optimal inactivation affection for Influenza A PR8. In the meantime, to reveal the inactivation mechanism of UVC irradiation for the virus at the molecule level, the spectral properties of four nucleotides are investigated using quantum chemical calculations. Furthermore, the transition state and reaction rate constant of uracil molecules are also considered to determine the difficulty level of dual-uracil reaction in the absence and presence of UVC irradiation. The absorption spectra suggest that the wavelengths of the absorption peaks are 248.7 nm, 226.1 nm (252.7 nm), 248.3 nm, and 205.8 nm (249.2 nm) for adenine, cytosine, guanine, and uracil molecules, respectively. These wavelengths are close to the optimal wavelength obtained in the experiment. Most importantly, the reaction rate constant of dual-uracil is expected to be 6.419×10^{-49} and 5.436×10^{11} $s^{-1}\cdot M^{-1}$ for the ground and excited states, respectively. The half-life for the ground and excited states is 1.56×10^{48} and 1.84×10^{-12} s, respectively, which means that the molecule reaction between adjacent nucleotides cannot almost occur in the absence of UVC irradiation.

Study on the viral inactivation and mechanism of electric fields generated by microelectrodes. The inactivation experiments are performed on three microelectrodes fabricated on microchips. The phi-6 virus is chosen as an alternative to SARS-CoV-2 in this study. It is found that the out-of-phase castellated microelectrode exhibits more outstanding antiviral activity compared to the interdigitated and the in-phase castellated microelectrodes because of its higher titer reduction. In the meantime, there is no significant viral inactivation following DC treatment. Conversely, there is after AC treatment. Furthermore, an AC treatment with high frequencies significantly reduces viral titer rather than low frequencies. It also finds that the titer reduction highly depends on the conductivity and viral concentration of the virus samples. Here, the inactivation of E. coli on microelectrodes is also evaluated. The morphological structure of E. coli demonstrates that the lipid envelope is damaged by electric fields, which leads to the death of enveloped pathogens. Eventually, in order to uncover the effect of electric fields on viruses, the dynamics of the lipid membrane at varying electric fields are investigated. The simulated results show that electric fields less than 250 mV/nm do not lead to the disruption of the bilayer structure even after 200 ns. Reaching 250 mV/nm results in the instantaneous collapse of the bilayer at around 130 ns. The structural information at dif-

ferent electric fields also provides robust evidence for this phenomenon. Therefore, 250 mV/nm is the threshold field at which the lipid membrane disruption happens.

SAMENVATTING

Historisch gezien zijn virussen altijd de veroorzaker geweest van de meeste menselijke ziekten. Als een van de meest verwoestende pandemieën in de menselijke geschiedenis is de COVID-19-pandemie, geassocieerd met SARS-CoV-2, verantwoordelijk voor tientallen miljoenen slachtoffers in de wereld sinds eind 2019. Ondertussen heeft zij ook de wereldeconomie gedestabiliseerd. Daarom, bij gebrek aan vaccins en bepaalde geneesmiddelen, is het verkennen van effectieve ontsmettingsmethoden voor dodelijke virussen van cruciaal belang om de verspreiding van pandemieën te voorkomen. Momenteel zijn in vele wetenschappelijke studies diverse inactiveringsmethoden voor bacteriën en virussen aangetoond, waaronder conventionele en geavanceerde methoden. Die methoden vertonen een hoge antivirale activiteit voor virussen zoals menselijke CoV's. Het meeste onderzoek richt zich echter op de doeltreffendheid en efficiëntie van virale inactivatie. Behalve door de ontwikkeling van de halfgeleidertechnologie is het mogelijk virale inactivatie uit te voeren met behulp van multi-UVC-LED's (UVC-bestraling) of micro-elektroden (elektrisch veld). Het belangrijkste is dat de mechanismen op moleculair niveau van virusinactivatie nog steeds onduidelijk en omstreden zijn. Daarom is het zinvol om het mechanisme op moleculair niveau van virusdesinfectiemethoden bloot te leggen en effectievere antivirale schema's voor de preventie van virusziekten te verkennen. In dit proefschrift richten de onderzoekswerkzaamheden zich voornamelijk op de volgende inhoud.

Studie naar het inactiveringsmechanisme van hoge temperatuur. Met behulp van de moleculaire-dynamische methode wordt het dynamisch gedrag van het bilaagmembraan zonder structurele eiwitten theoretisch onthuld bij verschillende temperaturen. De dynamiek kan worden weergegeven door de totale APL, membraandikte, massadichtheid, elektronendichtheid, laterale diffusie en radiale distributiefunctie. De simulatieresultaten suggereren dat de totale APL van de bilaag geleidelijk toeneemt met de temperatuur, terwijl de membraandikte omgekeerd evenredig is met de temperatuur. Er kunnen geen watermoleculen worden gevonden in de binnenkant van het membraan, ongeacht de temperatuur. Dit resultaat betekent dat meer dan de afstand tussen de lipidemoleculen nodig is om watermoleculen toe te laten tot de binnenkant van het lipidemembraan. Bijgevolg verstoren hoge temperaturen de bilaagstructuur niet, wat wordt bevestigd door de gepubliceerde experimentele resultaten. Bovendien tonen de massa- en elektronendichtheden duidelijk aan dat de kopgroepen van de lipiden gevoeliger zijn voor het effect van de temperatuur dan de vetzuurstaart. Bij verwarming gaat het bilaagmembraan over in de vloeibaar-geordende fase, waarin de lipidemoleculen actiever worden en intenser gaan diffunderen in het membraanvlak. Ondertussen buigen en buigen de vetzuurstaarten van de lipidemoleculen aanzienlijk. Uiteindelijk tonen 2D RDF's verder de laterale expansie van het lipidemembraan aan.

Studie naar het inactivatiemechanisme van chemische ontsmettingsmiddelen. Het interactiemechanisme van chemische middelen met SARS-CoV-2 is theoretisch onder-

zocht met behulp van MD- en DFT-berekeningen. Voor het geval van 3CL hydrolase tonen de resultaten aan dat de biociden zich bij voorkeur binden aan de onverzadigde zuurstofatomen van 3CL hydrolase. De interactie is afhankelijk van de concentratie van de biociden. Onder de verankerde structuren zijn de ingrediënt-S1-conformaties gunstiger dan andere conformaties, in die zin dat de actieve ingrediënten aan S2 of S3 zijn verankerd. Hun bindingsenergieën en ladingsoverdracht zijn prominenter dan respectievelijk 0,5 eV en 0,1 *e*. De structurele parameters van het lipidemembraan tonen aan dat de aanwezigheid van biocidale ingrediënten de bilaagstructuur van SARS-CoV-2 zou veranderen, zoals laterale zwelling en progressieve verdunning, en HClO in het bijzonder. Met toenemende concentratie bevinden zich meer ingrediëntmoleculen in het centrum van de bilaag. Net als in het geval van 3CL hydrolase geven de ingrediëntmoleculen er de voorkeur aan zich te binden aan de onverzadigde zuurstofatomen van de lipidemoleculen. 2D RDF's van P-P en N-N atoomparen suggereren rechtstreeks dat de laterale afstand tussen twee P of N atomen van de lipidekopgroepen toeneemt, hetgeen de oorzaak van de laterale zwelling van het bilaagmembraan illustreert.

Studie naar het inactiveringsrecept en het mechanisme van UVC-bestraling. De inactiveringsexperimenten voor Influenza A PR8 worden uitgevoerd op het ontworpen UVC-LED-platform om het optimale inactiveringsrecept te onderzoeken. Uit de beschikbare resultaten blijkt dat het schema met twee golflengten geen duidelijk voordeel heeft ten opzichte van het schema met één golflengte. De golflengte van 259 nm vertoont de optimale inactivering voor Influenza A PR8. Om het inactiveringsmechanisme van UVC-bestraling voor het virus op molecuulniveau te onthullen, worden de spectrale eigenschappen van vier nucleotiden onderzocht met behulp van kwantumchemische berekeningen. Voorts worden ook de overgangstoestand en de reactiesnelheidsconstante van uracilmoleculen beschouwd om de moeilijkheidsgraad van de dubbele-uracilreactie in afwezigheid en aanwezigheid van UVC-bestraling te bepalen. Uit de absorptiespectra blijkt dat de golflengten van de absorptiepieken 248,7 nm, 226,1 nm (252,7 nm), 248,3 nm en 205,8 nm (249,2 nm) bedragen voor respectievelijk adenine, cytosine, guanine en uracilmoleculen. Deze golflengten liggen dicht bij de in het experiment verkregen optimale golflengte. Het belangrijkste is dat de reactiesnelheid van dubbel-uracil naar verwachting $6{,}419\times10^{-49}$ en $5{,}436\times10^{11}$ s^{-1} M^{-1} zal bedragen voor de grondtoestand en de aangeslagen toestand. De halfwaardetijd voor de grondtoestand en de aangeslagen toestand is respectievelijk $1{,}56\times10^{48}$ en $1{,}84\times10^{-12}$ s, wat betekent dat de moleculaire reactie tussen aangrenzende nucleotiden bijna niet kan plaatsvinden bij afwezigheid van UVC-bestraling.

Studie naar de virale inactivatie en het mechanisme van elektrische velden gegenereerd door micro-elektroden. De inactiveringsexperimenten worden uitgevoerd op drie micro-elektroden, vervaardigd op microchips. Het phi-6-virus is gekozen als alternatief voor SARS-CoV-2 in deze studie. Gebleken is dat de out-of-phase castellated microelektrode een betere antivirale activiteit vertoont dan de interdigitated en de in-phase castellated micro-elektroden vanwege de hogere titerreductie. Ondertussen is er geen significante virale inactivatie na DC-behandeling. Na AC-behandeling daarentegen wel. Bovendien vermindert een AC-behandeling met hoge frequenties de virale titer aanzienlijk meer dan met lage frequenties. Ook blijkt dat de titervermindering sterk afhangt van de geleidbaarheid en de virusconcentratie van de virusmonsters. Hier wordt ook de in-

activering van E. coli op micro-elektroden geëvalueerd. De resultaten tonen aan dat de inactivering van E. coli sterk afhankelijk is van de wisselspanning en -frequentie. De morfologische structuur van E. coli toont aan dat het lipidenomhulsel wordt beschadigd door elektrische velden, wat leidt tot de dood van omhulde ziekteverwekkers. Om uiteindelijk het effect van elektrische velden op virussen bloot te leggen, wordt de dynamiek van het lipidemembraan bij variërende elektrische velden onderzocht. Uit de gesimuleerde resultaten blijkt dat elektrische velden van minder dan 250 mV/nm niet leiden tot verstoring van de bilaagstructuur, zelfs niet na 200 ns. Het bereiken van 250 mV/nm resulteert in de onmiddellijke instorting van de bilaag bij ongeveer 130 ns. De structurele informatie bij verschillende elektrische velden levert ook robuust bewijs voor dit verschijnsel. Daarom is 250 mV/nm het drempelveld waarbij de lipidemembraanbreuk plaatsvindt.

1

INTRODUCTION

Viruses, as the causative agent of viral diseases, have been the cornerstone of the evolution of the human genome. However, they are also one of the primary causes of mortality in human evolution. Therefore, to effectively prevent invading viruses, tremendous ongoing efforts and research in inactivation methods and technologies have been undertaken. Many methods and technologies with high effectiveness, including chemical, physical, and interdisciplinary methods, have been widely utilized in various health domains. In the absence of vaccines for novel viruses, these existing methods and technologies are powerful tools for controlling the spread of viral diseases. Nevertheless, it is unknown whether the positive effect of these methods can persist in new viral inactivation and their inactivation mechanisms at the molecular level. Moreover, discovering safe and efficient methods for virus disinfection is still considered a significant technical challenge. Consequently, it is worth investigating the underlying mechanism of the inactivation of distinct disinfection methods against viruses in depth to provide a theoretical fundament for developing antiviral methods and technologies.

1

1.1. BACKGROUND

In recent years, several viruses with pandemic potential, namely, SARS-CoV-2 [1], SARS-CoV [2], MERS-CoV [3], Ebola [4], HCoV-229E [5], HCoV-OC43 [6], HCoV-NL63 [7], HCoV-HKU1 [8], have emerged, which pose a severe threat to human health and the global economy. Nowadays, more than 200 countries and territories on a global scale are affected by the COVID-19 disease pandemic, with a total of 490,853,129 confirmed cases, including 6,155,344 associated deaths giving a case-fatality rate of 1.25% [9]. In order to better control infection and combat the spread of the epidemic, many countries have adopted non-pharmaceutical interventions, such as the inactivation of SARS-CoV-2. Unfortunately, the RNA genome of SARS-CoV-2 is constantly mutating, and the reassortment of the segmented genome leads to the formation of new virus subtypes/strains that may have novel pathogenic characteristics [10]–[12]. The SARS-CoV-2 genomic variation poses an immense challenge to the existing inactivation methods and techniques. To date, many scientific studies focusing on novel inactivation methods have made tremendous achievements and reached substantial milestones [13]–[20]. Nevertheless, most of the efforts put the spotlight on the effectiveness and efficiency of viral inactivation methods. The underlying mechanism that deeply reveals the viral inactivation at the molecular level is still unclear and debated. Besides, most the conventional disinfection methods suffer from some drawbacks, such as the generation of harmful by-products or indistinguishable inactivation [21]. Here, to get insight into viral functions and structures, the coronaviruses are chosen as the interpreting representative due to their lethality and relevance to humans.

1.2. OVERVIEW OF CORONAVIRUSES

1.2.1. CORONAVIRUSES

Coronaviruses (CoVs), a family of Coronaviridae within the superfamily of Nidoviales, are enveloped viruses that possess a linear single-stranded positive RNA genome [8], [22]. With genomes ranging from 27 to 32 kilobases (kb), CoVs have the largest genomes in discovered RNA viruses [23]. CoVs are classified phylogenetically into four genera, namely, α-coronavirus, β-coronavirus, γ-coronavirus, and δ-coronavirus [24]–[26], as shown in Figure 1.1 . CoVs primarily cause a variety of fatal diseases in mammals and birds, having an enormous impact on the poultry industry. Most importantly, CoVs are able to cross species barriers to infect humans and induce respiratory, enteric, hepatic, and neurologic diseases [27]. Up to now, seven strains of β-coronavirus including HCoV-229E, HCoV-HKU1, HCoV-NL63, HCoV-OC43, SARS-CoV, MERS-CoV, and SARS-CoV-2 have been identified. Thereinto, HCoV-229E, HCoV-HKU1, HCoV-NL63, and HCoV-OC43 typically cause upper respiratory tract illnesses with mild to moderate symptoms. In contrast, SARS-CoV, MERS-CoV, and SARS-CoV-2 can replicate in the lower respiratory tract, triggering severe and potentially fatal pneumonia. The genome-wide phylogenetic analysis indicates that SARS-CoV-2 has an 88~89% sequence similarity to two bat-derived SARS-like CoVs (i.e., bat-SL-CoVZC45 and bat-SL-CoVZXC21). In contrast, it is quite distant from SARS-CoV (~79%) and MERS-CoV (~50%) [28].

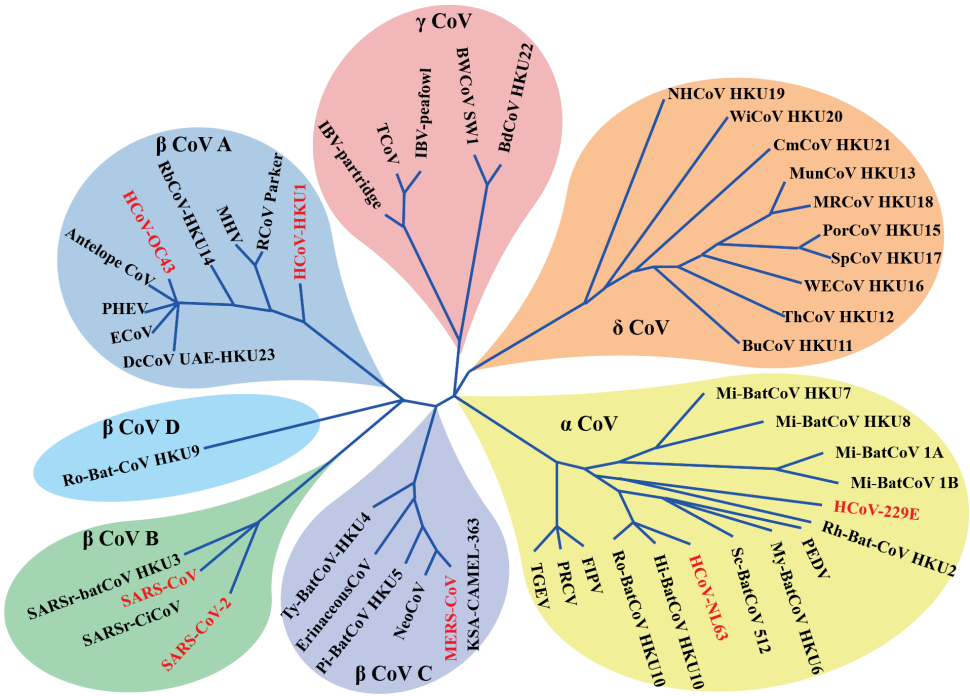


Figure 1.1: Phylogenetic classification of coronaviruses [29].

1.2.2. STRUCTURAL PROTEINS AND THEIR FUNCTION IN COVS

CoV particles are roughly spherical in the shape, approximately 80 to160 nm diameter [30], containing four major structural proteins (as plotted in Figure 1.2), namely, spike (S) protein (outer spiky glycoprotein), membrane (M) protein (a type III transmembrane glycoprotein), nucleocapsid (N) protein (within the phospholipid bilayer), and envelope (E) protein [31]. These structural proteins are encoded by the sub-genomic RNA (sgRNA) within the 3' end of the viral genome. Moreover, a minority of CoVs have a hemagglutinin-esterase (HE) protein on the viral surface.

S protein, a 150 kDa glycoprotein, contains an N-terminal signal sequence, which is heavily N-linked glycosylated at the endoplasmic reticulum (ER). The distinctive spike structure of CoVs, shaping crown-like projections on the viral surface, is composed of a homologous trimer of S protein [33]. Moreover, as a trimeric class I viral fusion protein, S protein is divided into two functionally interdependent subunits, a receptor-binding subunit S1, and a membrane-fusion subunit S2. The S1 subunit is constituted by the N-terminal domain (NTD), receptor-binding domain (RBD), and signal peptide. The S2 subunit comprises two heptad-repeat regions, called HR-C and HR-N, which form a coiled-helix structure surrounded by outer structural domains of proteins [34]. The entry of CoVs into host cells is attributed to the S1 and S2 subunits of the S protein. The S1 subunit is able to anchor the primary cellular receptor, angiotensin-converting enzyme 2 (ACE2), and the S2 subunit is responsible for the fusion of viral and cellular membranes.

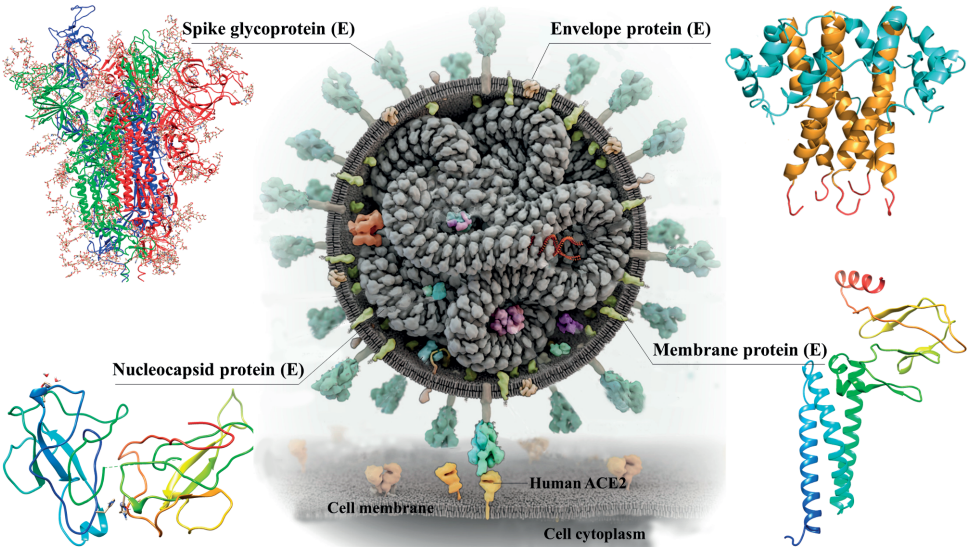


Figure 1.2: Schematic diagram of structural proteins in CoVs [32].

The furin cleavage sites are present at the interface of S1 and S2 subunits that are processed during biogenesis [33]. In addition to the ACE2 receptor, the transmembrane serine protease 2 (TMPRSS2) protein is also a significant target of CoVs, playing a critical role in initiating the entry of viruses into the host cells [35]. The S protein is cleaved through interacting with cellular proteases, TMPRSS2, and cysteine protease (cathepsin B/L), which allows viral entry into the susceptible host cells [34].

M protein, a 25~30 kDa transmembrane glycoprotein, is the most abundant protein in CoVs. It has a triple-helix bilayer with a short NH2-terminal structural domain in the extracellular region and a COOH-terminal in the cytoplasmic region. Besides, the M protein contains an N-terminal glycosylated ectodomain at the N-terminus, which consists of three transmembrane domains and a long C-terminal domain [36]. In host-pathogen interactions, the primary function of the M protein is to induce virus-specific humoral responses. Meanwhile, it also can neutralize antibodies produced by SARS patients. In addition, the transmembrane domain of the M protein likely contains a cluster of T-cell epitopes that are primarily cellular immunogenic [37]. The M and E proteins are indispensable for virus morphogenesis, assembly, and budding.

E protein, an 8~12 kDa transmembrane protein, functions as an ion channel, enabling human proteases to release the viral genome to access the cytoplasm [38]. The ion channel activity in the E proteins of CoVs is not essential for CoV replication in infected cells, but it plays a role in viral pathogenesis. It possesses two domains, the N-terminal and C-terminal endodomains. At the same time, it is found in small quantities of the E protein within CoVs. E proteins in CoVs are extremely divergent due to the differences in genetic sequence but have a typical architecture [33], [39]. The E protein is the smallest structural protein and perhaps the most enigmatic of the four main structural proteins. Interestingly, the absence of E proteins in recombinant CoVs results in

lower viral titers and crippled viral maturation, even yielding propagation incompetent progeny [33], [40]. Therefore, this confirms that the E protein is an essential structural protein for virus production and maturation. Although the E protein is abundantly expressed inside infected cells and is essential for viral assembly and release, only minimal portions are embedded within the lipid envelope.

N protein, a 50~60 kDa phosphorylated nucleocapsid protein [41], is the only protein in the nucleocapsid. It includes an NTD and a C-terminal domain (CTD) that are capable of binding the genetic material through distinct mechanisms. It is thought that optimal RNA binding requires contributions from both NTD and CTD [33]. The high phosphorylation of the N protein is thought to induce its structural changes, which could increase the affinity of viral to nonviral RNA. N proteins are involved in packaging the positive-sense single-stranded RNA genome in a beads-on-a-string type conformation. Genomic packaging signal (GPS) and transcription regulatory signal (TRS) are specific RNA substrates that can induce N protein-RNA binding [41]. It has been found that GPS is specifically bound to the second or C-terminal RNA binding domain [33]. Indeed, the nsp3 protein, a vital component of the replicase complex, also interacts with the N protein. Meanwhile, the binding between the N and M proteins is also found in CoVs. These protein bindings favor the linking of the virus genome to the replicase-transcriptase complex and the subsequent assembly of the encapsulated genome into CoV particles.

1.2.3. GENETIC STRUCTURE IN COVS

The RNA genome of all CoVs is organized into three regions, a 5' nonstructural protein (nsP) coding region with the replicase genes, a 3' structural protein coding region, and a nonessential accessory protein coding region. The 5' cap structure and a 3' poly (A) tail enable the genome to act as a messenger RNA (mRNA) to translate the replicase polyproteins [33]. The replicase genes associated with nsPs occupy two-thirds of the genome (~20 kb), while structural and accessory proteins occupy only ~10 kb of the viral genome. There are seven to nine viral-specific mRNAs with coterminal 3' ends in virus-infected cells [42]. The 5' end of the genomic RNA involves the leader sequence and the untranslated region (UTR) with the RNA stem-loop structures. These stem-loop structures can function in genome replication and transcription. Furthermore, the transcriptional regulatory sequences are essential for the expression of each structural or accessory gene, located at the beginning of these genes. The RNA structures associated with viral RNA replication and synthesis are also found in the 3' UTR. The CoV genome is organized as a 5'-leader-UTR-replicase-S-E-M-N-3' UTR-poly (A) tail, and accessory genes, such as open reading frame genes (ORFs), are interspersed within the structural genes at the 3' end of the RNA genome [43], as described in Figure 1.3. In tissue culture, most ORF proteins encoded by the accessory genes are almost exclusively unrequired. Nevertheless, some of them, such as ORF3a and ORF6, have been observed to play substantial roles in CoV pathogenesis [43], [44].

1.2.4. PATHOGENIC MECHANISM OF COVS

The entry of CoVs into the host cells is an essential determinant of disease pathogenesis, mediated by S proteins. During the establishment of CoV infection, the RBD of the S protein binds to the cellular receptor, ACE2 and a C-type lectin (also named CD209L)

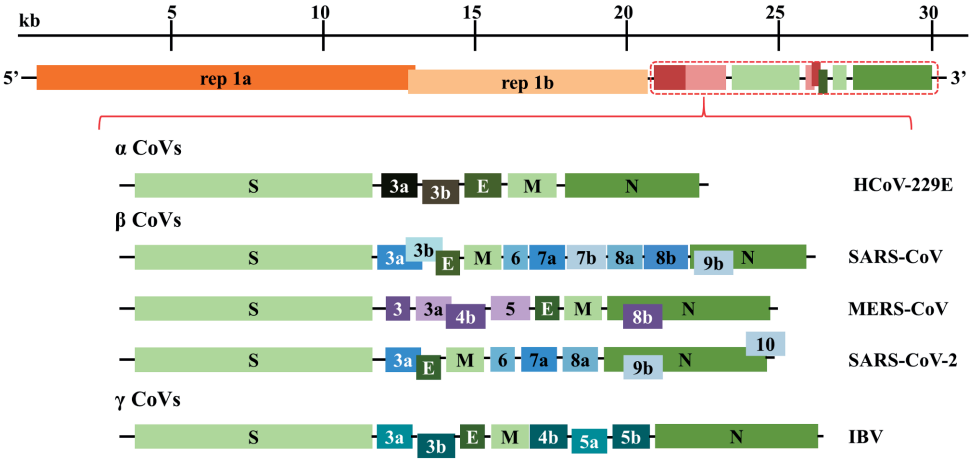


Figure 1.3: Genomic structures of the representative viruses of α-CoVs, β-CoVs, and γ-CoVs[33], [45]. The genome at the top of the illustration is representative of the MHV virus. The structural and accessory proteins within the 3' regions of HCoV-229E, SARS-CoV, MERS-CoV, SARS-CoV-2, and IBV are depicted in the expanded region.

for SARS-CoV, dipeptidyl peptidase 4 (DPP4, also called CD26) for MERS-CoV, and ACE2 for SARS-CoV-2 [45]. Previous studies have presented that the pathogenesis of CoV infections in humans and animals is mainly attributed to the papain-like protease (PLpro) mediated mechanism, DPP4 mediated mechanism, and accessory proteins mediated mechanism [46]. Figure 1.4 clearly shows the life cycle of human CoVs in the host cells.

PLpro mediated mechanism. Two cysteine proteases, PLpro and 3-chymotrypsin-like protease (3CLpro) cleave the replicase polyprotein into 15~16 nsPs involved in forming the membrane-associated replication complex. In addition to the protease activity in CoVs, PLpro is a multipurpose enzyme with designation and deubiquitination features [46], which contributes to the resistance against the host antiviral immune response and facilitates CoV replication. Moreover, PLpro can impede MAVS (mitochondrial antiviral signaling protein) triggered IFN-β (beta interferon) reporter behavior and reduce TNF-α (tumor necrosis factor-alpha) induced NF-κB (nuclear factor-kappa B) reporter events.

DPP4 mediated mechanism. Structural studies focusing on the DPP4 receptor reveal that this receptor comprises an α-/β-hydrolase domain and an eight-blade β-propeller domain, capable of binding to the RBD in CoVs [46]. ADA (adenosine deaminase), a DPP4-conjugating enzyme, is considered one of the vital blockers of the CoV S protein [48]. Structurally, the S protein contains two ectodomains, FD (fusion-catalyzing domain) and RBD. The RBD of S proteins is attached to DPP4 and then exhibits FDs by unfolding. The host proteases cleave the CoV S protein with the assistance of unfolding FDs. For CoV infection in target cells, sequential cleavage at two specific proteolytic cleavage sites between RBD and FD is essential. Upon infecting the host cells, it can be observed that IP10 (IFN-γ-inducible protein-10) and MCP-1 (monocyte chemoattractant protein-1) is stimulated, and human myeloid progenitor cell proliferation is inhibited. T cells in mammalian lymphoid organs can be contaminated with CoVs [49],

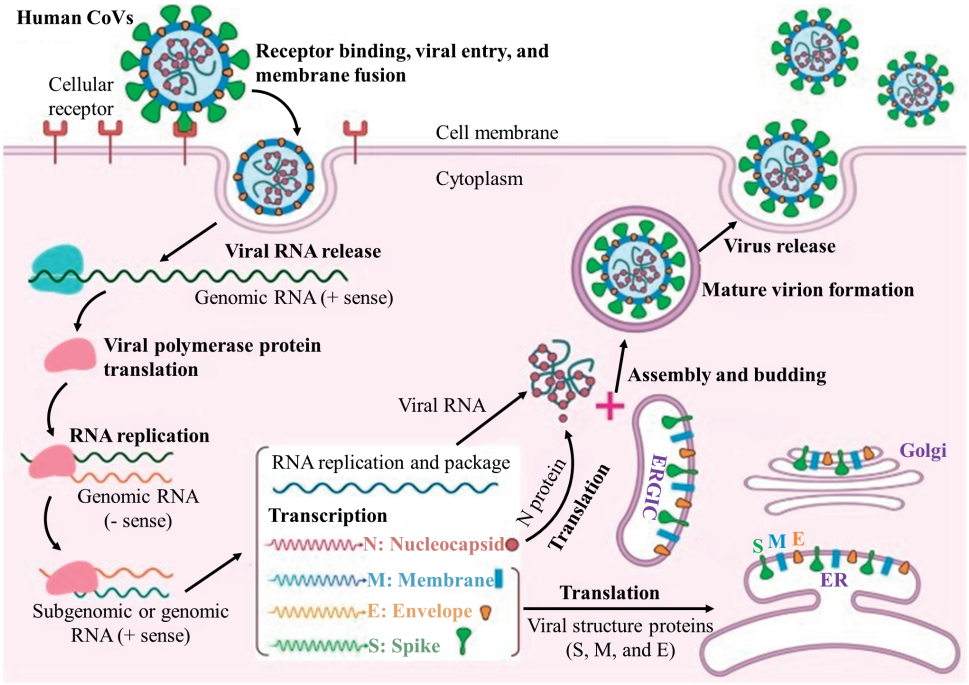


Figure 1.4: Schematic of human CoV infection [47].

which induces apoptosis through intrinsic and extrinsic pathways [50]. Previously, a study found that the initiation of transcriptional repressor and negative TLR signaling regulators become less efficient when inactivating DPP4, indicating that DPP4 controls the immunosuppressive intervention of the S protein [51].

Accessory proteins mediated mechanism. Owing to the existence of TLR3 (endosomal toll-like receptor 3), RIG-1 (retinoic acid-inducible gene-1), and MDA5 (melanoma differentiation-associated protein-5), the virus genome is recognized as PAMPs (pathogen-associated molecular patterns). CoVs can utilize proteins such as ORF 4a that comprises RBD for attachment in the case of excluding RIG-1 and MDA5 [46]. The motif overlaps the dsRNA of CoVs through a simple attachment. The ORF 4a contains an $\alpha\beta\beta\alpha$ fold in which a β1-β2 loop and α1 helix binding to the small dsRNA groove can be observed. It was proposed that NF-κB is maintained in the cytoplasm of infected cells, whereas ORF 4b is thought to be associated with the nucleus. Besides, the distribution of pro-inflammatory cytokines was found to be transferred to the nucleus in the form of NF-κB in the absence of ORF 4b. It was also found in the ORF 4b mutants without nucleus localization signals (NLSs), which indicates that the ORF 4b-controlled mechanism of NLSs is required for NF-κB expression [46], [52]. In the ER-Golgi complex, N proteins interact with the other three structural proteins (i.e., E, M, and S), which prevents the fusion of the cell and virus membranes [46], [53]. The interaction of CoV M proteins with TRAF3 (tumor necrosis factor receptor-associated factor 3) disrupts TRAF3-TBK1 (TANK binding kinase 1) association, contributing to reducing the activation of IFN regulatory

factor 3 [53].

Table 1.1: Generally accepted modes of respiratory transmission [54].

Transmission modes	Particles involved and their properties	Characteristics/definition of transmission
Contact		Self-inoculation of mucous membranes with contaminated hands
Direct	Deposited on person	Viruses are transferred from an infected to another
Indirect	Deposited on objects	Viruses are transferred through contaminated intermediates (fomites)
Airborne		
Droplet	Droplets (>5 μm)	Short distance transmission
	Only stay in the air for a short time (<17 min)	Direct inoculation to naive person through coughing/sneezing/breathing of an infected
	Dispersed over short distances (<1 m)	Mainly deposited on the mucosa and upper respiratory tract
Aerosol	Aerosols, droplet nuclei (<5 μm)	Long distance transmission
	Stay in the air for an almost infinite amount of time	Inhalation of aerosols in the respirable size range
	Dispersed over long distances (>1 m)	Deposition along the respiratory tract, including the lower respiratory tract

1.2.5. TRANSMISSION MODES OF COVS

The main transmission routes of CoVs are classified into animal-to-human and human-to-human, wherein the human-to-human route contains contact transmission, droplet transmission, and aerosol transmission, as listed in Table 1.1. Viral, host, and environmental factors affect each mode's transmission possibility. Contact transmission includes direct (physical contact) and indirect (fomite) transmission, defined as the direct transfer of CoVs from an infected individual to a susceptible host or the indirect transfer of CoVs through the contaminated intermediate objects [54], [55]. Airborne transmission of CoV particles can happen via aerosols and droplets. Typically, 5 μm is an acceptable cut-off between the large droplets and small aerosols, even if there are considerable variations between studies, up to 12 μm [56]–[58]. Droplets released from talking, sneezing, breathing, or coughing are not suspended in the air and travel less than 1 m before landing on the environmental surfaces or the mucous membranes of close contact [54]. In comparison, aerosols are small enough and slowly settle on objects. Thus, they can

stay suspended in the air for prolonged periods and travel longer distances [59], [60].

1.3. INACTIVATION APPROACHES FOR COVS

Historically, the outbreak of each worldwide pandemic due to CoVs and their associated diseases, in particular SARS-CoV-2, stimulated an enormous effort of public health institutes and governments on the disinfection campaigns of public facilities and community settings. Many published studies focusing on the survival of CoVs in different environmental conditions suggested that CoVs can retain their infectiousness and bioactivity for periods ranging from a few minutes to weeks on surfaces of different materials [61]–[65]. Therefore, in order to minimize the chance of viral infection, adopting practical approaches to deactivate CoVs and eliminate their infectivity is highly required. Depending on the technology route, disinfection approaches are commonly classified into chemical and physical inactivation approaches.

1.3.1. CHEMICAL INACTIVATION APPROACHES

Various biocidal chemical compounds, such as medical ethanol (75%), sodium hypochlorite (3%~6%), and 2-propanol (70% or 80%) have been powerful antiviral and antimicrobial agents, having been widely used for the inactivation of viruses and pathogens. The World Health Organization (WHO) recommended that alcohol-based hand sanitizer (at least 60% ethanol or 70% propanol) can be the common handwashing agent in the absence of soap and water [66]. Moreover, alcohol with 70%~90% concentration used for surface disinfection exhibits a similar inactivation effect against CoVs [9], [67]. Hydrogen peroxide, one of the oxidizing agents, induces viral deactivation by oxidizing proteins and denaturing them. Its optimal antiviral activity concentration is at 1%~3%, which can deactivate SARS-CoV within one minute [68]. In the gas phase, it has greater potency. Compared to hydrogen peroxide, peroxyacetic acid at lower concentrations (0.3%) is more effective against a broad spectrum of pathogens [68]. Thus, it is often used to sterilize medical devices. Due to its low toxicity, broad biocidal activity, low cost, and availability, sodium hypochlorite has become one of the most used household disinfectants. Reported studies show that sodium hypochlorite with a concentration of 0.1%~0.5% effectively disinfection human CoVs [69], [70]. Its minimum concentration is 0.001%, which also can effectively deactivate certain types of viruses in less than one minute [71]. Interestingly, when the concentration of sodium hypochlorite is 0.6%, it requires prolonged contact time to deactivate the viruses [71]. In the cleaning and disinfection of environmental surfaces, sodium hypochlorite at a concentration of 0.1%, recommended by the WHO, acts as an antiviral agent against SARS-CoV-2, and its contact time must ensure for at least one minute [9], [72]. Two biocidal agents, formaldehyde (0.7%~1%) and glutaraldehyde (0.5%~2.5%) are considered advanced disinfectants for medical and surgical instruments [68], [73]. Both compounds are capable of deactivating several CoVs (e.g., SARS-CoV-2) [74]. However, as a human carcinogen, the use of formaldehyde is discouraged. The deactivation efficacy of formaldehyde and glutaraldehyde against human CoVs is dependent on temperature. At 25 °C, glutaraldehyde entirely inactivates SARS-CoV by day 2, whereas it can completely deactivate SARS-CoV by day one at 37 °C [69]. Formaldehyde at a concentration of 0.5%~2% effectively inacti-

vates SARS-CoV-2 after one hour at room temperature [75]. However, the deactivation time against human CoVs decreases to 32.5, 3.7, and 2.5 minutes when the temperature increases to 60 °C, 80 °C, and 100 °C, respectively [76]. Silver and its compounds present a broad spectrum of antimicrobial action against various bacteria, fungi, and viruses. The virucidal activity studies displayed that silver ions possess virucidal efficacy against SARS-CoV and SARS-CoV-2 [77]–[79]. Meanwhile, silver nanoparticles at concentrations ranging from 1 to 10 ppm are also highly powerful microbicides against various human pathogenic viruses, including SARS-CoV and SARS-CoV-2 [80]. In addition, several metal-based nanoparticles, including zinc (Zn), copper (Cu), titanium (Ti), copper oxide (CuO), and zinc oxide (ZnO), have also shown antiviral potential [79], [81]. Recently, it has been found that stainless steel with 20 wt% Cu can significantly reduce the surface viability of SARS-CoV-2 by 99.75% and 99.99% within 3 hours and 6 hours, respectively [13].

1.3.2. PHYSICAL INACTIVATION APPROACHES

At present, the most commonly used physical approaches for inactivating viruses are classified into three categories, namely, high pressure (most often used for food sterilization), heat inactivation (applied to viruses in solution or dried on a surface), and irradiation (applied to viruses in solids, in solutions, or dried on surfaces) [82]. The irradiation methods involve electron beam irradiation, X-ray irradiation, gamma-ray irradiation, and ultraviolet light (UV, 100~400 nm) irradiation. The interaction of UV light with molecules can be separated into four wavelength bands: UVV at 100~200 nm, UVC at 200~280 nm, UVB at 280~320 nm, and UVA at 320~400 nm. UVA and UVB light are responsible for photocarcinogenesis and photoaging, but UVA light is a relatively weak complete carcinogen compared with UVB light [83]. Therefore, UVA light requires the addition of photoactive chemicals (e.g., titanium dioxide and psoralens) to enhance its germicidal and disinfection effects [84]. UVV light harms human health because it reacts immediately with oxygen atoms and organic molecules, even at low doses [84]. Due to its strong absorption by air, UVV light is usually not used for disinfection. Among four UV bands, UVC light possesses the most potent antibacterial and antiviral properties, and its efficacy for inactivating viruses (e.g., CoVs) has been confirmed by available scientific literature [85]. A study in UVC lethal dose for SARS-CoV-2 demonstrates that UVC is capable of deactivating more than 99% of SARS-CoV-2 in less than one second when the lethal dose is 0.706 mJ/cm^{-2} [86]. Meanwhile, 90% and 99.999% viral inactivation are reached at 0.016 mJ/cm^{-2} (0.01 second) and 108.714 mJ/cm^{-2} (49.42 seconds), respectively [86]. Gamma irradiation is ideal for pathogen reduction in plasticware due to the high penetrability and energy, especially tissue culture flasks, bottles, pipette tips, and pipettes [82]. A sufficiently high fluence could inactivate any microorganisms and viruses on the surface of the objects. For sterilization of frozen or liquid solutions, the interaction mode of gamma irradiation with the solutions depends on many factors, such as the temperature of the solution or the presence of radiation-scavenging compounds. At very low temperatures (e.g., -78 °C), microorganisms or viruses are less radiosensitive, which indicates that the inactivation efficacy of gamma irradiation is weak. On the contrary, the radiosensitivity of living organisms for gamma irradiation is enhanced at temperatures above freezing, but the original functions of the irradiated samples may be degraded.

For instance, the required dose for the inactivation of Escherichia coli is 0.41 kGy at 5 °C, whereas at -15 °C, it is 0.62 kGy [87]. As expected, CoVs, including SARS-CoV, MERS-CoV, and SARS-CoV-2, are highly radiosensitive to gamma irradiation. The inactivating efficacy of gamma irradiation on SARS-CoV, MERS-CoV, and SARS-CoV-2 is higher than 12 log10 when the irradiation dose is set to 25 kGy [82]. Similar to gamma irradiation, heat also has a high penetrability depending on the inactivating matrix. Most viruses, including enveloped and non-enveloped viruses, are high thermal-sensitive, thus heat is a commonly applied approach for deactivating viruses in solutions or on surfaces. In general, heat inactivation contains wet and dry heating. In comparison, wet heating for inactivating viruses is more effective than dry heating [82]. Many laboratories have investigated the efficacy of heat inactivation on CoVs at different exposure temperatures and times [75], [88]–[90]. At a temperature of 48∼54 °C, the deactivation of CoVs may be incomplete when the exposure time achieves 60 minutes [82]. Nevertheless, 10 minutes or more exposure time at temperatures ≥ 56 °C for inactivating CoVs is quite effective. For a temperature of ≥ 80 °C with an exposure time of one or two minutes, this condition presents an excellent inactivation effect for CoVs. High-pressure processing is one of the significant nonthermal technologies applied to deactivate foodborne microorganisms. Using high-pressure processing in food items can maintain freshness and extend shelf-life [91]. In addition to the above approaches, electric fields pose a potential probability of inactivating viruses. The published study has suggested that the S protein of SARS-CoV-2 is susceptible to electric fields, thus it could be a clean physical approach to inactivate SARS-CoV-2 without further biochemical treatment [19].

1.4. INACTIVATION MECHANISMS FOR PATHOGENS

The action mechanisms of chemical and physical inactivation methods can be summarized into three aspects: damage to the phospholipid membrane of viruses or the cytoplasmic membrane of microorganisms, protein denaturation (leading to inhibition of enzyme activity), and destruction of nucleic acids [92]. According to the action spectrum, the deactivation process can be achieved at three different levels, namely, high-level disinfectants deactivate all microorganisms (except for large numbers of bacterial spores); medium-level ones can inactivate Mycobacterium tuberculosis, bacterial trophic organisms, and most viruses and fungi, but do not all bacterial spores; low-level ones can damage most plant-based bacteria (e.g., Pseudomonas species and Salmonella species), some viruses (e.g., hepatitis B viruses and HIV), and fungi [92]. The alcohol-based disinfectants lead to the damage of membranes and denaturation of proteins but do not compromise RNA integrity [93], which supports the hypothesis that alcohol-based disinfectants target the viral envelope. The underlying mechanism of protein denaturation can be attributed to the damage of disulfide, hydrogen, and hydrophobic bonds [94]. The oxidizing agents, such as sodium hypochlorite and hydrogen peroxide, inactivate viruses by utilizing the oxidizing capability. It is reported that the hypochlorite molecule of sodium hypochlorite can react with peptide bonds and sulfhydryl groups to oxidize proteins and other biomolecules and eliminate their function chemically [95], [96]. Similarly, hydrogen peroxide utilizes hydroxyl radicals to cleave RNA or DNA backbone, disrupt biological membranes and sulfhydryl bonds in proteins and enzymes, ultimately causing nucleic acid degradation and protein denaturation [96]. Metal ions

can react directly or indirectly on the outside or inside of viruses to deactivate viruses. Mostly, their oxidation power is responsible for the inactivating capability. Silver ions' three possible mechanisms of action for sterilization and disinfection are proposed, including interaction with a lipid membrane, binding with DNA or RNA, and denaturing proteins [77]. Silver ion shows a strong affinity for biomolecules containing sulfur, oxygen, and nitrogen [97]. Thus, it easily attaches to the negatively charged molecules of viruses. Some studies have suggested that HCoVs are less sensitive to most physicochemical changes compared to many enveloped viruses [98]. Similar to chemical interventions, most physical treatments inactivate viruses by denaturing structural proteins and interfering with the effective interaction of viruses with host cells [99]. For thermal treatment, it is confirmed that the major causes of HCoVs inactivation are the denaturation of structural proteins (e.g., N and S proteins) and RNA degradation [99], [100]. As for heat treatment, UVC irradiation can effectively deactivate viruses by damaging genomes and proteins. However, compared with viral capsid proteins, UVC light has a more significant effect on nucleic acids because only about one-tenth of amino acid residues in proteins is sound UV absorbers [101]. Due to the excellent UV absorption of nucleotide bases, pyrimidine dimers or pyrimidine (6-4) pyrimidine lesions are easily formed. These genetic mutations may inhibit genome replication or genome injection, causing the loss of the original virulence of viral particles. Unlike UVC irradiation, it is commonly understood that the inactivation mechanism of electric field treatment is envelope damage, primarily through the formation of nanopores [102]–[104]. Furthermore, a simulation study confirms that an electric field could induce denaturation of the S protein (especially the heptad repeats 2 domain) of SARS-CoV-2, blocking the viral-membrane fusion.

1.5. PROBLEMS IN THE METHODS AND MECHANISMS OF VIRAL INACTIVATION

Numerous approaches (e.g., chemical oxidation, UVC irradiation, electric fields, and heating) for inactivating viruses have been widely used in the disinfection of food, water supplies, public facilities, medical instruments, and vaccine production for decades or even centuries. Surprisingly, however, very little is known about their biocidal activity. A prevailing perception of disinfection methods is that as long as they are effective, there is little reason (other than academic merit) to study how they achieve an inhibitory or lethal effect [105]. So far, relevant studies on deactivation kinetics have revealed the action mechanism of virus inactivation by chemical and physical methods at the experimental level [93], [99], [101]. Nevertheless, detailed interaction understanding between active components and viruses at the molecular level is largely not well uncovered, especially the inactivation mechanism of SARS-CoV-2. Highly related viruses may also display different kinetics when treated with the same methods or conditions [99]. As a result, this complicates virus inactivation. For instance, under the same conditions, the lethal effect of monochloramine for echovirus 1 is more significant than for echovirus 11 [106]. Likewise, such a phenomenon was observed in inactivation experiments of poliovirus I (Brunhilde) and poliovirus I (Mahoney). The result shows that the resistance of poliovirus I (Brunhilde)'s resistance to chlorine in water is twice as high as that of the

very similar poliovirus I (Mahoney) [99]. Such inactivation variabilities clearly exhibit that minor structural or genomic variations can dramatically impact on viral resistance to inactivation. The damage detected in proteins and nucleic acids reveals the underlying cause of viral inactivation [93], [95], [97], [100]. However, in many such reports, the experimental analysis focuses on the characterization of protein function/structure and the analysis of gene expression, and there is no more microscopic analysis. Furthermore, only a tiny fraction of viral particles is detected. Accordingly, the specific interaction mechanisms between biomolecules and biocidal components are largely unclear. For example, what type of reaction occurs between the acting substances and the target molecules, and what is their reaction process? An in-depth understanding of viral inactivation at the molecular level will potentially guide the development and optimization of biocidal methods, specific therapeutic bio-drugs, and vaccine production.

Meanwhile, with the advancement of industrial semiconductor technology, energy-saving, cost-effective, and eco-friendly light-emitting diodes (LEDs) are designed as light sources. LEDs are considered an alternative to traditional UV irradiation sources due to mercury-free and high reliability [107]. A variety of semiconductor materials have been widely explored for the design of LED devices. The reported semiconductor materials utilized in LEDs include GaN-related materials, silicon carbide (SiC), aluminum nitride (AlN), Ga_2O_3, GaAsP, and gallium phosphide (GaP) [108]–[111]. LED devices are capable of emitting different wavelengths of light because of differences in these material characteristics. Each of these lights can be matched to a specific pathogen. Unexpectedly, LEDs also can emit light with various wavelengths simultaneously [112]. This feature offers the possibility of inactivating viruses in an integrated multi-wavelength LED system [113]–[115]. Moreover, the combination of different wavelengths of UV treatment exhibits a better inactivation effect [116]. Numerous efforts have proved the effects and advantages of UV-LED treatment, whether employing single-wavelength UV-LED or a multi-wavelength UV-LED array combining UVA, UVB, and UVC wavelengths [117]. However, most studies mainly focus on the lethal effect of UV-LEDs, and the efficient inactivation recipe, the inactivation tendency, and the corresponding inactivation mechanism of UVC-LEDs against viruses are still unclear. Thus, it is meaningful to address these issues for the disinfection and treatment of SARS-CoV-2 and its variants.

In addition, many theoretical and experimental studies have demonstrated that electric fields could induce conformational changes and even irreversible damage in proteins [118]–[124]. In fact, an electric field strength larger than 1 V/nm can lead to the denaturation of viral proteins and even break chemical bonds, but there is no biological relevance. In moderate electric fields, the permanent dipoles in the backbone and the additional flexible dipoles of the protein side interact with electric fields [19]. On the one hand, to minimize the electrostatic energy, the electric dipole moment is reoriented along the electric-field direction. On the other hand, because of the loss of hydrogen bonds, conformational energy is used to rearrange the dipoles. These changes can result in the conformational alteration of proteins. The effect of electric fields (lower than 0.1 V/nm) on the secondary structure of proteins and peptides has been uncovered through molecular dynamics simulations [19], [123]–[125]. In most situations, proteins can give critical information about viruses, in particular S protein. Therefore, considering proteins as the studied objects is reasonable. Nevertheless, phospholipid membranes are

also a critical portion of viruses, and the disruption of the lipid membrane also could lead to the loss of viral viability. Besides, the molecular-level understanding of the interaction of phospholipid membranes with electric fields is still lacking. Similarly, most the theoretical research on high-temperature inactivation only focuses on the changes of S protein, not phospholipid membranes. As a result, the possible impact of high temperatures on phospholipid membranes still is unrevealed.

1.6. THE LAYOUT OF THIS DISSERTATION

In response to the above-mentioned problems in viral inactivation, with the motivation of revealing viral inactivation mechanisms of different disinfection methods at the molecular level and exploring new alternative methods for viral inactivation, the dissertation includes six chapters. The dissertation layout is plotted in Figure 1.5.

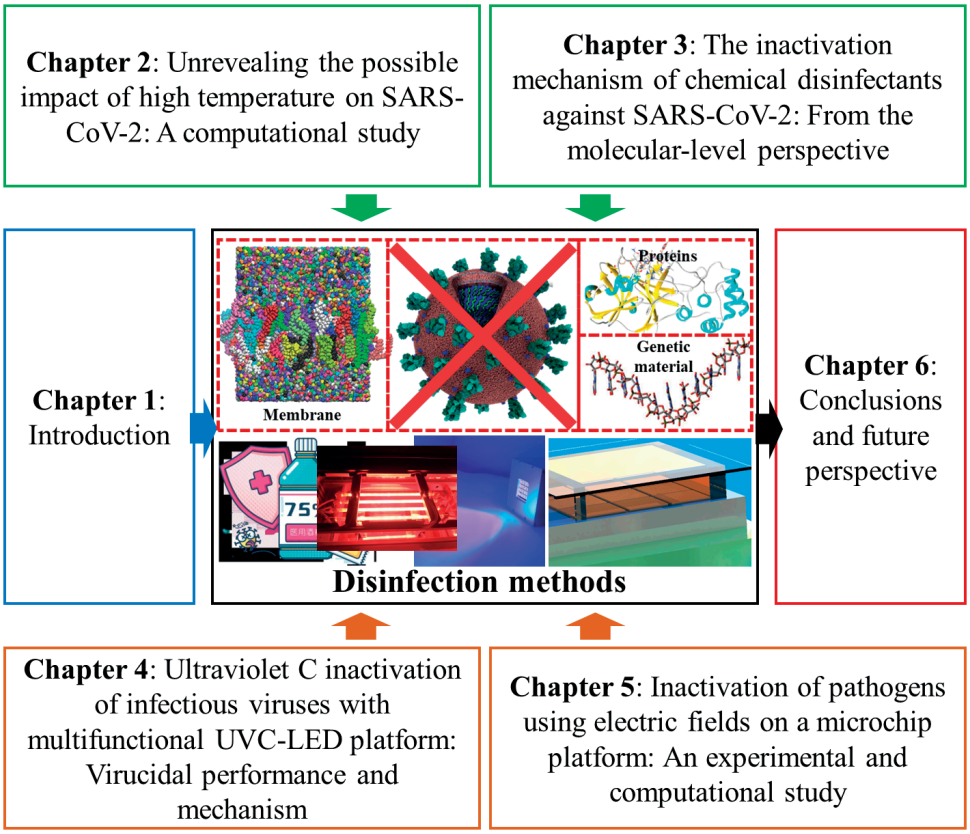


Figure 1.5: Dissertation layout.

In Chapter 2, heat treatment is a standard disinfection method, and its effect mechanism on phospholipid membranes is discussed. By adopting molecular dynamics simulations, the possible impact of high temperature on the phospholipid membranes of

SARS-CoV-2 is theoretically investigated. Compared to the changes in viral proteins, the structural alteration of phospholipid membranes is relatively small.

In Chapter 3, the underlying interaction mechanisms of chemical agents with 3CL hydrolase of SARS-CoV-2 are revealed in-depth by combining molecular dynamics and the density functional theory method. In addition, the phospholipid membranes of SARS-CoV-2 are also taken into account to explore the possible effect of chemical agents on the phospholipid membranes.

In Chapter 4, by designing and constructing the inactivation platform with a UVC-LED array, the inactivation experiments for Influenza A PR8 are conducted. In the meantime, the molecular-level mechanism of UVC irradiation for inactivating the selected virus is theoretically clarified by applying the quantum chemical method. In the theoretical calculations, four nucleotides are chosen as the investigated objects.

In Chapter 5, electric fields have posed a potential application in inactivating viruses. Based on the designed and constructed micro-chip platform with electric fields, the inactivation experiments of the phi-6 virus and E. coli are carried out. Meanwhile, a computational study on the interaction of phospholipid membranes with electric fields is also performed to reveal the potential impact of electric fields on viral structures.

Chapter 6 concluded the dissertation, summarized the contributions, pointing out the shortcomings of the research, and discussed the recommendation derived from the results of this dissertation for future research.

REFERENCES

[1] K. G. Andersen, A. Rambaut, W. I. Lipkin, E. C. Holmes, and R. F. Garry, "The proximal origin of sars-cov-2", *Nature medicine*, vol. 26, no. 4, pp. 450–452, 2020.

[2] K. V. Holmes and L. Enjuanes, "The sars coronavirus: A postgenomic era", *Science*, vol. 300, no. 5624, pp. 1377–1378, 2003.

[3] G. Lu, Y. Hu, Q. Wang, *et al.*, "Molecular basis of binding between novel human coronavirus mers-cov and its receptor cd26", *Nature*, vol. 500, no. 7461, pp. 227–231, 2013.

[4] M. J. Broadhurst, T. J. Brooks, and N. R. Pollock, "Diagnosis of ebola virus disease: Past, present, and future", *Clinical microbiology reviews*, vol. 29, no. 4, pp. 773–793, 2016.

[5] B. M. Crossley, R. E. Mock, S. A. Callison, and S. K. Hietala, "Identification and characterization of a novel alpaca respiratory coronavirus most closely related to the human coronavirus 229e", *Viruses*, vol. 4, no. 12, pp. 3689–3700, 2012.

[6] L. Vijgen, E. Keyaerts, P. Lemey, *et al.*, "Circulation of genetically distinct contemporary human coronavirus oc43 strains", *Virology*, vol. 337, no. 1, pp. 85–92, 2005.

[7] S. Abdul-Rasool and B. C. Fielding, "Understanding human coronavirus hcov-nl63", *The open virology journal*, vol. 4, p. 76, 2010.

[8] Q. Zhao, S. Li, F. Xue, *et al.*, "Structure of the main protease from a global infectious human coronavirus, hcov-hku1", *Journal of virology*, vol. 82, no. 17, pp. 8647–8655, 2008.

[9] "Available from: Https://www.who.int", *World Health Organization*,

[10] M. M. Rajah, M. Hubert, E. Bishop, *et al.*, "Sars-cov-2 alpha, beta, and delta variants display enhanced spike-mediated syncytia formation", *The EMBO journal*, vol. 40, no. 24, e108944, 2021.

[11] M. D. Hitchings, O. T. Ranzani, M. Dorion, *et al.*, "Effectiveness of chadox1 vaccine in older adults during sars-cov-2 gamma variant circulation in são paulo", *Nature communications*, vol. 12, no. 1, pp. 1–8, 2021.

[12] X. He, W. Hong, X. Pan, G. Lu, and X. Wei, "Sars-cov-2 omicron variant: Characteristics and prevention", *MedComm*, vol. 2, no. 4, pp. 838–845, 2021.

[13] L. Liu, A. Chin, P Yu, L. Poon, and M. Huang, "Anti-pathogen stainless steel combating covid-19", *Chemical Engineering Journal*, vol. 433, p. 133 783, 2022.

[14] M. Raeiszadeh and B. Adeli, "A critical review on ultraviolet disinfection systems against covid-19 outbreak: Applicability, validation, and safety considerations", *Acs Photonics*, vol. 7, no. 11, pp. 2941–2951, 2020.

[15] G. Xiling, C. Yin, W. Ling, *et al.*, "In vitro inactivation of sars-cov-2 by commonly used disinfection products and methods", *Scientific Reports*, vol. 11, no. 1, pp. 1–9, 2021.

[16] Y. Huang, S. Xiao, D. Song, and Z. Yuan, "Evaluating the virucidal activity of four disinfectants against sars-cov-2", *American journal of infection control*, vol. 50, no. 3, pp. 319–324, 2022.

[17] H. Inagaki, A. Saito, H. Sugiyama, T. Okabayashi, and S. Fujimoto, "Rapid inactivation of sars-cov-2 with deep-uv led irradiation", *Emerging Microbes & Infections*, vol. 9, no. 1, pp. 1744–1747, 2020.

[18] A. Ruiz-Fernández, M Rosemblatt, and T Perez-Acle, "Nanosecond pulsed electric field (nspef) and vaccines: A novel technique for the inactivation of sars-cov-2 and other viruses?", *Annals of Medicine*, vol. 54, no. 1, pp. 1749–1756, 2022.

[19] C. R. Arbeitman, P. Rojas, P. Ojeda-May, and M. E. Garcia, "The sars-cov-2 spike protein is vulnerable to moderate electric fields", *Nature communications*, vol. 12, no. 1, pp. 1–13, 2021.

[20] A. Bisag, P. Isabelli, R. Laurita, *et al.*, "Cold atmospheric plasma inactivation of aerosolized microdroplets containing bacteria and purified sars-cov-2 rna to contrast airborne indoor transmission", *Plasma Processes and Polymers*, vol. 17, no. 10, p. 2 000 154, 2020.

[21] A. M. Nasir, N. Awang, S. K. Hubadillah, *et al.*, "A review on the potential of photocatalysis in combatting sars-cov-2 in wastewater", *Journal of Water Process Engineering*, vol. 42, p. 102 111, 2021.

[22] D. Schoeman and B. C. Fielding, "Coronavirus envelope protein: Current knowledge", *Virology journal*, vol. 16, no. 1, pp. 1–22, 2019.

[23] P. S. Masters, "The molecular biology of coronaviruses", *Advances in virus research*, vol. 66, pp. 193–292, 2006.

[24] N. K. Jaiswal and S. K. Saxena, "Classical coronaviruses", in *Coronavirus Disease 2019 (COVID-19)*, Springer, 2020, pp. 141–150.

[25] S. Satarker and M. Nampoothiri, "Structural proteins in severe acute respiratory syndrome coronavirus-2", *Archives of medical research*, vol. 51, no. 6, pp. 482–491, 2020.

[26] A. Y. Volyansky, T. Davydova, M. Kuchma, I. Yudin, and I. Y. Kuchma, "Features of sars-cov-2 infection and directions of drug and vaccine creation", *Annals of Mechnikov's Institute*, no. 4, pp. 7–20, 2020.

[27] Y. Yin and R. G. Wunderink, "Mers, sars and other coronaviruses as causes of pneumonia", *Respirology*, vol. 23, no. 2, pp. 130–137, 2018.

[28] C.-C. Lai, T.-P. Shih, W.-C. Ko, H.-J. Tang, and P.-R. Hsueh, "Severe acute respiratory syndrome coronavirus 2 (sars-cov-2) and coronavirus disease-2019 (covid-19): The epidemic and the challenges", *International journal of antimicrobial agents*, vol. 55, no. 3, p. 105 924, 2020.

[29] P Parthasarathy and S Vivekanandan, "An extensive study on the covid-19 pandemic, an emerging global crisis: Risks, transmission, impacts and mitigation", *Journal of Infection and Public Health*, vol. 14, no. 2, pp. 249–259, 2021.

[30] S. W. Kim, M. Ramakrishnan, P. C. Raynor, and S. M. Goyal, "Effects of humidity and other factors on the generation and sampling of a coronavirus aerosol", *Aerobiologia*, vol. 23, no. 4, pp. 239–248, 2007.

[31] S. Yu, K. Chen, L. Fang, *et al.*, "Comparison and analysis of neutralizing antibody levels in serum after inoculating with sars-cov-2, mers-cov, or sars-cov vaccines in humans", *Vaccines*, vol. 9, no. 6, p. 588, 2021.

[32] J. M. Parks and J. C. Smith, "How to discover antiviral drugs quickly", *New England Journal of Medicine*, vol. 382, no. 23, pp. 2261–2264, 2020.

[33] A. R. Fehr and S. Perlman, "Coronaviruses: An overview of their replication and pathogenesis", *Coronaviruses*, pp. 1–23, 2015.

[34] A. C. Walls, Y.-J. Park, M. A. Tortorici, A. Wall, A. T. McGuire, and D. Veesler, "Structure, function, and antigenicity of the sars-cov-2 spike glycoprotein", *Cell*, vol. 181, no. 2, pp. 281–292, 2020.

[35] M. Hoffmann, H. Kleine-Weber, S. Schroeder, *et al.*, "Sars-cov-2 cell entry depends on ace2 and tmprss2 and is blocked by a clinically proven protease inhibitor", *cell*, vol. 181, no. 2, pp. 271–280, 2020.

[36] Y. Hu, J. Wen, L. Tang, *et al.*, "The m protein of sars-cov: Basic structural and immunological properties", *Genomics, proteomics & bioinformatics*, vol. 1, no. 2, pp. 118–130, 2003.

[37] J. Liu, Y. Sun, J. Qi, *et al.*, "The membrane protein of severe acute respiratory syndrome coronavirus acts as a dominant immunogen revealed by a clustering region of novel functionally and structurally defined cytotoxic t-lymphocyte epitopes", *The Journal of infectious diseases*, vol. 202, no. 8, pp. 1171–1180, 2010.

[38] R. Poduri, G. Joshi, and G. Jagadeesh, "Drugs targeting various stages of the sars-cov-2 life cycle: Exploring promising drugs for the treatment of covid-19", *Cellular signalling*, vol. 74, p. 109 721, 2020.

[39] T. R. Ruch and C. E. Machamer, "The coronavirus e protein: Assembly and beyond", *Viruses*, vol. 4, no. 3, pp. 363–382, 2012.

[40] Y. A. Malik, "Properties of coronavirus and sars-cov-2", *The Malaysian journal of pathology*, vol. 42, no. 1, pp. 3–11, 2020.

[41] R. Zolfaghari Emameh, R. Falak, and E. Bahreini, "Application of system biology to explore the association of neprilysin, angiotensin-converting enzyme 2 (ace2), and carbonic anhydrase (ca) in pathogenesis of sars-cov-2", *Biological Procedures Online*, vol. 22, no. 1, pp. 1–9, 2020.

[42] D. Yang and J. L. Leibowitz, "The structure and functions of coronavirus genomic 3 and 5 ends", *Virus research*, vol. 206, pp. 120–133, 2015.

[43] R. Yadav, J. K. Chaudhary, N. Jain, *et al.*, "Role of structural and non-structural proteins and therapeutic targets of sars-cov-2 for covid-19", *Cells*, vol. 10, no. 4, p. 821, 2021.

[44] J. A. Silvas, D. M. Vasquez, J.-G. Park, *et al.*, "Contribution of sars-cov-2 accessory proteins to viral pathogenicity in k18 human ace2 transgenic mice", *Journal of Virology*, vol. 95, no. 17, e00402–21, 2021.

[45] X. Li, M. Geng, Y. Peng, L. Meng, and S. Lu, "Molecular immune pathogenesis and diagnosis of covid-19", *Journal of pharmaceutical analysis*, vol. 10, no. 2, pp. 102–108, 2020.

[46] K. Raj, A. Ghosh, S. Singh, *et al.*, "Coronavirus as silent killer: Recent advancement to pathogenesis, therapeutic strategy and future perspectives", *VirusDisease*, vol. 31, no. 2, pp. 137–145, 2020.

[47] S. Jiang, C. Hillyer, and L. Du, "Neutralizing antibodies against sars-cov-2 and other human coronaviruses", *Trends in immunology*, vol. 41, no. 5, pp. 355–359, 2020.

[48] S. Jiang, C. Hillyer, and L. Du, "Neutralizing antibodies against sars-cov-2 and other human coronaviruses", *Trends in immunology*, vol. 41, no. 5, pp. 355–359, 2020.

[49] H. Ansariniya, S. M. Seifati, E. Zaker, and F. Zare, "Comparison of immune response between sars, mers, and covid-19 infection, perspective on vaccine design and development", *BioMed Research International*, vol. 2021, 2021.

[50] A. R. Fehr, R. Channappanavar, and S. Perlman, "Middle east respiratory syndrome: Emergence of a pathogenic human coronavirus", *Annual review of medicine*, vol. 68, pp. 387–399, 2017.

[51] A. R. Fehr, R. Channappanavar, and S. Perlman, "Middle east respiratory syndrome: Emergence of a pathogenic human coronavirus", *Annual review of medicine*, vol. 68, pp. 387–399, 2017.

[52] S. Mustafa, H. Balkhy, and M. N. Gabere, "Current treatment options and the role of peptides as potential therapeutic components for middle east respiratory syndrome (mers): A review", *Journal of infection and public health*, vol. 11, no. 1, pp. 9–17, 2018.

[53] P.-Y. Lui, L.-Y. R. Wong, C.-L. Fung, *et al.*, "Middle east respiratory syndrome coronavirus m protein suppresses type i interferon expression through the inhibition of tbk1-dependent phosphorylation of irf3", *Emerging microbes & infections*, vol. 5, no. 1, pp. 1–9, 2016.

[54] J. S. Kutter, M. I. Spronken, P. L. Fraaij, R. A. Fouchier, and S. Herfst, "Transmission routes of respiratory viruses among humans", *Current opinion in virology*, vol. 28, pp. 142–151, 2018.

[55] N. H. Leung, "Transmissibility and transmission of respiratory viruses", *Nature Reviews Microbiology*, vol. 19, no. 8, pp. 528–545, 2021.

[56] J. Gralton, E. Tovey, M.-L. McLaws, and W. D. Rawlinson, "The role of particle size in aerosolised pathogen transmission: A review", *Journal of Infection*, vol. 62, no. 1, pp. 1–13, 2011.

[57] T. P. Weber and N. I. Stilianakis, "Inactivation of influenza a viruses in the environment and modes of transmission: A critical review", *Journal of infection*, vol. 57, no. 5, pp. 361–373, 2008.

[58] R. Tellier, "Aerosol transmission of influenza a virus: A review of new studies", *Journal of the Royal Society Interface*, vol. 6, no. suppl_6, S783–S790, 2009.

[59] N. Pica and N. M. Bouvier, "Environmental factors affecting the transmission of respiratory viruses", *Current opinion in virology*, vol. 2, no. 1, pp. 90–95, 2012.

[60] A. Fernstrom and M. Goldblatt, "Aerobiology and its role in the transmission of infectious diseases", *Journal of pathogens*, vol. 2013, 2013.

[61] S. Riddell, S. Goldie, A. Hill, D. Eagles, and T. W. Drew, "The effect of temperature on persistence of sars-cov-2 on common surfaces", *Virology journal*, vol. 17, no. 1, pp. 1–7, 2020.

[62] N Van Doremalen, T Bushmaker, and V. Munster, "Stability of middle east respiratory syndrome coronavirus (mers-cov) under different environmental conditions", *Eurosurveillance*, vol. 18, no. 38, p. 20 590, 2013.

[63] K. Chan, S Sridhar, R. Zhang, *et al.*, "Factors affecting stability and infectivity of sars-cov-2", *Journal of Hospital Infection*, vol. 106, no. 2, pp. 226–231, 2020.

[64] M. Y. Lai, P. K. Cheng, and W. W. Lim, "Survival of severe acute respiratory syndrome coronavirus", *Clinical infectious diseases*, vol. 41, no. 7, e67–e71, 2005.

[65] F. Marzoli, A. Bortolami, A. Pezzuto, *et al.*, "A systematic review of human coronaviruses survival on environmental surfaces", *Science of The Total Environment*, vol. 778, p. 146 191, 2021.

[66] P. Matatiele, B. Southon, B. Dabula, T. Marageni, P. Poongavanum, and B. Kgarebe, "Assessment of quality of alcohol-based hand sanitizers used in johannesburg area during the covid-19 pandemic", *Scientific reports*, vol. 12, no. 1, pp. 1–7, 2022.

[67] A. Kratzel, D. Todt, P. V'kovski, *et al.*, "Inactivation of severe acute respiratory syndrome coronavirus 2 by who-recommended hand rub formulations and alcohols", *Emerging infectious diseases*, vol. 26, no. 7, p. 1592, 2020.

[68] M. H. Al-Sayah, "Chemical disinfectants of covid-19: An overview", *Journal of water and health*, vol. 18, no. 5, pp. 843–848, 2020.

[69] G. Kampf, D. Todt, S. Pfaender, and E. Steinmann, "Persistence of coronaviruses on inanimate surfaces and their inactivation with biocidal agents", *Journal of hospital infection*, vol. 104, no. 3, pp. 246–251, 2020.

[70] G. Kampf, "Potential role of inanimate surfaces for the spread of coronaviruses and their inactivation with disinfectant agents", *Infection Prevention in Practice*, vol. 2, no. 2, p. 100 044, 2020.

[71] A. Fadaei, "Viral inactivation with emphasis on sars-cov-2 using physical and chemical disinfectants", *The Scientific World Journal*, vol. 2021, 2021.

[72] C. Marnie and M. Peters, "Anmf evidence brief covid-19: Cleaning and disinfection of hospital surfaces and equipment", *Australian Nursing and Midwifery Federation*, 2020.

[73] H. A. Abdelkader, "Dermatopathology practice in the era of covid-19", *Archives of Dermatological Research*, vol. 313, no. 10, pp. 811–813, 2021.

[74] H. A. Abdelkader, "Dermatopathology practice in the era of covid-19", *Archives of Dermatological Research*, vol. 313, no. 10, pp. 811–813, 2021.

[75] M. E. Darnell, K. Subbarao, S. M. Feinstone, and D. R. Taylor, "Inactivation of the coronavirus that induces severe acute respiratory syndrome, sars-cov", *Journal of virological methods*, vol. 121, no. 1, pp. 85–91, 2004.

[76] A. S. Jureka, J. A. Silvas, and C. F. Basler, "Propagation, inactivation, and safety testing of sars-cov-2", *Viruses*, vol. 12, no. 6, p. 622, 2020.

[77] Y. Nishihara, H. Eguchi, and S. Zhou, "Silver ion (ag+) formulations with virucidal efficacy against severe acute respiratory syndrome coronavirus 2 (sars-cov-2)", in *Disinfection of Viruses*, IntechOpen, 2021.

[78] J. Zhu, S. Wu, Y. Fang, L. Lin, and J. Zhu, "Sars-cov-2 inactivation by persulfate-enhanced silver ions", *Medicine Research*, p. 1,

[79] A. R. Ghosh, A. Bhooshitha, H. Chandan, and K. Krishna, "Possible insights into the use of silver nanoparticles in targeting sars-cov-2 (covid-19)", *Indian J Pharm Educ Res*, vol. 55, no. 2, pp. 319–329, 2021.

[80] S. S. Jeremiah, K. Miyakawa, T. Morita, Y. Yamaoka, and A. Ryo, "Potent antiviral effect of silver nanoparticles on sars-cov-2", *Biochemical and biophysical research communications*, vol. 533, no. 1, pp. 195–200, 2020.

[81] P. Merkl, S. Long, G. M. McInerney, and G. A. Sotiriou, "Antiviral activity of silver, copper oxide and zinc oxide nanoparticle coatings against sars-cov-2", *Nanomaterials*, vol. 11, no. 5, p. 1312, 2021.

[82] R. W. Nims and M. Plavsic, "Physical inactivation of sars-cov-2 and other coronaviruses: A review", *Disinfection of Viruses*, p. 123, 2022.

[83] G. T. Bowden, "Prevention of non-melanoma skin cancer by targeting ultraviolet-b-light signalling", *Nature Reviews Cancer*, vol. 4, no. 1, pp. 23–35, 2004.

[84] F. Vatansever, C. Ferraresi, M. V. P. de Sousa, *et al.*, "Can biowarfare agents be defeated with light?", *Virulence*, vol. 4, no. 8, pp. 796–825, 2013.

[85] M. Heßling, K. Hönes, P. Vatter, and C. Lingenfelder, "Ultraviolet irradiation doses for coronavirus inactivation–review and analysis of coronavirus photoinactivation studies", *GMS hygiene and infection control*, vol. 15, 2020.

[86] C. P. Sabino, F. P. Sellera, D. F. Sales-Medina, *et al.*, "Uv-c (254 nm) lethal doses for sars-cov-2", *Photodiagnosis and Photodynamic Therapy*, vol. 32, p. 101 995, 2020.

[87] K. A. da Silva Aquino, "Sterilization by gamma irradiation", *Gamma radiation*, vol. 9, pp. 172–202, 2012.

[88] I. Leclercq, C. Batejat, A. M. Burguière, and J.-C. Manuguerra, "Heat inactivation of the m iddle e ast respiratory syndrome coronavirus", *Influenza and other respiratory viruses*, vol. 8, no. 5, pp. 585–586, 2014.

[89] C. Batéjat, Q. Grassin, and J.-C. Manuguerra, "Heat inactivation of the severe acute respiratory syndrome coronavirus 2", *Journal of biosafety and biosecurity*, vol. 3, no. 1, pp. 1–3, 2021.

[90] M. Yunoki, T Urayama, I Yamamoto, S Abe, and K Ikuta, "Heat sensitivity of a sars-associated coronavirus introduced into plasma products", *Vox sanguinis*, vol. 87, no. 4, pp. 302–303, 2004.

[91] S. Chakraborty, N. Kaushik, P. S. Rao, and H. Mishra, "High-pressure inactivation of enzymes: A review on its recent applications on fruit purees and juices", *Comprehensive Reviews in Food Science and Food Safety*, vol. 13, no. 4, pp. 578–596, 2014.

[92] M. Stawarz-Janeczek, A. Kryczyk-Poprawa, B. Muszyńska, W. Opoka, and J. Pytko-Polończyk, "Disinfectants used in stomatology and sars-cov-2 infection", *European journal of dentistry*, vol. 15, no. 02, pp. 388–400, 2021.

[93] S. Pfaender, J. Brinkmann, D. Todt, *et al.*, "Mechanisms of methods for hepatitis c virus inactivation", *Applied and environmental microbiology*, vol. 81, no. 5, pp. 1616–1621, 2015.

[94] M. Zavodszky, C.-W. Chen, J.-K. Huang, M. Zolkiewski, L. Wen, and R. Krishnamoorthi, "Disulfide bond effects on protein stability: Designed variants of cucurbita maxima trypsin inhibitor-v", *Protein Science*, vol. 10, no. 1, pp. 149–160, 2001.

[95] S. Fukuzaki, "Mechanisms of actions of sodium hypochlorite in cleaning and disinfection processes", *Biocontrol science*, vol. 11, no. 4, pp. 147–157, 2006.

[96] M. Khokhar, D. Roy, P. Purohit, M. Goyal, and P. Setia, "Viricidal treatments for prevention of coronavirus infection", *Pathogens and global health*, vol. 114, no. 7, pp. 349–359, 2020.

[97] R. B. Thurman, C. P. Gerba, and G. Bitton, "The molecular mechanisms of copper and silver ion disinfection of bacteria and viruses", *Critical reviews in environmental science and technology*, vol. 18, no. 4, pp. 295–315, 1989.

[98] C. Geller, M. Varbanov, and R. E. Duval, "Human coronaviruses: Insights into environmental resistance and its influence on the development of new antiseptic strategies", *Viruses*, vol. 4, no. 11, pp. 3044–3068, 2012.

[99] K. R. Wigginton, B. M. Pecson, T. Sigstam, F. Bosshard, and T. Kohn, "Virus inactivation mechanisms: Impact of disinfectants on virus function and structural integrity", *Environmental science & technology*, vol. 46, no. 21, pp. 12 069–12 078, 2012.

[100] F. Saadatpour and F. Mohammadipanah, "Physicochemical susceptibility of sars-cov-2 to disinfection and physical approach of prophylaxis", *Health Science Reports*, vol. 3, no. 4, e213, 2020.

[101] R. Thurman and C. Gerba, "Molecular mechanisms of viral inactivation by water disinfectants", *Advances in applied microbiology*, vol. 33, pp. 75–105, 1988.

[102] A. L. Garner, "Pulsed electric field inactivation of microorganisms: From fundamental biophysics to synergistic treatments", *Applied microbiology and biotechnology*, vol. 103, no. 19, pp. 7917–7929, 2019.

[103] S. Ho and G. S. Mittal, "Electroporation of cell membranes: A review", *Critical reviews in biotechnology*, vol. 16, no. 4, pp. 349–362, 1996.

[104] T. Y. Tsong, "On electroporation of cell membranes and some related phenomena", *Journal of electroanalytical chemistry and interfacial electrochemistry*, vol. 299, no. 3, pp. 271–295, 1990.

[105] A. Russell, "Mechanisms of antimicrobial action of antiseptics and disinfectants: An increasingly important area of investigation", *Journal of Antimicrobial Chemotherapy*, vol. 49, no. 4, pp. 597–599, 2002.

[106] T. L. Cromeans, A. M. Kahler, and V. R. Hill, "Inactivation of adenoviruses, enteroviruses, and murine norovirus in water by free chlorine and monochloramine", *Applied and environmental microbiology*, vol. 76, no. 4, pp. 1028–1033, 2010.

[107] T. Hayashi, K. Oguma, Y. Fujimura, *et al.*, "Uv light-emitting diode (uv-led) at 265 nm as a potential light source for disinfecting human platelet concentrates", *Plos one*, vol. 16, no. 5, e0251650, 2021.

[108] L. M. Hinds, C. P. O'Donnell, M. Akhter, and B. K. Tiwari, "Principles and mechanisms of ultraviolet light emitting diode technology for food industry applications", *Innovative Food Science & Emerging Technologies*, vol. 56, p. 102 153, 2019.

[109] B. T. Tran and H. Hirayama, "Growth and fabrication of high external quantum efficiency algan-based deep ultraviolet light-emitting diode grown on pattern si substrate", *Scientific reports*, vol. 7, no. 1, pp. 1–6, 2017.

[110] Q. Zhang, H. Parimoo, E. Martel, and S. Zhao, "Vertical semiconductor deep ultraviolet light emitting diodes on a nanowire-assisted aluminum nitride buffer layer", *Scientific Reports*, vol. 12, no. 1, pp. 1–7, 2022.

[111] C.-H. Lin and C.-T. Lee, "Ga2o3-based solar-blind deep ultraviolet light-emitting diodes", *Journal of Luminescence*, vol. 224, p. 117 326, 2020.

[112] W.-K. Jo and R. J. Tayade, "New generation energy-efficient light source for photocatalysis: Leds for environmental applications", *Industrial & Engineering Chemistry Research*, vol. 53, no. 6, pp. 2073–2084, 2014.

[113] S. E. Beck, H. Ryu, L. A. Boczek, *et al.*, "Evaluating uv-c led disinfection performance and investigating potential dual-wavelength synergy", *Water research*, vol. 109, pp. 207–216, 2017.

[114] M. Kojima, K. Mawatari, T. Emoto, *et al.*, "Irradiation by a combination of different peak-wavelength ultraviolet-light emitting diodes enhances the inactivation of influenza a viruses", *Microorganisms*, vol. 8, no. 7, p. 1014, 2020.

[115] H. Woo, S. E. Beck, L. A. Boczek, *et al.*, "Efficacy of inactivation of human enteroviruses by dual-wavelength germicidal ultraviolet (uv-c) light emitting diodes (leds)", *Water*, vol. 11, no. 6, p. 1131, 2019.

[116] M. P. Akgün and S. Ünlütürk, "Effects of ultraviolet light emitting diodes (leds) on microbial and enzyme inactivation of apple juice", *International journal of food microbiology*, vol. 260, pp. 65–74, 2017.

[117] Y. Kebbi, A. I. Muhammad, A. S. Sant'Ana, L. do Prado-Silva, D. Liu, and T. Ding, "Recent advances on the application of uv-led technology for microbial inactivation: Progress and mechanism", *Comprehensive Reviews in Food Science and Food Safety*, vol. 19, no. 6, pp. 3501–3527, 2020.

[118] D. R. Hekstra, K. I. White, M. A. Socolich, R. W. Henning, V. Šrajer, and R. Ranganathan, "Electric-field-stimulated protein mechanics", *Nature*, vol. 540, no. 7633, pp. 400–405, 2016.

[119] Q. Zhang, D. Shao, P. Xu, and Z. Jiang, "Effects of an electric field on the conformational transition of the protein: Pulsed and oscillating electric fields with different frequencies", *Polymers*, vol. 14, no. 1, p. 123, 2021.

[120] P. Ojeda-May and M. E. Garcia, "Electric field-driven disruption of a native β-sheet protein conformation and generation of a helix-structure", *Biophysical journal*, vol. 99, no. 2, pp. 595–599, 2010.

[121] I. Bekard and D. E. Dunstan, "Electric field induced changes in protein conformation", *Soft Matter*, vol. 10, no. 3, pp. 431–437, 2014.

[122] G. Urabe, T. Katagiri, and S. Katsuki, "Intense pulsed electric fields denature urease protein", *Bioelectricity*, vol. 2, no. 1, pp. 33–39, 2020.

[123] A. Budi, F. S. Legge, H. Treutlein, and I. Yarovsky, "Electric field effects on insulin chain-b conformation", *The Journal of Physical Chemistry B*, vol. 109, no. 47, pp. 22 641–22 648, 2005.

[124] Z. Jiang, L. You, W. Dou, T. Sun, and P. Xu, "Effects of an electric field on the conformational transition of the protein: A molecular dynamics simulation study", *Polymers*, vol. 11, no. 2, p. 282, 2019.

[125] P. Marracino, F. Apollonio, M. Liberti, G. d'Inzeo, and A. Amadei, "Effect of high exogenous electric pulses on protein conformation: Myoglobin as a case study", *The Journal of Physical Chemistry B*, vol. 117, no. 8, pp. 2273–2279, 2013.

2

UNREVEALING THE POSSIBLE IMPACT OF HIGH TEMPERATURE ON SARS-COV-2: A COMPUTATIONAL STUDY

Heat disinfection is considered an essential inactivation method in many fields. Using molecular dynamics simulations, we theoretically investigate the possible effect of high temperature on phospholipid membranes of SARS-CoV-2. It can be found that the total APL of the bilayer membrane is positively correlated with the temperature, whereas the membrane thickness gradually decreases with increasing temperature. Water molecules inside the bilayer membrane are not found, which means that the spacing between lipid molecules is insufficient to enable water molecules to penetrate the interior of the lipid membrane. Thus, high temperature would not result in the destruction of the bilayer structure, which is in agreement with the experimental result that the disruption of the viral envelope is rare. Meanwhile, the mass and electron densities in the head-groups of lipid molecules vary significantly as the temperature increases. Moreover, upon heating, the lipid membrane transitions into the liquid-disordered phase in which lipid molecules diffuse intensely in the membrane plane, and their fatty acid tails are considerably flexed and bent. The end snapshots of the bilayer membrane further confirm this phenomenon. Eventually, 2D RDFs of P-P and N-N pairs show that the probability of lipid molecules appearing at a certain distance decreases as the temperature increases, which may be attributed to the lateral expansion of the lipid membrane. Those findings reveal the dynamics of the bilayer membrane at different temperatures, and provide the molecular-level perspective on the possible role of the membrane dynamics in the heat inactivation of viruses.

2.1. MOLECULAR DYNAMICS THEORY

MOLECULAR dynamics (MD) is a method of modeling the motion of individual atoms in a system based on Newton's second law [1], [2]. Samples are drawn from the ensemble of different states of the molecular system, and the integral of the molecular system configuration is calculated to obtain the thermodynamic quantities and macroscopic properties of the system. By means of the MD method, not only the internal motion of the system with the variation of time can be studied, but also various properties of the system are predicted and analyzed. Therefore, the MD method plays a crucial role in the fields of physics, chemistry, biology, material science, and medicine [3]–[6]. MD method is used to simulate the trajectory of molecules over time by solving Newton's equation and then applies statistical mechanics to analyze various system properties [7]. Suppose that there are some particles in the motion system, and their motion laws conform to Newton's equation of motion [8]:

$$F_i(t) = m_i a_i = m_i \frac{\partial^2 r_i(t)}{\partial t^2} = m_i \frac{\partial v_i(t)}{\partial t} \tag{2.1}$$

$$F_i(t) = -\frac{\partial V(t)}{\partial r_i(t)} \tag{2.2}$$

$$r_i \mid_{t=0} = r_i(0) \tag{2.3}$$

$$\frac{dr_i}{dt} \mid_{t=0} = v_i(0) \tag{2.4}$$

In a complex multi-degree-of-freedom system, there is no analytical solution in Newton's equation of motion. Therefore, it is usually solved by the finite difference method. The main idea of the finite difference method is to divide the integration process into multiple steps. Based on this idea, many methods have been derived from the numerical solution of Newton's equation of motion, including Verlet [9], [10], leap-frog [11], [12], Velocity Verlet [13], Beeman [14], and predictor-corrector method [15], [16]. The Verlet method is the most widely used algorithm in MD simulations and has high numerical stability. It can be expanded by the Taylor series [9], [10]:

$$r(t+\delta t) = r(t) + \delta t v(t) + \frac{1}{2}\delta^2 a(t) + \frac{1}{6}\delta t^3 b(t) + \frac{1}{24}\delta t^4 c(t) + \ldots \tag{2.5}$$

$$v(t+\delta t) = v(t) + \delta t a(t) + \frac{1}{2}\delta^2 b(t) + \frac{1}{6}\delta t^3 c(t) + \ldots \tag{2.6}$$

$$a(t+\delta t) = a(t) + \delta t b(t) + \frac{1}{2}\delta^2 c(t) + \ldots \tag{2.7}$$

$$b(t+\delta t) = b(t) + \delta t c(t) + \ldots \tag{2.8}$$

in which v is the third derivative of velocity, a is the acceleration, and b is the coordinate time. The Verlet method is easy to implement, requiring only $r(t)$, $r(t+\delta t)$, and $a(t)$, thus it is moderately demanding on computer memory. However, there are two disadvantages: i) The position $r(t+\delta t)$ at $t+\delta t$ needs to be obtained by a short term $\delta t^2 a(t)$ plus the difference between two large terms $2r(t)$ and $r(t+\delta t)$. Its accuracy is therefore low. ii) the positions at $t-\delta t$ and t need to be determined when calculating the new

coordinates. Nevertheless, the position of the previous step cannot be obtained when $t = 0$. Accordingly, the position $r(t - \delta t)$ must be obtained through other approaches.

The leap-frog method is based on the Verlet method. When the system is modeled through the leap-frog method, the velocity $v(t + \frac{1}{2}\delta t)$ at $t + \frac{1}{2}\delta t$ is firstly calculated and then utilizing the obtained velocity to predict the position $r(t + \delta t)$ at $t + \delta t$ [11]:

$$v(t + \frac{1}{2}\delta t) = v(t - \frac{1}{2}\delta t) + \delta t a(t) \tag{2.9}$$

the next position is

$$r(t + \delta t) = r(t) + \delta t v(t)(t + \frac{1}{2}\delta t) \tag{2.10}$$

the velocity at time t based on the $v(t - \frac{1}{2}\delta t)$ and $v(t + \frac{1}{2}\delta t)$ is

$$v(t) = \frac{1}{2}[v(t - \frac{1}{2}\delta t) + v(t + \frac{1}{2}\delta t)] \tag{2.11}$$

Compared to the Verlet method, the leap-frog method has two advantages. One is low complexity, and only the velocity $v(t - \frac{1}{2}\delta t)$ and the position $r(t)$ need to be calculated in the leap-frog method. Another one is that the leap-frog method includes the velocity term, and its computational stability and accuracy are good. However, its defect is that the velocity and position of the system as well as the kinetic and potential energy, cannot be calculated simultaneously. Thus, the contribution of the kinetic energy to the total energy can be computed at different times, which is time-consuming.

The Velocity Verlet method contains the velocity term, correcting the significant defects of the Verlet and the leap-frog methods. The motion equation is integrated by utilizing the position $r(t)$ and velocity $v(t)$ at time t [13].

$$r(t + \delta t) = r(t) + \delta t v(t) + \frac{1}{2}\delta t^2 a(t) \tag{2.12}$$

$$v(t + \delta t) = v(t) + \frac{1}{2}\delta t[a(t) + a(t + \delta t)] \tag{2.13}$$

This method can simultaneously calculate the atoms' position, velocity, and acceleration, and the accuracy is not affected. Meanwhile, its calculating amount is moderate, thus it is widely used.

The Beeman method is developed from the refinement of the Verlet method, and its integral formula is [14]

$$r(t + \delta t) = r(t) + \delta t v(t) + \frac{2}{3}\delta t^2 a(t) - \frac{1}{6}\delta t^2 a(t - \delta t) \tag{2.14}$$

$$v(t + \delta t) = v(t) + \frac{1}{3}\delta t v(t) + \frac{5}{6}\delta t a(t) - \frac{1}{6}\delta t^2 a(t - \delta t) \tag{2.15}$$

The values of $r(t)$, $v(t)$, and $a(t - \delta t)$ need to be stored, thus the storage space of this method is more significant than that of the Verlet and the leap-frog methods.

The predictor-corrector method utilizes Taylor expansion to solve Newton's equation of motion, which consists of the prediction stage, defining the error stage, and the correction stage-in the prediction stage, predicting the position at the next moment through Taylor expansion [15].

$$r^p(t+\delta t) = r(t) + \delta t v(t) + \frac{1}{2}\delta t^2 a(t) + \frac{1}{6}\delta t^3 b(t) + \frac{1}{24}\delta t^4 c(t) + \ldots \tag{2.16}$$

$$v^p(t+\delta t) = v(t) + \delta t a(t) + \frac{1}{2}\delta t^2 b(t) + \frac{1}{6}\delta t^3 c(t) + \ldots \tag{2.17}$$

$$a^p(t+\delta t) = a(t) + \delta t b(t) + \frac{1}{2}\delta t^2 c(t) + \ldots \tag{2.18}$$

$$b^p(t+\delta t) = b(t) + \delta t c(t) + \ldots \tag{2.19}$$

where $v(t)$, $a(t)$, $b(t)$, and $c(t)$ are the first, second, third, and fourth derivatives of $r(t)$, respectively. In defining the error stage, the corrected $d(t+\delta t)$ is obtained from the position r^p of atoms, and the error is predicted. The formula is

$$a(t+\delta t) = a^c(t+\delta t) - a^p(t+\delta t) \tag{2.20}$$

In the correction stage, using the error to correct the predicted variables such as velocity, acceleration, and position. The formula is

$$r^c(t+\delta t) = r^p(t) + c_0 \triangle a(t+\delta t) \tag{2.21}$$

$$v^c(t+\delta t) = v^p(t) + c_1 \triangle a(t+\delta t) \tag{2.22}$$

$$a^c(t+\delta t) = a^p(t) + c_2 \triangle a(t+\delta t) \tag{2.23}$$

$$b^c(t+\delta t) = b^p(t) + c_3 \triangle a(t+\delta t) \tag{2.24}$$

in which c_0, c_1, c_2, and c_3 are correction coefficients and their values are $\frac{1}{6}$, $\frac{5}{6}$, 1, and $\frac{1}{3}$ respectively. The Taylor expansion with higher order can enhance the calculation accuracy. However, this method needs a better stability. Therefore, it recommends using the predictor-corrector method when δt decreases, whereas for the δt increased case, the Verlet method is used.

2.2. THE STABILITY OF SARS-COV-2 IN DIFFERENT ENVIRONMENTAL CONDITIONS

SARS-CoV-2 is the seventh coronavirus, following six other CoVs, and its high transmission ability led to the rapid outbreak of the COVID-19 epidemic. The basic reproductive number (R_0) of SARS-CoV-2 is between 1.8 and 3.6, which is higher than SARS-CoV (2.0) [17]. Moreover, the R0 of its delta variant is estimated to range from 3.2 to 8, with a mean of 5.08 [18]. It has been observed that the known CoVs, including SARS-CoV-2 mainly affect humans in particular environmental conditions. For instance, both the SARS-CoV infection in 2002 and the SARS-CoV-2 infection in 2019 started in the cold winter, but in the hot summer, the number of confirmed infection cases became lesser or nearly negligible [19]–[21]. Statistical results suggest fewer SARS-CoV or SARS-CoV-2 confirmed

cases in countries with hot and humid weather [21], [22]. In contrast, the 2012 MERS-CoV identified in the Middle East can affect humans in hot weather [19]. Consequently, each virus has its specific climatic conditions for survival.

The survivability of SARS-CoV-2 under different environmental conditions has been reported by Chin et al., who observed that SARS-CoV-2 could survive at 277.15 K but quickly inactivate at the high temperature of 343.15 K [23]. Meanwhile, another study reported by Sun et al. revealed the effect of different temperatures on the viability of SARS-CoV-2, as listed in Table 2.1 [24]. SARS-CoV-2 droplets lose infectivity following exposure to a temperature of 329.15 K for 30 min, and it only requires 10 min and 5 min for 343.15 K and 363.15 K, respectively. The findings in another report showed that the infectious SARS-CoV-2 virions on surfaces could be drastically reduced within an hour in the environment where the temperature reaches 327.65 K at least (see Figure 2.1) [25]. Another inactivation study found that exposure to 329.15 K or 333.15 K for up to 60 min could not completely inactivate SARS-CoV-2 virions, whereas at 353.15 K for 90 min or 368.15 K for 1 min or 5 min, it reaches complete inactivation, as listed in Table 2.2 [26]. Compared to printing, tissue paper, wood, and cloth, SARS-CoV-2 shows more robust viral viability on smooth surfaces, e.g., glass, stainless steel, plastic, and banknote. For example, SARS-CoV-2 can only survive a few hours on the printing surface, whereas it a couple of days on stainless steel [23]. Interestingly, SARS-CoV-2 on the outer layer of the surgical mask is capable of retaining viability for seven days [23]. In contrast to the viability (seven days) of SARS-CoV-2 in solution, it only survives three to five days in dried form at room temperature [27]. SARS-CoV-2 is susceptible to the commonly used disinfectants, which can effectively reduce viral viability. No SARS-CoV-2 can be detected under a 5-min incubation with hand soap at room temperature [23], [28]. Thus, the adjustment of environmental conditions can affect viral viability.

Table 2.1: Effect of temperature on SARS-CoV-2 virion inactivation. Note that a value less than 5.17 presents that there are varying amounts of virus survives following the treatment, while a value of ≥5.17 indicates that no viable viruses can be detected after the treatment [24].

Concentration (%)	Log_{10} reduction in infectious SARS-CoV-2 titer achieved Mean (Min~Max)			
	5 min	10 min	20 min	30 min
329.15	–	4.25 (4.00-4.50)	4.84 (4.75-5.00)	≥5.17
343.15	–	≥5.17	≥5.17	–
363.15	≥5.17	–	–	–

2.3. EFFECT OF TEMPERATURE ON THE SPIKE PROTEIN OF SARS-COV-2

Heat disinfection is one of the most commonly used methods of physically inactivating viruses. According to the above described, SARS-CoV-2 virions is highly sensitive to heat. When SARS-CoV-2 virions are exposed to different elevated temperatures over

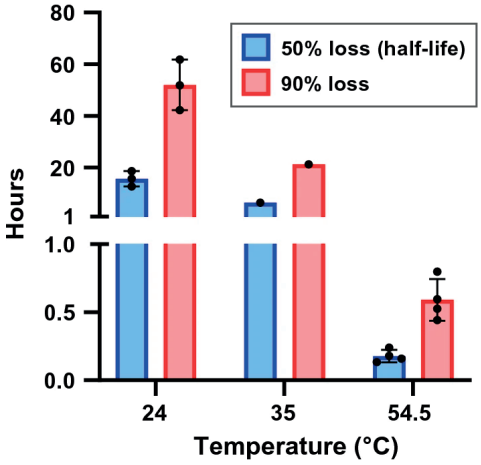


Figure 2.1: Effect of temperature on the surface deacy of SARS-CoV-2 virions [26].

Table 2.2: Effect of heat on the viability of SARS-CoV-2 England 2 virus assessed by plaque assay, observation of cytopathic effect (cpe) and RT-PCR. For the untreated control virus, its titer is 5.68 $\log_{10}$ pfu/mL (St dev 0.1; mean 14 replicates). N (no plaques) are observed therefore 5.68 $\log_{10}$ titer reduction. [26].

Heat treatment		Log_{10} titer reduction (pfu/mol) compared to untreated		
Temperature (K)	Incubation time (min)	Replicate 1	Replicate 2	Replicate 3
Untreated	N-A	0 (14 replicates)		
329.15	30	4.65	N	4.95
333.15	15	N	N	N
333.15	30	5.15	N	N
333.15	60	N	N	4.85
353.15	30	N	4.00	N
353.15	60	N	N	N
353.15	90	N	N	N
368.15	1	N	N	N
368.15	5	N	N	N

the expected incubation time, the biological properties of the viral materials (e.g., structural proteins) will be changed. These changes result in the loss of viral virulence and infectivity, and then the virions are unable to bind and infect a cell to enter through an endocytosis mechanism. Temperature is an essential variable parameter for proteins because of the differential response to high and low temperatures [29]. Many proteins have

good heat resistance while unfolding, or even denaturation phenomena in others at high temperatures [30], [31]. Experimentally, it is found that a mutated S protein generated by Xiong et al. has excellent heat stability [32]. Further research has proven that the viability of SARS-CoV-2 virions at high temperatures is obviously weakened in contrast to that of SARS-CoV. As a result, SARS-CoV-2 virions have a relatively lower energy barrier, which leads to a higher transmission rate [33]. Even though statistical and experimental evidence has suggested that temperature can affect viral bioactivity and infectivity, the molecular-level understanding of structural changes that occur in viruses at various environmental conditions is still lacking.

To provide a molecular-level understanding of structural changes of SARS-CoV-2 virions, Rath et al. theoretically investigated the possible impact of temperature on the S protein of SARS-CoV-2 by applying all-atom MD simulations [29]. The results following 200 ns MD simulations showed that the S protein's S1 (i.e., the solvent-exposed domain) is more mobile than the S2 (i.e., the transmembrane domain). Meanwhile, at 10-30 °C, several charged residues on the surface of the N-terminal domain of the S1 have the best directionality. Furthermore, the receptor-binding motif on the receptor-binding domain (RBD) of the S1 starts to close at around 40 °C and then reaches a completely closed conformation at 50 °C, as shown in Figure 2.2 [29]. The closed conformation leads to the failure of the RBD binding to ACE2 because of the burial of its receptor-binding residues. Another MD study also confirmed that the RBD-ACE2 binding of SARS-CoV-2 is more sensitive to temperatures compared to that of SARS-CoV [34]. This could be contributed to the required higher entropy penalty in the RBD-ACE2 binding process of SARS-CoV-2. Therefore, with the increasing temperature, the infectivity of SARS-CoV-2 virions could be reduced much faster and become less viable.

2.4. THE POSSIBLE IMPACT OF TEMPERATURE ON THE PHOSPHOLIPID MEMBRANE OF SARS-COV-2

2.4.1. PHOSPHOLIPID MEMBRANE OF SARS-COV-2

As an essential component, the phospholipid membrane is critical for the structure and function of enveloped viruses, such as SARA-CoV, MERS-CoV, and SARS-CoV-2 [35]. In the early stages of viral propagation, there is a membrane fusion between viruses and host cells, releasing the viral genome into the host cytoplasm. In addition to the denaturation and coagulation of proteins, the solubilization of lipid membranes of enveloped viruses is one of the leading causes of viral inactivation. For instance, soap or high concentrations of ethanol (>60%) can dissolve lipid membranes and deactivate viruses. Therefore, phospholipid membranes can be a potential target for antiviral therapies or disinfection. At present, one study focusing on the lipid composition of SARS-CoV-2 has shown that the viral envelope mainly consisted of phospholipids with low amounts of cholesterol or sphingolipids [35]. However, the molar ratio of each component of viral lipid membrane is affected by the types of target cells, as listed in Table 2.3. The molar ratio of some lipid composition in their study is similar to that shown in the study focusing on drug-membrane permeability of antiviral for SARS-CoV-2, as reported in Table 2.4 [36]. Furthermore, one clinical evidence suggests the viricidal effect of rinses containing surfactant against SARS-CoV-2 in patients with COVID-19 [35]. These findings confirm

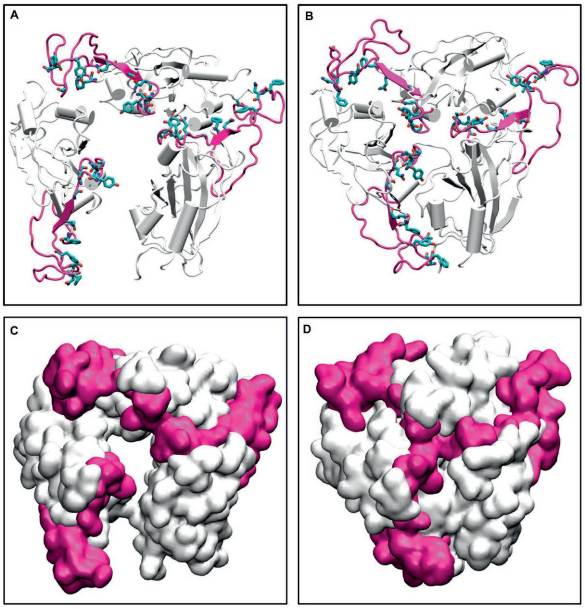


Figure 2.2: The conformations of the receptor binding motif. The time-averaged structures of the S protein showing the open and closed conformations of the receptor binding domain at 30°C and 70°C [29].

the feasibility and possibility of lipid membrane as an important inactivated target is unlikely to be impacted by viral mutations. Thence, it is essential to deeply uncover the interaction mechanisms of lipid membranes of SARS-CoV-2 with active ingredients of chemical disinfectants at the molecular level for controlling the COVID-19 pandemic or other enveloped respiratory viruses in the future.

2.4.2. CONSTRUCTION OF THE INITIAL MODEL

In this study, the lipid bilayer is designed to investigate the possible impact of temperature on the SARS-CoV-2 bilayer membrane. The lipid composition of viral membranes is taken from Angela Violi et al., as displayed in Table 2.4 [36]. SARS-CoV-2 membrane is comprised of POPC (1-palmitoyl-2-oleoyl-sn-phosphatidylcholine), POPE (1-palmitoyl-2-oleoyl-sn-phosphatidylethanolamine), POPI (1-palmitoyl-2-oleoyl-sn-phosphoinositol), POPS (1-palmitoyl-2-oleoyl-sn-glycero-phosphatidylserine), PSM (palmitoyl sphingomyelin), and cholesterol molecules, and their corresponding atomistic structures are plotted in Figure 2.3. In order to make the investigated viral membrane less complex and to exclude the effect of proteins, the protein structures embedded in the lipid membrane of SARS-CoV-2 are ignored in the construction of its membrane. The membrane without protein structures possesses two hundred lipid molecules in total and has an approximate size of 8.8 nm by 8.8 nm. It should be noted that minor rounding is required in modeling to meet the requirements of SARS-CoV-2 lipid composition. The number of POPC, POPE, POPI, POPS, PSM, and cholesterol molecules are 130, 20, 18, 10, 8, and 14, respectively. Besides, appropriate amounts

Table 2.3: The phospholipid composition of SARS-CoV-2, and rat liver membranes reproduced by Vance and Van Meer [35]. The value of Chol/PL is molar ratio.

	Vance								
Lipid	ER	Mito inner	Mito outer	Lysos-omes	Nuclei	Golgi	Plasma	Vero	A549
PC	57	41	49	42	52	45	43	61	40
PE	21	38	34	21	25	17	21	19	23
SM	4	2	2	16	6	12	23	0.024	0.009
PI	9	2	9	6	4	9	7	18	37
PS	4	1	1	1	6	4	4	0.013	0.005
CL	0	16	5	0	0	0	0		
Other	5	<1	<1	14	7	13	2	1.75	0.33
Chol/PL	0.07	0.06	0.06	0.49		0.15	0.76	0.0006	0.0005
	Van Meer								
PC	58					50	39		
PE	22					20	23		
SM	3					8	16		
PI	10					12	8		
PS	3					6	9		
Chol/PL	0.08					0.16	0.35		

Table 2.4: The lipid composition of membranes [36].

Membrane	POPC	POPE	POPI	POPS	CL	PSM	Cholesterol
Plasma	25	15	5	6	1	11	38
Lysosome	25	9	3	2	1	13	48
Golgi	47	19	11	6	1	7	9
Mitochondrial	43	33	5	1	14	1	4
Endoplasmic Reticulum	72	17	6	4	0	2	7
CoV without S protein	65	10	9	5	0	4	7
CoV with S protein	89	13	13	7	0	5	9

of ions are added to neutralize the charge of the membrane complex structure. The membrane builder of the CHARMM-GUI program suite is applied to construct the pre-equilibrated initial model with various lipids, water molecules, and ions [37]. The membrane system of SARS-CoV-2 virions is plotted in Figure 2.4.

2.4.3. COMPUTATIONAL METHODOLOGIES

All MD simulations are performed using the GROMACS package (version 2019.6) with a time step of 2 fs [38]. The constructed membrane system is parameterized with CHARMM36 all-atom force field published in 2020 [39]. Meanwhile, the TIP3P water model is used to describe the solvation of the membrane system, and 0.15M KCl is added to neutralize the net charge of the membrane system. In order to mimic the infinite system, periodic boundary conditions (PBC) are imposed in three directions of the mem-

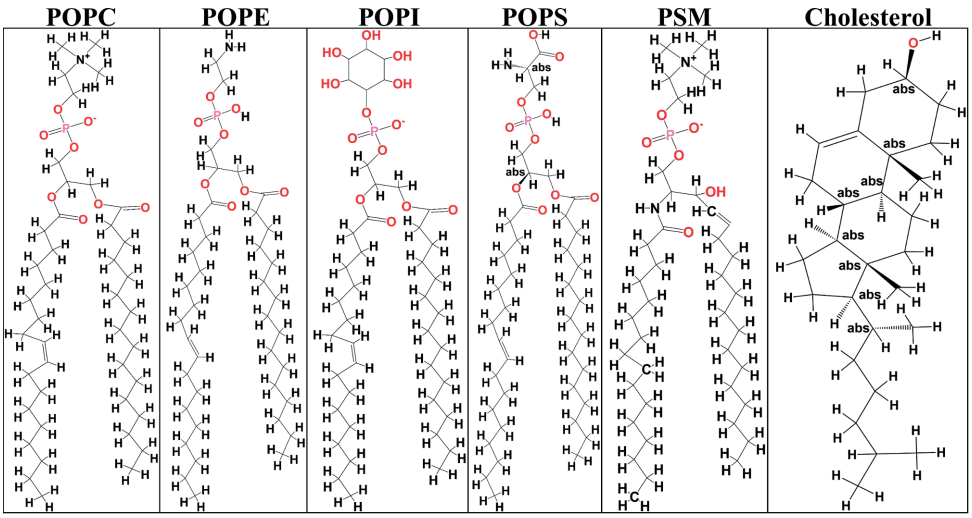


Figure 2.3: The atomistic structures of POPC, POPE, POPI, POPS, PSM, and cholesterol molecules.

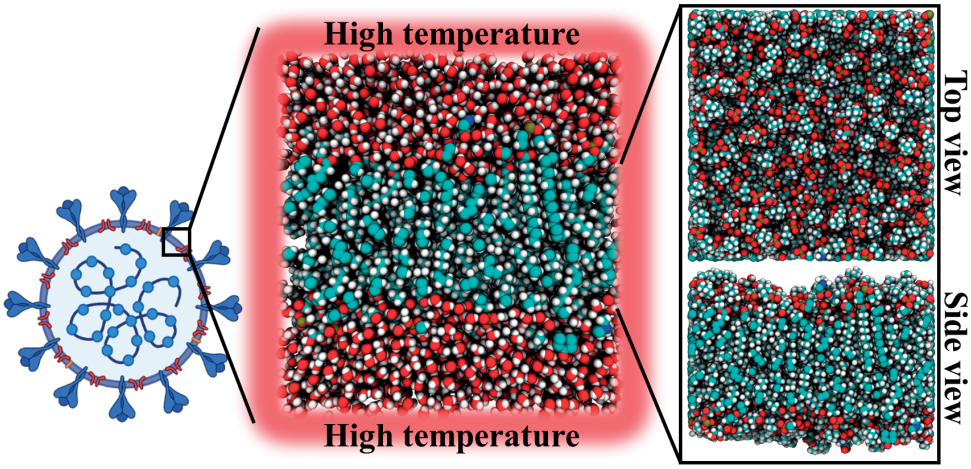


Figure 2.4: The phospholipid membrane model of SARS-CoV-2 with (a) and without (b) water molecules and neutralizing ions.

brane system. In the simulation process, a 315 K temperature and a 1 bar pressure are coupled with the components of the membrane system, including water molecules, neutralizing ions, and lipid molecules. The energy minimization of the membrane system is carried out through the steepest descent method, and the convergence value of the maximum is 100 kJ $\cdot$mol^{-1} $\cdot$nm^{-1}. In the equilibration process, the temperature and pressure coupling adopt the velocity rescaling (V-rescale) thermostat and Berendsen schemes, respectively [40], [41]. The total equilibration time is 50 ns. Eventually, the production semi-isotropic NPT simulations with 100 ns using the equilibrated structure

are conducted to reveal the changes in the membrane structure. In this step, we apply the Parrinello-Rahman algorithm to control the pressure equilibration of the membrane system [42]. It should be noted that the pressure is controlled in the x and y directions of the membrane by employing the same compression factor, and the pressure control in the z direction is separated from the x and y directions. In addition, for the constraints on the bonds connected to hydrogen atoms, the h-bonds are applied. The van der Waals (vdW) and long-range electrostatic interactions are evaluated on the basis of the cut-off and particle mesh Ewald (PME) methods, respectively. The cut-off distance for calculating the electrostatic and vdW interactions is 1 nm. The Visual Molecule Dynamics (VMD) package (version 1.9.3) is employed to visualize and analyze the investigated structures [43]. Five temperatures of 315, 329.15, 340.15, 348.15, and 363.15 K are taken into account in the MD simulations, having demonstrated their inactivation effectiveness against viruses including SARS-CoV-2 in previous studies [24], [26], [44], [45]. Furthermore, the production semi-isotropic NPT simulations with 1000 ns are also performed at the same simulation conditions to further explore the changing trend in the membrane structure following longer simulation times and prove the reasonableness of the chosen simulation times. The area per lipid, membrane thickness, mass density, electron density, mean square displacement, and radial distribution function of the membrane structure at different temperatures are discussed to reveal the possible impact of temperature on the bilayer membrane of SARS-CoV-2.

2.4.4. RESULTS AND DISCUSSION

Bilayer area and bilayer thickness. The area per lipid (APL), as an essential feature for comparison with experiments, largely determines other structural and dynamical features, such as membrane thickness, lateral diffusion of lipids, and membrane compressibility [46]. In order to reveal the structural variation of the bilayer membrane at different temperatures,the total APL and thickness of the bilayer membrane are first discussed. As illustrated in Figure 2.5(a), it can be observed that there is an increase in the total APL of the bilayer membrane with increasing temperature following 100 ns of production simulation. Meanwhile, the statistical result in Figure 2.5(c) further provides visible evidence for changing the total APL at different temperatures. It can be found that the average total APL of the bilayer membrane gradually increases with temperature. The averaged total APLs are 60.45, 62.56, 64.26, 65.25, and 66.84 $Å^2$ for the temperature of 315, 329.15, 340.15, 348.15, and 363.15 K, respectively. The averaged total APL at 315 K is very close to the reported APL of 60.0 $Å^2$ for the multi-lipid membrane without S proteins in an earlier study [36]. In agreement with the increased total APL, the thickness of the bilayer membrane shows a reduction with the increasing temperature, as displayed in Figure 2.5(b). The box-chart analysis of the membrane thickness in Figure 2.5(d) further gives robust evidence. The averaged membrane thickness gradually decreases with temperature. However, the variation magnitude in the bilayer thickness is slightly more minor than that of the total APL. The average thicknesses of bilayer membrane are calculated over 100 ns time, being turned out to be 40.61, 39.90, 39.41, 39.15, and 38.55 Å for 315, 329.15, 340.15, 348.15, and 363.15 K, respectively. Overall, the investigated temperatures have a negligible impact on the bilayer structure within 100 ns simulation time, giving the underlying interpretation for temperature-induced deformation in the bilayer mem-

brane.

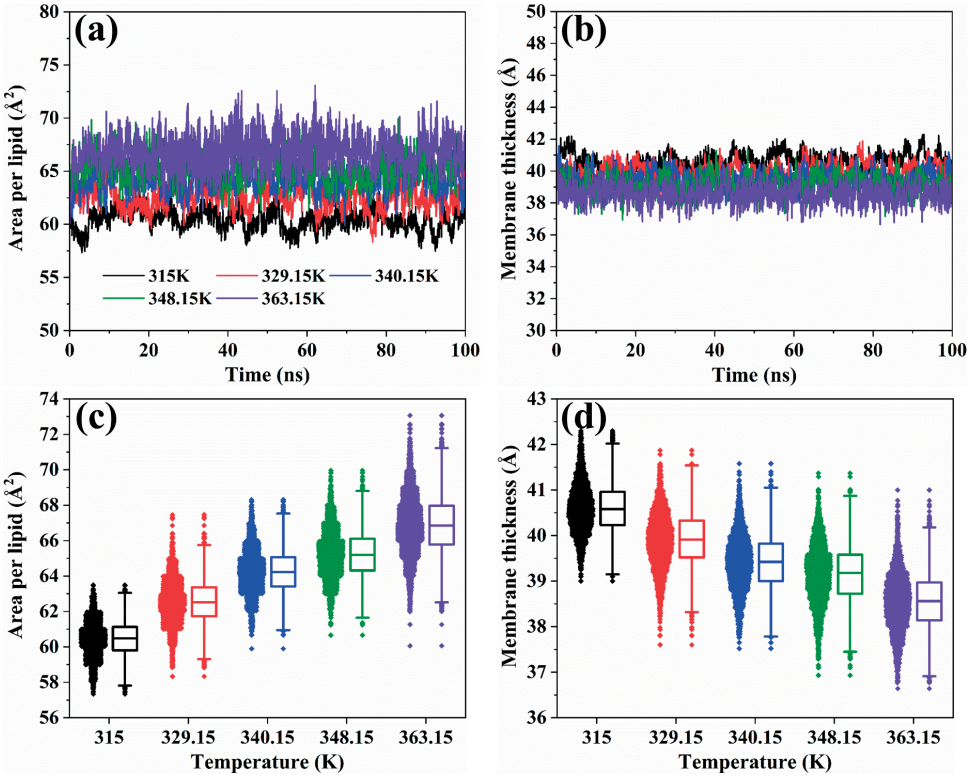


Figure 2.5: The total APL (a) and membrane thickness (b) of the multi-lipid bilayer structure as a function of temperature over a 100 ns simulation time. The box-chart analysis of the total APL (c) and membrane thickness (d) of the multi-lipid bilayer structure during a 100 ns simulation time.

Furthermore, the total APL and thickness of the bilayer membrane following the 1000 ns simulation are also discussed. As shown in Figure 2.6(a), the total APL of the bilayer membrane exhibits an increasing phenomenon when the temperature is changed from 315 K to 363.15 K, which is similar to the observed in the case of 100 ns time. Figure 2.6(c) also further supports this phenomenon. The averaged total APLs following 1000 ns simulation are 59.62, 61.95, 62.97, 64.11, and 66.24 Å^2 for 315, 329.15, 340.15, 348.15, and 363.15 K, respectively. Those values are smaller than those in the case of 100 ns time. The average difference in the total APL between these two simulation times is 0.9 Å^2, only 1.4% of the total APL. The membrane thickness exhibits a reduction behavior with increasing temperature, as plotted in Figure 2.6(b), which is the same as one shown in Figure 2.5(b). Meanwhile, the box-chart analysis in Figure 2.6(d) further provides a more visual perspective for changing the total APL. The average thickness of bilayer membrane over 1000 ns time is 40.57, 39.90, 39.42, 39.10, and 38.55 Å for 315, 329.15, 340.15, 348.15, and 363.15 K, respectively. Those thickness values are incredibly close to those obtained in the case of 100 ns time, and their difference could be neglected. There-

fore, 100 ns simulation time is sufficient to describe the dynamic behavior of the bilayer membrane at different temperatures, which is also proved by the results published in an earlier study [36].

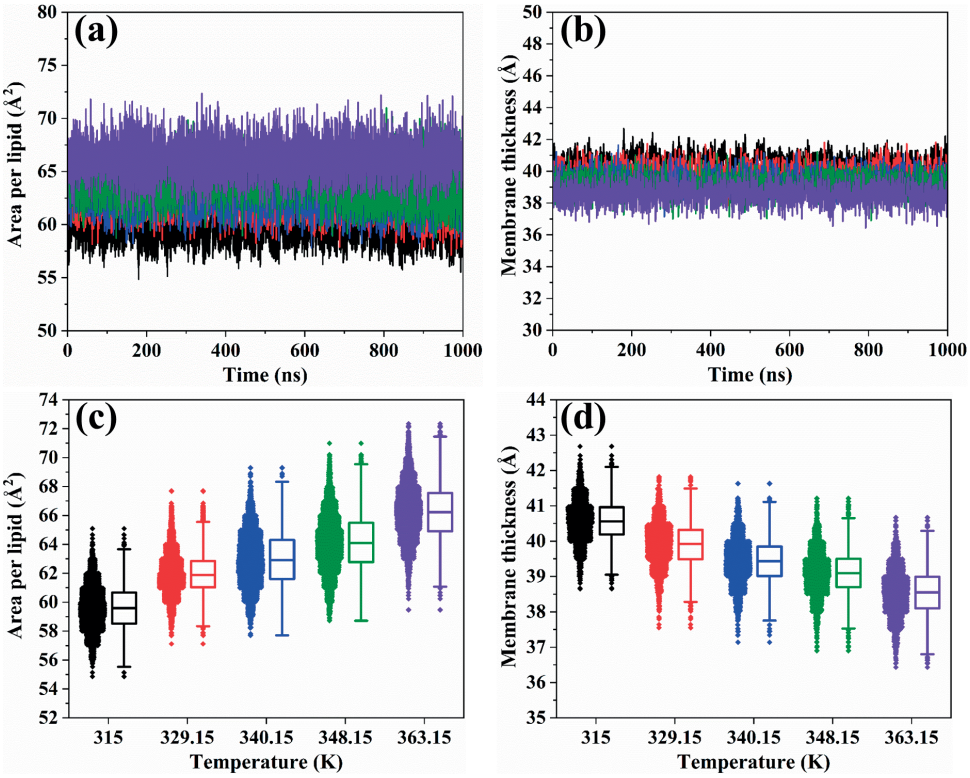


Figure 2.6: The total APL (a) and membrane thickness (b) of the multi-lipid bilayer structure as a function of temperature over a 1000 ns simulation time. The box-chart analysis of the total APL (c) and membrane thickness (d) of the multi-lipid bilayer structure during a 1000 ns simulation time.

Mass density of the lipids and water molecules. In order to get insight into the structural changes of the bilayer membrane, the simulated mass density profiles of the lipids and water molecules along the bilayer normal for the multi-lipids bilayer system at different temperatures are taken into account. The mass density profiles for the temperature of 315, 329.15, 340.15, 348.15, and 363.15 K under 100 ns simulation time are plotted in Figure 2.7. As shown in Figure 2.7(a), it can be found that the height of the entire profile of the lipid mass densities visibly drops as the temperature increases. In particular, the variation in two peaks of the mass density profile for the lipids is larger than that in the valley, suggesting that head-groups of the bilayer are more susceptible to temperature than the hydrophobic portion. Meanwhile, the horizontal coordinates of the two peaks are slightly shifted towards the origin of the coordinate with the increasing temperature, which further gives evidence that the decreased thickness of the bilayer. For water molecules, Figure 2.7(b) clearly presents that the mass density profile of water

molecules in the head-groups portion slightly changes when the temperature increases. The mass density of water molecules in the bilayer center still remains zero, regardless of the increasing temperature. This suggests that the spacing between lipid molecules is insufficient to enable water molecules to penetrate the membrane. However, there is a tiny change in the mass density of water molecules in the hydrophobic region. Therefore, it reveals that an increase in temperature does not eliminate the unfavorable interactions with alkyl lipid tails and further effectively assists the permeation of water molecules into the bilayer interior. Besides, the mass density profile of lipid and water molecules at the same temperature under 1000 ns time is very similar to that under 100 ns time. Meanwhile, the changing induced by different temperatures also exhibits the same trend. This result further provides powerful evidence for the reasonableness of 100 ns production time.

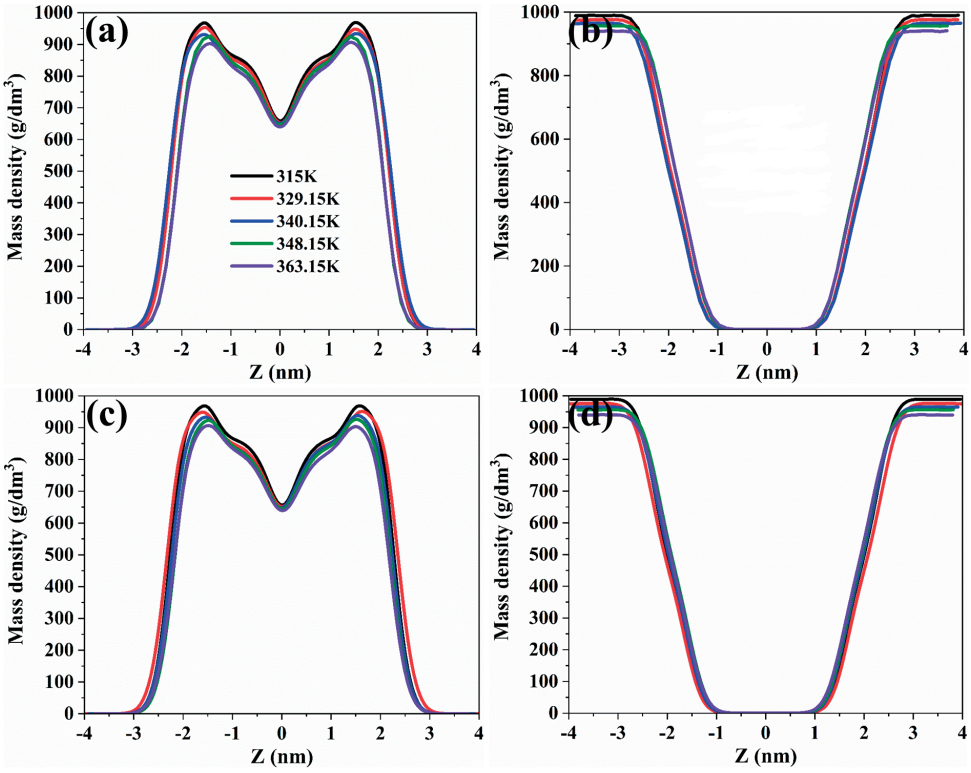


Figure 2.7: Mass density profiles of lipids and water molecules along the bilayer normal over the membrane system at different temperatures. (a) and (c) represent the mass density of lipids at 100 ns and 1000 ns, respectively. (b) and (d) correspond to the mass density of lipids after 100 ns and 1000 ns of simulation time, respectively.

Electron density profiles of the lipids. Electron density profiles along the normal to the bilayer membrane are more informative for the membrane structure than the membrane thickness and APL. X-ray diffraction provides a method of obtaining this quantity in the experimental level, measuring the corresponding information that produces the

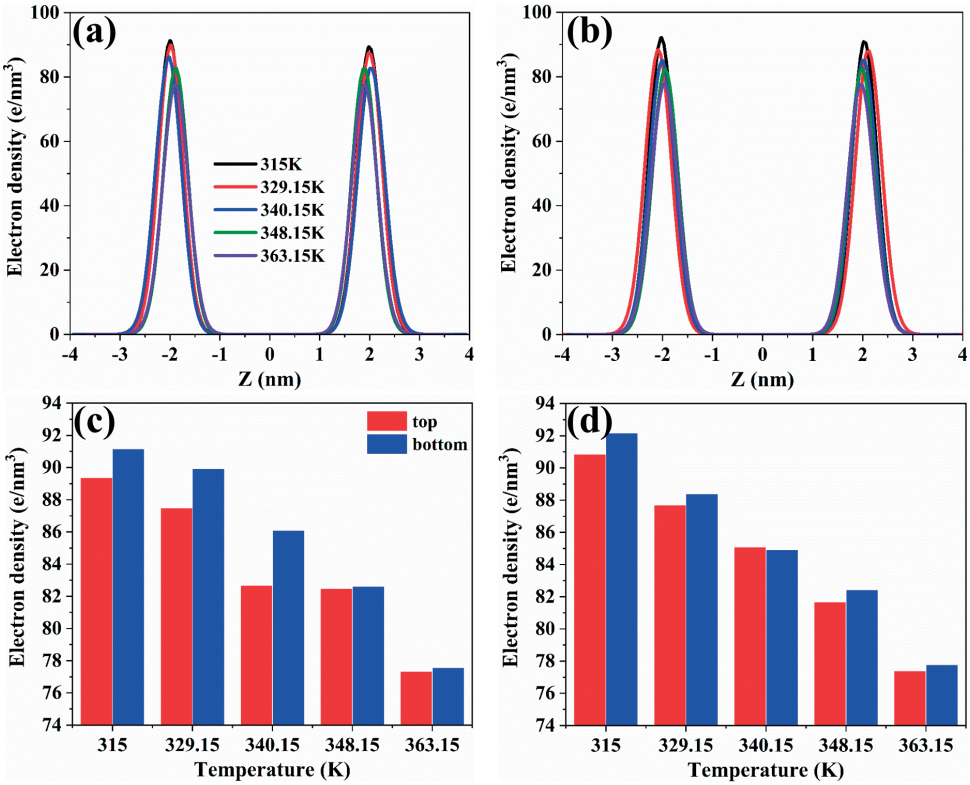


Figure 2.8: Electron density profiles of the lipids along the bilayer normal for the multi-lipid bilayer system at different temperatures after 100 ns (a) and 1000 ns (b) of simulation time. The electron densities at the two peaks for the top and bottom leaflets at 100 ns (c) and 1000 ns (d) simulation times.

electron density distribution. Figure 2.8 illustrates the electron density profiles of the bilayer membrane at different temperatures under 100 ns and 1000 ns simulation times. As displayed in Figure 2.8(a), it is found that the temperature has an evident impact on the head-groups of lipid molecules. When the temperature increases from 315 K to 329.15 K, the electron density profile of the lipids exhibits a slight dropping on two peaks. However, there is a significant reduction at the two peaks of the electron density profile as the temperature increases further, increasing to 363.15 K in particular, which is visually described in Figure 2.8(c). Furthermore, it should be noted that the heights of two peaks in the density profile at the same temperature are different. Figure 2.8(c) clearly shows that there is a clear difference between the electron density peaks of the top and bottom leaflets at 315, 329.15, and 340.15 K, whereas at 348.15 and 363.15 K, it is negligible. At the same time, it is also noted that the coordinates of two peaks at 348.15 K are closer to the origin of the coordinate than those at other temperatures. As a result, a higher temperature may cause a more remarkable effect on the electron density profile of the lipids. In addition, it is found that the difference in two density peaks following 1000 ns simulation is smaller than that at 100 ns time. Meanwhile, two density peaks at 1000 ns time

are slightly higher than that obtained at 100 ns time. Importantly, the changing behavior in two density peaks at 1000 ns time is better than that following 100 ns simulation, as presented in Figure 2.8(b) and (d). However, the changing trend of density peaks in both density value and coordinate with increasing temperature are still maintained, regardless of simulation time. Compared to the total APL, membrane thickness, and mass density profile, the electron density profile is more sensitive to the simulation time.

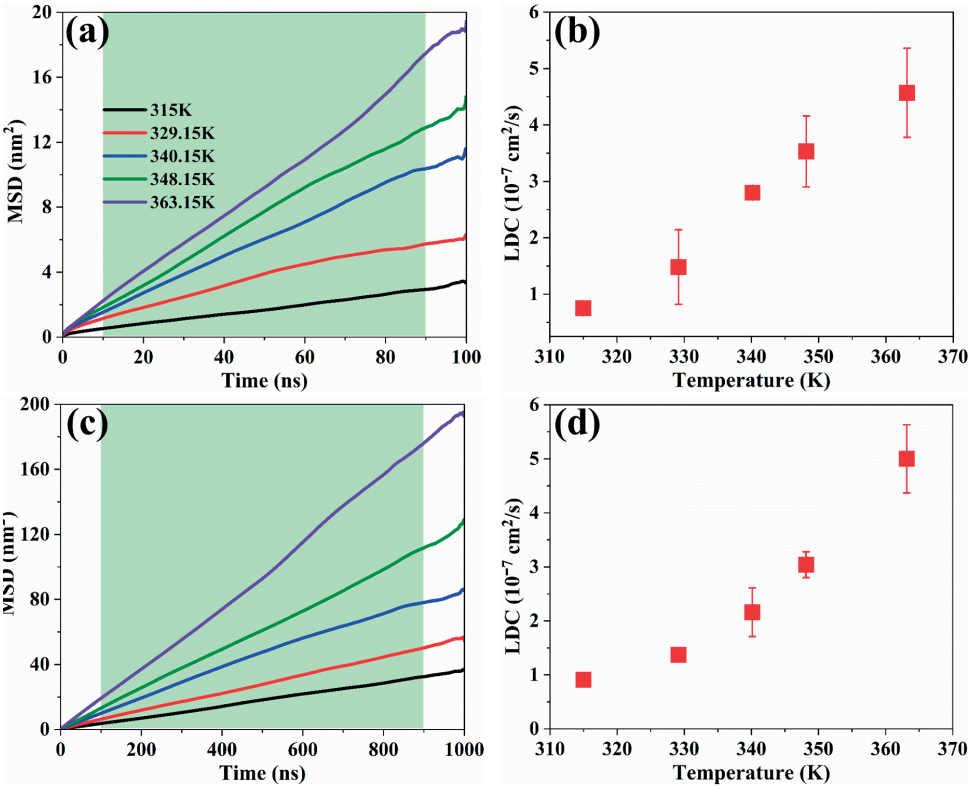


Figure 2.9: The MSD and LDC in the plane of the bilayer membrane at different temperatures following 100 ns (a-b) and 1000 ns (c-d) simulations.

Lateral diffusion behavior of the lipids. Here, the time dependence of the dynamic behavior of lipid molecules inside the bilayer membrane is evaluated. Notably, we are only concerned with the lateral diffusion behavior of lipid molecules. Figure 2.9 summarizes the mean square displacement (MSD) and the lateral diffusion coefficient (LDC) for different temperatures at 100 ns and 1000 ns simulation time. The LDC can be obtained by fitting the 10%~90% range of the production time, as depicted in the light green region of Figure 2.9(a) and (c). In Figure 2.9(a), it can be found that the MSD significantly increases with increasing temperature, suggesting that lipid molecules move more actively. This result is powerfully confirmed by the calculated data in Figure 2.9(b). The LDCs of the lipids are (0.75±0.11), (1.48±0.66), (2.80±0.05), (3.53±0.63), and (4.57±0.79)$\times 10^{-7}$ cm^2/s for the temperature of 315, 329.15, 340.15, 348.15, and 363.15

K, respectively. Obviously, the increasing temperature results in an increase in the LDC of the lipids. At the same time, the LDCs exhibit an almost linear relationship with temperatures. In the case of 1000 ns time, the response relationship of the MSD with temperatures is the same as that of 100 ns time, as displayed in Figure 2.9(c). The LDCs of the lipids are (0.91±0.04), (1.37±0.08), (2.16±0.45), (3.04±0.24), and (5.00±0.63)×10^{-7} cm^2/s at 315, 329.15, 340.15, 348.15, and 363.15 K, respectively. The LDC values between 100 ns and 1000 ns time are very close, and their relationship with temperatures is also similarly illustrated in Figure 2.9(d).

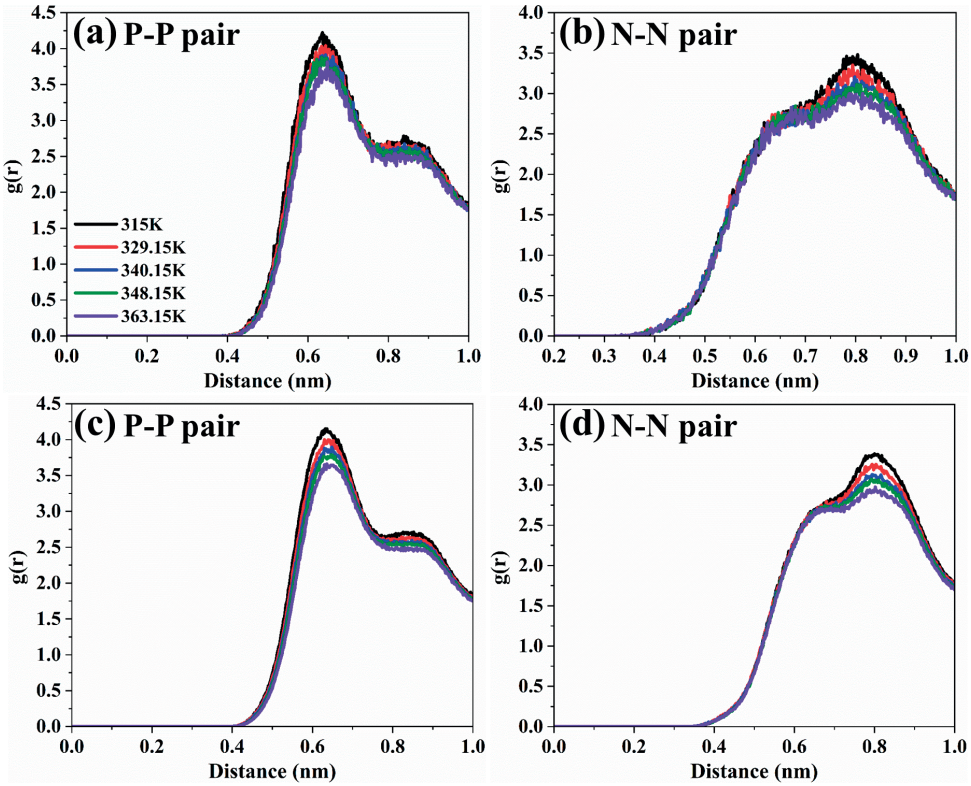


Figure 2.10: Two-dimensional RDFs $g(r)$ of atomic pairs of lipid molecules in the bilayer membrane at different temperatures following 100 ns (a-b) and 1000 ns (c-d) simulations.

2D RDF of the bilayer system. To gain insight into the effect of temperature on the membrane structure, we eventually discuss the 2D RDFs of P-P and N-N pairs of the lipid head-groups, as displayed in Figure 2.10. For the P-P pair, Figure 2.10(a) manifests that the P-P RDF has the first peak around 0.63 nm followed by the second peak around 0.84 nm. The first peak is much higher than the second peak, which suggests that the probability of lipid molecules appearing at 0.63 nm is higher than at 0.84 nm. Meanwhile, the drop in the first peak is more significant than in the second peak as the temperature increases. Unexpectedly, the P-P RDF at 340.15 K is very similar to that at 348.15 K, which implies that the lateral spacing between P atoms in the lipid head-groups is almost the

same at these two temperatures. The total APLs of the bilayers also support this at 340.15 and 348.15 K. In Figure 2.10(b), we can observe that the N-N RDF only presents a peak around 0.8 nm. Similar to the P-P RDF, the peak in the N-N RDF also decreases with the temperature increases. However, the drop in the peak of the N-N RDF is more considerable compared to that in the P-P RDF, which means that a high temperature induces the increase of the lateral spacing between lipid molecules. Overall, both the P-P and the N-N RDFs present a drop in the highest peak as the temperature increases, but the peak position remains unchanged. As plotted in Figure 2.10(c) and (d), the P-P and N-N pair RDFs at 1000 ns production time are almost indentical to those at 100 ns production time. The change of the pair RDFs also mainly occurs at the peaks where the peak values gradually reduce with the increase of the temperature. The only difference is the volatility of the values. In comparison, because of the difference in statistics, the visualization of the peak changes at 1000 ns time is more apparent. However, applying 100 ns production time is sufficient to directly observe the changing behavior of the pair RDFs at different temperatures from the qualitative perspective.

The most vulnerable part of viral particles is the lipid envelope, thus enveloped viruses are easier to inactivate compared to nonenveloped viruses [47]. The phases of viral membranes depend on the temperature. The lipids exhibit a solid gel phase at a low temperature, and their lateral movement is low. After heating, the bilayer membrane transitions into a liquid-disordered phase in which lipid molecules diffuse in the plane of the bilayer membrane, and their fatty acid tails show considerable flexing and bending. As depicted in Figure 2.11, the bilayer membranes at varying temperatures present disorders of the lipids and different magnitudes of flexing and bending in their fatty acid tails. Meanwhile, as the temperature increases, the fatty acid tails of lipid molecules are flexed and bent more significantly. Besides, the LDC values of lipid molecules gradually increase with varying temperatures. Those results clearly suggest that the diffusion of lipid molecules is more active at high temperatures. SARS-CoV-2 exposure to a moderate temperature (even a mild temperature increase) would result in a dramatic disruption of viral structural stability [48]. Vershinin et al. have demonstrated that high temperatures can lead to the rapid degradation of SARS-CoV-2 particles by atomic force microscope imaging [48]. The atomic force microscope imaging indicates that rarely a few viral particles can retain their shape, thus their structures may have been damaged. Meanwhile, their results also suggest that the disruption of the viral envelope caused by high temperatures is rare. This result is in agreement with the simulation result that the structure of the bilayer membrane remains intact at elevated temperatures. Another HIV study supposes that a minimum ordering in the viral envelope is essential for viral stability and infectivity [49]. Another study on influenza viruses confirms that viral fusion appears to be independent of ordered lipid content, and lipid order may be beneficial for viral stability at lower temperatures [50]. Furthermore, an MD study has shown that the structure and dynamic of embedded protein dimers are correlated to membrane structure and its ordered or disorderedness. However, the presence of proteins has little impact on the overall properties of the lipid membrane [51]. At the same time, the dynamics in the lipid membrane and M proteins contribute to the binding and aggregation of M proteins within a specific temperature range [51]. Unfortunately, only two types of lipid molecules, i.e., DPPC and DPPG lipids, are used to construct the lipid membrane of

SARS-CoV-2. The temperature stability and infectivity of viral particles are dependent on the cholesterol magnitude in the viral membrane [52], [53]. Lower cholesterol level leads to stronger heat-stability of viral particles [52]. The present MD results are consistent with the previous investigations where the structural stability of viral particles exposed to a temperature is analyzed, especially in the lipid membranes [48], [50], [51]. This result further suggests that the bilayer membrane plays a crucial role in the temperature stability of SARS-CoV-2 particles.

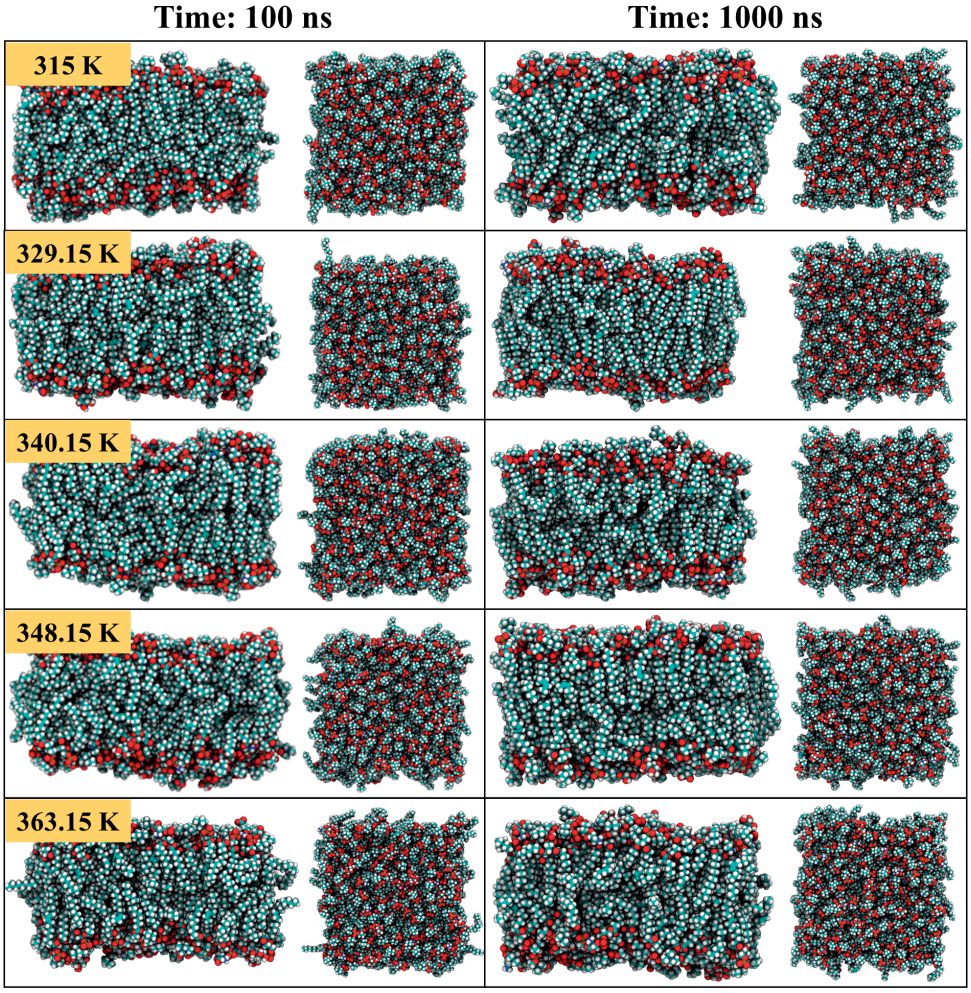


Figure 2.11: End snapshots of the bilayer system without water molecules and neutralizing ions following the production simulation at 315, 329.15, 340.15, 348.15, and 363.15 K. In the snapshots, the H, C, O, N, and P atoms are colored in white, cyan, red, blue, and brown, respectively.

To the best of our knowledge, the thermal aggregation or denaturation of structural proteins in the bilayer membrane may be one of the leading causes for inactivating CoVs by heat disinfection [29], [51], [54], [55]. In particular, the S protein plays a critical role

in the entry of viral particles into host cells. As mentioned above, the S protein of SARS-CoV-2 transitions into the closed state at a specific temperature, which leads to the failure of RBD-ACE2 binding. This result implies the loss of viral infectivity. Besides, a published study on SARS-CoV has confirmed that M proteins in SARS-CoV are more susceptible to heat and are aggregated following heat treatment [54]. The aggregation of M proteins and the shape alteration of viral particles appear to be associated with the dynamics of the lipid membrane. Therefore, the changes in the bilayer membrane caused by varying temperatures also have a pivotal impact on viral viability and infectivity. The limitation of the current study is that the lipid membrane does not include the structural proteins.

2.5. CONCLUSIONS

In summary, we theoretically reveal the possible impact of temperature on the bilayer membrane of SARS-CoV-2 virions on the basis of molecular dynamics simulations. The structural information, including total APL, membrane thickness, mass density, electron density, and radial distribution function, are discussed. The simulation results clearly show that the total APL of the lipid membrane gradually increases with the increasing temperature, and conversely the membrane thickness is inversely correlated with the temperature. The mass density profiles of water molecules directly demonstrate that the spacing between lipid molecules is insufficient to enable water molecules to enter the lipid membrane. This result indicates that high temperatures do not lead to the destruction of the membrane structure, which is consistent with the reported experimental results. Meanwhile, it is found that the mass and electron densities in the head-groups of lipid molecules vary significantly as the temperature increases. Besides, the bilayer membrane transitions into the liquid-disordered phase at the elevated temperature, where lipid molecules become more active and intensely diffuse in the membrane plane. The fatty acid tails of lipid molecules show considerable flexing and bending, and at 363.15 K in particular. The end snapshots of the bilayer membranes further demonstrate this result. Eventually, 2D RDFs clearly display that the probability of lipid molecules appearing at a certain distance decreases when the temperature increases, which may be attributed to the lateral expansion of the lipid membrane. Those findings provide the molecular-level perspective for uncovering the effect of temperature on the bilayer membrane of SARS-CoV-2 virions and the possible role of the dynamics of the lipid membrane in the heat inactivation of viruses.

REFERENCES

[1] M. E. Tuckerman and G. J. Martyna, *Understanding modern molecular dynamics: Techniques and applications*, 2000.

[2] T. Hansson, C. Oostenbrink, and W. van Gunsteren, "Molecular dynamics simulations", *Current opinion in structural biology*, vol. 12, no. 2, pp. 190–196, 2002.

[3] H. Qin, Q.-X. Pei, Y. Liu, and Y.-W. Zhang, "Thermal transport in graphene-based layered materials: An analytical model validated with extensive molecular dynamics simulations", *Carbon*, vol. 155, pp. 114–121, 2019.

[4] J. D. Durrant and J. A. McCammon, "Molecular dynamics simulations and drug discovery", *BMC biology*, vol. 9, no. 1, pp. 1–9, 2011.

[5] F. Khalili-Araghi, J. Gumbart, P.-C. Wen, M. Sotomayor, E. Tajkhorshid, and K. Schulten, "Molecular dynamics simulations of membrane channels and transporters", *Current opinion in structural biology*, vol. 19, no. 2, pp. 128–137, 2009.

[6] R. F. Ribeiro, L. A. Martínez-Martínez, M. Du, J. Campos-Gonzalez-Angulo, and J. Yuen-Zhou, "Polariton chemistry: Controlling molecular dynamics with optical cavities", *Chemical science*, vol. 9, no. 30, pp. 6325–6339, 2018.

[7] D. Beeman, "Some multistep methods for use in molecular dynamics calculations", *Journal of computational physics*, vol. 20, no. 2, pp. 130–139, 1976.

[8] S. U. I. NOSÉ, "A molecular dynamics method for simulations in the canonical ensemble", *Molecular Physics*, vol. 100, no. 1, pp. 191–198, 2002.

[9] H. J. Berendsen, J. v. Postma, W. F. Van Gunsteren, A. DiNola, and J. R. Haak, "Molecular dynamics with coupling to an external bath", *The Journal of chemical physics*, vol. 81, no. 8, pp. 3684–3690, 1984.

[10] M. Tuckerman, B. J. Berne, and G. J. Martyna, "Reversible multiple time scale molecular dynamics", *The Journal of chemical physics*, vol. 97, no. 3, pp. 1990–2001, 1992.

[11] W. F. Van Gunsteren and H. J. Berendsen, "A leap-frog algorithm for stochastic dynamics", *Molecular Simulation*, vol. 1, no. 3, pp. 173–185, 1988.

[12] R. W. Hockney and J. W. Eastwood, *Computer simulation using particles*. crc Press, 2021.

[13] W. C. Swope, H. C. Andersen, P. H. Berens, and K. R. Wilson, "A computer simulation method for the calculation of equilibrium constants for the formation of physical clusters of molecules: Application to small water clusters", *The Journal of chemical physics*, vol. 76, no. 1, pp. 637–649, 1982.

[14] R. W. Pastor, B. R. Brooks, and A. Szabo, "An analysis of the accuracy of langevin and molecular dynamics algorithms", *Molecular Physics*, vol. 65, no. 6, pp. 1409–1419, 1988.

[15] C. W. Gear, "The automatic integration of ordinary differential equations", *Communications of the ACM*, vol. 14, no. 3, pp. 176–179, 1971.

[16] M. Bockstedte, A. Kley, J. Neugebauer, and M. Scheffler, "Density-functional theory calculations for poly-atomic systems: Electronic structure, static and elastic properties and ab initio molecular dynamics", *Computer physics communications*, vol. 107, no. 1-3, pp. 187–222, 1997.

[17] H. Inagaki, A. Saito, H. Sugiyama, T. Okabayashi, and S. Fujimoto, "Rapid inactivation of sars-cov-2 with deep-uv led irradiation", *Emerging Microbes & Infections*, vol. 9, no. 1, pp. 1744–1747, 2020.

[18] Y. Liu and J. Rocklöv, "The reproductive number of the delta variant of sars-cov-2 is far higher compared to the ancestral sars-cov-2 virus", *Journal of travel medicine*, 2021.

[19] S. Su, G. Wong, W. Shi, *et al.*, "Epidemiology, genetic recombination, and pathogenesis of coronaviruses", *Trends in microbiology*, vol. 24, no. 6, pp. 490–502, 2016.

[20] A. J. Smit, J. M. Fitchett, F. A. Engelbrecht, R. J. Scholes, G. Dzhivhuho, and N. A. Sweijd, "Winter is coming: A southern hemisphere perspective of the environmental drivers of sars-cov-2 and the potential seasonality of covid-19", *International journal of environmental research and public health*, vol. 17, no. 16, p. 5634, 2020.

[21] C. C. Mandal and M. S. Panwar, "Can the summer temperatures reduce covid-19 cases?", *Public health*, vol. 185, pp. 72–79, 2020.

[22] K.-H. Chan, J. M. Peiris, S. Lam, L. Poon, K. Yuen, and W. H. Seto, "The effects of temperature and relative humidity on the viability of the sars coronavirus", *Advances in virology*, vol. 2011, 2011.

[23] A. W. Chin, J. T. Chu, M. R. Perera, *et al.*, "Stability of sars-cov-2 in different environmental conditions", *The Lancet Microbe*, vol. 1, no. 1, e10, 2020.

[24] G. Xiling, C. Yin, W. Ling, *et al.*, "In vitro inactivation of sars-cov-2 by commonly used disinfection products and methods", *Scientific Reports*, vol. 11, no. 1, pp. 1–9, 2021.

[25] J. Biryukov, J. A. Boydston, R. A. Dunning, *et al.*, "Sars-cov-2 is rapidly inactivated at high temperature", *Environmental chemistry letters*, vol. 19, no. 2, pp. 1773–1777, 2021.

[26] J. Burton, H. Love, K. Richards, *et al.*, "The effect of heat-treatment on sars-cov-2 viability and detection", *Journal of virological methods*, vol. 290, p. 114 087, 2021.

[27] K. Chan, S Sridhar, R. Zhang, *et al.*, "Factors affecting stability and infectivity of sars-cov-2", *Journal of Hospital Infection*, vol. 106, no. 2, pp. 226–231, 2020.

[28] H. Eslami and M. Jalili, "The role of environmental factors to transmission of sars-cov-2 (covid-19)", *Amb Express*, vol. 10, no. 1, pp. 1–8, 2020.

[29] S. L. Rath and K. Kumar, "Investigation of the effect of temperature on the structure of sars-cov-2 spike protein by molecular dynamics simulations", *Frontiers in molecular biosciences*, vol. 7, p. 583 523, 2020.

[30] Y.-w. Dong, M.-l. Liao, X.-l. Meng, and G. N. Somero, "Structural flexibility and protein adaptation to temperature: Molecular dynamics analysis of malate dehydrogenases of marine molluscs", *Proceedings of the National Academy of Sciences*, vol. 115, no. 6, pp. 1274–1279, 2018.

[31] J. Lan, J. Ge, J. Yu, *et al.*, "Structure of the sars-cov-2 spike receptor-binding domain bound to the ace2 receptor", *Nature*, vol. 581, no. 7807, pp. 215–220, 2020.

[32] X. Xiong, K. Qu, K. A. Ciazynska, *et al.*, "A thermostable, closed sars-cov-2 spike protein trimer", *Nature structural & molecular biology*, vol. 27, no. 10, pp. 934–941, 2020.

[33] X. Ou, Y. Liu, X. Lei, *et al.*, "Characterization of spike glycoprotein of sars-cov-2 on virus entry and its immune cross-reactivity with sars-cov", *Nature communications*, vol. 11, no. 1, pp. 1–12, 2020.

[34] J. He, H. Tao, Y. Yan, S.-Y. Huang, and Y. Xiao, "Molecular mechanism of evolution and human infection with sars-cov-2", *Viruses*, vol. 12, no. 4, p. 428, 2020.

[35] Z. Saud, V. J. Tyrrell, A. Zaragkoulias, *et al.*, "The sars-cov2 envelope differs from host cells, exposes pro-coagulant lipids, and is disrupted in vivo by oral rinses", *Journal of lipid research*, p. 100 208, 2022.

[36] C. Liu, P. Elvati, and A. Violi, "On drug-membrane permeability of antivirals for sars-cov-2", *The journal of physical chemistry letters*, vol. 12, no. 5, pp. 1384–1389, 2021.

[37] M. Schmick and P. I. Bastiaens, "The interdependence of membrane shape and cellular signal processing", *Cell*, vol. 156, no. 6, pp. 1132–1138, 2014.

[38] M. J. Abraham, T. Murtola, R. Schulz, *et al.*, "Gromacs: High performance molecular simulations through multi-level parallelism from laptops to supercomputers", *SoftwareX*, vol. 1, pp. 19–25, 2015.

[39] J. B. Klauda, R. M. Venable, J. A. Freites, *et al.*, "Update of the charmm all-atom additive force field for lipids: Validation on six lipid types", *The journal of physical chemistry B*, vol. 114, no. 23, pp. 7830–7843, 2010.

[40] A. Nash, T. Collier, H. L. Birch, and N. H. de Leeuw, "Forcegen: Atomic covalent bond value derivation for gromacs", *Journal of molecular modeling*, vol. 24, no. 1, pp. 1–11, 2018.

[41] D. K. Vanatta, D. Shukla, M. Lawrenz, and V. S. Pande, "A network of molecular switches controls the activation of the two-component response regulator ntrc", *Nature communications*, vol. 6, no. 1, pp. 1–7, 2015.

[42] R. E. Miller, E. B. Tadmor, J. S. Gibson, N. Bernstein, and F. Pavia, "Molecular dynamics at constant cauchy stress", *The Journal of chemical physics*, vol. 144, no. 18, p. 184 107, 2016.

[43] W. Humphrey, A. Dalke, and K. Schulten, "Vmd: Visual molecular dynamics", *Journal of molecular graphics*, vol. 14, no. 1, pp. 33–38, 1996.

[44] J. P. Abraham, B. D. Plourde, and L. Cheng, "Using heat to kill sars-cov-2", *Reviews in medical virology*, vol. 30, no. 5, e2115, 2020.

[45] F. Saadatpour and F. Mohammadipanah, "Physicochemical susceptibility of sars-cov-2 to disinfection and physical approach of prophylaxis", *Health Science Reports*, vol. 3, no. 4, e213, 2020.

[46] A. A. Gurtovenko and J. Anwar, "Interaction of ethanol with biological membranes: The formation of non-bilayer structures within the membrane interior and their significance", *The journal of physical chemistry B*, vol. 113, no. 7, pp. 1983–1992, 2009.

[47] M. Simon, M. Veit, K. Osterrieder, and M. Gradzielski, "Surfactants–compounds for inactivation of sars-cov-2 and other enveloped viruses", *Current Opinion in Colloid & Interface Science*, vol. 55, p. 101 479, 2021.

[48] A Sharma, B Preece, H Swann, *et al.*, "Structural stability of sars-cov-2 virus like particles degrades with temperature", *Biochemical and biophysical research communications*, vol. 534, pp. 343–346, 2021.

[49] R. C. Aloia, F. C. Jensen, C. C. Curtain, P. W. Mobley, and L. M. Gordon, "Lipid composition and fluidity of the human immunodeficiency virus.", *Proceedings of the National Academy of Sciences*, vol. 85, no. 3, pp. 900–904, 1988.

[50] I. V. Polozov, L. Bezrukov, K. Gawrisch, and J. Zimmerberg, "Progressive ordering with decreasing temperature of the phospholipids of influenza virus", *Nature chemical biology*, vol. 4, no. 4, pp. 248–255, 2008.

[51] S. L. Rath, M. Tripathy, and N. Mandal, "How does temperature affect the dynamics of sars-cov-2 m proteins? insights from molecular dynamics simulations", *The Journal of Membrane Biology*, pp. 1–16, 2022.

[52] C. Beer, A. Meyer, K. Müller, and M. Wirth, "The temperature stability of mouse retroviruses depends on the cholesterol levels of viral lipid shell and cellular plasma membrane", *Virology*, vol. 308, no. 1, pp. 137–146, 2003.

[53] X. Sun and G. R. Whittaker, "Role for influenza virus envelope cholesterol in virus entry and infection", *Journal of virology*, vol. 77, no. 23, pp. 12 543–12 551, 2003.

[54] Y.-N. Lee, L.-K. Chen, H.-C. Ma, H.-H. Yang, H.-P. Li, and S.-Y. Lo, "Thermal aggregation of sars-cov membrane protein", *Journal of virological methods*, vol. 129, no. 2, pp. 152–161, 2005.

[55] S. Seifer and M. Elbaum, "Thermal inactivation scaling applied for sars-cov-2", *Biophysical Journal*, vol. 120, no. 6, pp. 1054–1059, 2021.

3

THE INACTIVATION MECHANISM OF CHEMICAL DISINFECTANTS AGAINST SARS-CoV-2: FROM THE MOLECULAR-LEVEL PERSPECTIVE

Exploring effective disinfection methods and understanding their mechanisms on the new coronavirus is becoming more active due to the outbreak of the COVID-19 caused by SARS-CoV-2 virues. Using molecular dynamics and density functional theory methods, we investigate the interaction mechanism of chemical agents with 3CL hydrolase and phospholipid membranes of SARS-CoV-2. The simulation results indicate that the biocidal molecules are sensitive to the unsaturated oxygen atoms of 3CL hydrolase, and the interaction remarkably depends on the concentration of the biocidal molecules. Moreover, the biocidal molecules prefer to bind with the unsaturated oxygen atoms compared to other styles of atoms. In the case of the phospholipid membrane, the presence of biocidal molecules significantly affects the membrane structure, such as lateral swelling and progressive thinning of the lipid membrane, and HClO molecules in particular. Meanwhile, as the concentration of biocidal molecules increases, more biocidal molecules appear at the interior of the lipid membrane. This result suggests that biocidal molecules would penetrate through the lipid membrane and enter the viral interior. The 2D RDFs of the atomic pairs reveal that biocidal molecules prefer to bind to the O13 atoms of lipid molecules, which is consistent with the observed in the case of 3CL hydrolase. These computational findings not only decipher the inactivation mechanism of chemical agents against SARS-CoV-2 from the molecular-level perspective but also provide a theoretical basis for developing and applying new chemical methods with a high disinfection efficiency.

3.1. DENSITY FUNCTIONAL THEORY

DENSITY functional theory (DFT) is a quantum mechanical method to study the electronic structure using the density distribution of electrons instead of the wave function of electrons as a physical quantity to describe the system. It does not depend on empirical parameters and is therefore the first-principles calculation. In DFT calculations, the exchange-correlation functional directly determines the accuracy of calculated results. Thus, it is crucial to select the exchange-correlation functional. The exchange-correlation functional mainly includes LDA (local density approximation) [1], GGA (generalized gradient approximation) [2], and hybrid functional [3].

The LDA is based on a homogeneous electron-gas model, and its exchange-correlation functional $E_{xc}[n]$ can be expressed as [1]:

$$E_{xc}^{LDA}[n] = \int n(r)\,\varepsilon_{xc}(n)\,\mathrm{d}r \tag{3.1}$$

where ε_{xc} is the exchange-correlation energy of single electron in a homogeneous electron gas of density $n(r)$. The LDA usually underestimates the exchange energy but also overestimates the correlation energy. Thus, the overall error is more minor. The LDA only considers the local charge density $n(r)$, thus it is suitable for describing some systems (e.g., crystal) where the charge density changes slowly. On the contrary, the LDA often exhibits more significant errors for systems where the charge density varies rapidly or the exchange-correlation interaction is strong. In addition, it can be described by two spin-charge densities instead of the total charge density $n(r)$ on the basis of the LDA when considering the spin of electrons. This is called the LSDA (the local spin density approximation).

The GGA is able to better describe the systems where the charge density varies quickly due to the introduction of a gradient of charge density in the exchange-correlation functional. Its exchange-correlation functional $E_{xc}[n]$ is expressed as[2]:

$$E_{xc}^{GGA}[n_\sigma] = \int f(n_\sigma, \bigtriangledown n_\sigma)\,\mathrm{d}r \tag{3.2}$$

where σ is the spin coordinate of the spin-charge density. $f(n_\sigma, \bigtriangledown n_\sigma)$ can contain empirical parameters for the purpose of fitting a real system. It is therefore not strictly the first principles. However, the PBE functional applied in our study does not contain any empirical parameters[4].

The hybrid functional is the product of combining the Hartree-Fock exchange energy function with the DFT exchange-correlation energy function. For examples, B3LYP functional proposed by Stephens et al. in 1994 is expressed as [3]:

$$E_{xc}^{B3LYP} = (1-a_0)E_x^{LSDA} + a_0 E_x^{HF} + a_x E_x^{B88} + a_c \triangle E_c^{LYP} + (1-a_c)E_c^{VWN} \tag{3.3}$$

where HF, LYP, and VWN are Hartree-Fock, a GGA, and an LDA, respectively. E_x and E_c represent the exchange and correlation energy functional, respectively. a_0, a_x, and a_c are three empirical parameters, being 0.20, 0.72, and 0.81, respectively.

3.2. INACTIVATION OF SARS-COV-2 VIRIONS BY COMMONLY AVAILABLE DISINFECTANTS

The high stability of SARS-CoV-2 under favorable environmental conditions enables it survive for a couple of minutes or even longer [5]–[7]. This viability in vitro is conducive to coronavirus transmission between vectors and humans. Consequently, in the absence of vaccines, adopting effective methods that are helpful in cleaning and disinfecting community settings, healthcare settings, and the home environment is highly pressing for the prevention and control of epidemic situations. Applying chemical disinfectants has been an effective disinfection measure in minimizing the occurrence and spread of viruses. Recently, several inactivation studies on alcohol, hypochlorite, and silver ion-based solutions have been reported in order to clarify their effectiveness in inactivating SARS-CoV-2 [8]–[13]. Ethanol disinfectants are recommended by World Health Organization (WHO) as hand rub solutions [14]. The ethanol concentration in commerically available medical alcohol is 70%-75%. In previous studies, 78% to 95% of ethanol concentrations have been confirmed to effectively diminish the infectivity of CoVs in 30 s contact time by greater than 4 $\log_{10}$ [15], [16]. Previous research shows that the solution containing 20% ethanol is unable to inactivate SARS-CoV-2 virions, which is strongly proved by the morphology of Vero-E6 cells in different infection states(see Figure 3.1) [15]. Furthermore, the virucidal solutions with a 30% or higher ethanol concentration could efficiently inactivate SARS-CoV-2 virions in 60 s, with a reduction in viral titer of 4 $\log_{10}$ in only 30 s contact time (see Table 3.1) [17]. Another study reports that the WHO-recommended hand rub formulation I is capable of inactivating SARS-CoV-2 viruses within sufficient contact time [14]. Formulation I contain 80% ethanol, 1.45% glycerol, and 0.125% hydrogen preoxide, and its viral titer could be up to 3.8 $\log_{10}$ reduction at least. To further improve its inactivation ability, the glycerol concentration is reduced to 0.725%. This modified formulation I provide a 5.9 $\log_{10}$ reduction at least. It has been reported in the literature that the viral envelope might be a major target of ethanol molecules [18]. An AFM research clearly reveals the effect of ethanol solutions on the morphology of SARS-CoV-2, where the viral shape is deformed and flattened after exposing 80% of ethanol solution [19]. However, the problem is that it is difficult to prove whether the virus has completely lost its infectivity.

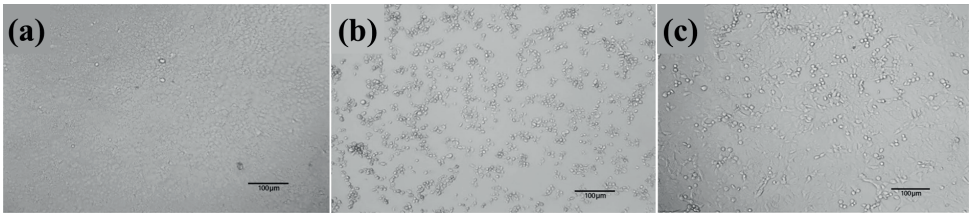


Figure 3.1: The morphology of Vero-E6 cells in different infection states [15]. (a) Before infection. Vero-E6 cells form an intact monolayer. (b) After infection with SARS-CoV-2. All Vero-E6 cells die and are completely dislodged from the bottom of the 96-wells plate. (c) After infection with SARS-CoV-2 and 20% of ethanol. Vero-E6 cells partially die and are detached from the bottom of the 96-wells plate.

Hypochlorite-based solutions are high-efficacy disinfectants. Even at low concentra-

Table 3.1: Effect of ethanol concentration on SARS-CoV-2 virion inactivation [15]. Note that the value less than 4.75 presents that there are varying amounts of virus survives following the treatment, while the value of ≥4.75 indicates that no viable viruses can be detected after the treatment.

Temperature (K)	Log_{10} reduction in infectious SARS-CoV-2 titer achieved Mean (Min~Max)			
	0.5 min	1 min	3 min	5 min
20	1.08 (0.75-1.50)	1.33 (1.00-1.50)	1.75 (1.50-2.00)	1.92 (1.50-2.25)
30	4.42 (4.25-4.50)	≥4.75	≥4.75	≥4.75
40	≥4.75	≥4.75	≥4.75	≥4.75
50	≥4.75	≥4.75	≥4.75	≥4.75
60	≥4.75	≥4.75	≥4.75	≥4.75
75	≥4.75	≥4.75	≥4.75	≥4.75

tions, sodium hypochlorite or hypochlorite acid rapidly inactivates most viruses, including CoVs, within the recommended contact time [20], [21]. The available chlorine concentration of the WHO-recommended chlorinated disinfectants is 0.1%. For instance, the concentration of sodium hypochlorite is ≥0.1%, which could effectively reduce the infectivity of CoVs in 60 s [22], [23]. Sodium hypochlorite played prominent role in the global public health emergencies caused by SARS-CoV and MERS-CoV virions. Because of the high similarity to SARS-CoV, it is supposed that sodium hypochlorite is expected to has a similar effect against SARS-CoV-2. Previous literature finds that bleach solutions with 0.1% and 0.5% concentrations of sodium hypochlorite have outstanding inactivation effectiveness for SARS-CoV-2 [22]. Nevertheless, the extended contact time leads to being unable to differentiate the effect of different concentrations. Besides, another published literature proves that 0.21 g/L of sodium hypochlorite within 30 s contact time is completely effective against SARS-CoV-2, and the reduction in viral titer is close to 4 log $TCID_{50}$, as plotted in Figure 3.2(a) [24]. In water disinfection, the published literature has confirmed that sodium hypochlorite has more rapid virucidal activity against SARS-CoV-2 compared to other waterborne viruses of interest [25]. In DI water, sodium hypochlorite with <1 mg-min/L gives a reduction of >3 log_{10} $TCID_{50}$, while in primary influent, a 3 log_{10} $TCID_{50}$ reduction requires >5 mg-min/L. It might be attributed to the shielding of the virus by the suspended solid materials. In addition to sodium hypochlorite, the hypochlorous acid solution is a potent disinfectant against CoVs including SARS-CoV-2. The inactivation experiments on SARS-CoV-2 viruses present that a hypochlorite acid solution at 56.3 ppm is sufficient to provide a 5 log $TCID_{50}$ reduction per mL following 10 s exposure in the suspension test. In comparison, in the carrier test, the reduction in viral titer caused by 125 ppm hypochlorite acid solution could reach 4 log $TCID_{50}$ after 10 min of incubation (see Figure 3.2(b)) [26]. Moreover, the antiviral activity of hypochlorite acid is independent of the presence or absence of organic matter in the suspension

test. Aiming at aerosolized coronavirus (IBV) in human-dispersed droplets, Kazuaki et al. explore the virucidal activity of slightly acidic hypochlorite acid water with varying concentrations for the IBV [21]. It is found that slightly acidic hypochlorous acid waters at 100 and 200 ppm of free available chlorine provide 0.21 $\log_{10}$ and 0.80 $\log_{10}$ reductions over a couple of seconds, respectively. For the solutions containing 300 and 500 ppm of free available chlorine, their reductions in viral titer are 1.16 $\log_{10}$ and 1.67 $\log_{10}$ within a few seconds, respectively. Those findings indicate that slightly acidic hypochlorous acid waters have rapid in vitro inactivation ability for aerosolized IBV. Based on the similarity of IBV and SARS-CoV-2, the authors suggest that slightly acidic hypochlorite acid water might also rapidly inactivate SARS-CoV-2.

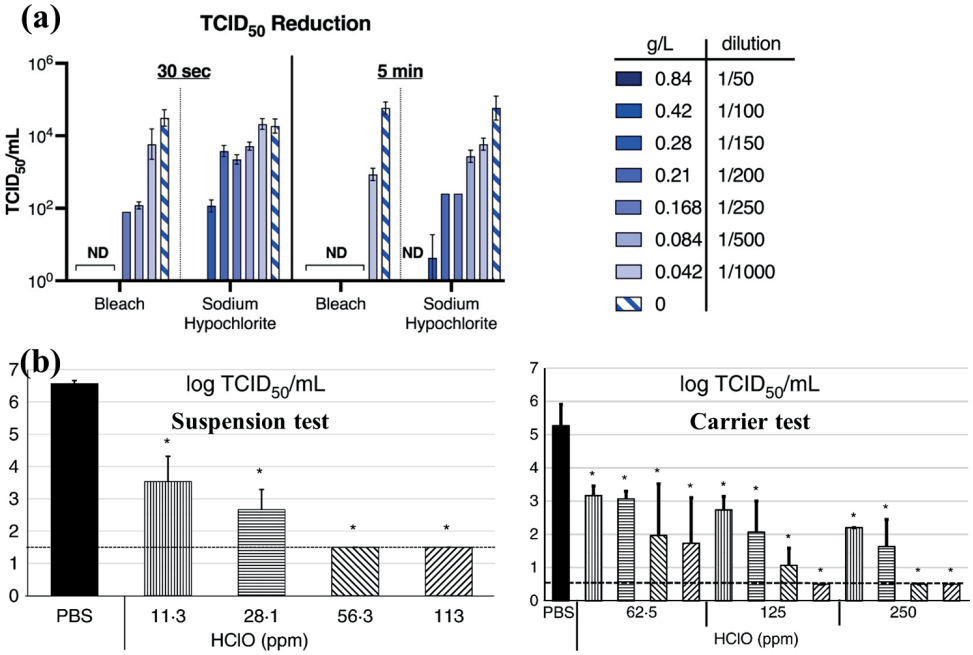


Figure 3.2: The inactivation effectiveness of sodium hypochlorite and hypochlorite acid solutions against SARS-CoV-2. (a) $TCID_{50}$ reduction in SARS-CoV-2 at sodium hypochlorite solutions with varying concentrations [24]. (b) The antiviral activity of hypochlorite acid solutions against SARS-CoV-2 viruses in the suspension and carrier tests [25].

Silver, as a precious metal, has been consciously utilized to act as a biocidal agent since ancient times. Its biocidal property in ionic form shows a substantial inactivation for the influenza A virus [27]. In 2003, silver ions-based disinfectants were included in the SARS prevention and treatment manual compiled by No. 302 Hospital of Chinese People's Liberation Army. Meanwhile, the efforts in the virucidal activity of silver ions toward coronavirus further confirm that silver ions have significant antiviral activity for SARS-CoV [28]. To the best of our knowledge, metal nanoparticles less than 10 nm could penetrate though the biomembrane and inhibit the replication of the pathogen genome (DNA or RNA), eventually leading to the loss of the pathogen's abil-

ity to reproduce [29], [30]. A previous study confirms that the antiviral activity of silver nanoparticles on SARS-CoV-2 has a size-dependent effect [31]. As shown in Figure 3.3, VeroE6/TMPRSS2 cells are not infected by SARS-CoV-2 in the presence of 10 nm silver particles, but it is the opposite for 100 nm particles. Other related research also suggests that silver nanoparticles-based coatings have an extreme antiviral activity on SARS-CoV-2 [32], [33]. A special nanotechnology-based solution containing titanium dioxide and silver ions is reportedly being applied for disinfecting Milan's buildings in Italy to stop the spread of SARS-CoV-2 virions [34]. A previous study has proven that there is only a 0.70 $\log_{10}$ reduction in titer after exposure to 5 ppm Ag^+ solution results for 1 min, but 360 min contact time is required for a reduction in viral titer of 3.05 $\log_{10}$ [35]. It is also found that the addition of 26% ethanol could significantly improve the antiviral activity of Ag^+ solution, where the reduction in viral titer achieves ≥3.72 $\log_{10}$ for 1 min incubation time.

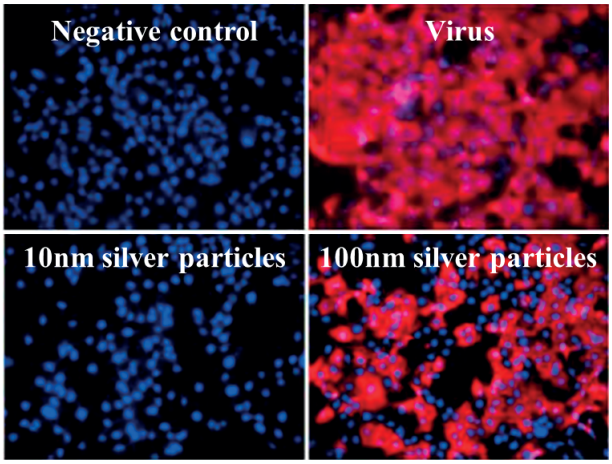


Figure 3.3: Immunofluorescence imaging of SARS-CoV-2 infection in VeroE6/TMPRSS2 cells in the presence of 10 and 100 nm silver particles. Notably, Blue is cell nuclei and red is SARS-CoV-2 nucleocapsid protein in cytoplasm [31].

3.3. THE INTERACTION MECHANISMS OF CHEMICAL DISINFECTANTS WITH 3CL HYDROLASE

3.3.1. 3CL HYDROLASE OF SARS-COV-2

The 3CL hydrolase, a crucial protein required for the maturation of SARS-CoV-2, is extremely important for the life cycle of such viruses [36], which makes it the most attractive target for the development of anti-coronavirus drugs in addition to four structural proteins (i.e., N protein, M protein, E protein, and S protein) [37]–[39]. Similar to SARS-CoV protease, SARS-CoV-2 3CL hydrolase (Figure 3.4) includes nine α-helices and thirteen β-strands, constituting domain I (residues 8-101), domain II (102-184), and domain III (201-306) [36], [40], [41]. The domain I and II have one antiparallel β-fold structure, similar to the trypsin-like serine proteases. For domain III, it contains five

α-helices forming an antiparallel polymer, which are connected to domain II through an extended loop region (residues 185-200). The leading substrate-binding site of the SARS-CoV-2 3CL hydrolase is located in the cleft between domain I and II, where there is a His41-Cys145 catalytic dyad. The lone pair of electrons on the Cys sulfhydryl sulfide attack the positively charged carbonyl carbon, breaking the peptide bond between Gln-(Ser/Ala/Gly) and thereby acting as a hydrolase [42], [43].

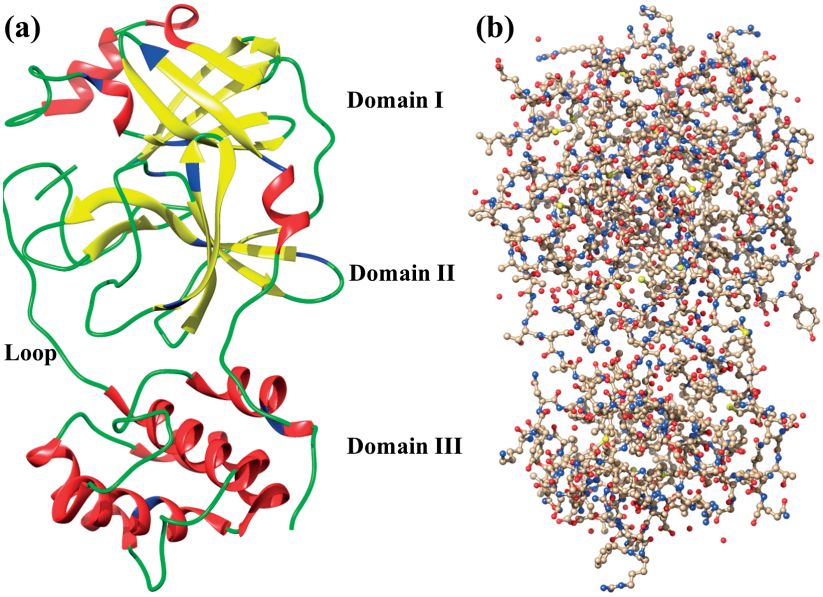


Figure 3.4: (a) and (b) show the ribbon and atomistic representation of the 3CL hydrolase of SARS-CoV-2 (PDB code: 6LU7), respectively. Different structural elements are highlighted with different colors, with α-helices, δ-strands, and loops colored in red, yellow, and green, respectively. The catalytic dyad residues His41 and Cys145 are colored in blue.

3.3.2. CONSTRUCTION OF THE INITIAL MODELS

In this study, the atomistic structure of 3CL hydrolase of SARS-CoV-2 is established to investigate the interaction mechanism with the biocidal ingredients, presented in Figure 3.4. Chemical biocides have been an effective disinfection measure in minimizing the occurrence and spread of viruses. Currently, it has been reported that 75% medical ethanol and 0.55% sodium hypochlorite can effectively reduce the infectivity of SARS-CoV-2 within the recommended time [44], [45]. These two disinfectants play a prominent role in several global public health emergencies caused by SARS-CoV, MERS-CoV, and SARS-CoV-2. Silver, as a precious metal, has been consciously utilized to act as a biocidal agent since ancient times, and its biocidal property in ionic form shows a substantial inactivation for the influenza A virus [27]. In 2003, silver ions-based disinfectants were included in the SARS prevention and treatment manual compiled by No. 302 Hospital of Chinese People's Liberation Army. In addition, the efforts in the action activity of silver ions on the coronaviruses further confirm that silver ions have significant

antiviral activity for SARS-CoV-2 [46]. Therefore, three biocidal ingredients, including ethanol, hypochlorite, and silver ions, are considered the investigated molecules. The complex systems consisting of the investigated molecules and 3CL hydrolase are constructed within the framework of the Packmol program and shown in Figure 3.5. Adding one thousand ingredient molecules ensures all complex systems are small enough for dynamic simulations over picosecond time scales [47], [48].

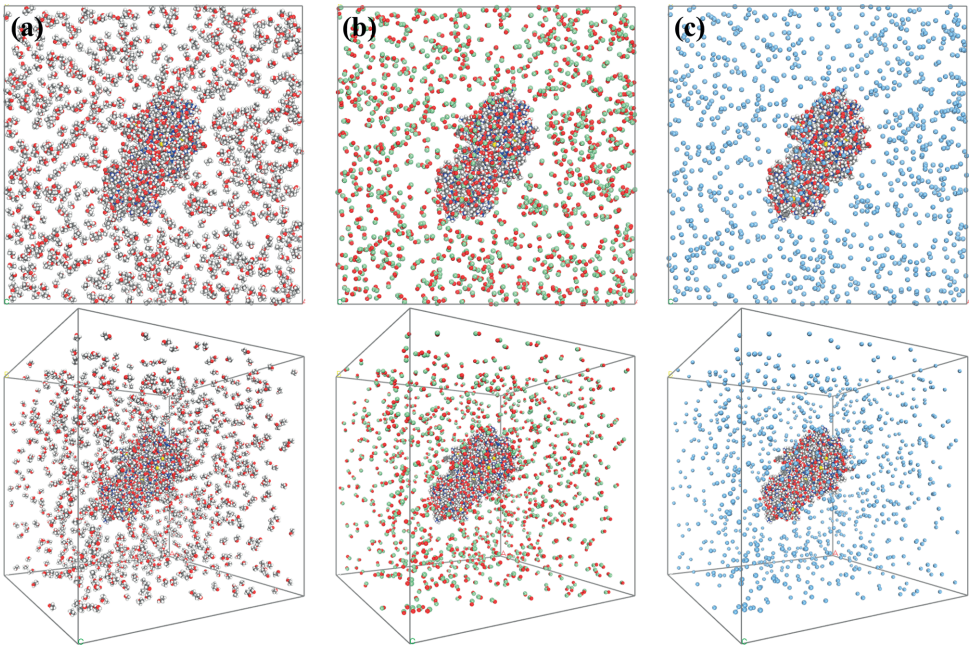


Figure 3.5: The front and 3D views of the complex systems consisting of 3CL hydrolase and (a) ethanol, (b) hypochlorite, and (c) silver ions.

3.3.3. COMPUTATIONAL METHODS

MD simulations are performed with the current state-of-art Forcite program using the COMPASS (Condensed-phase Optimized Molecular Potentials for Atomistic Simulation Studies) forcefield parameters [47], [49], [50]. The approximate atomic charges are assigned by utilizing the Gasteriger method for the ethanol–/hypochlorite–3CL hydrolase systems to evaluate electrostatic interactions [51]. For the silver ion–3CL hydrolase system, the charge of silver atom is set to 1.0 *e*. The energy minimization calculations of all complex systems are conducted by adopting both the steepest descent and conjugate gradient algorithm at atmospheric pressure of 10^{-4} GPa. Concurrently, the electrostatic and van der Waals interactions are described using Ewald and atom-based summation methods in all simulations, respectively. Considering the actual situations, the MD simulations of all complex systems are carried out within the framework of NVT ensemble (constant number of particles, constant volume, and constant temperature). The system temperature is set as 300 K, which is regulated by adopting the Berendsen thermostat

[51], [52].

All calculations at the DFT level are conducted using the DMol^3 package, as implemented in the Materials Studio [53]. The exchange–correlation interaction is described by the Perdew–Burke–Ernzerhof (PBE) functional within the generalized gradient approximation (GGA) [54], [55]. The vdW dispersion interaction has a significant influence on the interaction potential of intermolecular. This potential is a crucial ingredient in the adsorption structures and binding energies [56], [57]. For a proper treatment of the long-range van der Waals (vdW) interactions between the biocidal ingredients and amino acid residues, the dispersion-corrected DFT (DFT-D) approach proposed by Grimme is employed [58], [59]. The atomic orbital is treated through a double numeric quality basis set, including polarization functions (DNP), and the global orbital cut-off keeps at 5.0 Å [60], [61]. To quantitatively analyze the interactions of the biocidal ingredients with amino acid residues, the binding energies ($\triangle E$) are determined by using the formula [62]

$$\triangle E = E_{system} - E_{ingredient} - E_{residue} \tag{3.4}$$

where E_{system}, $E_{ingredient}$, and $E_{residue}$ represent the total energy of the ingredient–residue system, ingredient molecule, and amino acid residue, respectively. The interaction process with a negative binding energy is spontaneous and energetically favorable, being expected to occur in chemical reactions where a smaller value indicates a more potent constraint force [54]. Simultaneously, charge transfer ($\triangle Q$) is deduced by Mulliken population analysis, determining whether the biocidal ingredient act as an acceptor or donor.

3.3.4. MOLECULAR DYNAMICS SIMULATIONS

Before investigating the dynamic behaviors of the ethanol–, hypochlorite–, and silver ion–3CL hydrolase systems, their geometric structures fully relaxed by combining the steepest descent and conjugate gradient algorithm are first discussed. After minimizing energies, it is found that 3CL hydrolase is almost surrounded by ethanol molecules, and their minimum distance is less than 2.0 Å in the ethanol–3CL hydrolase system. Interestingly, the ethanol molecules are mainly concentrated in the vicinity of glutamate acid (GLU) and aspartic acid (ASP) residues of 3CL hydrolase. Although ethanol molecules also occur near other amino acid residues such as arginine (ARG), asparagine (ASN), and isoleucine (ILE) residues, the number of adsorbed molecules by them is relatively small compared with that by GLU and ASP residues. The hypochlorite–3CL hydrolase system clearly shows that the distribution of hypochlorite molecules in the vicinity of 3CL hydrolase is similar to that of ethanol molecules. However, their concentrations near the above-mentioned residues are lower than that of ethanol molecules, and the minimum distance is less than 3.0 Å. In contrast, in the case of the silver ion–3CL hydrolase system, there are only a small amount of silver ions near the 3CL hydrolase within the range of 4.0 Å. Meanwhile, we find that silver ions are primarily clustered in the vicinity of threonine acid (THR) and phenylalanine acid (PHE) residues and partly occur near other residues (e.g., lysine, leucine, glutamate acid, etc.).

In order to better decipher the underlying mechanism of interaction between the biocidal ingredients and 3CL hydrolase, the radial distribution function (RDF) of three complex systems is investigated by analyzing the MD simulation trajectories. RDF is

also referred to the pair correlation function, characterizing the probability of the existence of an atom at the origin of an arbitrary reference frame [63]–[65]. The RDFs $g(r)_{O-O}$, $g(r)_{N-O}$, and $g(r)_{S-O}$ of O(GLU residues)-/O(ASP residues)-/O(ARG residues)-/O(ASN residues)-/O(MET residues)-O(ethanol), N(ARG residues)-/N(ASN residues)-O(ethanol), and S(MET residues)-O(ethanol) pairs for the ethanol-hydrolase system are shown in Figure 3.6(a) and (b). It is well known that the peak of the RDF curve within 3.5 Å represents the hydrogen bonds and chemical bonds and that outside 3.5 Å is contributed by the non-bond (Coulomb and vdW) interactions [66]. As shown in Figure 3.6(a), the first peak of $g(r)_{O-O}$ of O(GLU residues)-/O(ASP residues)-O(ethanol) pairs appear around 2.6 Å, which is smaller than 3.5 Å, indicating the bond interactions between ethanol and these two residues, Meanwhile, there is a second peak illustrated in the range 4-5 Å for GLU and ASP residues, which can be explained as the non-bond interactions. For ARG and ASN residues, it is found that the first peak of their $g(r)_{O-O}$ is located within the range of 6.5-7.5 Å. Thus, the non-bond interactions are responsible for the constraint of ARG and ASN residues with ethanol molecules, which is further confirmed by the $g(r)_{N-O}$ of N(ARG residues)-/N(ASN residues)-O(ethanol) pairs (see Figure 3.6(b)). In addition, MET residue is also considered due to the presence of S and O atoms in it. In Figure 3.6(b), the location of the first peak of $g(r)_{O-O}$ and $g(r)_{S-O}$ clearly shows that the O-O interactions are stronger than the interactions between the S atom of MET residue and the O atom of ethanol. Furthermore, we find that the peak height of $g(r)_{O-O}$ of O(ARG residues)-/O(ASN residues)-/O(MET residues)-O(ethanol) pairs is lower than that of O(GLU residues)-/O(ASP residues)-O(ethanol), which indicates higher binding energy between GLU residues, ASP residues, and ethanol molecules.

Owing to the similar distribution of ingredient molecules near 3CL hydrolase, five amino acid residues discussed in the ethanol-3CL hydrolase system are also used for the RDF analysis of the hypochlorite-3CL hydrolase system. In Figure 3.6(c), it can be observed that the first peak of $g(r)_{O-Cl}$ of O(GLU residues)–/O(ASP residues)-Cl(hypochlorite) pairs is found around 3.0 Å, which is less than 3.5 Å. This result indicates that the constraints between these two residues and hypochlorite molecules are contributed by hydrogen bonds or chemical bonds. The position of the first peak of $g(r)_{O-Cl}$ of O(ARG residues)-/O(ASN residues)-Cl(hypochlorite) pairs are close to 3.2 Å, but their second peaks occur in the range from 7.0 Å to 8.0 Å. As a result, the hypochlorite-GLU/ASP residue interactions are more robust than that attracted by ARG and ASN residues. It is further demonstrated by the non-bond constraints of Cl atoms with N atoms of ARG and ASN residues, as depicted in Figure 3.6(d). For MET residues, it can be noted that the first peak of $g(r)_{S-Cl}$ is around 3.0 Å, whereas that of $g(r)_{O-Cl}$ is outside 3.5 Å. Thus, the S-Cl interactions are more robust than those between O and Cl atoms. Among these five residues, there are considerable binding energies in the O(GLU residues)-/O(ASP residues)-Cl(hypochlorite) pairs due to their higher peak height.

Unfortunately, the distribution behaviors of the biocidal ingredients occurring in the ethanol- and hypochlorite-3CL hydrolase systems cannot be well-preserved in the case of silver ions. The above-discussed results have shown that silver ions are mainly concentrated near THR and PHE residues. Therefore, these two residues are the protagonists in the calculations of RDFs. For comparison, we also consider GLU, ASP, and MET residues. Figure 3.6(e) presents the RDFs of silver ions appearing around the O

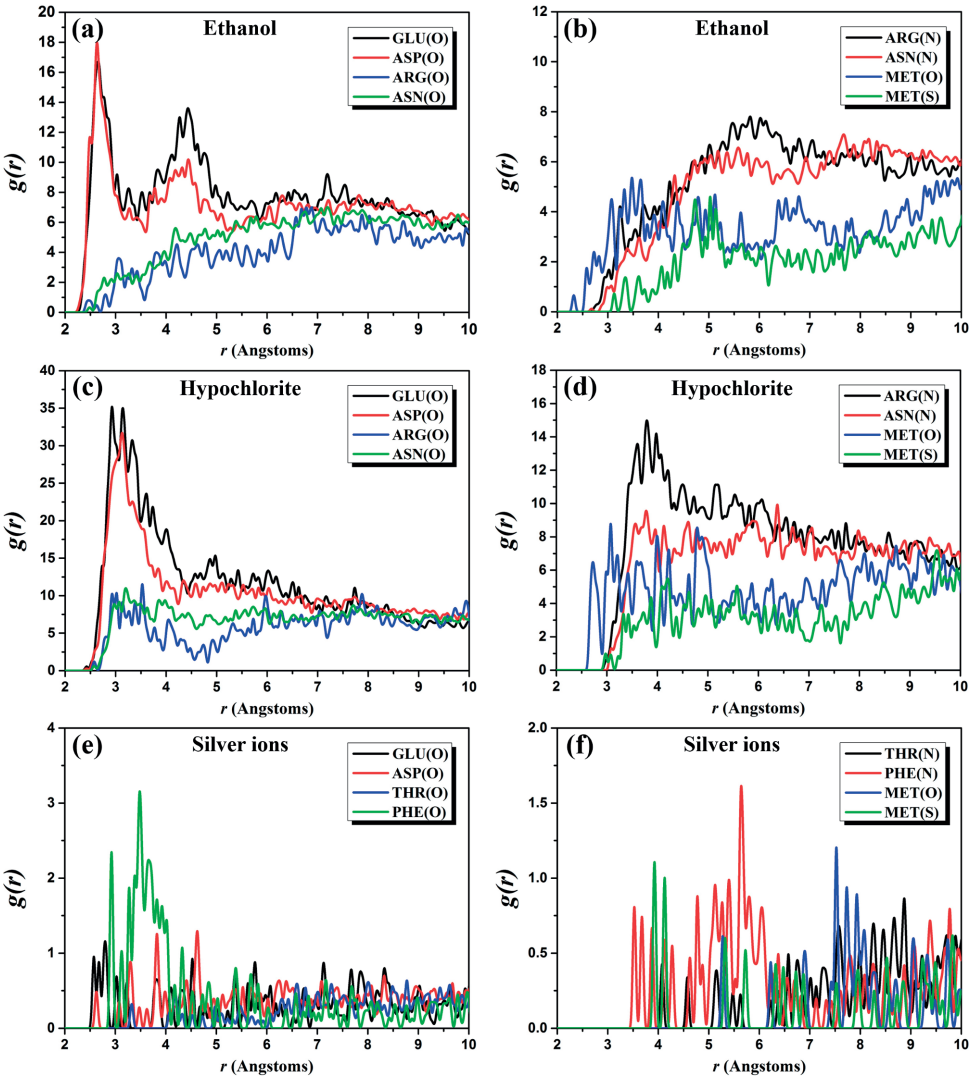


Figure 3.6: The pair correlation function (a and b) $g(r)$ of ethanol, (c and d) $g(r)$ of hypochlorite and (e and f) $g(r)$ of silver ions with the 3CL hydrolase of SARS-CoV-2.

atoms of GLU, ASP, THR, and PHE residues. It can be found that the first peak of O(GLU residues)-/O(ASP residues)-Ag(silver ions) pairs are observed at ~3.0 Å, which is less than that (>3.0 Å) of O-Ag pairs from THR and PHE residues. However, the peak height of $g(r)_{O-O}$ of O(PHE residues)-Ag(silver ions) pairs is more significant than that of other three residues. Consequently, the binding energy of O atoms of PHE residues with silver ions is relatively strong, which is further confirmed by the RDF curves plotted in Figure 3.6(f). The first peaks of $g(r)$ of N(THR residues)-/N(PHE residues)-/O(MET residues)-/S(MET residues)-Ag(silver ions) pairs are located in the scope of the non-bond interac-

tions.

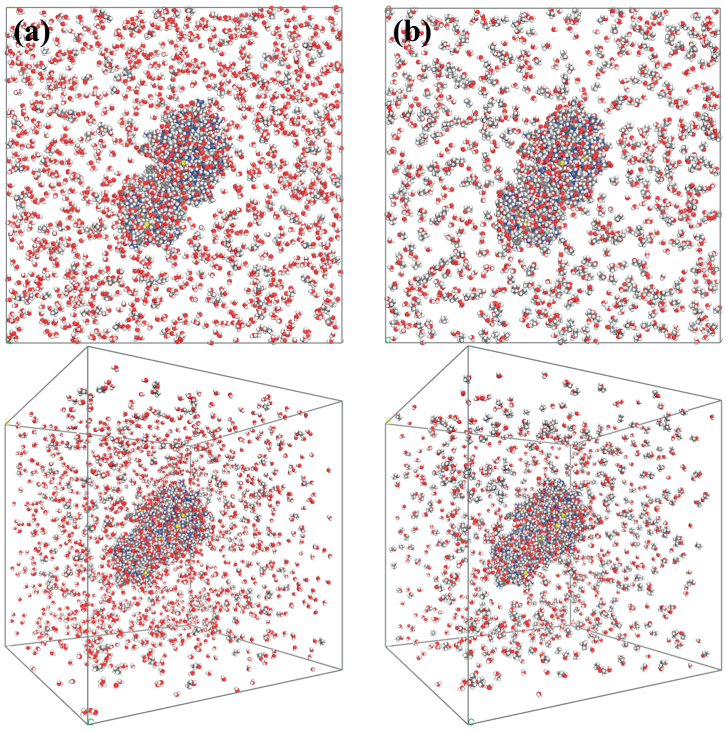


Figure 3.7: The front and 3D views of the complex systems with ethanol of (a) 30% and (b) 75%, respectively.

Previous studies focusing on the disinfection effectiveness of ethanol with different concentrations have clearly shown that the inactivation of coronaviruses is sensitive to ethanol concentrations [67]–[70]. Ethanol with a concentration of 75% to 95% readily inactivates coronavirus infectivity by approximately 4 $\log_{10}$ or more, and outside this concentration range is less effective [71], [72]. Although this phenomenon is well-proven at the experiment level, its molecular-level mechanism is still unknown. As a result, two complex systems with 30% and 75% ethanol are discussed to gain insight into the molecular-level mechanism of this phenomenon, depicted in Figure 3.7. The relaxation calculations indicate that the main distribution of ethanol molecules near 3CL hydrolase is similar to in the case of pure ethanol (Figure 3.5(a)). Nevertheless, there are some differences between these two complex systems. For the case of 30% ethanol, water (H_2O) molecules are the primary aggregation in the vicinity of 3CL hydrolase, which might reduce the probability of ethanol contacting amino acid residues. The ethanol molecules cannot effectively interact with amino acid residues, thereby the bioactivity of 3CL hydrolase cannot be disturbed. On the contrary, an expected distribution phenomenon for ethanol molecules is exhibited in the complex system with 75% ethanol. We find that there are more ethanol molecules near 3CL hydrolase compared to the case of 30% ethanol, which suggests that ethanol molecules are more likely to interact directly with

amino acid residues. H_2O molecules have a weak impact on the interactions between ethanol molecules and 3CL hydrolase. Additionally, ethanol solvent with a high concentration can readily damage the structure of 3CL hydrolase. By comparison, it is found that 3CL hydrolase is completely enclosed by ethanol molecules when the alcoholicity is set to 75%, and the amounts of molecules attracted by 3CL hydrolase are smaller than that of pure ethanol. However, ethanol molecules that first interact with 3CL hydrolase could impede the subsequent interaction processes of other molecules with 3CL hydrolase in the system of pure ethanol. This could be the underlying reason that 75% ethanol has more remarkable disinfection effect than pure ethanol.

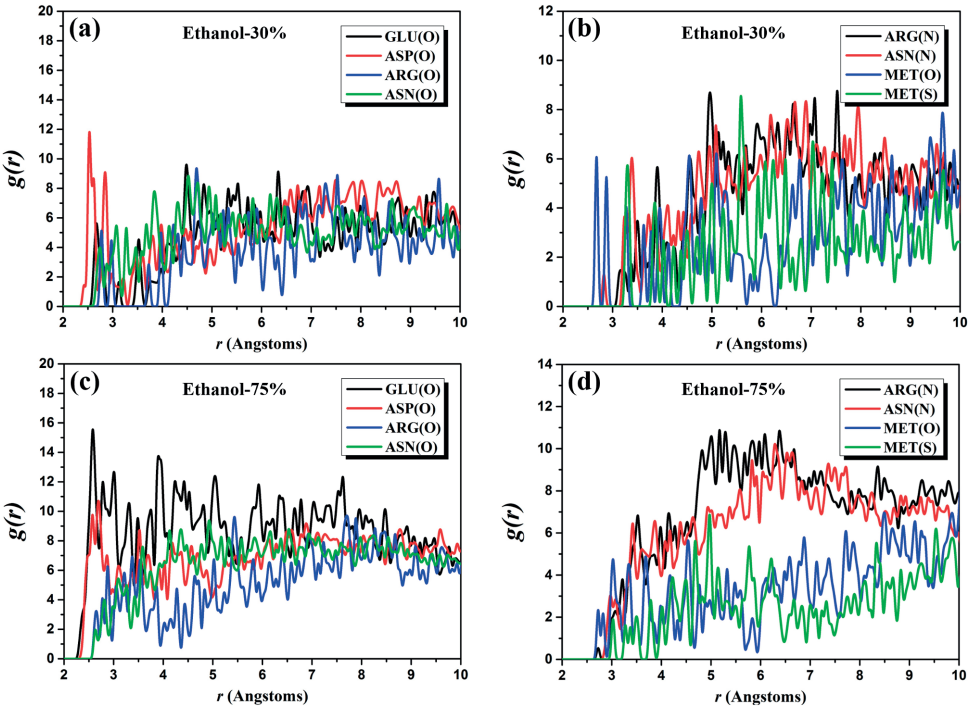


Figure 3.8: RDFs $g(r)$ for the complex systems with (a and b) 30% and (c and d) 75% ethanol, respectively.

Similarly, RDFs of two complex systems with alcoholicity of 30% and 75% is also considered to provide further evidence for the above-discussed results. We investigate the identical five amino acid residues (i.e., GLU, ASP, ARG, ASN, and MET residues) as for the pure ethanol system, and the $g(r)$ plots of the corresponding atom pairs are presented in Figure 3.8. It can be noted that the first peak of $g(r)_{O-O}$ of O(GLU)-/O(ASP)-O(ethanol) pairs occur around 2.5 Å, which indicates that the position of the first peak is independent of ethanol content. The height of the $g(r)_{O-O}$ curve of O(GLU)-O(ethanol) pairs increases significantly when the alcoholicity changes from 30% to 75%. However, its peak height within the range of 4.5-10.0 Å has an apparent decrease when the ethanol concentration is up to 100%, which is expected to be observed at the molecular level. Simultaneously, we note that the peak height of $g(r)_{O-O}$ curves of O(ARG)-/O(ASN)-

O(ethanol) pairs firstly increases and then decreases with the increasing concentration of ethanol, especially in the range from 2.0 Å to 4.0 Å. A similar behavior also observed in the $g(r)_{N-O}$ curves of N(ARG)-/N(ASN)-O(ethanol) pairs, and the most apparent section is in the range of 4.5-7.5 Å. For MET residues, the ethanol content has a slight influence on the overall tendency of $g(r)_{O-O}$ and $g(r)_{S-O}$ of O(MET)- and S(MET)-O(ethanol) pairs, but the peak height of these two curves (4.5-5.5 Å) exhibits a relationship of first rise and then drop with the ethanol concentration. These results are in good agreement with the reported phenomenon in the experiments where the desired inactivation effect cannot be achieved under low concentrations and/or pure ethanol.

3.3.5. FIRST PRINCIPLES SIMULATIONS

According to the above-described MD results, four amino acid residues, namely, GLU, ASP, THR, and PHE residues, are used for further estimating the interaction with ethanol, hypochlorite, and silver ion. To explore the most favorable binding structure of amino acid between residues and the active ingredients, we consider three possible anchoring sites for each residue, as illustrated in Figure 3.9. For GLU and ASP residues, owing to the similar terminal structure (-CH2CO2), two O atoms and one H atom of the -CH2CO2 group are set as the anchoring positions of ethanol and hypochlorite molecules. In the THR residue, the binding sites include the H atom of the –CH3 group, the O atom of the -OH group, and the O atom of the -CO group, whereas for the PHE residue, they are the H and C atoms of the -C6H5 group and the O atom of the -CO group. It should be noted that the C and H atoms of the ethanol molecule and the O atom of hypochlorite are not tested on these anchoring positions. On the basis of the aforementioned DFT approach, we perform the geometric optimization of the ingredient–residue configurations. The computational results of the most favorable conformation are listed in Table 3.2.

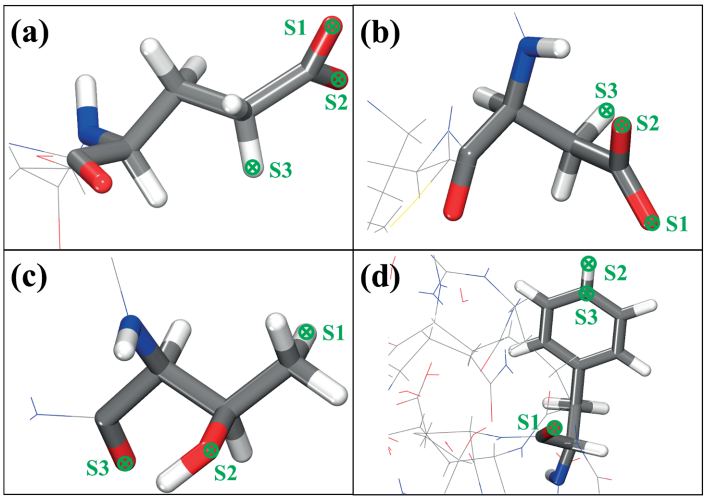


Figure 3.9: The molecular structure of the glutamate, aspartic, threonine, and phenylalanine residues in the 3CL hydrolase of SARS-CoV-2.

Ethanol molecule. There are six possible configurations depending on the anchor-

Table 3.2: Binding energy ($\triangle E$), charge transfer ($\triangle Q$) from the ingredient to the amino acid residue, minimum distance (d_{min}) between atoms of the constituent molecule and the amino acid residue.

Composition	Residue	Site	$\triangle E$ (eV)	$\triangle Q$ (e)	d_{min} (Å)
Ethanol	GLU	S1	-0.78	0.240	1.63
Hypochlorite	GLU	S1	-0.64	0.115	2.39
Silver ions	PHE	S1	-1.44	0.402	2.16

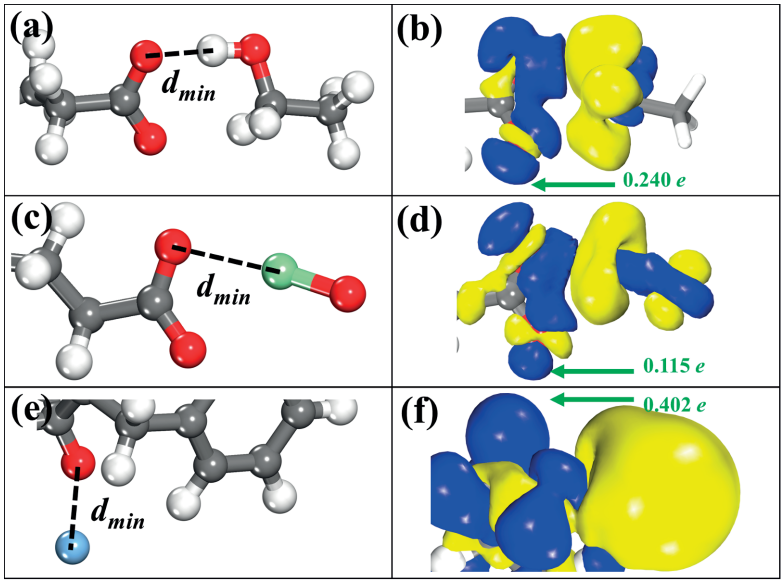


Figure 3.10: The atomic structure and charge density difference of the most favorable conformation. (a and b) Ethanol-GLU configuration, (c and d) hypochlorite-GLU configuration, and (e and f) silver ion–PHE configuration. The isosurface is set to 5×10^{-3} eÅ^{-1}. The yellow and blue color represent depletion and accumulation of charges, respectively. The green arrow denotes the direction of charge transfer.

ing positions of GLU and ASP residues. Among six anchoring positions, the most favorable binding site is the S1 of GLU residue, and the corresponding conformation with the lowest energy is displayed in Figure 3.10(a). As we can see, the O-H bond of the ethanol molecule points to the S1 site, and the structural parameters have some slight variations. The minimum distance (dmin) of the atom of the ethanol molecule to the GLU residue ranges from 1.63 Å to 2.20 Å for six binding configurations. The magnitude is slightly close to that (1.87 Å) of ethanol on graphene oxide [73], [74]. The binding energies ($\triangle E$) of six configurations are lower than -500 eV, confirming that the ethanol molecule is bound by GLU or ASP residue through the chemical interaction. The reference length of the O-H covalent bond is 0.95 Å, obtained by summing the covalent radii of O and H atoms [60], [75]. Meanwhile, a strong hydrogen bonding force is defined in the range from 1.5 Å to 2.5 Å [76]. As a result, the interaction process between ethanol molecules and GLU (or ASP) residue is dominated by a strong hydrogen bonding force.

To understand the interaction nature, we represent the charge density difference (CDD) image for the ethanol/GLU structure with the lowest energy by using the below formula:

$$\triangle\rho = \rho_{ethanol/residue} - \rho_{ethanol} - \rho_{residue} \tag{3.5}$$

where $\rho_{(ethanol/residue)}$, $\rho_{(ethanol)}$, and $\rho_{(residue)}$ are the total charge density of the ethanol/residue structure, isolated ethanol molecule, and amino acid residue, respectively. It should be noted that $\rho_{(ethanol)}$ and $\rho_{(residue)}$ are calculated with each fragment of the ethanol/residue structure at the same positions. From the CDD graph (Figure 3.10(b)), we can observe that the majority of the charges are significantly depleted on the H atoms of -CH2OH group of ethanol molecule, while the charges are mainly accumulated on the -CO2 group of GLU residue. This reveals that the charges are transferred from the ethanol molecule to the GLU residue. The charge transfer ($\triangle Q$) from the ethanol molecule to the GLU residue based on the Mulliken population analysis is 0.240 e per molecule (Table 3.2), suggesting that a strong electrostatic interaction in the ethanol/GLU residue structure.

Hypochlorite. Similar to the case of ethanol molecules, six possible binding configurations are tested. Figure 3.10(c) shows the most favorable conformation in which the Cl-O bond of hypochlorite is almost on the same horizontal line as the S1 site. In this configuration, the geometric parameters of the -CO2 group are 1.268 Å for the C-O bond and 125.7° for the O-C-O angle. Meanwhile, the plane constituted by three atoms of the -CO2 group of GLU residue is obviously twisted to 54.3° from 19.1°. The $\triangle E$ values of all binding configurations are less than -500 eV except for the Cl atom-S3 site (originating from ASP residue) configuration, which is -0.497 eV. Nevertheless, their binding stability is inferior to the ethanol/GLU structures due to the larger $\triangle E$ values. This result indicates that the interaction between hypochlorite and GLU residue is relatively weak compared with the adsorption of ethanol molecules. In addition, the dmin in the hypochlorite/GLU residue configuration with the lowest energy is 2.39 Å, similar to that (2.28 Å) of the Cl2 molecule adsorbed on the ZnO nanocluster [77]. Based on the reference length (1.62 Å) of the O-Cl covalent bond and the defined scope of hydrogen bonds, we can get a conclusion that hydrogen bonding is responsible for the constraint of hypochlorite with GLU residue. The CDD image in Figure 3.10(d) clearly reflects the primary depletion of charges in the region around the Cl atom, indicating the accumulation of charges on the O atoms of the -CO2 group and partly on the hypochlorite. This is in accordance with expectations because elemental O is more electronegative than Cl [74]. Quantitative charge analysis (Table 3.2) shows that hypochlorite serves as a charge donor to GLU residue with a $\triangle Q$ of 0.115 e per molecule, validating the relatively molecule-GLU residue interaction again.

Silver ions. Regarding the adsorption of silver ions, we examine six initial binding configurations where THR and PHE residues act as adsorbents. The most favorable conformation is found when the silver ion is aligned to the S1 site of the PHE residue as depicted in Figure 3.10(e). Although the bond length and bond angle of PHE residue have slight changes after adsorption, the carbon ring is twisted by 6°. We find that the distance between the silver ion and the O atom of PHE residue is 2.16 Å which is in accordance with that of silver nanoparticle on graphene oxide [78]. The dmin value is only 0.23 Å larger than the reference length (1.93 Å) of the Ag-O covalent bond. Consequently,

the constraint of silver ions with PHE residue is contributed by a pseudo-covalent bond. From Table 3.2, it can be found that the $\triangle E$ (-1.44 eV) is almost twofold that (-0.78 eV) of the case of ethanol molecule, which characterizes a robust binding force. The CDD isosurface diagram of the silver ion-S1 site (in the PHE residue) configuration is shown in Figure 3.10(f). It clearly indicates a depletion of charges in the spatial region near silver ion and an accumulation of charges in the proximity of -NH and -CO groups of PHE residue. The total $\triangle Q$ from the silver ion to the PHE residue is found to be 0.402 e per silver ion, suggesting that the silver ion acts as a donor.

3.3.6. COMPARISON OF INACTIVATION MECHANISMS

For ethanol disinfection, the primary mechanism of pathogen inactivation can be attributed to the denaturation and coagulation of proteins [79]. The proteins of pathogens are bonded with hydroxide radical (-OH) of ethanol molecules via hydrogen bonding, which damages the structural and functional integrity of viral proteins [80]. On the basic of the calculated results, it is found that the interactions between the -OH of ethanol molecules and the O atoms of amino acid residues of 3CL hydrolase and spike proteins belong to the category of hydrogen bonds and chemical bonds. This is in accordance with the conclusion from Yoo [80]. For sodium hypochlorite disinfection, pathogen inactivation depends on high pH (-OH action) and ClO- oxidation, which can lead to the destruction of the membrane and denaturation of proteins [81]. Due to the presence of the hydrophobic layer, ionized ClO- is challenging to penetrate the envelope membrane of pathogens. However, the amino acid residues of S glycoprotein, envelope protein, and membrane protein possess highly nucleophilic sites that can react with ClO- or HClO molecules [82], [83]. In the case of the 3CL hydrolase-hypochlorite system, the calculated results show that the O atoms of hypochlorite bind to the O atoms of GLU and ASP residues with a strong interaction. For silver ion disinfection, interference with electron transport, interaction with the cell membrane, and binding to the DNA are three possible mechanisms for pathogen inhibition [84]. Similar to most heavy metals, silver also can bind to electron donor groups containing S, O, and N atoms [85]. Additionally, metals might be complex with bases or molecules in the order: sulfur-rich bases, nitrogen/oxygen bases, oxygen bases, and coordination to water molecules [86]. In our works, the amino acid residues containing S atoms are not exposed to the surface of 3CL hydrolase, thus it is difficult to interact with silver ions. By contrast, the amino acid residues with the unsaturated O atoms, such as GLU and ASP residues, have a strong constraint force with silver ions. This is in agreement with the results of previous studies [85], [86].

3.4. THE INTERACTION MECHANISMS OF CHEMICAL DISINFECTANTS WITH THE PHOSPHOLIPID MEMBRANE

3.4.1. CONSTRUCTION OF THE INITIAL MODELS

In this study, the lipid bilayer is designed to investigate the interactions of the SARS-CoV-2 membrane with active ingredients of chemical disinfectants. The lipid composition of the CoV membrane is taken from Angela Violi et al. (see Table 2.4) [87]. The lipid membrane of SARS-CoV-2 virions consists of POPC, POPE, POPI, POPS, PSM, and cholesterol molecules (see Figure 2.3). In order to make the viral membrane less complex and to

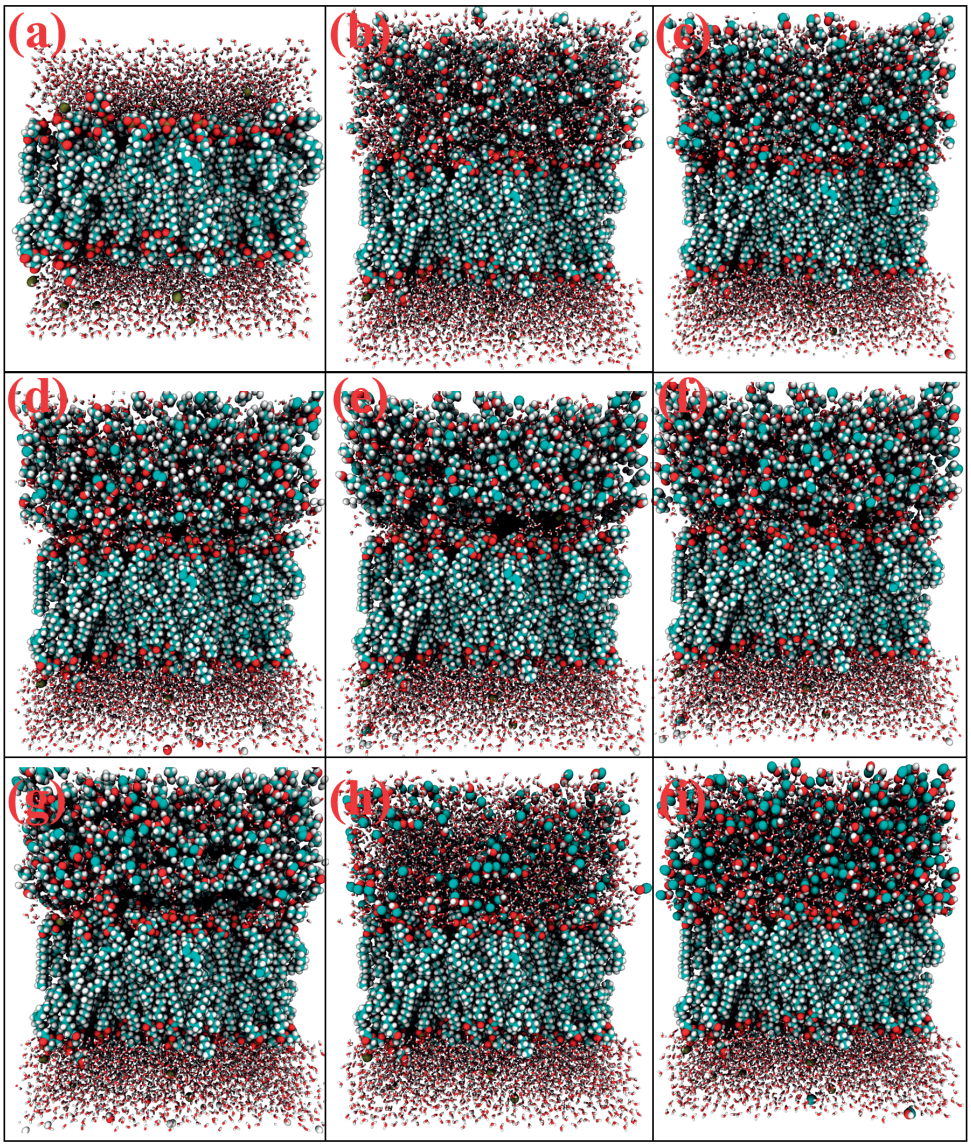


Figure 3.11: The membrane systems without and with ethanol (or HClO) molecules. (a) The membrane systems without and with water molecules and ions. (b-g) The ethanol-membrane systems with varying concentrations of ethanol, including 10%, 30%, 50%, 70%, 75%, and 90% respectively. (h-i) The HClO-membrane systems with HClO concentrations of 10% and 30%, respectively.

eliminate the effect of viral proteins, the protein structures embedded in the lipid membrane of SARS-CoV-2 are not considered in this study. The lipid membrane without viral proteins possesses 200 lipid molecules in total and has an approximate size of 8.8 nm by 8.8 nm. It should be noted that minor rounding is required in modeling to meet the

requirements of SARS-CoV-2 lipid composition. POPC, POPE, POPI, POPS, PSM, and cholesterol molecules are 130, 20, 18, 10, 8, and 14, respectively. In addition, appropriate amounts of ions are added to neutralize the charge of the membrane systems. The membrane builder of the CHARMM-GUI program suite is applied to construct the pre-equilibrated initial models with lipids, water molecules, and ions [88]. Two chemical disinfectants, including ethanol and hypochlorous acid (HClO), are chosen to be representatives to uncover the interactions with the lipid membrane of SARS-CoV-2. To construct the ethanol- and HClO-membrane mixed structures, Packmol program is used, and the corresponding active molecules are placed through the replacement of water molecules in the initial membrane model generated by the CHARMM-GUI program, as depicted in Figure 3.11. For ethanol, we consider concentrations of 10%, 30%, 50%, 70%, 75%, and 90% to reveal the effect of different concentrations on viral inactivation. In the case of HClO, only two concentrations of 10% and 30% are selected to investigate its acting mechanism with the lipid membrane because it exhibits excellent virucidal activity even at a low concentration.

3.4.2. COMPUTATIONAL METHODS

All MD simulations are performed using GROMACS 2019.6 with a time step of 2 fs [89]. The ethanol-/HClO-membrane systems are parameterized with CHARMM36 all-atom force field 2020 [90]. Meanwhile, the TIP3P model is used to describe the solvation of the membrane systems, and 0.15M KCl are added to neutralize the net charge of the systems. To mimic the infinite system, the PBC condition is imposed in three directions of all membrane systems. In all simulations, a 315 K temperature and a 1 bar pressure are coupled with the components of the membrane systems. The energy minimization of the membrane systems is conducted using the steepest descent method and the maximum convergence value sets as 100 kJ $\cdot$mol^{-1} $\cdot$nm^{-1}. In the equilibration process, the temperature and pressure coupling adopt V-rescale thermostat and Berendsen schemes, respectively [91], [92]. The total equilibration time is 50 ns. Eventually, the production semi-isotropic NPT simulations with 100 ns time is carried out to analyze interactions between ingredient molecules and the lipid membrane. In this step, we apply the Parrinello-Rahman algorithm to control the pressure equilibration of the membrane systems [93]. Note that the pressure is controlled in the x and y directions of the lipid membrane by employing the same compression factor, and the pressure control in the z direction is separated from the x and y directions. Besides, the h-bonds are required for the constraints on the bonds connected to hydrogen atoms. The vdW and long-range electrostatic interactions are evaluated on the basis of the cut-off and PME methods, respectively. The cut-off distance for calculating the electrostatic and vdW interactions is set to 1.0 nm. The CGenFF program is used to generate the topology files of ethanol and HClO molecules [94]. VMD 1.9.3 is applied for the visualization and analysis of the simulation results [95].

3.4.3. MOLECULAR DYNAMICS CALCULATIONS

Bilayer area and bilayer thickness. The APL is an essential characteristic for comparison with the experiment, which largely determines other structural and kinetic features, such as membrane thickness and lateral diffusion of lipids [96]. The time evolution of the

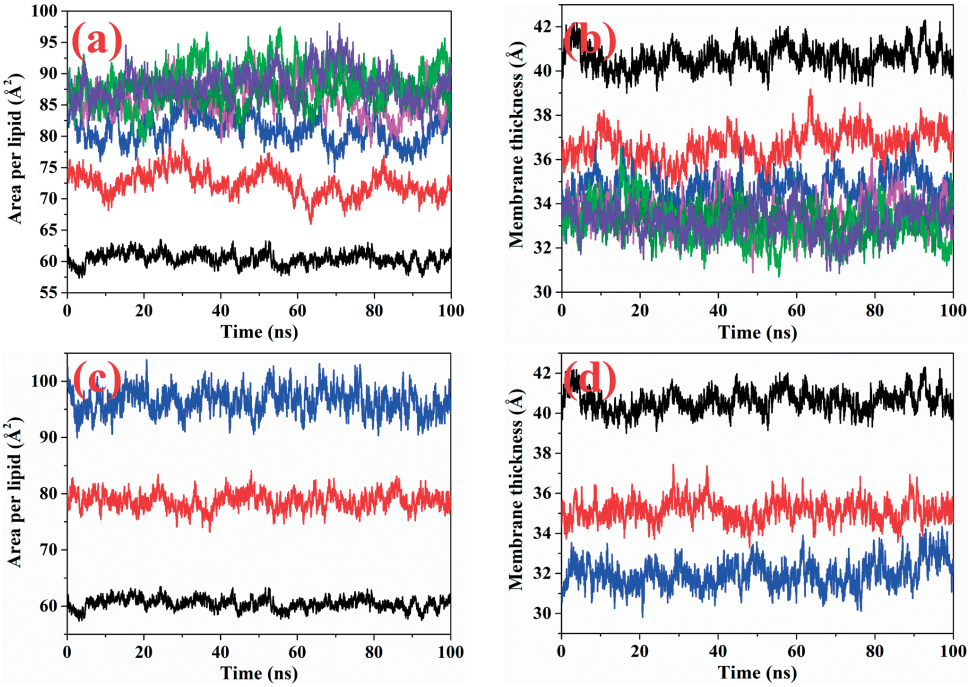


Figure 3.12: The temporal behavior of total APL and bilayer thickness of the multi-lipid bilayer systems with ethanol (a-b) and HClO (c-d) molecules over a 100 ns simulation. Here, the colored lines are denoted as follows: black lines, the bilayer system without ethanol or HClO molecules; red lines, 10% ethanol (or HClO) molecules; blue line, 30% ethanol (or HClO) molecules; megenta lines, 50% ethanol molecules; olive lines, 70% ethanol molecules; green lines, 75% ethanol molecules; violet lines, 90% ethanol molecules.

area per lipid in the membrane systems without and with ethanol and HClO molecules is depicted in Figure 3.12. In the absence of the acting molecules, the averaged total APL is 60.45 Å^2 for the pure lipid system, being extremely close to the reported APL of 60.0 Å^2 for the multi-lipid membrane without S proteins in an earlier study [88]. As seen from Figure 3.12(a) and (c), the presence of ethanol and HClO molecules significantly effect the total APL and bilayer thickness of multi-lipid bilayer membrane systems. In the case of multi-lipid bilayer systems with ethanol molecules, we find a remarkable increase in the total APL of the multi-lipid bilayer when the ethanol concentration changes from 0 to 50%. With increasing ethanol concentration, the varying magnitude of the total APL becomes smaller. However, when the concentration of ethanol increases from 75 to 90%, the total APL is approximately unchanged. The averaged total APLs for 50%, 70%, 75%, and 90% ethanol concentrations are 85.86 Å^2, 87.11 Å^2, 88.88 Å^2, and 88.34 Å^2, respectively. Interestingly, compared to the bilayer system without ethanol, the magnitude of change in the total APL of the bilayer with ethanol becomes more prominent within the same simulated time window. These findings suggest that the structure of bilayer membrane is precarious. Similarly, we also find that increasing the HClO concentration could lead to a loosening of the bilayer membrane structure. As plotted in Figure

3.12(c), when HClO concentrations set to 10% and 30%, the total APLs change around 80 $Å^2$ and 95 $Å^2$ over the simulated time, respectively. The averaged total APLs for 10% and 30% HClO concentrations are 78.74 $Å^2$ and 96.40 $Å^2$ respectively. In comparison, the increasing magnitude of the total APL caused by HClO molecules is more extensive than that induced by ethanol molecules at the same concentration. This indicates that the interaction of HClO with lipid molecules is more robust than between ethanol and lipid molecules.

The membrane thicknesses for the bilayer membrane systems without and with ethanol or HClO molecules are determined from the projected mass distribution and are shown in Figure 3.12(b) and (d). In the absence of ethanol or HClO molecules, the average thickness of the bilayer membrane is 40.61 Å, which is close to the reported results of the PSM-POPC bilayer system (40.5 Å at 323 K) and pure POPC bilayer system (39.3 Å at 300 K) in the previous studies [97], [98]. For the bilayer membrane systems containing ethanol or HClO molecules, it can be observed that there is a distinctive decrease in the membrane thickness with increasing ethanol or HClO concentration. This behavior is attributed to the gradual increase in the width of the bilayer systems. Nevertheless, for the case of ethanol, the membrane thicknesses of the bilayer systems are almost the same at 50%, 70%, 75%, and 90% of ethanol concentration, respectively, which is consistent with the changing behavior of the total APL observed in Figure 3.12(a). The corresponding membrane thicknesses at 50%, 70%, 75%, and 90% ethanol concentrations are 33.54 Å, 33.27 Å, 33.05 Å, and 33.21 Å, respectively. In the presence of HClO, the membrane thicknesses at 10% and 30% HClO concentrations are 35.15 Å and 31.97 Å, respectively. Therefore, we can get a conclusion that the introduction of ethanol and HClO molecules leads to a lateral swelling of the bilayer membrane and reduces its thickness. These simulated results are in good agreement with the earlier studies focusing on the effect of ethanol molecules on the lipid bilayer [96], [97].

Partitioning of the acting molecules into the bilayer membrane system. In order to get an insight into the structural changes of the bilayer membrane and the distribution of ethanol (or HClO) molecules inside the membrane at various concentrations, the simulated mass density profiles of the lipids, ethanol, and HClO molecules along the bilayer normal for the multi-lipids bilayer systems with different concentrations of ethanol or HClO molecules are considered. The mass density profiles for the ethanol- and HClO-containing bilayer systems are plotted in Figure 3.13. It can be noted that the presence of ethanol and HClO molecules exhibits an apparent effect on the studied mass density profiles. In Figure 3.13(a) and (d), we find that two peaks of the mass density profile for the lipids occur near 2 nm from the center of the bilayer without ethanol or HClO. In the presence of ethanol or HClO, the mass density values of the lipids remarkably decrease, and the profile width reduces toward the bilayer center. Most importantly, with the increasing ethanol (or HClO) concentration, two peaks in the mass density profiles of the lipids gradually vanish and eventually turn out to be one peak occurring at the bilayer center. This suggests that the lipid molecules move toward the center of the bilayer membrane. In comparison, HClO molecules exhibit a more substantial effect on the mass densities of the lipids than ethanol molecules. Because the mass densities of the lipids in the case of HClO are lower than that of ethanol at the same concentration level. In addition, we note that the effect of ethanol molecules on the mass densities of

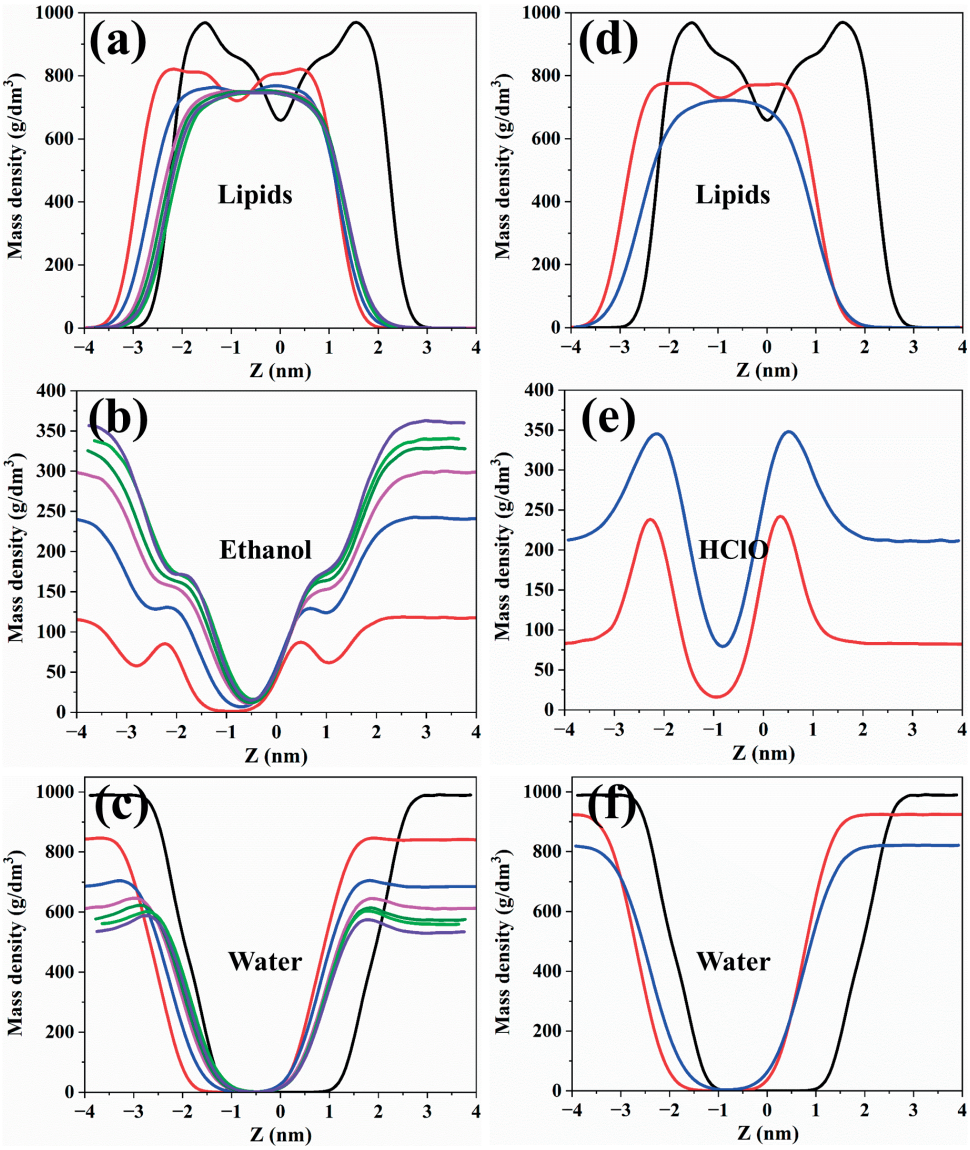


Figure 3.13: Mass density profiles of lipids, ethanol or HClO molecules, and water along the bilayer normal over the investigated membrane system. The lipids (a), ethanol molecules (b), and water (c) of the bilayer system with ethanol molecules. The lipids (d), HClO molecules (e), and water (f) of the bilayer system with HClO molecules. Here, the colored profiles are denoted as follows: black lines, the bilayer system without ethanol or HClO molecules; red lines, 10% ethanol (or HClO) molecules; blue line, 30% ethanol (or HClO) molecules; megenta lines, 50% ethanol molecules; olive lines, 70% ethanol molecules; green lines, 75% ethanol molecules; violet lines, 90% ethanol molecules.

the lipids is slightly enhanced as ethanol concentration is increased from 50% to 90%.

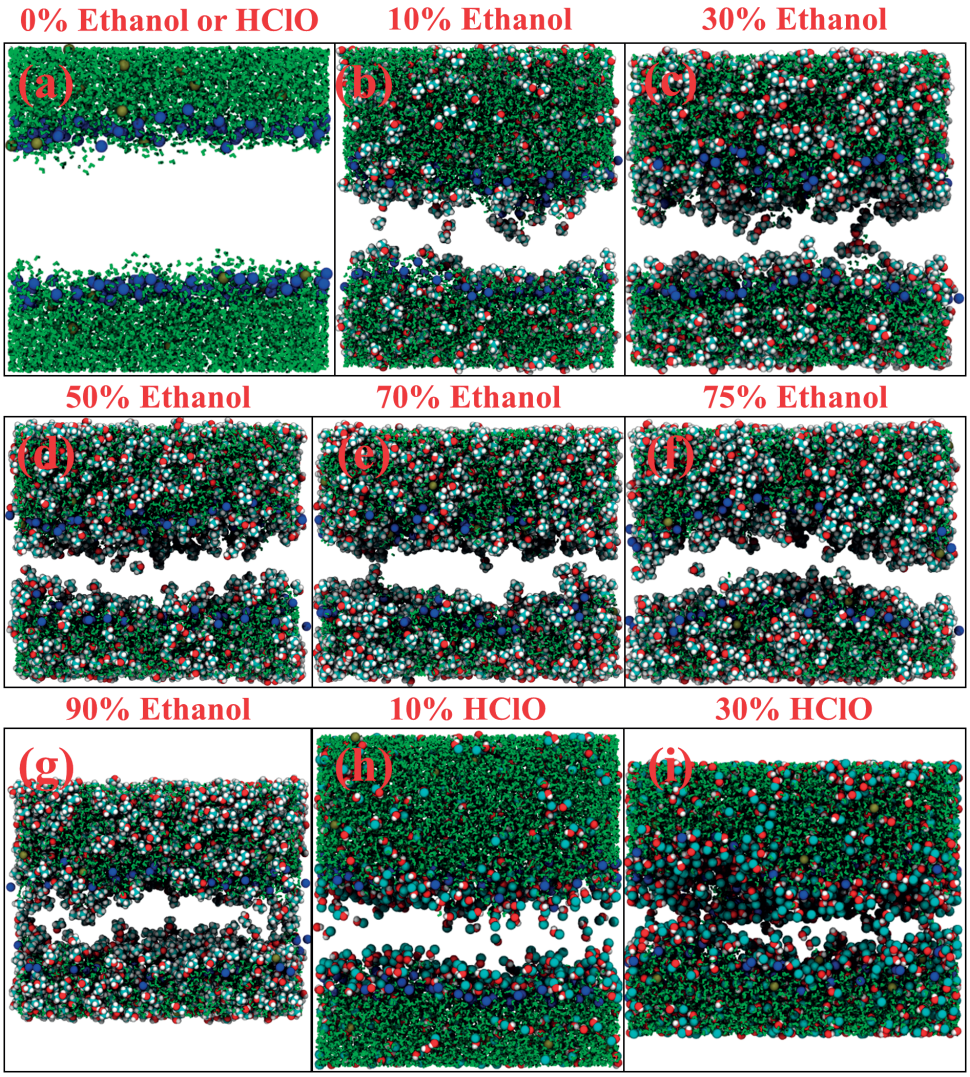


Figure 3.14: Snapshots presenting the partitioning of ethanol (or HClO) molecules in multi-lipid bilayer systems without and with different concentrations of ethanol (or HClO) molecules. The POPC, POPE, POPI, POPS, PSM, and cholesterol molecules are not shown to clearly observe the location of ethanol (or HClO) molecules in the lipid bilayer. Here, olive, brown, and blue are denoted as water molecules, ions used to neutralize the charges of the bilayer systems, and P atoms of POPC, POPE, POPI, POPS, and PSM molecules, respectively.

For ethanol and HClO molecules, as displayed in Figure 3.13(b) and (e), the mass densities of both molecules inside the bilayer are rising due to the increasing concentration and lateral expansion of the bilayer. Similarly, the profile width in the mass density also shrinks toward the bilayer center. The number of HClO molecules inside the bilayer is

higher than ethanol molecules, and their distribution is closer to the bilayer center. For the pure bilayer membrane system, we directly observe a dramatic decrease in the mass densities of water molecules at the water-lipid interface and become zero at the bilayer center. The penetration of water molecules from the water-lipid interfacial region to the membrane interior is mainly hindered by unfavorable interactions with the alkyl lipid tails. Many studies have demonstrated that water molecules occupy the voids in the head-groups of the lipid molecules, but entering the hydrophobic section of the bilayer membrane experiences high barriers [99]–[101]. With the addition of ethanol or HClO, water molecules apparently penetrate more deeply into the lipid membrane, as shown in Figure 3.13(c) and (f). This is due to the lateral expansion of the bilayer membrane. Although the mass densities of water molecules inside the membrane increase with more ethanol or HClO, these increments are small, as reported in the previous study focusing on the effect of alcoholic on the pure DPPC membrane [102]. All these findings are further demonstrated by the end snapshots of various membrane systems (see Figure 3.14). Figure 3.14 clearly visualizes the distribution of ethanol and HClO molecules in the hydrophobic portion of the bilayer, directly giving evidence that the increasing concentration facilitates the entry of ethanol or HClO molecules into the bilayer interior. Meanwhile, we note that the number of water molecules entering the bilayer interior is significantly lesser than that of ethanol and HClO molecules.

As above mentioned, ethanol, HClO, and a very small number of water molecules penetrate into the region below the head-groups of the lipid membrane, and their molecular numbers increase with higher concentration. This represents that the presence of ethanol and HClO molecules is conducive to the permeation of water molecules into the interior of the lipid membrane. One previous study has shown that ethanol molecules tend to be located in the head-to-tail section of the bilayer at low ethanol concentrations, and the ethanol densities increase with more ethanol [102]. In our study, we also observe the same phenomenon that the mass densities in the bilayer center remain a low level at the lowest concentration for both ethanol and HClO cases. More ethanol or HClO molecules are in the bilayer center at higher concentrations. However, the density peaks of ethanol and HClO molecules still prefer to lie at the interface between hydrophilic and hydrophobic region.

Electron densities of the lipids and acting molecules. Electron density profiles along the normal to the bilayer membrane are more informative for the membrane structure than the membrane thickness and APL. X-ray diffraction provides a method of obtaining this quantity in the experimental level, measuring the corresponding information that produces the electron density distribution. Figure 3.15 summarizes the electron density profiles of lipids, ethanol, and HClO molecules in different cases. For the ethanol-containing bilayer systems, we find that a gradually decreased electron density in the phospholipid head-groups occurs as the ethanol concentration increases from 0% to 90%, as plotted in Figure 3.15(a). However, it should be noted that the electron density for the phospholipid head-groups of the bottom leaflet at 90% ethanol concentration is more significant than that in the same position at 75% ethanol case. Meanwhile, when ethanol concentration is further increased to 90% from 50%, the varying magnitude of the electron densities becomes smaller. Additionally, the changing trend of the distance of two peaks in the electron density profile is in good agreement with that

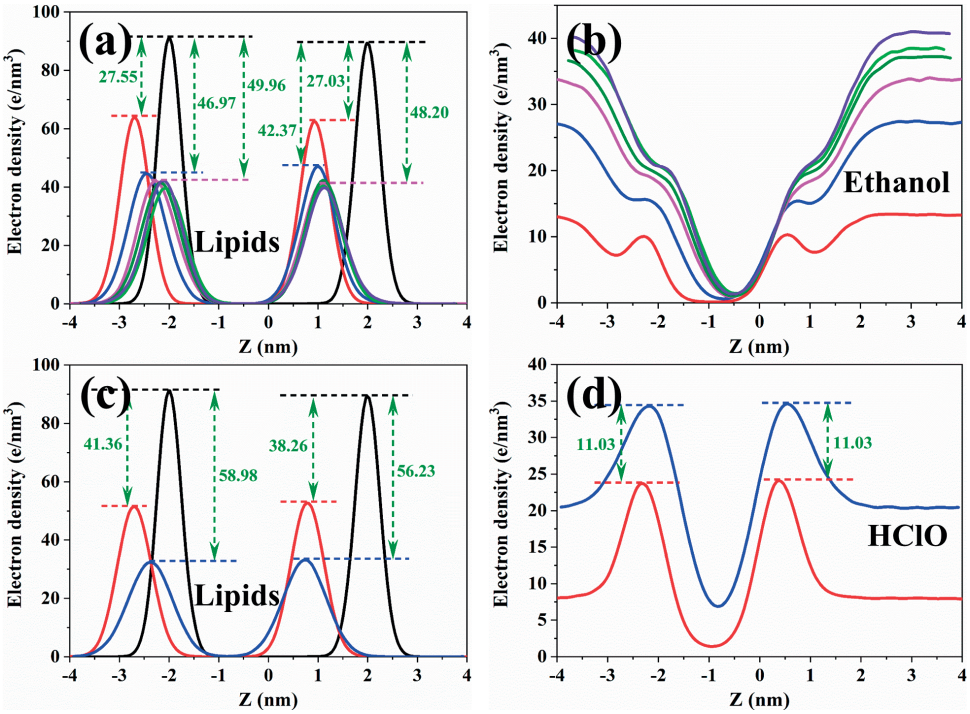


Figure 3.15: Electron density profiles of lipids and ethanol (or HClO) molecules along the bilayer normal over the bilayer membrane system. The lipids (a) and ethanol molecules (b) of the bilayer system with ethanol molecules. The lipids (c) and HClO molecules (d) of the bilayer system with HClO molecules. Here, the colored profiles are denoted as follows: black lines, the bilayer system without ethanol or HClO molecules; red lines, 10% ethanol (or HClO) molecules; blue line, 30% ethanol (or HClO) molecules; megenta lines, 50% ethanol molecules; olive lines, 70% ethanol molecules; green lines, 75% ethanol molecules; violet lines, 90% ethanol molecules.

of the membrane thickness. In Figure 3.15(b), it is observed that the electron densities for ethanol molecules along the bilayer normal increase due to the increase of ethanol concentration. Simultaneously, the electron densities in the region between two headgroups of lipids also exhibit an increasing behavior with an increment of ethanol concentration and are increasingly moving toward the center of the bilayer membrane. It provides powerful evidence that ethanol molecules penetrate the membrane interior, consistent with the illustrated result in Figure 3.14. Nevertheless, the moving magnitude of the density profile towards the bilayer's center decreases with increasing ethanol concentration. For the HClO-containing bilayer system, as displayed in Figure 3.15(c), we also find that the electron densities for the lipids decrease with the increasing HClO concentration. Meanwhile, two peaks of the electron density profile are significantly getting closer to the center of the bilayer membrane. Most notably, the varying magnitude of electron densities in the HClO case is higher than in the ethanol case. Figure 3.15(d) clearly presents that the electron densities for HClO molecules increase because of the increasing HClO concentration. At the same concentration level, the electron density

profile for HClO molecules is much closer to the center of the bilayer membrane compared with that for ethanol molecules. There is a higher electron density value in the HClO case. This result indicates that HClO molecules penetrate more easily into the bilayer membrane than ethanol molecules, which is in accordance with the plotted result in Figure 3.14(h) and (i). It might be attributed to the two molecules's differences in size and chemical properties.

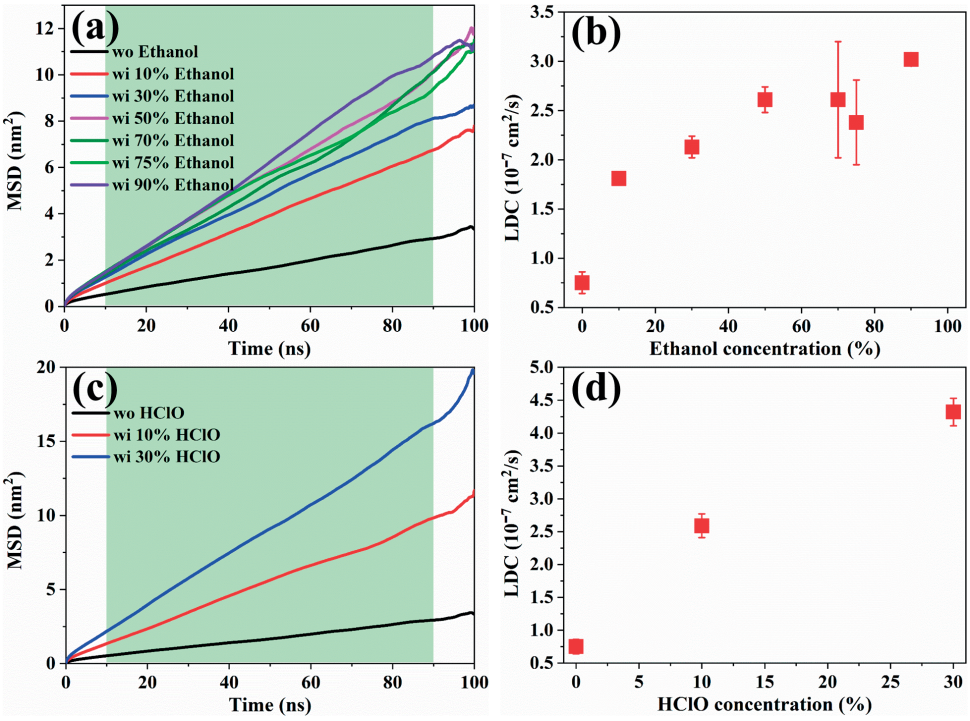


Figure 3.16: The MSD and LDC of lipid molecules in the bilayer membrane plane, indicating their lateral motion in the presence of different concentrations of ethanol (a and b) or HClO (c and d) in the system.

Lateral diffusion behavior of the lipids. We evaluate the time dependence of dynamic behavior of lipids inside the bilayer membrane. Here, we focus on its lateral diffusion behavior. The MSD and its LDC are shown in Figure 3.16. As observed in Figure 3.16(a) and (b), it can be found that the presence of ethanol molecules remarkably impacts the MSD of lipids. With the increase of ethanol concentration, the MSD gradually increases within the same simulated time except for the cases of 70% and 75% ethanol concentrations. The LDCs obtained through fitting 10 to 90 ns section of the MSD curves turn out to be (0.7514±0.11), (1.81±0.06), (2.13±0.11), (2.61±0.13), (2.61±0.59), (2.38±0.43), (3.02±0.05)$\times 10^{-7}$ cm^2/s for 0%, 10%, 30%, 50%, 70%, 75%, and 90% ethanol concentrations, respectively. Obviously, the calculated LDCs with ethanol molecules is higher than two times that in the absence of ethanol molecules, indicating that the lateral diffusion of the bilayer membrane is significantly affected by ethanol molecules. In the previous study, the LDCs in the presence of ethanol molecules are larger than the re-

ported LDC of $(1.80\pm0.3)\times10^{-7}$ or $(1.14\pm0.2)\times10^{-7}$ cm^2/s for pure PDPC or DPPC membrane with ethanol [103]. However, the LDC without ethanol is lower than that ranging from 1.0×10^{-7} to 1.5×10^{-7} cm^2/s obtained from experiments [103]. This phenomenon is attributed to the presence of cholesterol molecules. With the increase in cholesterol concentration, the diffusion coefficients of lipids decrease [104]. As a result, we can get a conclusion that ethanol molecules more easily impact the structural stability of the multi-lipid bilayer membrane compared to the single-lipid bilayer membrane. Similar phenomenon is also observed in the case of HClO, as illustrated in Figure 3.16(c) and (d). The presence of HClO molecules induces the increase of the LDC of lipids. Meanwhile, the LDC exhibits a positive correlation with HClO concentration. The LDCs for 10% and 30% HClO concentrations are $(2.59\pm0.18)\times10^{-7}$ and $(4.32\pm0.21)\times10^{-7}$ cm^2/s, respectively, larger than three times that without HClO. Furthermore, compared with the ethanol-containing membrane system, the HClO-containing membrane system has a higher LDC at the same concentration. This suggests that the HClO molecule has a more substantial influence on the structural stability of the bilayer membrane. Meanwhile, a low HClO concentration can achieve the same or better acting effect as a high ethanol concentration. This is roughly consistent with the actual situation that a 0.1% HClO solution can inactivate most viruses and pathogens. A direct comparison of our diffusion results of the HClO-containing bilayer membrane with the reported experiments is difficult because the LDC values for lipids in the bilayer membrane system with HClO have yet to be previously described in the literature. The data for lipid diffusion in the presence of HClO is more significant than the experimental LDCs of 1.9×10^{-7} cm^2/s at 313 K and 1.4×10^{-7} cm^2/s at 308 K for the POPC membrane [105].

RDF of the ethanol- and HClO-containing bilayer systems. To quantify the interactions between the lipids, ethanol, and HClO molecules, we consider RDFs for ethanol and HClO coordination with the head-groups of the lipids. Here, we put forward the probability of finding ethanol and HClO molecules at a specified distance (r) from the lipid head-groups' N, P, and O13 atoms. The 2D RDFs for A-B pairs of the bilayer systems with different concentrations are described in Figure 3.17, where A represents the N, P, and O13 atoms of the lipid head-groups, and B is the O8 atom of ethanol and the O1 and Cl3 atoms of HClO. For the ethanol-containing bilayer systems, the 2D RDFs manifest that the peak height of O13-O8 RDF is larger than that of N-O8 RDF within the range of 0.20 to 0.34 nm. Therefore, ethanol molecules preferentially bind to the O13 atoms of the lipid head-groups in the region from 0.20 to 0.34 nm, in accordance with the reported RDFs in the previous study [106]. In the region, hydrogen bonds are formed between ethanol molecules and lipids because their distance is less than 0.34 nm. The peak position of P-O8 RDF is closer to the coordinate of forming hydrogen bonds than that of N-O8 RDF in the region of 0.34 to 0.50 nm, suggesting that ethanol molecules prefer to bind to the P atoms of the lipid head-groups. The peak height of both P-O8 and N-O8 RDFs in the region between 0.34 and 0.50 nm demonstrates this result. Similar to O13-O8 RDF, the first peak of O13-O1 RDF is also located at the range from 0.20 to 0.34 nm, revealing that there are hydrogen bonds occur between O13 and O1 atoms. In the range of 0.34 to 0.40 nm, the O1 atoms of HClO molecules prefer to bind to the P atoms of the lipids due to a higher peak height of P-O1 RDF shown in Figure 3.17(g) and (h). For the region within 0.40 to 0.55 nm, it is found that the atom that HClO molecules tend to

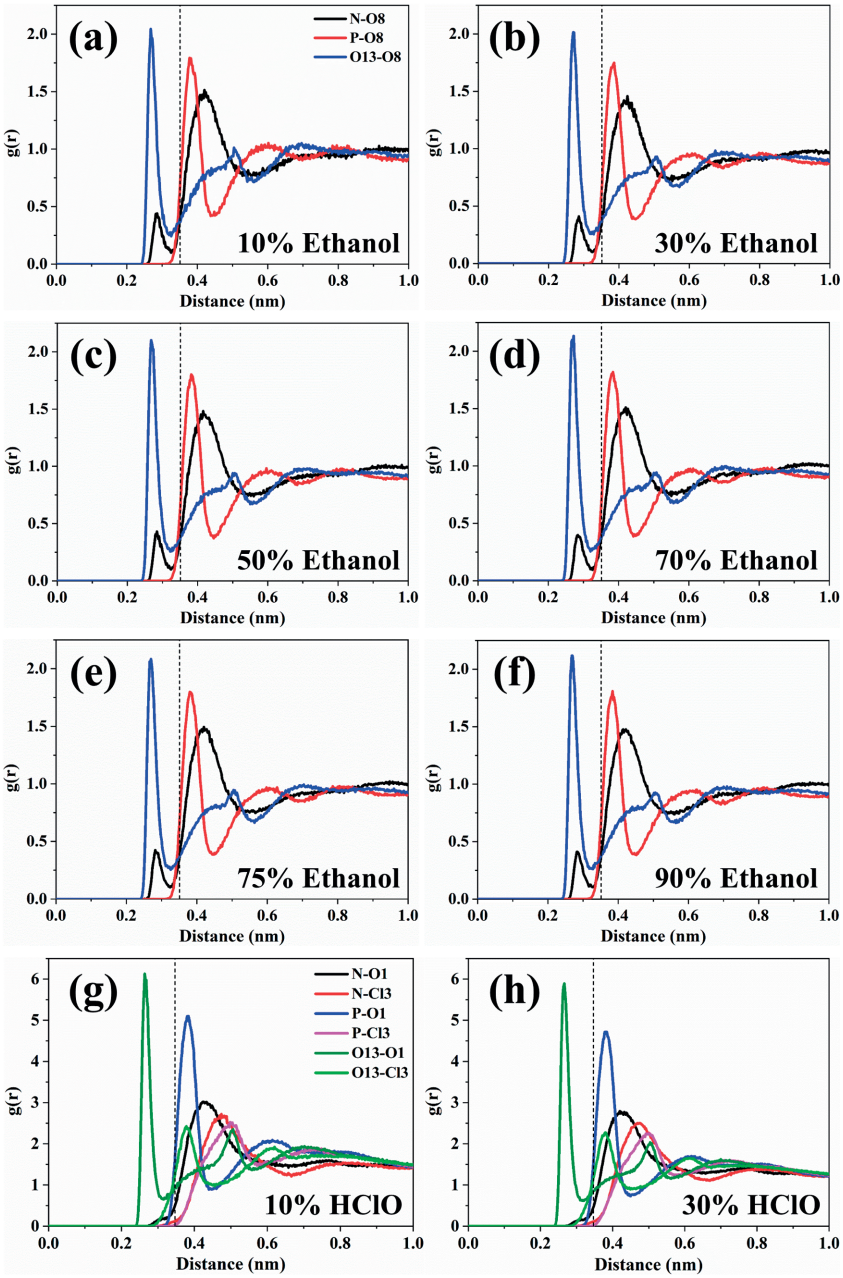


Figure 3.17: Two-dimensional RDFs $g(r)$ for atomic pairs of lipids and ethanol (or HClO) molecules in bilayer systems containing different concentrations of ethanol or HClO molecules. The dotted line at 3.4 Å is used to indicate the presence of hydrogen bonds.

bind is N, P, and O13 atoms in order. As we see in the 2D RDFs, the RDFs of A-B pairs are unaffected by the variation of ethanol or HClO concentration. Furthermore, compared to ethanol molecules, the head-groups of the lipids tend to bind with HClO molecules because the 2D RDFs for the bilayer systems with HClO have higher peak values than that of the ethanol-containing bilayer systems at the same coordinate. This is responsible for the difference in the variation of the APL and membrane thickness of the bilayer caused by ethanol and HClO molecules at the same concentration, respectively.

3.5. CONCLUSIONS

In summary, we theoretically study the interaction mechanism of selected chemical agents with 3CL hydrolase and the bilayer membrane of SARS-CoV-2 using molecular dynamics and first principles methods. In the case of 3CL hydrolase, we find that ethanol and hypochlorite molecules are more sensitive to the GLU and ASP residues of 3CL hydrolase compared to other residues. In contrast, it is readily adsorbed by THR and PHE residues for silver ions. The RDF results reveal that the unsaturated oxygen atoms of GLU, ASP, THR, and PHE residues play an essential role in the adsorption process of three biocidal ingredients. Besides, it is noted that the interactions of ethanol molecules with 3CL hydrolase increase with increasing concentration. However, when the concentration reaches a specific value, the probability of ingredient molecules occurring in a certain range will decrease. This indicates that concentrations determine the disinfection efficiency. Our DFT results further confirm that ethanol, hypochlorite, and silver ions tightly bound to the unsaturated oxygen atom of GLU, ASP, THR, and PHE residues, and the adsorption of three biocidal ingredients by amino acid residues is an exothermic process. Furthermore, the calculated minimum distances clearly show that the pseudo-covalent bond is responsible for the constraint of silver ions with PHE residue, and the molecule–residue interaction for ethanol and hypochlorite is mainly contributed by hydrogen bonds.

In the case of the bilayer membrane, we find that the presence of ethanol and HClO induces the structural change of the bilayer membrane, such as lateral expansion and thickness decrease. In the presence of ethanol and HClO, we observe that the total APL of the bilayer gradually increases with the increasing concentration, whereas the bilayer thickness progressively decreases. At higher ethanol or HClO concentration, the lipids' mass and electron density profiles reveal that the bilayer structure has a very significant variation. The end snapshots of the bilayer systems clearly show that the number of ethanol molecules entering the bilayer's hydrophobic portion is obviously less than that of HClO molecules at the same concentration. Ethanol and HClO molecules mainly accumulate in the lipid-water interface. Gradual thinning of thickness, lateral expansion, and accumulation of hydrophilic substances eventually accelerate the decomposition of virus membrane. In these systems, ethanol and HClO molecules prefer to bind to the O13 atoms of the lipids rather than their N and P atoms. The present findings provide possible information for a molecular-level understanding of inactivation mechanism of chemical disinfectants against SARS-CoV-2.

REFERENCES

[1] R. Jones and O Gunnarsson, "Density-functional formalism: Sources of error in local-density approximations", *Physical review letters*, vol. 55, no. 1, p. 107, 1985.

[2] R. Peverati and D. G. Truhlar, "Communication: A global hybrid generalized gradient approximation to the exchange-correlation functional that satisfies the second-order density-gradient constraint and has broad applicability in chemistry", *The Journal of Chemical Physics*, vol. 135, no. 19, p. 191 102, 2011.

[3] O. A. Vydrov and G. E. Scuseria, "Assessment of a long-range corrected hybrid functional", *The Journal of chemical physics*, vol. 125, no. 23, p. 234 109, 2006.

[4] G. K. Madsen, "Functional form of the generalized gradient approximation for exchange: The pbe α functional", *Physical Review B*, vol. 75, no. 19, p. 195 108, 2007.

[5] N. Van Doremalen, T. Bushmaker, D. H. Morris, *et al.*, "Aerosol and surface stability of sars-cov-2 as compared with sars-cov-1", *New England journal of medicine*, vol. 382, no. 16, pp. 1564–1567, 2020.

[6] J. Bu, D.-D. Peng, H. Xiao, *et al.*, "Analysis of meteorological conditions and prediction of epidemic trend of 2019-ncov infection in 2020", *MedRxiv*, 2020.

[7] A. W. Chin, J. T. Chu, M. R. Perera, *et al.*, "Stability of sars-cov-2 in different environmental conditions", *The Lancet Microbe*, vol. 1, no. 1, e10, 2020.

[8] D Singh, K Joshi, A Samuel, J Patra, and N Mahindroo, "Alcohol-based hand sanitisers as first line of defence against sars-cov-2: A review of biology, chemistry and formulations", *Epidemiology & Infection*, vol. 148, 2020.

[9] R. A. Leslie, S. S. Zhou, and D. R. Macinga, "Inactivation of sars-cov-2 by commercially available alcohol-based hand sanitizers", *American Journal of Infection Control*, vol. 49, no. 3, pp. 401–402, 2021.

[10] N. Hatanaka, M. Yasugi, T. Sato, M. Mukamoto, and S. Yamasaki, "Hypochlorous acid solution is a potent antiviral agent against sars-cov-2", *Journal of Applied Microbiology*, vol. 132, no. 2, pp. 1496–1502, 2022.

[11] C. F. Almeida, D. F. Purcell, D. I. Godfrey, and J. L. McAuley, "The efficacy of common household cleaning agents for sars-cov-2 infection control", *Viruses*, vol. 14, no. 4, p. 715, 2022.

[12] M. C. Sportelli, M. Izzi, E. A. Kukushkina, *et al.*, "Can nanotechnology and materials science help the fight against sars-cov-2?", *Nanomaterials*, vol. 10, no. 4, p. 802, 2020.

[13] P. Merkl, S. Long, G. M. McInerney, and G. A. Sotiriou, "Antiviral activity of silver, copper oxide and zinc oxide nanoparticle coatings against sars-cov-2", *Nanomaterials*, vol. 11, no. 5, p. 1312, 2021.

[14] A. Kratzel, D. Todt, P. V'kovski, *et al.*, "Inactivation of severe acute respiratory syndrome coronavirus 2 by who-recommended hand rub formulations and alcohols", *Emerging infectious diseases*, vol. 26, no. 7, p. 1592, 2020.

[15] H. Rabenau, G. Kampf, J. Cinatl, and H. W. Doerr, "Efficacy of various disinfectants against sars coronavirus", *Journal of Hospital Infection*, vol. 61, no. 2, pp. 107–111, 2005.

[16] G. Kampf, D. Todt, S. Pfaender, and E. Steinmann, "Persistence of coronaviruses on inanimate surfaces and their inactivation with biocidal agents", *Journal of hospital infection*, vol. 104, no. 3, pp. 246–251, 2020.

[17] G. Xiling, C. Yin, W. Ling, *et al.*, "In vitro inactivation of sars-cov-2 by commonly used disinfection products and methods", *Scientific Reports*, vol. 11, no. 1, pp. 1–9, 2021.

[18] J. Maillard, S. Sattar, and F Pinto, *Principles and practice of disinfection, preservation, and sterilization*, 2004.

[19] U. Celik, K. Celik, S. Celik, *et al.*, "Interpretation of sars-cov-2 behaviour on different substrates and denaturation of virions using ethanol: An atomic force microscopy study", *RSC advances*, vol. 10, no. 72, pp. 44 079–44 086, 2020.

[20] A. Fadaei, "Viral inactivation with emphasis on sars-cov-2 using physical and chemical disinfectants", *The Scientific World Journal*, vol. 2021, 2021.

[21] Y. Miyaoka, M. Yamaguchi, C. Kadota, *et al.*, "Rapid in vitro virucidal activity of slightly acidic hypochlorous acid water toward aerosolized coronavirus in simulated human-dispersed droplets", *Virus Research*, vol. 311, p. 198 701, 2022.

[22] A. W. Chin, J. T. Chu, M. R. Perera, *et al.*, "Stability of sars-cov-2 in different environmental conditions", *The Lancet Microbe*, vol. 1, no. 1, e10, 2020.

[23] A. Fadaei, "Viral inactivation with emphasis on sars-cov-2 using physical and chemical disinfectants", *The Scientific World Journal*, vol. 2021, 2021.

[24] C. F. Almeida, D. F. Purcell, D. I. Godfrey, and J. L. McAuley, "The efficacy of common household cleaning agents for sars-cov-2 infection control", *Viruses*, vol. 14, no. 4, p. 715, 2022.

[25] J. Greaves, R. J. Fischer, M. Shaffer, *et al.*, "Sodium hypochlorite disinfection of sars-cov-2 spiked in water and municipal wastewater", *Science of the Total Environment*, vol. 807, p. 150 766, 2022.

[26] N. Hatanaka, M. Yasugi, T. Sato, M. Mukamoto, and S. Yamasaki, "Hypochlorous acid solution is a potent antiviral agent against sars-cov-2", *Journal of Applied Microbiology*, vol. 132, no. 2, pp. 1496–1502, 2022.

[27] M. Minoshima, Y. Lu, T. Kimura, *et al.*, "Comparison of the antiviral effect of solid-state copper and silver compounds", *Journal of Hazardous Materials*, vol. 312, pp. 1–7, 2016.

[28] J. Han, L. Chen, S.-M. Duan, *et al.*, "Efficient and quick inactivation of sars coronavirus and other microbes exposed to the surfaces of some metal catalysts.", *Biomedical and environmental sciences: BES*, vol. 18, no. 3, pp. 176–180, 2005.

[29] M. Rai, S. D. Deshmukh, A. P. Ingle, I. R. Gupta, M. Galdiero, and S. Galdiero, "Metal nanoparticles: The protective nanoshield against virus infection", *Critical reviews in microbiology*, vol. 42, no. 1, pp. 46–56, 2016.

[30] G. A. Sotiriou and S. E. Pratsinis, "Antibacterial activity of nanosilver ions and particles", *Environmental science & technology*, vol. 44, no. 14, pp. 5649–5654, 2010.

[31] S. S. Jeremiah, K. Miyakawa, T. Morita, Y. Yamaoka, and A. Ryo, "Potent antiviral effect of silver nanoparticles on sars-cov-2", *Biochemical and biophysical research communications*, vol. 533, no. 1, pp. 195–200, 2020.

[32] P. Merkl, S. Long, G. M. McInerney, and G. A. Sotiriou, "Antiviral activity of silver, copper oxide and zinc oxide nanoparticle coatings against sars-cov-2", *Nanomaterials*, vol. 11, no. 5, p. 1312, 2021.

[33] M. Baselga, I. Uranga-Murillo, D. de Miguel, *et al.*, "Silver nanoparticles–polyethyleneimine-based coatings with antiviral activity against sars-cov-2: A new method to functionalize filtration media", *Materials*, vol. 15, no. 14, p. 4742, 2022.

[34] M. C. Sportelli, M. Izzi, E. A. Kukushkina, *et al.*, "Can nanotechnology and materials science help the fight against sars-cov-2?", *Nanomaterials*, vol. 10, no. 4, p. 802, 2020.

[35] Y. Nishihara, H. Eguchi, and S. Zhou, "Silver ion (ag+) formulations with virucidal efficacy against severe acute respiratory syndrome coronavirus 2 (sars-cov-2)", in *Disinfection of Viruses*, IntechOpen, 2021.

[36] S. Tian, Z. Meng, L. Yang, *et al.*, "Insight derived from molecular docking and molecular dynamics simulations into the binding interactions between hiv-1 protease inhibitors and sars-cov-2 3clpro", 2020.

[37] A. D. Reddy, S.-B. Suh, R. Ghaffari, *et al.*, "Bioinformatics analysis of sars proteins and molecular dynamics simulated structure of an alpha-helix motif", *Bulletin of the Korean Chemical Society*, vol. 24, no. 7, pp. 899–900, 2003.

[38] I.-L. Lu, N. Mahindroo, P.-H. Liang, *et al.*, "Structure-based drug design and structural biology study of novel nonpeptide inhibitors of severe acute respiratory syndrome coronavirus main protease", *Journal of medicinal chemistry*, vol. 49, no. 17, pp. 5154–5161, 2006.

[39] B. Xia and X. Kang, "Activation and maturation of sars-cov main protease", *Protein & cell*, vol. 2, no. 4, pp. 282–290, 2011.

[40] Y. M. Báez-Santos, S. E. S. John, and A. D. Mesecar, "The sars-coronavirus papain-like protease: Structure, function and inhibition by designed antiviral compounds", *Antiviral research*, vol. 115, pp. 21–38, 2015.

[41] C.-C. Lee, C.-J. Kuo, M.-F. Hsu, *et al.*, "Structural basis of mercury-and zinc-conjugated complexes as sars-cov 3c-like protease inhibitors", *FEBS letters*, vol. 581, no. 28, pp. 5454–5458, 2007.

[42] H. Yang, W. Xie, X. Xue, *et al.*, "Design of wide-spectrum inhibitors targeting coronavirus main proteases", *PLoS biology*, vol. 3, no. 10, e324, 2005.

[43] X. Xue, H. Yu, H. Yang, *et al.*, "Structures of two coronavirus main proteases: Implications for substrate binding and antiviral drug design", *Journal of virology*, vol. 82, no. 5, pp. 2515–2527, 2008.

[44] Y. Yi, P. N. Lagniton, S. Ye, E. Li, and R.-H. Xu, "Covid-19: What has been learned and to be learned about the novel coronavirus disease", *International journal of biological sciences*, vol. 16, no. 10, p. 1753, 2020.

[45] C. Bryson-Cahn, J. Duchin, V. A. Makarewicz, *et al.*, "A novel approach for a novel pathogen: Using a home assessment team to evaluate patients for covid-19", *Clinical Infectious Diseases*, vol. 71, no. 16, pp. 2211–2214, 2020.

[46] P. Merkl, S. Long, G. M. McInerney, and G. A. Sotiriou, "Antiviral activity of silver, copper oxide and zinc oxide nanoparticle coatings against sars-cov-2", *Nanomaterials*, vol. 11, no. 5, p. 1312, 2021.

[47] Y. Yu, S. Chen, X. Li, *et al.*, "Molecular dynamics simulations for 5, 5-bistetrazole-1, 1-diolate (tkx-50) and its pbxs", *RSC advances*, vol. 6, no. 24, pp. 20 034–20 041, 2016.

[48] D. Van Niekerk and J. P. Mathews, "Molecular dynamic simulation of coal–solvent interactions in permian-aged south african coals", *Fuel processing technology*, vol. 92, no. 4, pp. 729–734, 2011.

[49] C. Reece, D. J. Willock, and A. Trewin, "Modelling analysis of the structure and porosity of covalent triazine-based frameworks", *Physical Chemistry Chemical Physics*, vol. 17, no. 2, pp. 817–823, 2015.

[50] P. Govindaraj, B. Kandasubramanian, and K. M. Kodam, "Molecular interactions and antimicrobial activity of curcumin (curcuma longa) loaded polyacrylonitrile films", *Materials Chemistry and Physics*, vol. 147, no. 3, pp. 934–941, 2014.

[51] X. Wu, C. Dai, S. Fang, *et al.*, "The effect of hydroxyl on the solution behavior of a quaternary ammonium gemini surfactant", *Physical Chemistry Chemical Physics*, vol. 19, no. 24, pp. 16 047–16 056, 2017.

[52] Y. Li, S. Wang, B. Arash, and Q. Wang, "A study on tribology of nitrile-butadiene rubber composites by incorporation of carbon nanotubes: Molecular dynamics simulations", *Carbon*, vol. 100, pp. 145–150, 2016.

[53] P. Wang, X. Jiang, J. Hu, *et al.*, "Robust spin manipulation in 2d organometallic kagome lattices: A first-principles study", *Physical Chemistry Chemical Physics*, vol. 22, no. 19, pp. 11 045–11 052, 2020.

[54] S. Mukherjee, A. Banwait, S. Grixti, N. Koratkar, and C. V. Singh, "Adsorption and diffusion of lithium and sodium on defective rhenium disulfide: A first principles study", *ACS applied materials & interfaces*, vol. 10, no. 6, pp. 5373–5384, 2018.

[55] J. P. Perdew, K. Burke, and M. Ernzerhof, "Generalized gradient approximation made simple", *Physical review letters*, vol. 77, no. 18, p. 3865, 1996.

[56] T. Lu and F. Chen, "Revealing the nature of intermolecular interaction and configurational preference of the nonpolar molecular dimers (h2) 2,(n2) 2, and (h2)(n2)", *Journal of molecular modeling*, vol. 19, no. 12, pp. 5387–5395, 2013.

[57] A. M. Reilly and A. Tkatchenko, "Van der waals dispersion interactions in molecular materials: Beyond pairwise additivity", *Chemical Science*, vol. 6, no. 6, pp. 3289–3301, 2015.

[58] C. Tan, Q. Yang, R. Meng, *et al.*, "An alas/germanene heterostructure with tunable electronic and optical properties via external electric field and strain", *Journal of Materials Chemistry C*, vol. 4, no. 35, pp. 8171–8178, 2016.

[59] X. Chen, C. Tan, Q. Yang, *et al.*, "Ab initio study of the adsorption of small molecules on stanene", *The Journal of Physical Chemistry C*, vol. 120, no. 26, pp. 13 987–13 994, 2016.

[60] Y. Inada and H. Orita, "Efficiency of numerical basis sets for predicting the binding energies of hydrogen bonded complexes: Evidence of small basis set superposition error compared to gaussian basis sets", *Journal of computational chemistry*, vol. 29, no. 2, pp. 225–232, 2008.

[61] S. Zhang, Y. Zhang, S. Huang, H. Liu, P. Wang, and H. Tian, "First-principles study of field emission properties of graphene-zno nanocomposite", *The Journal of Physical Chemistry C*, vol. 114, no. 45, pp. 19 284–19 288, 2010.

[62] X. Ye, X. Jiang, L. Chen, *et al.*, "Effect of manganese dioxide crystal structure on adsorption of so2 by dft and experimental study", *Applied Surface Science*, vol. 521, p. 146 477, 2020.

[63] N. Li, Z. Chang, X. Wu, C. Sun, and W. Li, "Interactions among trioctylamine-sulfuric acid-water: Experiments and molecular dynamics simulations", in *IOP Conference Series: Earth and Environmental Science*, IOP Publishing, vol. 199, 2018, p. 032 002.

[64] Z. Luo and J. Jiang, "Molecular dynamics and dissipative particle dynamics simulations for the miscibility of poly (ethylene oxide)/poly (vinyl chloride) blends", *Polymer*, vol. 51, no. 1, pp. 291–299, 2010.

[65] L. Liu, R. Zhang, Y. Liu, W. Tan, and G. Zhu, "Insight into hydrogen bonds and characterization of interlayer spacing of hydrated graphene oxide", *Journal of Molecular Modeling*, vol. 24, no. 6, pp. 1–9, 2018.

[66] J.-P. Zeng, F.-H. Wang, and X.-D. Gong, "Molecular dynamics simulation of the interaction between polyaspartic acid and calcium carbonate", *Molecular Simulation*, vol. 39, no. 3, pp. 169–175, 2013.

[67] A. Siddharta, S. Pfaender, N. J. Vielle, *et al.*, "Virucidal activity of world health organization–recommended formulations against enveloped viruses, including zika, ebola, and emerging coronaviruses", *The Journal of infectious diseases*, vol. 215, no. 6, pp. 902–906, 2017.

[68] H. Rabenau, J Cinatl, B Morgenstern, G Bauer, W Preiser, and H. Doerr, "Stability and inactivation of sars coronavirus", *Medical microbiology and immunology*, vol. 194, no. 1, pp. 1–6, 2005.

[69] H. Rabenau, G. Kampf, J. Cinatl, and H. W. Doerr, "Efficacy of various disinfectants against sars coronavirus", *Journal of Hospital Infection*, vol. 61, no. 2, pp. 107–111, 2005.

[70] M. SAKNIMIT, I. INATSUKI, Y. SUGIYAMA, and K.-i. YAGAMI, "Virucidal efficacy of physico-chemical treatments against coronaviruses and parvoviruses of laboratory animals", *Experimental animals*, vol. 37, no. 3, pp. 341–345, 1988.

[71] H.-M. Song, *Keeping up with the progress in the diagnosis and management of pediatric rheumatic diseases*, 2020.

[72] G. Kampf, D. Todt, S. Pfaender, and E. Steinmann, "Persistence of coronaviruses on inanimate surfaces and their inactivation with biocidal agents", *Journal of hospital infection*, vol. 104, no. 3, pp. 246–251, 2020.

[73] J.-S. Kim, C.-J. Yu, K.-C. Ri, S.-H. Choe, and J.-C. Ri, "Revealing the mechanism of graphene oxide reduction by supercritical ethanol with first-principles calculations", *The Journal of Physical Chemistry C*, vol. 123, no. 14, pp. 8932–8942, 2019.

[74] A. A. Kistanov, Y. Cai, D. R. Kripalani, K. Zhou, S. V. Dmitriev, and Y.-W. Zhang, "A first-principles study on the adsorption of small molecules on antimonene: Oxidation tendency and stability", *Journal of Materials Chemistry C*, vol. 6, no. 15, pp. 4308–4317, 2018.

[75] P. Pyykkö and M. Atsumi, "Molecular single-bond covalent radii for elements 1–118", *Chemistry–A European Journal*, vol. 15, no. 1, pp. 186–197, 2009.

[76] M. J. Minch, *An introduction to hydrogen bonding (jeffrey, george a.)* 1999.

[77] J. Beheshtian, A. A. Peyghan, and Z. Bagheri, "Adsorption and dissociation of cl2 molecule on zno nanocluster", *Applied surface science*, vol. 258, no. 20, pp. 8171–8176, 2012.

[78] S. Tang, W. Wu, and J. Yu, "Interfacial interaction of ag nanoparticles with graphene oxide supports for improving nh 3 and no adsorption: A first-principles study", *Physical Chemistry Chemical Physics*, vol. 18, no. 11, pp. 7797–7807, 2016.

[79] F. Saadatpour and F. Mohammadipanah, "Physicochemical susceptibility of sars-cov-2 to disinfection and physical approach of prophylaxis", *Health Science Reports*, vol. 3, no. 4, e213, 2020.

[80] J.-H. Yoo, "Review of disinfection and sterilization–back to the basics", *Infection & chemotherapy*, vol. 50, no. 2, pp. 101–109, 2018.

[81] C. Estrela, C. R. Estrela, E. L. Barbin, J. C. E. Spanó, M. A. Marchesan, and J. D. Pécora, "Mechanism of action of sodium hypochlorite", *Brazilian dental journal*, vol. 13, pp. 113–117, 2002.

[82] J. M. Albrich, C. A. McCarthy, and J. K. Hurst, "Biological reactivity of hypochlorous acid: Implications for microbicidal mechanisms of leukocyte myeloperoxidase.", *Proceedings of the National Academy of Sciences*, vol. 78, no. 1, pp. 210–214, 1981.

[83] S. Fukuzaki, "Mechanisms of actions of sodium hypochlorite in cleaning and disinfection processes", *Biocontrol science*, vol. 11, no. 4, pp. 147–157, 2006.

[84] R. C. Tilton and B. Rosenberg, "Reversal of the silver inhibition of microorganisms by agar", *Applied and environmental microbiology*, vol. 35, no. 6, pp. 1116–1120, 1978.

[85] N. Silvestry-Rodriguez, E. E. Sicairos-Ruelas, C. P. Gerba, and K. R. Bright, "Silver as a disinfectant", *Reviews of environmental contamination and toxicology*, pp. 23–45, 2007.

[86] R. B. Thurman, C. P. Gerba, and G. Bitton, "The molecular mechanisms of copper and silver ion disinfection of bacteria and viruses", *Critical reviews in environmental science and technology*, vol. 18, no. 4, pp. 295–315, 1989.

[87] C. Liu, P. Elvati, and A. Violi, "On drug-membrane permeability of antivirals for sars-cov-2", *The journal of physical chemistry letters*, vol. 12, no. 5, pp. 1384–1389, 2021.

[88] M. Schmick and P. I. Bastiaens, "The interdependence of membrane shape and cellular signal processing", *Cell*, vol. 156, no. 6, pp. 1132–1138, 2014.

[89] M. J. Abraham, T. Murtola, R. Schulz, *et al.*, "Gromacs: High performance molecular simulations through multi-level parallelism from laptops to supercomputers", *SoftwareX*, vol. 1, pp. 19–25, 2015.

[90] J. B. Klauda, R. M. Venable, J. A. Freites, *et al.*, "Update of the charmm all-atom additive force field for lipids: Validation on six lipid types", *The journal of physical chemistry B*, vol. 114, no. 23, pp. 7830–7843, 2010.

[91] A. Nash, T. Collier, H. L. Birch, and N. H. de Leeuw, "Forcegen: Atomic covalent bond value derivation for gromacs", *Journal of molecular modeling*, vol. 24, no. 1, pp. 1–11, 2018.

[92] D. K. Vanatta, D. Shukla, M. Lawrenz, and V. S. Pande, "A network of molecular switches controls the activation of the two-component response regulator ntrc", *Nature communications*, vol. 6, no. 1, pp. 1–7, 2015.

[93] R. E. Miller, E. B. Tadmor, J. S. Gibson, N. Bernstein, and F. Pavia, "Molecular dynamics at constant cauchy stress", *The Journal of chemical physics*, vol. 144, no. 18, p. 184 107, 2016.

[94] K. Vanommeslaeghe and A. D. MacKerell Jr, "Automation of the charmm general force field (cgenff) i: Bond perception and atom typing", *Journal of chemical information and modeling*, vol. 52, no. 12, pp. 3144–3154, 2012.

[95] W. Humphrey, A. Dalke, and K. Schulten, "Vmd: Visual molecular dynamics", *Journal of molecular graphics*, vol. 14, no. 1, pp. 33–38, 1996.

[96] A. A. Gurtovenko and J. Anwar, "Interaction of ethanol with biological membranes: The formation of non-bilayer structures within the membrane interior and their significance", *The journal of physical chemistry B*, vol. 113, no. 7, pp. 1983–1992, 2009.

[97] P. Kumari, M. Kumari, and H. K. Kashyap, "Counter-effects of ethanol and cholesterol on the heterogeneous psm–popc lipid membrane: A molecular dynamics simulation study", *The Journal of Physical Chemistry B*, vol. 123, no. 45, pp. 9616–9628, 2019.

[98] K. Pluhackova, S. A. Kirsch, J. Han, *et al.*, "A critical comparison of biomembrane force fields: Structure and dynamics of model dmpc, popc, and pope bilayers", *The Journal of Physical Chemistry B*, vol. 120, no. 16, pp. 3888–3903, 2016.

[99] M. Orsi, W. E. Sanderson, and J. W. Essex, "Permeability of small molecules through a lipid bilayer: A multiscale simulation study", *The Journal of Physical Chemistry B*, vol. 113, no. 35, pp. 12 019–12 029, 2009.

[100] B. Qiao and M. Olvera de la Cruz, "Driving force for water permeation across lipid membranes", *The Journal of Physical Chemistry Letters*, vol. 4, no. 19, pp. 3233–3237, 2013.

[101] E. Falck, M. Patra, M. Karttunen, M. T. Hyvönen, and I. Vattulainen, "Impact of cholesterol on voids in phospholipid membranes", *The Journal of chemical physics*, vol. 121, no. 24, pp. 12 676–12 689, 2004.

[102] H. Eslami, S. Das, T. Zhou, and F. Muller-Plathe, "How alcoholic disinfectants affect coronavirus model membranes: Membrane fluidity, permeability, and disintegration", *The Journal of Physical Chemistry B*, vol. 124, no. 46, pp. 10 374–10 385, 2020.

[103] E. Terama, O. S. Ollila, E. Salonen, *et al.*, "Influence of ethanol on lipid membranes: From lateral pressure profiles to dynamics and partitioning", *The Journal of Physical Chemistry B*, vol. 112, no. 13, pp. 4131–4139, 2008.

[104] A. Polley and S. Vemparala, "Partitioning of ethanol in multi-component membranes: Effects on membrane structure", *Chemistry and physics of lipids*, vol. 166, pp. 1–11, 2013.

[105] M. Stepniewski, M. Kepczynski, D. Jamroz, *et al.*, "Interaction of hematoporphyrin with lipid membranes", *The journal of physical chemistry B*, vol. 116, no. 16, pp. 4889–4897, 2012.

[106] M. Patra, E. Salonen, E. Terama, *et al.*, "Under the influence of alcohol: The effect of ethanol and methanol on lipid bilayers", *Biophysical journal*, vol. 90, no. 4, pp. 1121–1135, 2006.

4

ULTRAVIOLET C INACTIVATION OF INFECTIOUS VIRUSES WITH MULTIFUNCTIONAL UVC-LED PLATFORM: VIRUCIDAL PERFORMANCE AND MECHANISM

UVC irradiation is a well-adopted method of pathogen inactivation in cleaning and disinfection processes due to its ability to damage genetic material. Most irradiation damage to viruses is associated with photochemical changes to nucleic acids at the molecule level. In this chapter, the inactivation platform with UVC-LED array is designed, and the related experiments are carried out to explore the optimal inactivation recipe. The experimental results suggest that the optimal wavelength recipe is 259 nm. The dual-wavelength scheme has no significant advantage over the single-wavelength scheme. Furthermore, the inactivation mechanism at the molecular level is studied by means of quantum chemical calculation. Meanwhile, dual uracil's transition state and reaction rate constant are calculated to determine the difficulty level of adjacent uracil reaction without and with UVC irradiation. The spectrum result without surrounding aqueous solution shows that the peak wavelength is 248.7 nm, 226.1 nm (second peak: 252.7 nm), 248.3 nm, and 205.8 nm (second peak: 249.2 nm) for adenine, cytosine, guanine, and uracil nucleotides, respectively. This is in agreement with the experimental data. With surrounding water, the position of the strongest absorption peak for four nucleotides is more or less shifted, and the height of absorption peak is enhanced. Finally, the reaction rate constant of dual uracil is 6.419×10^{-49} *and* 5.436×10^{11} $s^{-1}\cdot M^{-1}$ *for the ground and excited states, respectively.* 1.56×10^{48} *and* 1.84×10^{-12} *s are their corresponding half-life. This suggests that molecular reaction between nucleotides is a photochemical process, and the reaction without UVC irradiation cannot almost occurs compared to the case with UVC irradiation.*

4.1. INTRODUCTION

OVER the past few decades, several lethal pathogens including SARS-CoV [1], MERS-CoV [2], Ebola [3], H1N1 [4], and SARS-CoV-2 [5], have hugely impacted public health and the economic outlook worldwide. Meanwhile, the emergence of these viruses also continuously brings the available viral and bacterial inactivation approaches into the spotlight. For sterilization, a number of disinfection methods, e.g., chemical [6]–[8], thermal [6], photochemical [9], [10], and advanced approaches [11], [12], have been explored to inactivate lethal pathogens from contaminated surfaces or in the air. Among these methods, UVC disinfection is regarded as the most promising technique for inactivating pathogens due to its manageable risk and low cost [13]. UVC irradiation using photons of light from the 100–280 nm region of the electromagnetic spectrum, an effective and non-contact method for inactivating viruses and bacteria, has been widely used for disinfecting food, water supplies, public facilities, and medical instruments [14]–[17]. The UVC range shows the strongest antiviral and antibacterial activity among the three applied UV wavelength ranges, including UVA (315–400 nm) and UVB (280–315 nm) ranges [18]. The available scientific literature shows that three UVC range subsets (i.e., 207–222 nm [19], [20], 254 nm [21], [22], and 260–280 nm [23], [24]) are considered to be optimal for pathogen disinfection. A wavelength of 254 nm is the commonly used inactivation wavelength in most disinfection systems. Studies suggest that the 260–280 nm wavelength range is more efficient than 254 nm because these wavelengths are closer to the maximum absorption wavelength of genome materials [25], [26]. Besides, there is increasing interest in 207–222 nm wavelengths because of their high germicidal effectiveness [27], [28]. These literature studies intensely highlight the high feasibility of UVC irradiation in disinfection. Nevertheless, those studies have only focused on the virucidal performance of single-wavelength schemes, while dual-wavelength inactivation has rarely been reported. Furthermore, compared with conventional bulky, hazardous, and broad wavelength band mercury lamps, UVC-LEDs based on semiconductor processes have a more excellent single-wavelength characteristic. Therefore, it is worth investigating an energy-efficient UVC antiviral formulation, including figuring out the germicidal curve and the effectiveness of single-/dual-wavelength.

For UVC disinfection, the mechanism of action of UVC irradiation on pathogens is still debatable. It was commonly understood that the inactivation mechanism of UVC irradiation against pathogens is DNA and RNA damage, primarily through the formation of thymine and pyrimidine dimers [29]–[31]. This genome damage would disrupt nucleic acid replications, thus leading to the death of various pathogens. To uncover the inactivation mechanism of UVC irradiation, considerable efforts have been made, and substantial achievements have been made [32]–[34]. Four possible mechanisms have been reported to be responsible for UVC light inactivation against pathogens. One is viral protein oxidation, which is related to the reduction of viral infectivity in feline calicivirus and bacteriophage MS2 [35]–[37]. Second is the destruction of the viral capsid protein, found in the treatment of MNV-1 (murine norovirus 1) using UVC irradiation [38]. Third is the viral protein–genome cross-linking, observed in poliovirus treatment [39]. Fourth is the viral genome damage, being supported by the UVC irradiation of influenza viruses [40]. Briefly, the viral inactivation mechanism with UVC irradiation can be attributed to genome damage and/or protein destruction due to the absorption of UVC photons

by nucleotides and/or proteins. Furthermore, one published study reported that UVC irradiation induces the genome damage of adenovirus but has almost no effect on its proteins [32]. Until now, most previous studies focusing on UVC inactivation have only been at the experimental level, and theoretical research studies on interactions between UVC light and nucleotides still do not provide quantitative evidence to illustrate the effect of UVC light. Consequently, the necessity and scientific significance of studying the inactivation mechanism of UVC irradiation against viruses by a molecular-level simulation is strongly emphasized.

4.2. VIRUS INACTIVATION EXPERIMENTS BASED ON THE CUSTOMIZED UVC-LED PLATFORM

4.2.1. EXPERIMENTAL PREPARATION

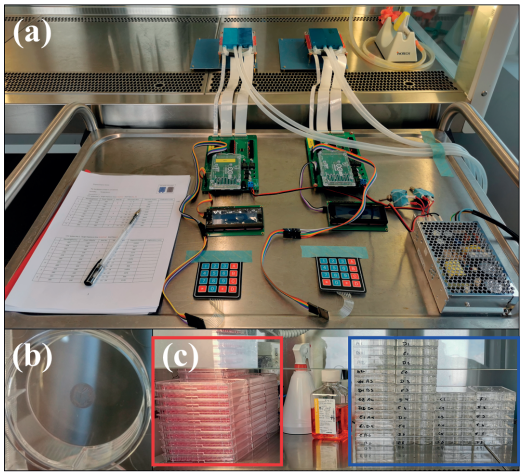


Figure 4.1: (a) The experimental platform with a UVC-LED array. (b) Dried viruses located at the center of a single well in a 6-well cell culture plate. (c) The 6-well and 96-well cell culture plates for storing the target viruses and post-inactivation back titration.

Figure 4.1(a) shows the UVC-LED platform that would be used to carry out the viral inactivation experiments. Before starting the experiments, the power and signal connection of all modules and external devices must be done, and ensure that each module and device works properly. Influenza A PR8 (A/Puerto Rico/8/1934), a single-strained RNA virus, is selected as the target inactivated virus. As presented in Figure 4.1(b), the dried viruses are placed as a dot at each well in the 6-well cell culture plate, and would be exposed to UVC light. To meet the experimental design, preparing enough 6-well cell culture plates for storing the target viruses is necessary, as displayed in the blue box of Figure 4.1(c). The red box in Figure 4.1(c) is 96-well cell culture plates with EMEM Eagle/EBSS solution, used for post-inactivation titration. As a method that can calibrate the existence of viruses, hemagglutination is usually used to diagnose certain enveloped viruses, such as Influenza viruses. Therefore, this method would be applied to our inac-

tivation experiments. Its usefulness is dependent on the features of enveloped viruses that can adsorb to red blood cells. Without virus particles, the red blood cells would land at the bottom of the well, forming the red dot. Conversely, the red blood cells are scattered, and no red dot is formed. In addition, we determine the humidity of the fume hood, the temperature of the cooling liquid, and exposure distance to eliminate their effects on viral inactivation. The values are 38% RH, 25 °C, and 2 cm, respectively.

4.2.2. EXPERIMENTAL DESIGN

Order of log magnitude. In viral inactivation, the logarithm base 10 is usually used as a criterion that judges the degree of viral inactivation. The reading limit with a base of 10 is 4.17, less than the experimental values in the research. Consequently, a more minor dilution step by back titration brings the logarithm base to 5 to make the readings more accurate. The logarithm reduction with a base of 5 can be calculated by the formula $Log_{Reduction} = log_5(N_0/N)$, where N_0 and N are the numbers of vital viruses before and after UVC treatment, respectively. In Table 4.1, each logarithm reduction with base 5 is converted to the corresponding reduction percentage. As we can see, the inactivation percentage reaches 99.99% when the N equals 6 or 7, indicating a high inactivation level.

Table 4.1: The calculation of Logarithm Reduction with a base of 5.

Reduction N	Reduction Percentage (%)
1-$\log_5$	80
2-$\log_5$	96
3-$\log_5$	99.2
4-$\log_5$	99.84
5-$\log_5$	99.968
6-$\log_5$	99.9936
7-$\log_5$	99.99872

Exposure dose design. Different exposure doses are designed in the experiments to determine the effective dose range for inactivating viruses and reveal the relationship of dose with logarithm reduction. According to the reported results in the previous studies focusing on viral inactivation, the effective dose for inactivating various viruses ranges from 3 to 100 mJ/cm^2, as listed in Table 4.2. The exposure doses are designed to be 30, 65, and 100 mJ/cm^2 to ensure effective inactivation of Influenza A PR8. The experimental results show that the doses designed have good viral inactivation except for the 30 mJ/cm^2 dose. In accordance with the negative control limitation, the reduction value of the inactivating group with 30 mJ/cm^2 is less than 4.17, indicating that there is a viable virus remaining. Hence, the 30 mJ/cm^2 dose is set as the upper limit for viral inactivation in subsequent experiments. Besides, it must achieve a balance between radiation power and exposure time to ensure that UVC-LEDs with different wavelengths have the same dosage. The characterization of UVC-LEDs has demonstrated that the radiance as a function of current remains an excellent linear relationship within the characterized range. Therefore, the corresponding light intensity per power step can be deduced through this linear curve. It should be noted that UVC-LEDSs in the single-wavelength

group would uniformly share the target dosage, whereas for the dual-wavelength group, each wavelength equally possesses half of the target dosage. A dose of 15 mJ/cm^2, serves as an example, is listed in Table 4.3. In our experiments, the estimated doses are set to 1, 3, 6, 10, 15, 20, and 25 mJ/cm^2 with a repetition of 4 based on the preset upper limit and the rule of inactivation curve. The linearity or smoothness of inactivation or sterilization curves is used as a criterion to determine whether the number of replicates in the same experiment is sufficient to infer a reliable inactivation mode. Consequently, the $N = 4$ is designed for the inactivation curve, and the repetition number is increased to 6 to collect sufficient data points for the germicidal curve. The 6 and 15 mJ/cm^2 doses are available for the current experiments. The precision of exposure time improves to a millisecond to better control the exposure dose, thus the power duty cycle can be set to 100%. Moreover, the characterized power step is applied to be closer to the actual light intensity.

Table 4.2: Effective doses for inactivating different viruses.

UVC Type	Virus	Dose (mJ/cm^2)	Reduction	Ref.
Tube	SARS-CoV	100	3.4	[41]
Tube	SARS-CoV	25	3.8	[42]
Lamp	Phi 6 corona	25.5	4.2	[43]
Signify's UVC light source	SARS-CoV-2	5	2	[44]
Signify's UVC light source	SARS-CoV-2	22	6	[44]
Lamp	SARS-CoV-2	3	2.51	[45]

Table 4.3: Dosage distribution of single- and dual-wavelength groups.

Wavelength(nm)	Light Intensity (mW/cm^2)	Exposure Time (s)	Estimated Dose(mJ/cm^2)
259	0.2270	16.520	15
259	0.2270	16.520	7.5
269	1.5528	2.415	7.5

Exposure wavelength design. In addition to exposure dose, the wavelength also plays a critical role in viral inactivation. The sensitivity of viruses for different wavelengths in the UVC band still needs to clarify. Table 4.4 lists the design of single- and dual-wavelength groups. In the UVC-LED platform, there are five characterized single-wavelength UVC-LEDs.

Design of ozone reference group. In UVC-LED manufacturing, doped quartz glass is introduced as a low-pass filter to block short spectrums. In principle, UVC-LEDs would not produce ozone because of the absence of short-wavelength lights, including 185 nm. All the selected UVC-LEDs in our platform have doped quartz glass except for the one with a peak wavelength of 269 nm. Experimentally, the absence of the wavelength of 185 nm in the selected UVC-LEDs is confirmed by the characterization analysis of UVC-

Table 4.4: The design of the exposure wavelength for each UVC-LED group.

UVC-LED Array No.1						
Well No.	1	2	3	4	5	6
λ(nm)	260|269	259|274	259|284	259	259|269	269
UVC-LED Array No.2						
Well No.	1	2	3	4	5	6
λ(nm)	260|274	269|274	274|284	260|269	260|284	269|284
UVC-LED Array No.3						
Well No.	1	2	3	4	5	6
λ(nm)	260|274	274|284	28	260	260|284	274

LEDs. However, it is necessary to verify the presence of ozone in the experiment process through ozone monitoring to better eliminate the interference of the ozone factor for viral inactivation. Therefore, an ozone reference group is designed in the inactivation study. Additionally, to ensure the credibility of the reference group, UVC-LED light is blocked by metal strips instead of transparent glasses and plastics, even though UVC light cannot penetrate most transparent glasses and plastics due to its weak penetration. In Figure 4.2, half of wells in the 6-well cell culture plate are covered by a metal strip with yellow tape, and the remaining wells are exposed to UVC light. The dual-wavelength group with 260 and 269 nm is chosen as the light source to irradiate the experiment and reference groups. Meanwhile, the radiance for the ozone reference group is designed to be 25 mJ/cm^2, and the generating ozone is allowed to enter the corresponding wells.

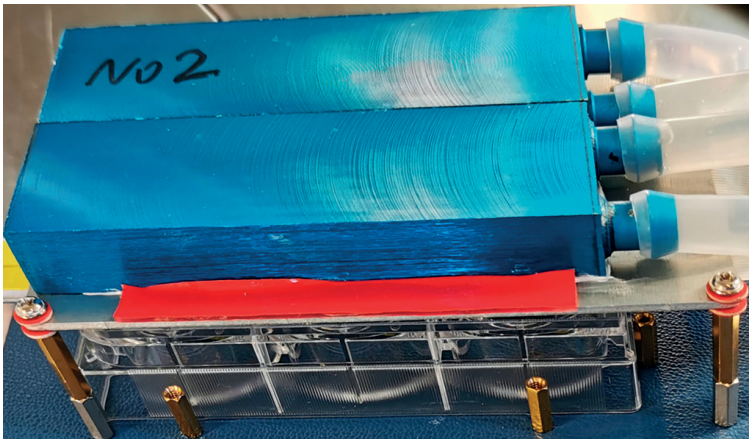


Figure 4.2: The diagram of the ozone reference group, where a metal strip is used to block UVC light for half of the wells.

4.2.3. EXPERIMENTAL RESULT

Ozone reference group. The viral inactivation results are derived from experiments with the same detection limit of 7.2 hemagglutination units because of the possible variability of viruses. Figure 4.3 shows the design of the ozone reference group, where there are two ozone control groups and four adjacent leakage checking groups. It aims to identify the impossibility that ozone is involved in viral inactivation in our experiments. As described above, two ozone reference groups are covered by metal strips to block UVC light completely. Meanwhile, two of the six UVC-LED groups are exposed to the corresponding wells in the 6-well cell culture plate, and the others are turned off. Therefore, it can be easy to confirm whether there is a leakage of UVC light by means of checking the viruses of adjacent wells. Before starting all experiments, a negative reference for dried viruses is carried out, as listed in Table 4.5. The detection limit for dried Influenza A/Puerto Rico/34 virus is 7.2 hemagglutination units. It means that viruses are not almost inactivated as achieving the detection limit for viruses. As expected, the ozone sensing results demonstrate no ozone generation in the experiment process. This directly suggests that our hypothesis is correct. As a result, the effect of ozone on virus inactivation can be ignored completely and only consider UVC-involved factors.

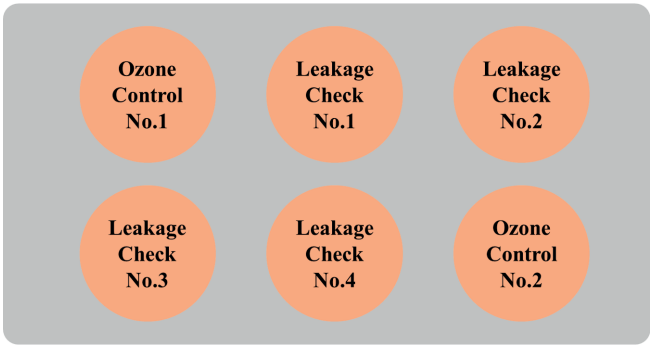


Figure 4.3: The distribution diagram of the ozone control group.

Table 4.5: Negative reference results of the ozone control group.

Ozone Control		Leakage Check				Reference Dried Virus
No.1	No.1	No.1	No.1	No.1	No.1	Negative control
7.20	7.20	7.20	7.20	7.20	7.20	7.20

Inactivation curve. An appropriate exposure dose is prerequisite for effective virus inactivation, and reaching 3-4 logarithm reduction is expected in epidemic prevention. Therefore, it is essential to explore the viral reduction tendency with increasing exposure doses and reveal a suitable dosage for germicidal curve. As presented in Figure 4.4, the UVC-LED group with both 260 and 269 nm is the most effective wavelength combination because it reaches 7-log reduction at a lower exposure dose compared to other UVC-LED groups. The reduction of the 260|269 group is at least 2-log higher than other UVC-LED

groups at the exposure dose of 10 mJ/cm^2. As the exposure dose reaches 15 mJ/cm^2, 260|274, 269|274, and 274|284 groups achieve 7-log reduction. Their optimal exposure doses for 260, 260|284, and 274 groups are 20 mJ/cm^2. Within the studied dose window, the inactivation level of 269|284 and 284 groups don't reach 7-log, but their logarithm reductions are much higher than 6-log. It should be noted that the inactivation ability of single-wavelength groups is not entirely different. Under a dose of 20 mJ/cm^2, it can be observed that the single-wavelength groups with 260 nm and 274 nm respectively result in a 7-log reduction of the target virus.

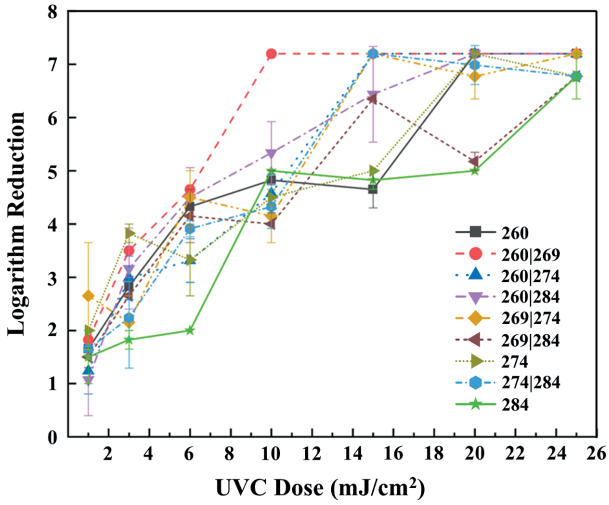


Figure 4.4: The relationship between the exposure dose of UVC light and logarithmic reduction.

Germicidal curve. Both 6 mJ/cm^2 and 15 mJ/cm^2 are selected to better observe the divergence between single- and dual-wavelength groups. The repetition number is six for each exposure dose to obtain a reliable germicidal curve. Dried viruses without UVC irradiation could not be read after 7.2-log five titers (i.e., 7.2 Hemagglutination units) through the negative reference. Figure 4.5 plots the germicidal curve fitting line of five single-wavelength groups. It is clearly displayed that the variation tendency of logarithm reduction under both 6 mJ/cm^2 and 15 mJ/cm^2 is similar. The logarithm reduction decreases gradually with the increasing UVC-LED wavelength. 259 nm is the most effective inactivation wavelength due to its considerable logarithm reduction among all the studied single-wavelengths under 15 mJ/cm^2. Furthermore, the same UVC-LED group in logarithm reduction exhibits a 2-3 log difference under two selected doses. A similar changing tendency of logarithm reduction described in single-wavelength groups can also be observed in dual-wavelength groups. As displayed in Figure 4.6, with the increasing wavelength, the logarithm reduction decreases slowly. Meanwhile, a 1.4-3 log of difference exists between two selected doses for the same UVC-LED group. In comparison, the logarithm reduction (7.06-log) of the single-wavelength group with only 259 nm is superior to that (6.69-log) of the dual-wavelength group with both 259 nm and 269 nm. Among all the evaluated wavelength recipes, 259 nm is the optimal recipe for

inactivating viruses.

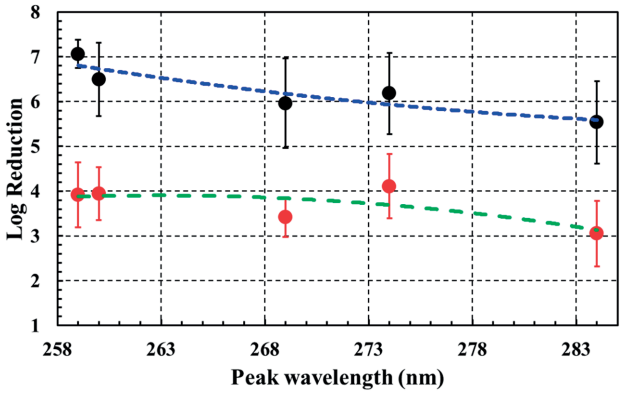


Figure 4.5: The germicidal curve for single-wavelength groups. The red and black dots represent doses of 6 mJ/cm^2 and 15 mJ/cm^2, respectively. The green and blue lines are fitting lines for the logarithmic reduction of two selected doses, respectively.

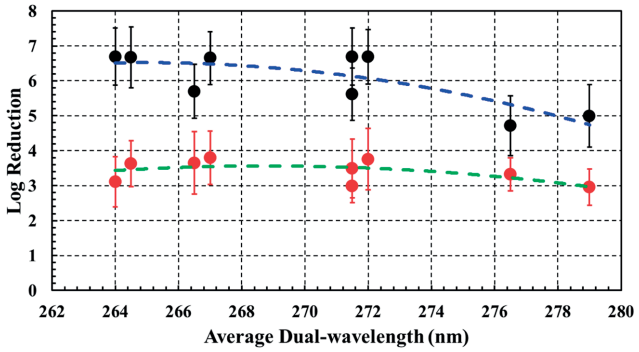


Figure 4.6: The germicidal curve for dual-wavelength groups. The red and black dots represent doses of 6 mJ/cm2 and 15 mJ/cm2, respectively. The green and blue lines are fitting lines for the logarithmic reduction of two selected doses, respectively.

4.3. MOLECULAR-LEVEL STUDY ON THE INACTIVATION MECHANISM OF UVC IRRADIATION

4.3.1. THEORETICAL FOUNDATIONS OF COMPUTATIONAL CHEMISTRY

Time-dependent density functional theory. On the basis of the minimal-value action generalized variational principle, Peuckert firstly proposed the time-dependent density functional theory (TDDFT) by considering a time-perturbation of the fixed potential [46]. This theory defines the time-dependent exchange-correlation potential and the effective potential in a new way, providing new methods to better deal with optical properties and excited states. The core of the TDDFT is to consider the situation of an inter-

acting multi-particle system moving in a time-dependent external field, and the time-dependent particle density of this system can be calculated.

Until now, the TDDFT has been a relatively well-developed theory, and its application in practical systems is becoming increasingly important. This method can not only calculate the harmonic oscillator strengths and energies of the excited states of the system but also obtain the dipole moments of geometric structures of the excited states. Compared to the multi-configurational self-consistent field and configuration interaction method, The TDDFT method is computationally tiny and highly accurate. Therefore, the TDDFT has received increasing attention and is now the most effective method for studying the excited state properties of intermediate and even large molecules. In recent years, the TDDFT has emerged as a low-cost and efficient method for calculating the spectral properties of large conjugated molecular systems. However, due to the spurious self-interaction, classical DFT tends to underestimate the energies of excited states with charge transfer (CT) characteristics. The hybrid DFT methods (i.e., B3LYP) can relatively improve the energies of CT states but still underestimate the energies of the CT states. In response to the shortcomings of classical DFT for describing the excited states, a method with long-range coulomb corrections is proposed, which correctly considers long-range corrections. The DFT method combined with coulomb-attenuated hybrid exchange-correlation functional and long-range correction is used to investigate the electronic structure of the excited states with CT characteristics. In view of this, we first consider two hybrid DFT methods, namely B3LYP and WB97XD, with dispersion correction.

Electron transition process. In fact, the absorption and emission of light by matter involve both the change of the electronic and vibrational states. To simplify calculations, the quantum effects of nuclear vibrations are generally ignored and only the electronic potential energy surface is considered. In excited state calculations, electronic transitions are mainly divided into the following three ways (see Figure 4.7): I) Vertical absorption. Electrons at the ground state absorb photons and then transition to the excited states, but the corresponding structure maintains the structure with the energy minimum at the ground state. II) Vertical emission. Electrons at the excited states emit photons and subsequently de-excite to the ground state, and the corresponding structure remains the structure with the energy minimum at the excited states. III) Adiabatic absorption. Electrons are excited from the ground state to the excited states and the corresponding structure also changes from the structure with the energy minimum at the ground state to the structure with the energy minimum at the excited states. Adiabatic emission is the inverse process of adiabatic absorption with the same transition energy. These three transition methods are idealized and helpful for theoretical studies and the investigation of practical problems. The maximum peak position in the actual absorption and emission spectra is generally closer to the vertical absorption and emission energies, respectively.

Solvent effect. The effect of solvents on the present state of solutes and chemical reactions are complex, thus it is difficult to obtain accurate studies. In order to study the complex phenomena of chemical reactions and the chemical-physical properties of substances in solutions, many computational methods have been proposed to represent molecules and their interactions in solutions. The PCM (polarized continuum model),

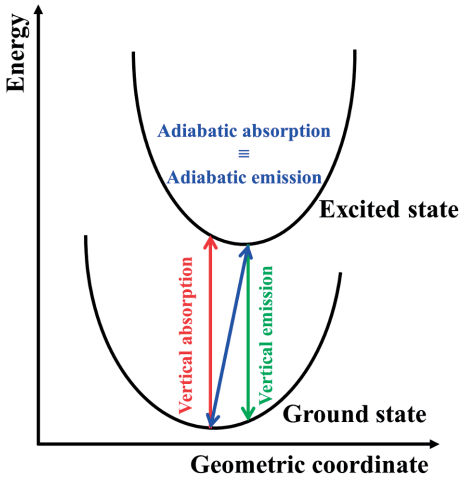


Figure 4.7: The hypothetical model of electron transition

proposed by Tomasi et al., is one of the common methods in the self-consistent reaction field (SCRF) approach [47]. It describes solvents as a continuous amorphous medium characterized by their dielectric constant. In the PCM method, molecular-shaped cavities are excavated in a continuous amorphous medium to carry a solute adequately described by a quantum mechanical charge distribution. The dielectric polarization by the solute charge distribution acts as a reaction field that polarizes the solute. This interaction is evaluated by solving its electrostatic problem, described by Poisson and Laplace equations with appropriate boundary states at the cavity surface.

At the TDDFT level, the response of the solvent field at the implicit solvent model to the excited states is considered in different ways. There are two commonly used methods, namely linear response and state specific. In the linear response method, solvents are corrected to excitation energies due to the interactions between transition densities. For the state-specific method, the solvent is made to respond directly to the density of the specified excited state, and the solvent field is made fully self-consistent with the density of the excited state by repeated iterations. In each iteration, the electron excitation calculation is required to obtain the density of excited states, thus also called external iteration.

Transition state theory. The transition state (TS) theory was first proposed by Eyring et al. in 1935 and has been successfully applied to chemical reaction mechanisms and the relationship between structure and reactivity [48]. The core idea of TS theory is that when reactant molecules are transformed into product molecules, they must pass through a TS with a high energy level (i.e., activated complex). This TS is intermediate between bond formation and breakage. The corresponding structures is very unstable can generate products or return to the original reactants. Unfortunately, the short lifetime of the TS in the reaction process enables it challenging to obtain data on the structure and properties of the TS from experiments. Nevertheless, it is theoretically possible to obtain the relevant data on TSs by means of computational methods, such as molec-

ular dynamics and quantum chemistry. Mathematically, the reactants, products, and TSs in the reaction process are the extreme points on the potential energy surface, and the TSs are the saddle point of the potential energy surface. In the vibrational frequency calculations, the TS is the structure with an imaginary frequency. During the reaction, there is a minimal energy reaction pathway on the potential energy surface, which directly links the reactants, TSs, and products, as presented in Figure 4.8.

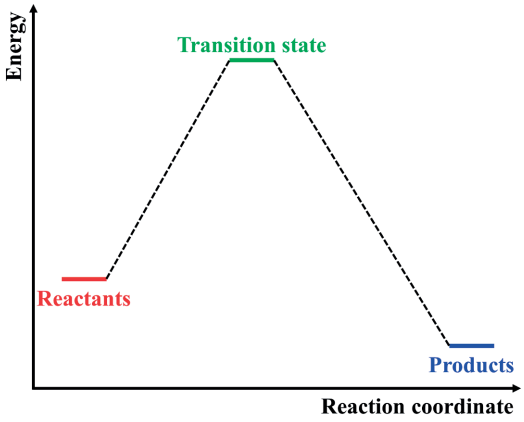


Figure 4.8: The reaction potential energy curve.

4.3.2. EVALUATION OF BASIS SETS

All density functional benchmark tests depend on the convergence results produced by the basis set, or give more minor errors than conventional experimental or theoretical studies. Thus, firstly, utilizing different atomic basis sets to conduct the optimization and frequency calculations of the uracil molecule and calculate its absorption wavelength in the excited state 1 (S1). The bond length, the total energy in the ground state (S0), and UV-vis absorption spectrum for the S1 are listed in Table 4.6. The atomic symbols in the table are based on the atomic numbers of the corresponding structure of the uracil base in Figure 4.9. In this calculation, wB97XD hybrid functional is adopted because it could describe the weak noncovalent interactions, such as van der Waals and charge transfer interactions [49], [50]. Moreover, for TDDFT analysis,the wB97XD method is capable of meeting the computational accuracy requirements.

From the overall structure perspective, the basis sets have no significant effect on the uracil molecule. However, Table 4.6 displays that the bond lengths calculated by triple-zeta basis sets (e.g., 6-311G) are shorter than that for double-zeta basis sets (e.g., 6-31G). The length of bonds binding to the H atom is almost independent of the selected basis sets. At the same time, there is a similar result from the total energy perspective. The total energies of the uracil molecule based on triple-zeta basis sets are approximately 0.1 Hartree lower than that calculated by double-zeta basis sets, apart from the basis set D95. As a result, the optimized molecular structure using triple-zeta basis sets is more stable compared with that of double-zeta basis sets. According to the calculated spectral properties, it is noted that the effect of the selected basis sets on the spectral properties

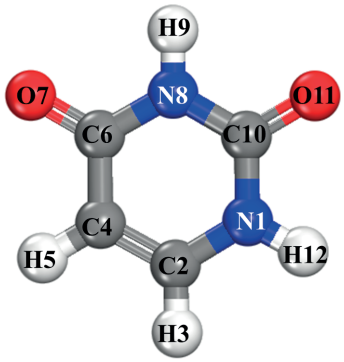


Figure 4.9: The atomic structure of the ground state of the uracil molecule and its corresponding atomic numbers.

Table 4.6: Effect of basis set on structural parameters of the uracil molecule in its ground state and its absorption wavelength in the S1 state, where bong length in Å, steady-state energy in Hartree, and absorption wavelength in nm.

Basis set	Ground state							
	N1-H12	N1-C2	C2-H3	C2-C4	C4-C6	C6-O7	E	λabs
D95	1.009	1.376	1.085	1.349	1.465	1.218	-414.77	247.6
6-31G	1.007	1.381	1.082	1.348	1.467	1.239	-414.55	245.2
6-31G (d,p)	1.008	1.373	1.084	1.344	1.461	1.214	-414.69	243.6
6-31++G (d,p)	1.009	1.374	1.084	1.345	1.460	1.217	-414.71	248.4
6-31++G (2d,2p)	1.007	1.372	1.082	1.343	1.459	1.212	-414.73	250.0
6-311G	1.004	1.380	1.079	1.344	1.454	1.237	-414.65	246.8
6-311G (d,p)	1.006	1.371	1.083	1.341	1.460	1.207	-414.79	244.4
6-311++ G(d,p)	1.007	1.372	1.083	1.341	1.459	1.209	-414.80	248.4
6-311++G (2d,2p)	1.004	1.370	1.080	1.338	1.457	1.209	-414.82	250.8
Def2tvzp	1.005	1.368	1.082	1.338	1.456	1.208	-414.85	248.4
Aug-cc-pvtz	1.004	1.368	1.080	1.338	1.456	1.209	-414.84	250.8

of the uracil molecule is quite limited due to their similar absorption wavelengths at the S1. For example, the difference in absorption wavelengths of 6-31G and 6-311++G(2d, 2p) under the S0 is 3.7 nm, whereas it is 4.4 nm in the S1. Therefore, combining all the above considerations, as well as the excited state structures and spectral properties to be studied, and referring to the basis sets adopted in the literature for nucleotide TDDFT

studies, the basis set 6-311+G(d, p) with polarization and dispersion function added to all atoms is employed in the calculation of spectral properties. Besides, by means of a high-level basis set def2tvzp to search the transition state of nucleotide reaction in the S0 and S1, as well as calculate the reaction rate constant of nucleotide photoreaction in the S0 and S1 in order to obtain better computational results.

4.3.3. EVALUATION OF DFT FUNCTIONALS

Six DFT functionals, including PBE1PBE, B3LYP, CAM-B3LYP, wB97XD, M06, and M06-2X, are used to perform the calculations of the S0 (and S1) structure optimization, frequency, and excited energy of the uracil molecule. The basis set 6-311+G(d, p) is considered in this evaluation. According to the optimized molecular structures, the S0 structures obtained by different functionals are basically similar and all atoms are in the same plane, as shown in Figure 4.10. In contrast, the S1 structures of the uracil molecule relaxed with various DFT functionals, especially the C-C and C-O double bonds. For PBE1PBE, B3LYP, and M06 functionals, there is no significant difference in the overall structures of the uracil molecule in the S1, and the C-C double bond is located at the same position. Meanwhile, one of the C-O double bonds changes into the C-O single bond. In the case of M06-2X functional, we observe that the position of the C-C double bond is unchanged. Interestingly, one of C-O double bonds has the same changing behavior as in the PBE1PBE, B3LYP, and M06 functionals. For the case employing CAM-B3LYP and wB97XD functionals, it is found that there are two C-C double bonds in the S1 structures of the uracil molecule, and the C-O double bond immediately adjacent to the C-C double bond becomes the C-O single bond. These differences suggest that distinct DFT functionals obviously affect the molecular structure in the excited states.

In order to further get an insight into the structural difference of the uracil molecule in the different DFT functionals, the bond lengths between two atoms in the uracil molecule and the vertical absorption energies transitioning from S0 into S1 (S0→S1) are discussed. These bond lengths and vertical absorption energies are listed in Table 4.7. As we can see, there is a tiny difference in the bond lengths of the uracil molecule calculated with PBE1PBE, B3LYP, and M06 functionals, which is negligible. For instance, the lengths of the C4-C6 double bond are 1.368 Å, 1.368 Å, and 1.365 Å for PBE1PBE, B3LYP, and M06 functionals, respectively, and the difference is much less than 0.01 Å. Therefore, these three functionals could obtain the same excited-state structures. Similarly, we find a negligible difference between bond lengths relaxed by CAM-B3LYP and wB97XD functionals. The overall difference in the bond length is also much less than 0.01 Å, thus excited-state structures optimized by using these functionals are almost the same. The vertical absorption energies for PBE1PBE, B3LYP, CAM-B3LYP, wB97XD, M06, and M06-2X functionals further give powerful evidence to these findings. As listed in Table 4.7, the vertical absorption energies for PBE1PBE, B3LYP, and M06 functionals are 4.858 eV, 4.711 eV, and 4.863 eV, respectively, which are relatively close. For CAM-B3LYP and wB97XD functionals, their vertical absorption energies are 5.143 eV and 5.131 eV respectively, and their difference is much smaller than 0.1 eV. Among these six DFT functionals, the absorption wavelength (263.2 nm for the S1) calculated by adopting B3LYP functional is the closest to the experimental wavelength between 259 nm and 284 nm. Consequently, B3LYP functional is used to calculate the spectral properties of four single

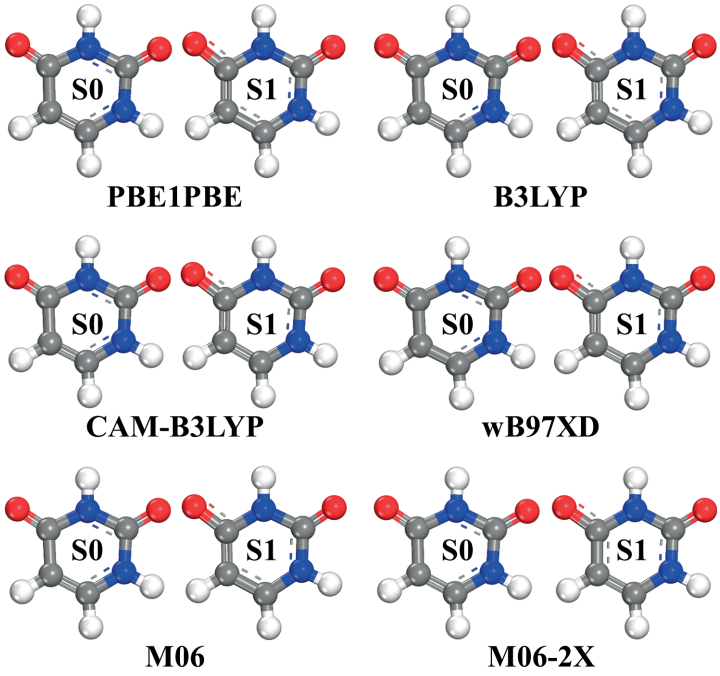


Figure 4.10: The atomic structures of the uracil molecule in the ground and excited states, optimized using various DFT functionals.

nucleotides. Although wB97XD functional performs mediocrely in predicting the absorption wavelength of the uracil molecule, it introduces both DFT-D2 dispersion correction and long-range correction that enable it to possess good computational accuracy for weak interaction, charge transfer excitation and Rydberg excitation. Therefore, wB97XD functional is adopted to investigate electron excitation characteristics of four single nucleotides.

Table 4.7: Structural parameters of the S1 stable structure of the uracil molecule and its vertical absorption energy (Eav) in different DFT functional, with bond length measured in Å and Eva in eV.

Parameters	PBE1PBE	B3LYP	CAM-B3LYP	wB97XD	M06	M06-2X
N1-C2	1.397	1.404	1.404	1.403	1.401	1.404
C2-C4	1.398	1.408	1.372	1.375	1.395	1.362
C4-C6	1.368	1.368	1.381	1.380	1.365	1.398
C6-O7	1.314	1.321	1.317	1.316	1.314	1.313
C6-N8	1.387	1.392	1.394	1.394	1.387	1.406
N8-C10	1.39	7 1.407	1.394	1.396	1.401	1.389
C10-O11	1.209	1.213	1.207	1.207	1.205	1.206
C10-N1	1.359	1.364	1.365	1.365	1.361	1.372
Eva	4.858	4.711	5.143	5.131	4.863	5.046

4.3.4. COMPUTATIONAL METHODS AND NUCLEOTIDE MODELS

All DFT and TDDFT calculations are performed using the Gaussian 16 program package [51]. The geometrical structures, and UV-vis absorption spectrums of four single nucleotides, namely adenine, cytosine, guanine, and uracil with the sugar-phosphate backbone displayed in Figure 4.11, are calculated by adopting B3LYP hybrid functional with the basis set of 6-311+G(d, p) for all atoms [52]. For the electron excitation feature, transition state, and intrinsic reaction coordinate, we also invoke wB97XD hybrid functional with def2tvzp basis set in order to obtain better electron excitation description and more accurate energy parameters (e.g., electronic energy). These computational methods are usually adequate and affordable for four investigated nucleotides. Note that most TDDFT calculations are conducted in the gas phase. However, we also perform the calculations of vertical electronic excitation with water surrounding described by the polarizable continuum model (PCM) to consider the bulk solvent effect [53]. The UV-vis absorption spectrum and hole-electron analysis are dealt with by the Multiwfn program, which is powerful for implementing electronic wavefunction analysis [54]. The VMD package (version 1.9.3) is used to better visualize the investigated nucleotides and their hole-electron distribution [55]. In addition, the thermodynamic parameters of the reactant and transition state, required in the reaction rate constant calculation, are calculated by utilizing the Shermo code [56].

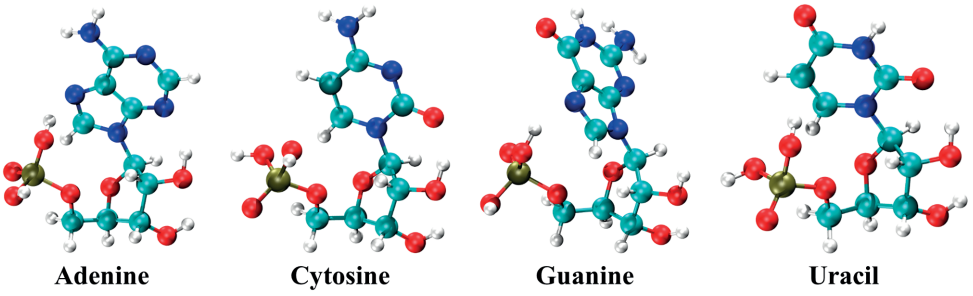


Figure 4.11: Molecular models of four individual nucleotides, with white, cyan, blue, red, and brown colors representing H, C, N, O, and P atoms, respectively.

4.3.5. UV-VIS ABSORPTION SPECTRUMS OF FOUR RNA NUCLEOTIDES

Absorption spectra, also called absorption curve, refers to the spectrum resulting from the transition of electrons from a low-energy level to a high-energy level when substances absorb photons, which mainly depends on samples' atomic and molecular composition [57]. The absorption spectrum can be employed to characterize the excited state of electrons, and provide a meeting point between experimental and theoretical studies on the absorption properties of biological molecules. In addition, the knowledge of the absorption spectrum also plays an important role in the optical applications of biological molecules. Most importantly, some previous studies focusing on viral inactivation through UV light have clearly revealed that the UV photon-energy absorption is the leading cause of producing intrastrand cyclobutyl-pyrimidine dimers, which directly results in genetic mutations or viral death [58]–[61]. Consequently, this section

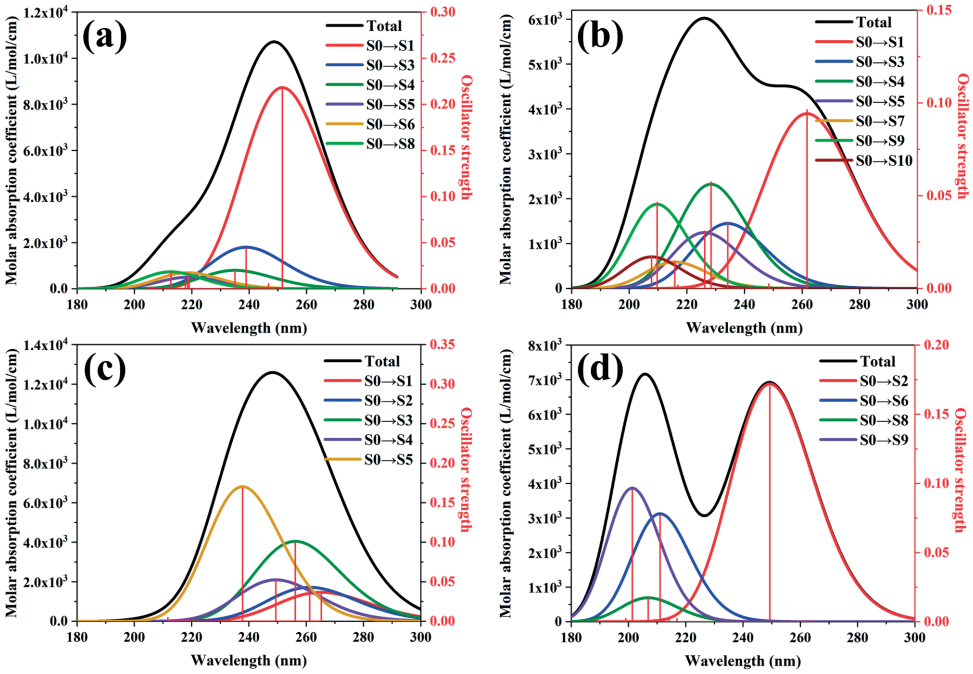


Figure 4.12: UV-vis absorption spectra of the nucleotides adenine (a), cytosine (b), guanine (c), and uracil (d).

discusses the absorption spectrum of four single nucleotides in the gas phase and with water surrounding them. Note that ten excited states are considered, namely S1, S2, S3, S4, S5, S6, S7, S8, S9, and S10. To clarify the contribution of each excited state, only the excited states with an oscillator strength greater than 0.01 are concerned. Figure 4.12 shows the absorption spectrums of adenine, cytosine, guanine, and uracil nucleotides in the gas phase. From the perspective of the total absorption curve, the strongest absorption peaks for adenine, cytosine, guanine, and uracil nucleotides are at 248.7 nm, 226.1 nm (second peak: 252.7 nm), 248.3 nm, and 205.8 nm (second peak: 249.2 nm) respectively, which are close to the experimental wavelength lied in between 259 nm and 284 nm. Meanwhile, these absorption peaks are also near to the reported values in the literature in which the absorption peaks for adenine, cytosine, guanine, and uracil in the gas phase are at 255.84 nm, 262.27 nm, 259.18, and 255.70 nm, respectively [62]. As shown in Figure 4.12 (a), we can observe that the total absorption spectrum of adenine is dominantly composed of the S1, S3, and S4, and the contribution magnitudes for the absorption peak are 0.80, 0.13, and 0.04, respectively. Therefore, the adsorption peak is led by the S1. For the cytosine, it can be found that the S1, S3, S4, S5, S7, and S9 dominate the total absorption spectrum, as plotted in Figure 4.12(b). Its strongest peak mainly consists of the S3, S4, S5, S7, and S9; their contribution rates are 0.19, 0.38, 0.21, 0.06, and 0.09, respectively. The S1 almost dominates the second peak around 260 nm, and the corresponding contribution rate is 0.72. Figure 4.12(c) displays that the S1, S2, S3, S4, and S5 mainly form the total absorption spectrum of guanine. The order of contribu-

tion magnitude for the absorption peak is S5>S3>S4>S2>S1, and the specific values are 0.40, 0.28, 0.17, 0.09, and 0.06, respectively. In the case of uracil, as presented in Figure 4.12(d), the total absorption spectrum is almost contributed by the S2, S6, S8, and S9. Its first absorption peak around 200 nm is led by the S6, S8, and S9; their contribution rates are 0.38, 0.10, and 0.48, respectively. The S2 almost completely dominates the second absorption peak near 250 nm, and the contribution magnitude is 0.99.

In order to explore the effect of solvents on the absorption properties of four single nucleotides, their steady-state absorption properties in an aqueous solution are discussed. Figure 4.13 depicts the UV-vis absorption spectrums of four nucleotides in the presence of water. For comparison, their spectrums in the gas phase are also shown. As we can observe, it is found that the UV-vis absorption spectrums for the investigated nucleotides in and aqueous solution are overall more robust than that in gas phase. Meanwhile, the positions of the absorption peaks are also changed, which move towards a short or long wavelength region. Therefore, the solvents have a significant effect on the absorption properties. As shown in Figure 4.13(a), a new absorption peak occurs around 210 nm when the aqueous solution is introduced, and the corresponding strongest absorption peak moves towards the long wavelength region. The strongest absorption peak for adenine in an aqueous solution is at 252.2 nm, which is 3.5 nm larger than in the gas phase. In Figure 4.13(b), the strongest absorption peak in aqueous solution shifts towards the short wavelength region, whereas the absorption peak around 250 nm exhibits a slight red-shift. Clearly, the absorption peak at 253.1 nm is enhanced compared to that in the gas phase at 252.7 nm. Cytosine surrounded by water strongly absorbs the UVC light with a maximum of 221.6 nm and a lower peak of 253.1 nm. There is a red shift (see Figure 4.13(c)) for guanine when surrounded by water. We observe that the strongest absorption peak in the aqueous solution is at 250.7 nm, which is 2.4 nm larger than in the gas phase. Eventually, for uracil, as depicted in Figure 4.13(d), it is obviously shown that the strongest absorption peak is changed from the peak at 205.8 nm in the gas phase to the peak at 250.2 nm in the aqueous solution. As a result, the absorption of uracil to the UVC light at 250.2 nm is stronger than that with a shorter wavelength in the aqueous solution. Moreover, the wavelength corresponding to the strongest absorption peak of uracil in the aqueous solution is 250.2 nm, consistent with the reported spectra with water surrounding in the previous study [52].

4.3.6. ELECTRON EXCITATION CHARACTERISTICS OF FOUR RNA NUCLEOTIDES

Adenine molecule. Hole-electron analysis has been widely used in many research studies as an intuitive and versatile method for revealing the excitation characteristics of electrons in a system, [63]–[66]. Therefore, to interpret the excitation characteristics of electrons of the adenine nucleotide, the isosurface diagrams of hole and electron distributions under different excited states are plotted in Figure 4.14 and 4.15. The corresponding excitation characteristic parameters are listed in Table 4.8. The electron excitation involved in UV-vis spectroscopy can be divided into two categories, namely valence and Rydberg excitations. Valence excitation refers to the excitation of electrons from the valence-occupied orbital to the valence-empty orbital. Rydberg excitation is described as the excitation of electrons from the valence-occupied orbital to the Rydberg orbital.

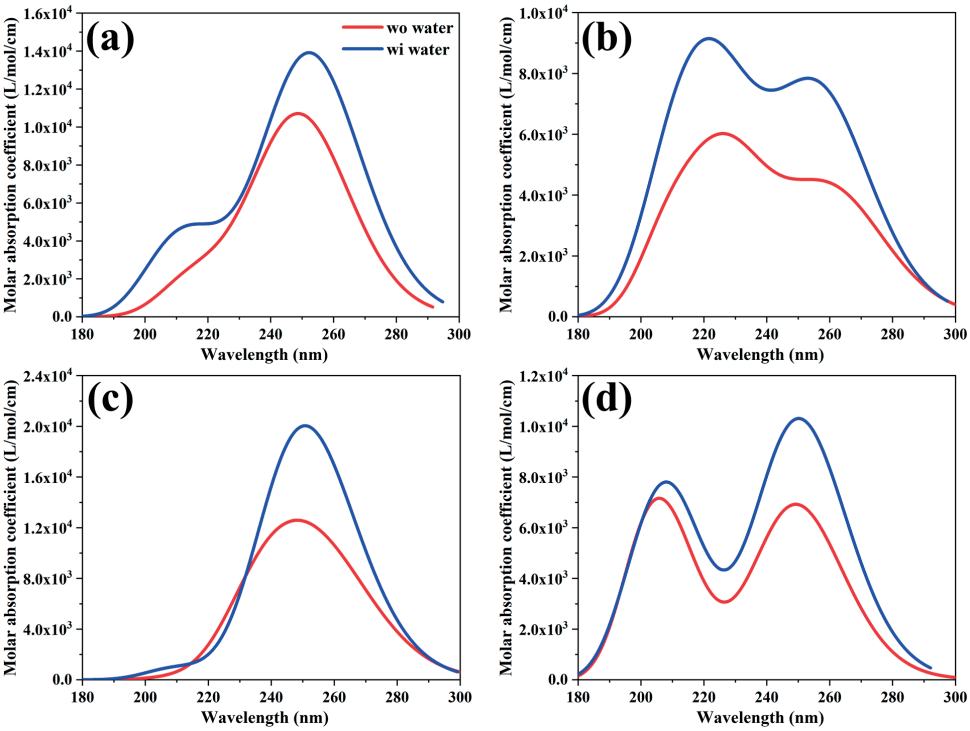


Figure 4.13: UV-vis absorption spectra of the nucleotides adenine (a), cytosine (b), guanine (c), and uracil (d) in water solvent.

From the perspective of charge transfer, valence excitation includes local excitation (LE) and charge-transfer (CT) excitation. According to the natural transition orbital (NTO) analysis, the excited state ranging from 1 to 10 can be classified into three transition categories: $\pi \rightarrow \pi^*$, $n \rightarrow \pi^*$, and $\pi \rightarrow 3s$. Among all the excited states, the excited state 7 (S7) is the $\pi \rightarrow 3s$ transition type that is a Rydberg excitation, whereas S3, S4, S5, and S10 belong to the $n \rightarrow \pi^*$ category. The rest of the excited states, including S1, S2, S6, S8, and S9, are determined as the excited type of $\pi \rightarrow \pi^*$. Note that the isosurface maps of the NTOs of different excited states of the adenine nucleotide are not presented here. On the basis of charge transfer, combining the results shown in Figure 4.14-4.15 and Table 4.8, all the excited states of the adenine nucleotide belong to the LE except for S7. For instance, the S1 is clearly the LE because it possesses the small D-index, the large Sr-index, the apparently negative t-index, and the modest $\triangle\sigma$-index. The isosurface map of the Chole-Celectron of the S1 shown in Figure 4.14 further verifies this analytical result. At the same time, the corresponding four indexes in the S8 also exhibit the same feature as the S1. Interestingly, the D, Sr, t, and $\triangle\sigma$ indexes of the S3 and S4 are unlike that of the S1, where these indexes can be used to determine what type of transition the S1 belongs. These four indexes of the S3 and S4 are in an intermediate state, being difficult to determine their excitation features. However, their HDI and EDI indexes are the largest

among these excited states, which means a small uniformity in the hole and electron distribution, as shown in Figure 4.14. For the S6 and S9, although their D indexes are similar with that of the S3 and S4, their t indexes are more negative than that of the S3 and S4. Thus, the excitation features of the S6 and S9 can be easy to determine as the LE. In the S2 and S10, we also find similar behavior with the S6 and S9.

Table 4.8: Excitation characteristic parameters of various excited states for adenine. The D index refers to the total magnitude of charge transfer length. The Sr index quantifies the extent of overlapping of holes and electrons. The H index provides an overall measure of the average degree of the spatial extension of hole and electron distributions in $x/y/z$ direction. The t index specifically designed to measure the degree of separation between holes and electrons in the charge transfer direction. The $\triangle\sigma$ index reflects the difference in the overall spatial distribution breadth of electrons and holes. The HDI and EDI are delocalization indexes for holes and electrons, respectively, being pretty valuable for quantifying the breadth of spatial distribution. Ecoul measures the Coulomb attraction between holes and electrons. The T type represents the type of transition for excited states.

Excited state	D (Å)	Sr	H (Å)	t (Å)	$\triangle\sigma$ (Å)	Ecoul (eV)	HDI	EDI	T type
S0→S1	0.243	0.827	2.393	-1.240	0.308	5.90	8.50	8.78	$\pi \rightarrow \pi^*$
S0→S2	0.449	0.885	2.254	-0.842	0.011	6.23	8.17	8.28	$\pi \rightarrow \pi^*$
S0→S3	0.660	0.485	2.197	-0.637	0.293	6.35	15.38	9.69	$n \rightarrow \pi^*$
S0→S4	0.650	0.524	2.118	-0.620	0.148	6.61	15.63	9.77	$n \rightarrow \pi^*$
S0→S5	0.330	0.526	2.428	-1.104	0.235	5.79	14.33	8.80	$n \rightarrow \pi^*$
S0→S6	0.670	0.778	2.611	-1.078	0.310	5.37	8.23	6.97	$\pi \rightarrow \pi^*$
S0→S7	1.149	0.532	2.892	-0.618	1.079	4.65	9.45	2.72	$\pi \rightarrow 3s$
S0→S8	0.342	0.810	2.649	-1.400	0.092	5.37	8.31	7.70	$\pi \rightarrow \pi^*$
S0→S9	0.632	0.821	2.481	-0.946	0.403	5.59	8.20	7.65	$\pi \rightarrow \pi^*$
S0→S10	0.438	0.615	2.492	-1.214	-0.182	5.67	10.77	8.45	$n \rightarrow \pi^*$

Cytosine molecule. By means of NTO analysis, the excitation of the cytosine nucleotide can be designated into three categories, namely $n \rightarrow \pi^*$, $\pi \rightarrow \pi^*$, and $\pi \rightarrow 3s$. Surprisingly, all the excited states ranging from 1 to 10 are provided with the $n \rightarrow \pi^*$ transition type except for S5 and S9. The NTO result suggests that the S5 and S9 belong to the $\pi \rightarrow \pi^*$ and $\pi \rightarrow 3s$, respectively. Hence, it is clear that the S9 is Rydberg excitation. Depending on the hole-electron analysis, there are three excitation categories (i.e., the LE, CT, and Rydberg excitations) of electrons for the cytosine nucleotide within the investigated excited states. As listed in Table 4.9, all the D indexes are larger than 0.5 Å, thus it is necessary to utilize other indexes to better determine the excitation feature of electrons. It should be noted that there is no criterion for determining that the excitation of electrons is a CT excitation if the D index is greater than a specific value. Therefore, adopting the strict classification criterion for determining the excitation features is misleading. In the S1, we can observe a minimum D value, a maximum Sr value, and a most negative t, thus the S1 is determined as the LE. Even if the $\triangle\sigma$ index of the S7 is much larger than that of the S1, its D and Sr indexes are close to that of the S1, and the corresponding t index is more negative than that of the S1. Hence, it has the same excitation category as the S1, which is verified by the Chole-Celectron maps of the S1 and S7. They have a similar Chole-Celectron distribution, as shown in Figure 4.16 and 4.17. Impor-

tantly, it is found that the t indexes of the S2 and S8 are positive, suggesting that these two excited states belong to the CT excitation. The corresponding isosurface maps of Chole-Celectron of the S2 and S8 provide the power evidence, presenting that the separation of holes and electrons is sufficient. Besides, their D values also further confirm this discussion. In the S3 and S10, it is evident that their D, Sr, and t values are pretty close, but there is a big difference between their $\triangle\sigma$ values. Meanwhile, these focused indexes need help to determine their excitation features. Combining their isosurface diagrams of hole and electron distributions, the S3 and S10 are determined as the LE due to the insufficient hole-electron separation. The S4, S5, and S6 possess a sufficiently large D value (see Table 4.9), which means that these three excited states are the CT excitation. At the same time, their t values are slightly negative compared to the S1 and S7. This provides evidence for this determination. In addition, it should be noted that the Sr value of the S6 is larger than the S4 and S5, indicating that the hole-electron overlap of the S6 is higher than the other two excited states. As we can observe in the isosurface maps of the Chole-Celectron of the S4, S5, and S6, it is found that their hole-electron separation is not yet sufficient.

Table 4.9: Excitation characteristic parameters of various excited states for cytosine.

Excited state	D (Å)	Sr	H (Å)	t (Å)	$\triangle\sigma$ (Å)	Ecoul (eV)	HDI	EDI	T type
S0→S1	0.750	0.727	2.137	-0.612	-0.048	6.47	11.09	10.00	$n\rightarrow\pi^*$
S0→S2	1.244	0.457	1.879	0.114	0.448	6.82	19.31	10.44	$n\rightarrow\pi^*$
S0→S3	0.959	0.712	2.264	-0.303	-0.082	6.04	11.98	9.36	$n\rightarrow\pi^*$
S0→S4	1.294	0.553	2.083	-0.111	0.282	6.35	20.92	10.50	$n\rightarrow\pi^*$
S0→S5	1.641	0.507	2.836	-0.130	1.093	4.59	10.30	3.53	$\pi\rightarrow\pi^*$
S0→S6	1.534	0.643	2.514	-0.161	0.534	5.24	12.93	6.85	$n\rightarrow\pi^*$
S0→S7	0.763	0.673	2.457	-0.833	0.417	5.70	10.48	8.42	$n\rightarrow\pi^*$
S0→S8	1.247	0.536	2.082	0.072	0.416	6.26	17.39	9.63	$n\rightarrow\pi^*$
S0→S9	1.699	0.409	3.102	-0.099	1.683	4.21	11.47	2.79	$\pi\rightarrow 3s$
S0→S10	0.925	0.610	2.428	-0.323	0.446	5.71	13.45	8.82	$n\rightarrow\pi^*$

Guanine molecule. Differentiating with adenine and cytosine nucleotides, there are five transition categories for all the studied excited states in the guanine nucleotide based on the NTO analysis, as listed in Table 4.10. Among these five categories, the valence excitation includes $\pi\rightarrow\pi*$ and $n\rightarrow\pi^*$, whereas $\pi\rightarrow 3s$, $\pi\rightarrow 3py$, and $\pi\rightarrow dx^2-dy^2$ correspond to the Rydberg excitation. As the above discussion, only one type ($\pi\rightarrow 3s$) of Rydberg excitation is found in adenine and cytosine nucleotides. We can observe that the S1, S2, and S7 belong to the $\pi\rightarrow\pi^*$ transition type, while the S3, S6, S8, and S10 are determined as the $n\rightarrow\pi^*$ transition type. Moreover, the NTO results for the S4, S5, and S9 obviously illustrate that their isosurface maps of hole and electron distributions have significant Rydberg excitation characteristics, thus their transition features correspond to $\pi\rightarrow 3s$, $\pi\rightarrow 3py$, and $\pi\rightarrow dx^2-dy^2$ respectively. Similar to adenine and cytosine nucleotides, the LE and CT excitations are also determined as the transition features of remaining excited states except for the S4, S5, and S9. The S8 possesses the

minimum D value in the excited states ranging from 1 to 10, but its corresponding Sr value is modest. Fortunately, its t value is sufficiently negative, and the $\triangle\sigma$ value is not considerable. Accordingly, we can get a conclusion that the S1 belongs to the LE, and its Chole-Celectron distribution also confirms this conclusion. For the S6 and S7 with similar D values, the magnitude of their D and t values is consistent with the numerical characteristics of the LE. In particular, the Sr value of the S7 is the maximum in the investigated excited states. Hence, it is easy to determine that the excitation type of electrons for the S7 is the LE. In contrast, it is challenging to decide on the excitation type of the S6 because of its small Sr value. However, through observing the Chole-Celectron isosurface diagram of the S6, it is clearly shown that its separation of holes and electrons is insignificant. Above all, the S6 is provided with the LE. In the S2, although its D value is not large or small, it is easy to decide that the S2 belongs to the LE by combining the Sr and t values and its Chole-Celectron map. For the S3 and S10, the positive value of the t index directly displays that both excited states are the CT excitation due to their sufficient separation of holes and electrons, further demonstrated by the corresponding Chole-Celectron distribution diagrams (see Figure 4.18 and 4.19).

Table 4.10: Excitation characteristic parameters of various excited states for guanine.

Excited state	D (Å)	Sr	H (Å)	t (Å)	$\triangle\sigma$ (Å)	Ecoul (eV)	HDI	EDI	T type
S0→S1	0.475	0.758	2.338	-0.874	0.034	5.99	9.34	9.05	$\pi \rightarrow \pi^*$
S0→S2	0.933	0.731	2.466	-0.560	0.362	5.54	9.13	9.05	$\pi \rightarrow \pi^*$
S0→S3	1.231	0.474	1.791	0.086	0.581	7.16	25.41	12.78	$n \rightarrow \pi^*$
S0→S4	2.100	0.326	2.944	0.375	1.135	4.24	9.78	2.78	$\pi \rightarrow 3s$
S0→S5	2.132	0.375	3.134	0.335	1.600	3.98	9.06	3.12	$\pi \rightarrow 3py$
S0→S6	0.339	0.460	2.332	-1.020	0.341	5.98	15.53	9.39	$n \rightarrow \pi^*$
S0→S7	0.331	0.769	2.696	-1.228	0.687	5.16	8.95	7.24	$\pi \rightarrow \pi*$
S0→S8	0.219	0.524	2.282	-1.025	0.283	6.17	16.16	9.64	$n \rightarrow \pi^*$
S0→S9	2.015	0.409	3.339	-0.130	1.917	3.91	8.81	2.58	$\pi \rightarrow dx^2 - dy^2$
S0→S10	2.453	0.407	2.261	1.142	0.925	4.75	22.69	9.62	$n \rightarrow \pi^*$

Uracil molecule. Similar to the cytosine nucleotide, three transition categories, namely $n \rightarrow \pi^*$, $\pi \rightarrow \pi^*$, and $\pi \rightarrow dx^2 - dy^2$, are observed in uracil nucleotide by means of the NTO analysis. Meanwhile, most of the excited states for both nucleotides belong to the $n \rightarrow \pi^*$ transition type. As listed in Table 4.11, it is found that the S2 and S4 are determined as the $\pi \rightarrow \pi^*$ transition type, while the remaining excited states belong to the $n \rightarrow \pi^*$ transition type except for the S7. Because of the $\pi \rightarrow dx^2 - dy^2$ transition feature, the S7 is identified as the Rydberg excitation. For the S2, a small D value, an immense Sr value, a negative t value, and a modest $\triangle\sigma$ value directly provide powerful evidence that the S2 belongs to the LE. In the S3 and S4, the D and t values of these two excited states are close, but their magnitude is not large or small. Thus, it is difficult to determine the excitation features of the S3 and S4. Fortunately, the Sr value of the S4 appears to be large enough. Therefore, the LE is given to the S4. Linking with the Chole-

Celctron isosurface map of the S3, we find no apparent hole-electron separation. As a result, the S3 belongs to the LE. Even if the S6 possesses relatively small D and Sr values, an obviously negative t value gives a hypothesis that the S6 may be the LE. Hereafter, this hypothesis is confirmed by the insufficient hole-electron separation, as plotted in the Chole-Celectron isosurface map of the S6. Surprisingly, the remaining excited states, i.e., the S1, S5, S8, S9, and S10, are assigned to the CT excitation because their t indexes are positive. At the same time, the corresponding D values also further give other robust evidence (see Figure 4.20 and 4.21).

Table 4.11: Excitation characteristic parameters of various excited states for uracil.

Excited state	D (Å)	Sr	H (Å)	t (Å)	$\triangle\sigma$ (Å)	Ecoul (eV)	HDI	EDI	T type
S0→S1	1.448	0.456	1.802	0.116	0.414	7.16	24.91	11.86	$n\rightarrow\pi^*$
S0→S2	0.325	0.747	2.170	-1.114	-0.117	6.60	11.15	9.77	$\pi\rightarrow\pi^*$
S0→S3	0.826	0.466	2.204	-0.351	-0.193	6.31	20.11	11.85	$n\rightarrow\pi^*$
S0→S4	0.859	0.680	2.311	-0.292	0.026	6.05	10.89	11.39	$\pi\rightarrow\pi^*$
S0→S5	1.633	0.562	2.044	0.654	0.081	5.90	15.90	10.18	$n\rightarrow\pi^*$
S0→S6	0.735	0.484	2.476	-0.996	-0.463	5.85	16.15	9.03	$n\rightarrow\pi^*$
S0→S7	0.411	0.455	2.949	-1.355	1.110	4.68	10.39	2.71	$\pi\rightarrow dx^2-dy^2$
S0→S8	2.309	0.456	2.436	0.604	-0.281	4.97	16.00	8.64	$n\rightarrow\pi^*$
S0→S9	3.427	0.297	2.189	1.992	-0.170	4.16	17.28	9.59	$n\rightarrow\pi^*$
S0→S10	2.175	0.471	2.270	0.717	-0.086	5.19	18.40	9.65	$n\rightarrow\pi^*$

4.3.7. TRANSITION STATE OF DUAL URACIL REACTION

Biologically, nucleic acids have excellent photostability. However, photochemical damage has been observed in adjacent base monomers, oligonucleotides, and DNA [67], [68]. UV irradiation on nucleic acids could cause the breakage of bonds and strands, inter-strand cross-linking, and formation of photochemical reaction products. In particular, the formation of photochemical reaction products disrupts the normal pairing of pyrimidines and purines, altering the biological activity of nucleic acids. Obviously, most irradiation damage to organisms is significantly related to physical and chemical alteration in nucleic acids at the molecular level. Under UV irradiation conditions, adjacent thymines on the same DNA strand can undergo an addition reaction of C-C double bonds to produce cyclobutane pyrimidine dimers (CPD), the most frequent photochemical reaction product (Figure 4.22) [69], [70]. Pyrimidine dimers weaken the double helix of nucleic acids and lead to localized structural deformation, severely affecting the replication and transcription of nucleic acids and consequently generating mutations. Furthermore, adjacent pyrimidine bases on DNA strands can also undergo an addition reaction of C-C and C-O double bonds, resulting in the formation of 6-4 cross-linking products [71]. Purine bases of DNA have low oxidation potential and undergo singlet-electron oxidation to produce G cation radicals, subsequently oxidative damage products such as 8-OxoG [72], [73]. Numerous studies have presented that pyrimidine dimers

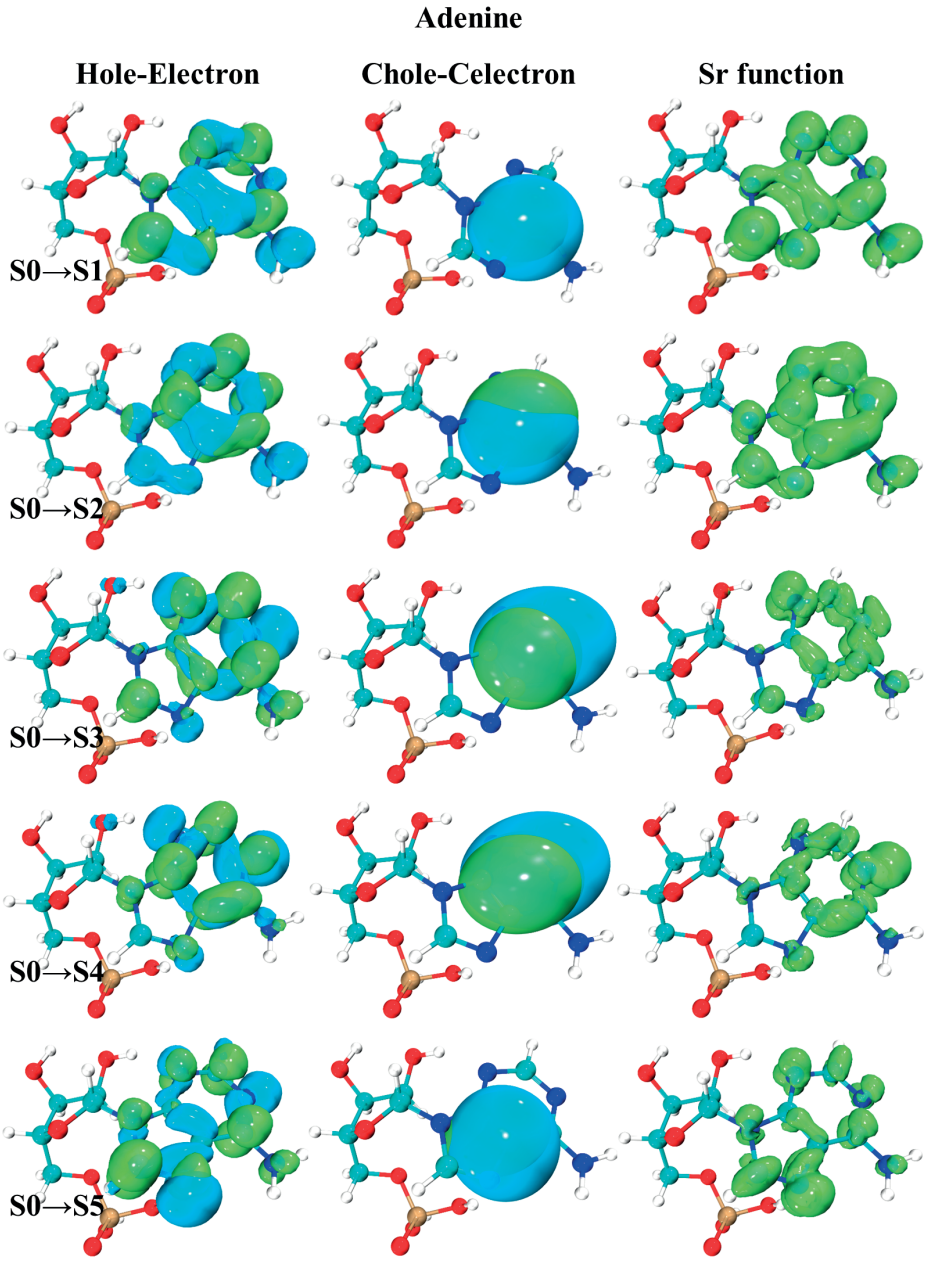


Figure 4.14: The illustration of hole-electron, Chole-Celectron, and Sr function for S1 to S5 of adenine. The isovalues for the hole and electron distributions are 0.003 au for the hole-electron, while they are set to 0.002 au for the Chole-Celectron and Sr function. The electron and hole distributions are denoted by green and blue colors, respectively.

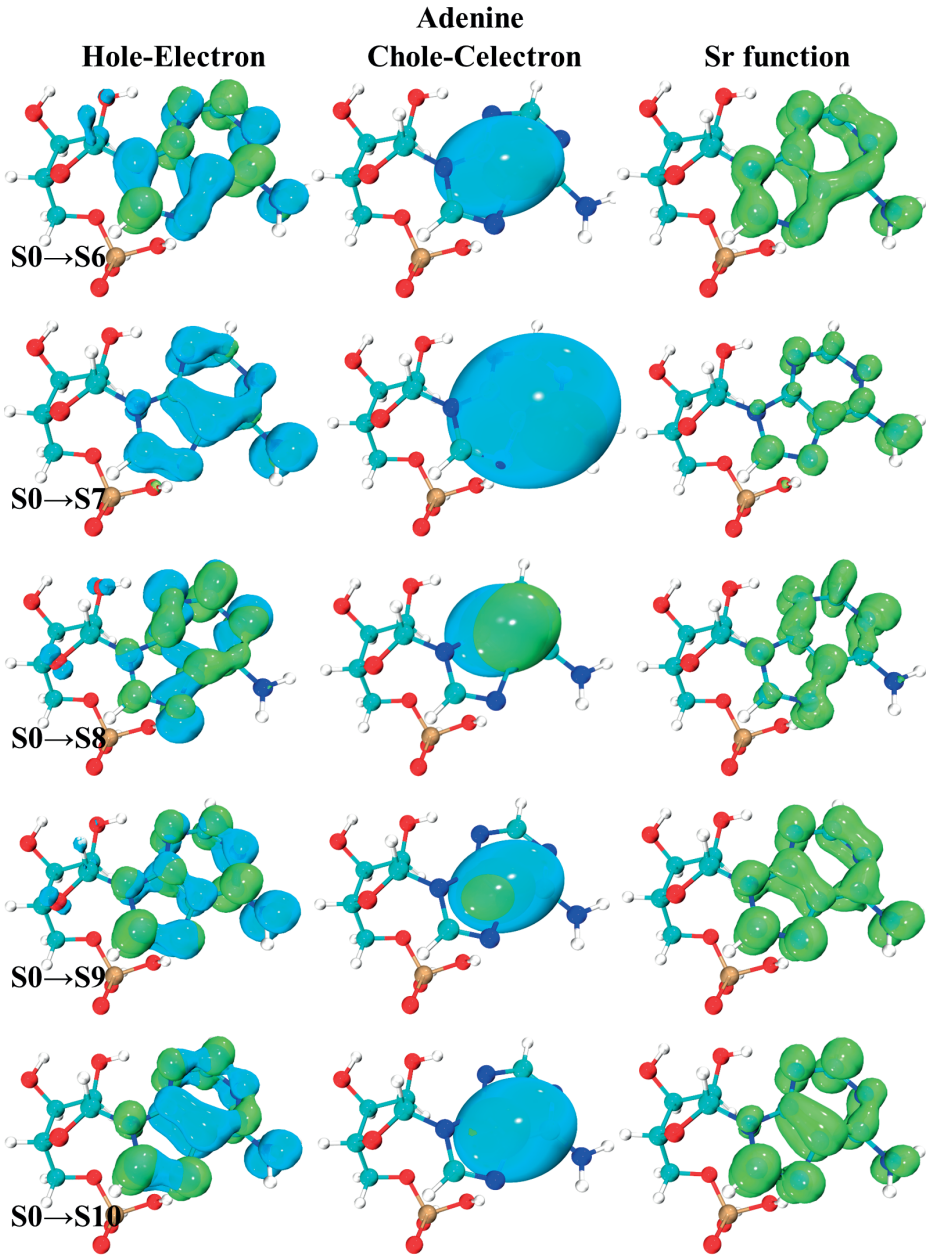


Figure 4.15: The illustration of hole-electron, Chole-Celectron, and Sr function for S6 to S10 of adenine. The isovalues for the hole and electron distributions are 0.003 au for the hole-electron, while they are set to 0.002 au for the Chole-Celectron and Sr function. The electron and hole distributions are denoted by green and blue colors, respectively.

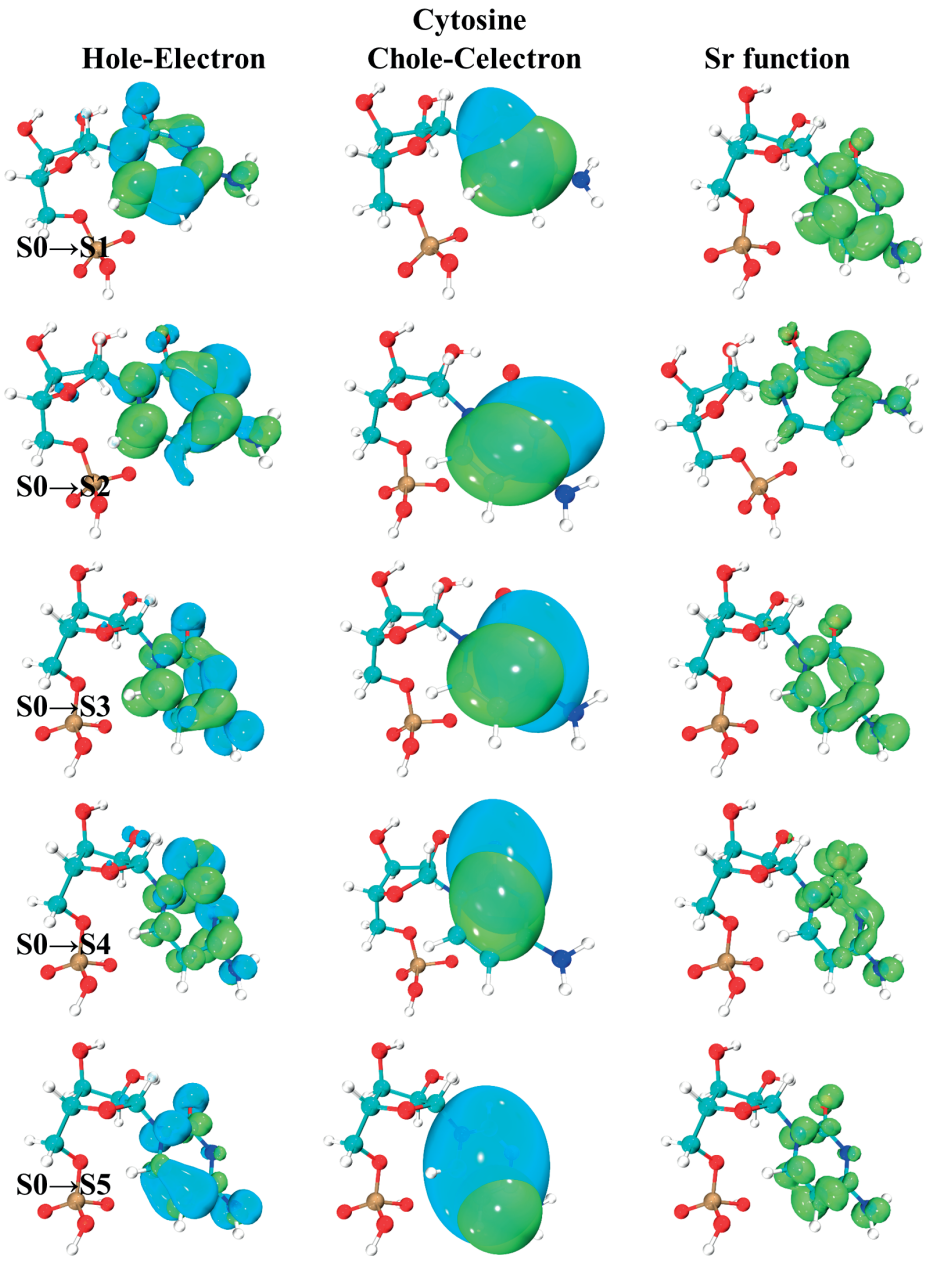


Figure 4.16: The illustration of hole-electron, Chole-Celectron, and Sr function for S1 to S5 of cytosine. The isovalues for the hole and electron distributions are 0.003 au for the hole-electron, while they are set to 0.002 au for the Chole-Celectron and Sr function. The electron and hole distributions are denoted by green and blue colors, respectively.

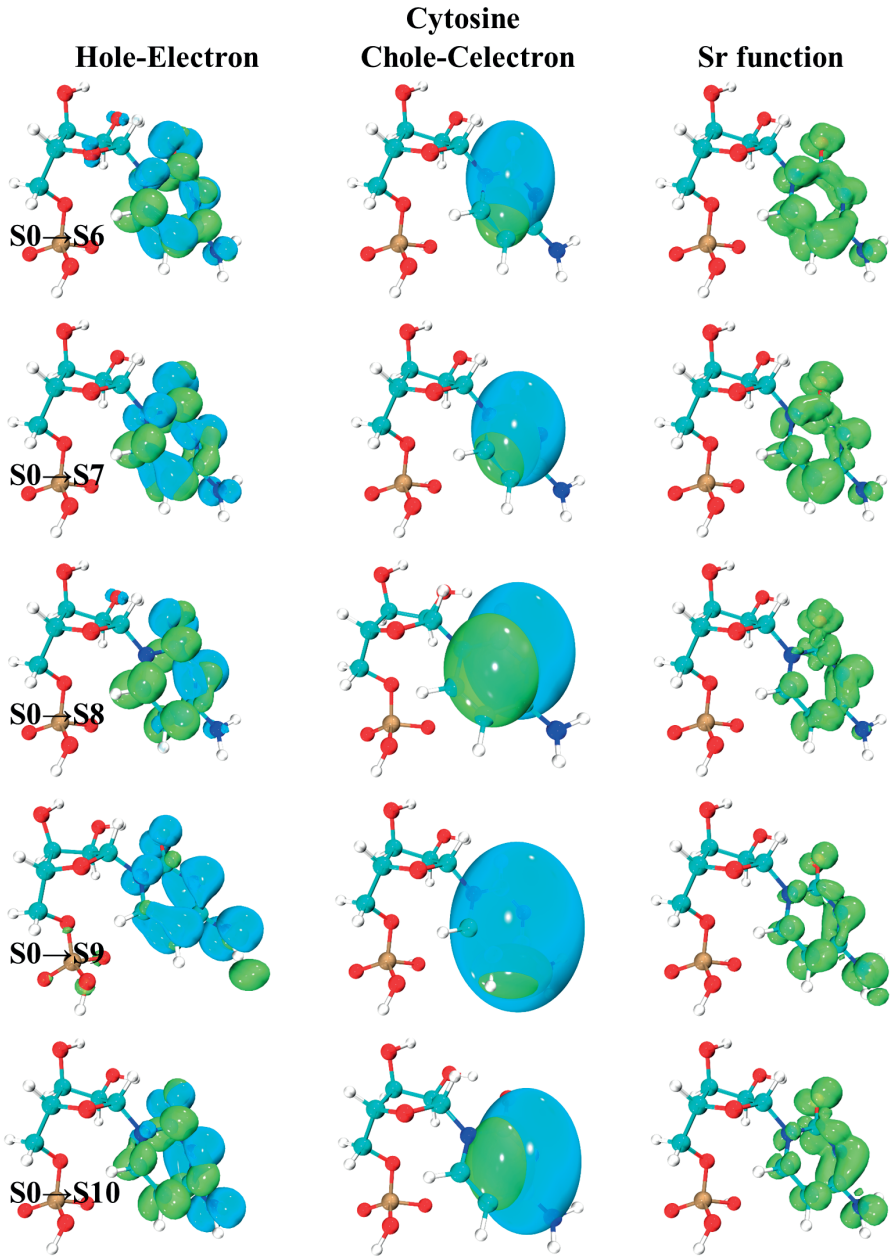


Figure 4.17: The illustration of hole-electron, Chole-Celectron, and Sr function for S6 to S10 of cytosine. The isovalues for the hole and electron distributions are 0.003 au for the hole-electron, while they are set to 0.002 au for the Chole-Celectron and Sr function. The electron and hole distributions are denoted by green and blue colors, respectively.

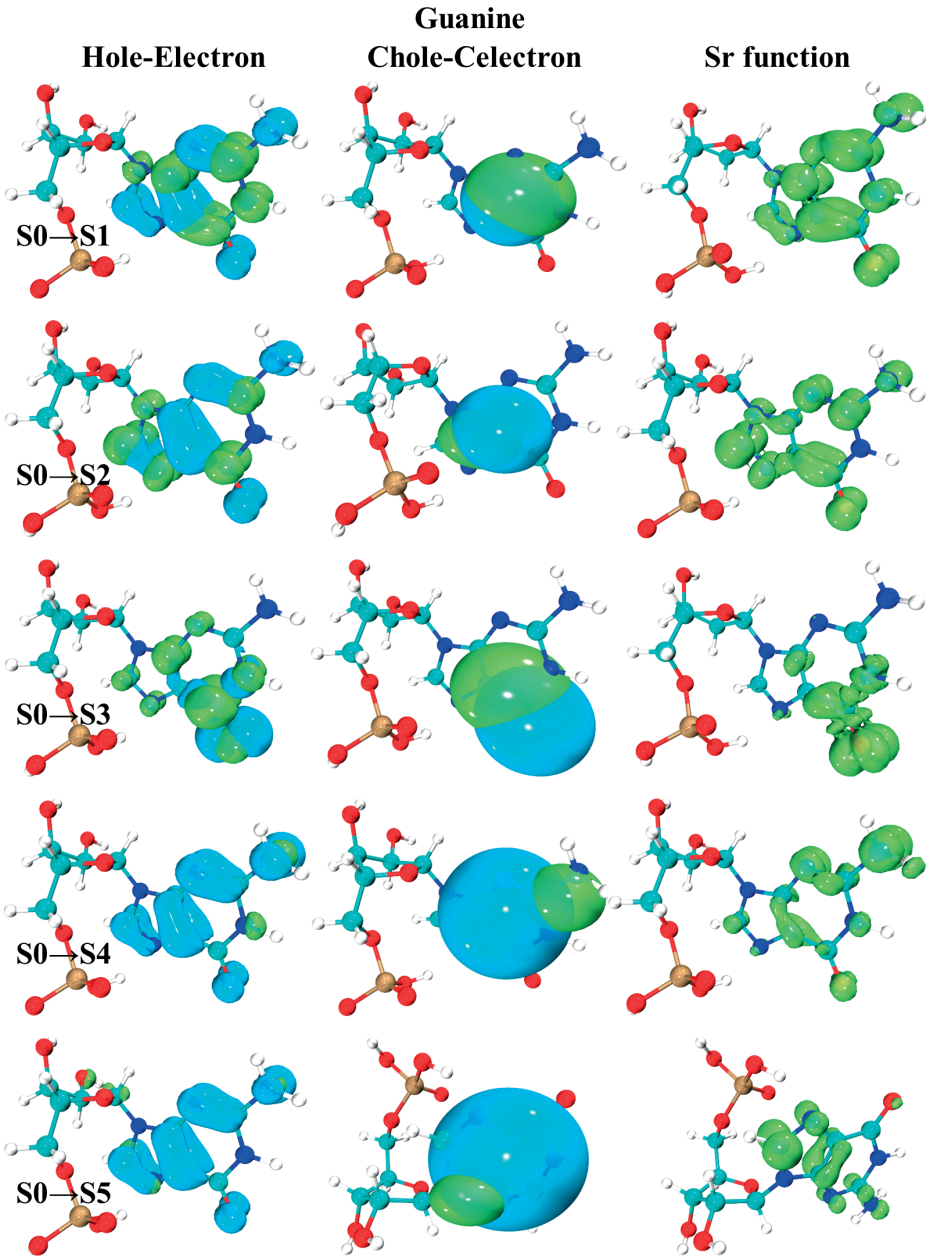


Figure 4.18: The illustration of hole-electron, Chole-Celectron, and Sr function for S1 to S5 of guanine. The isovalues for the hole and electron distributions are 0.003 au for the hole-electron, while they are set to 0.002 au for the Chole-Celectron and Sr function. The electron and hole distributions are denoted by green and blue colors, respectively.

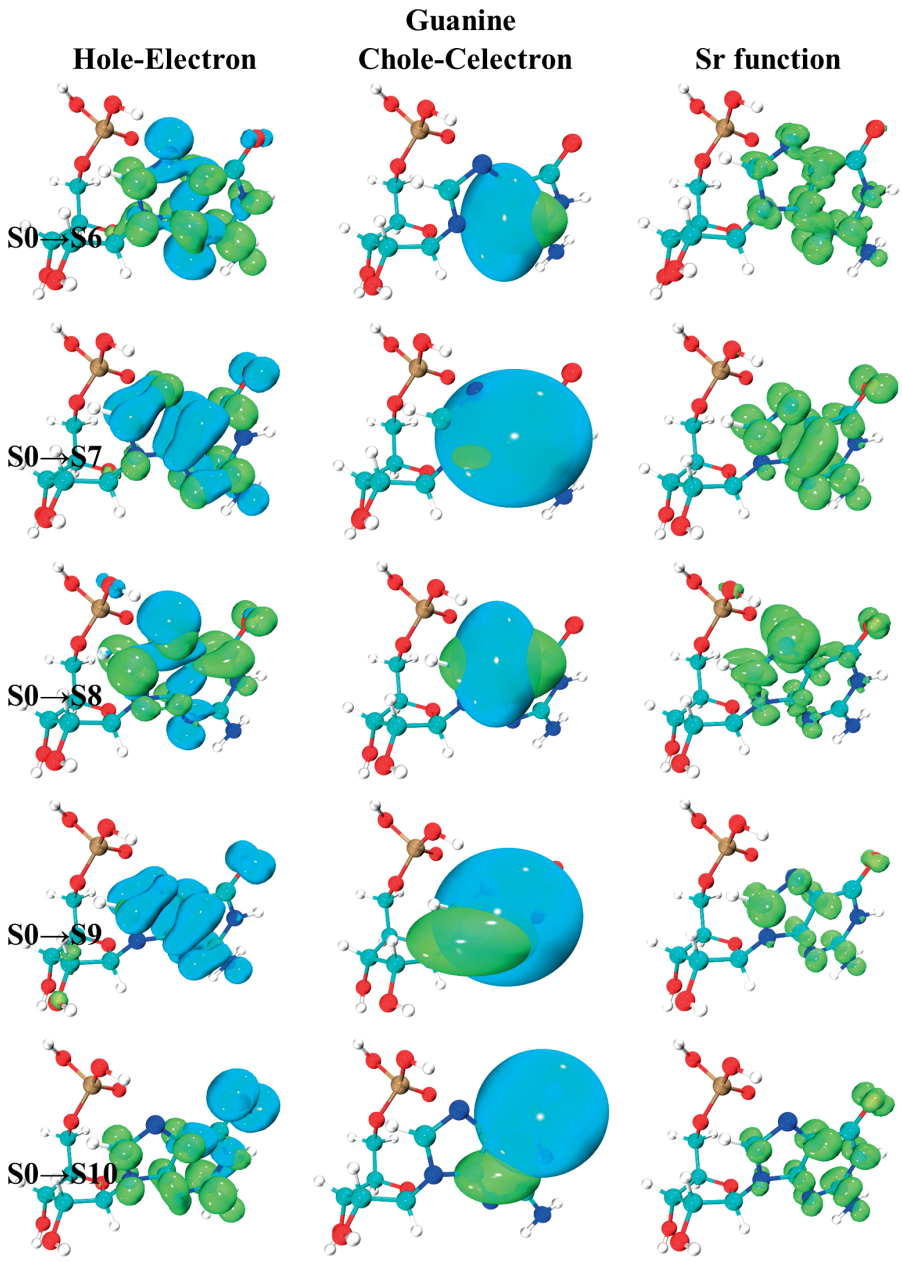


Figure 4.19: The illustration of hole-electron, Chole-Celectron, and Sr function for S6 to S10 of guanine. The isovalues for the hole and electron distributions are 0.003 au for the hole-electron, while they are set to 0.002 au for the Chole-Celectron and Sr function. The electron and hole distributions are denoted by green and blue colors, respectively.

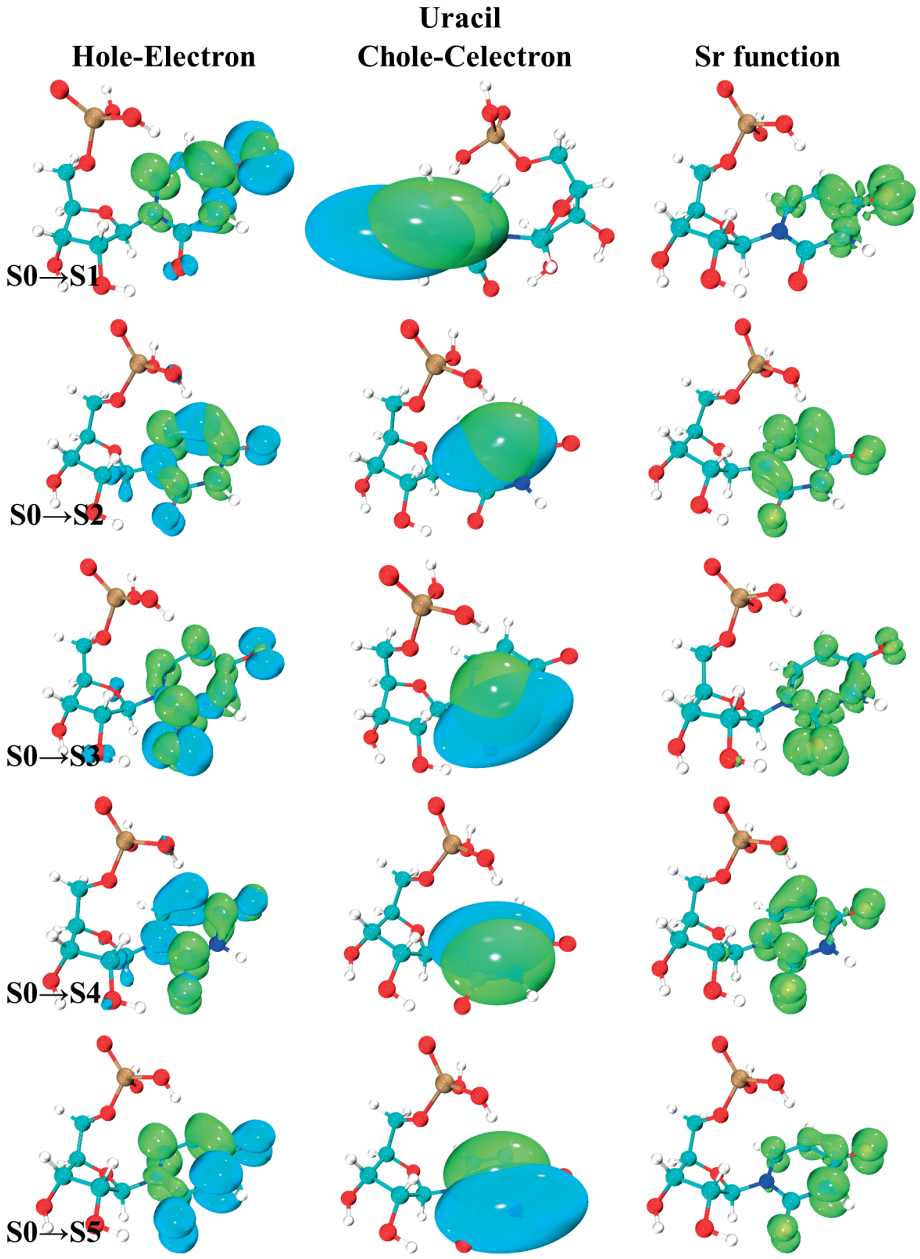


Figure 4.20: The illustration of hole-electron, Chole-Celectron, and Sr function for S1 to S5 of uracil. The isovalues for the hole and electron distributions are 0.003 au for the hole-electron, while they are set to 0.002 au for the Chole-Celectron and Sr function. The electron and hole distributions are denoted by green and blue colors, respectively.

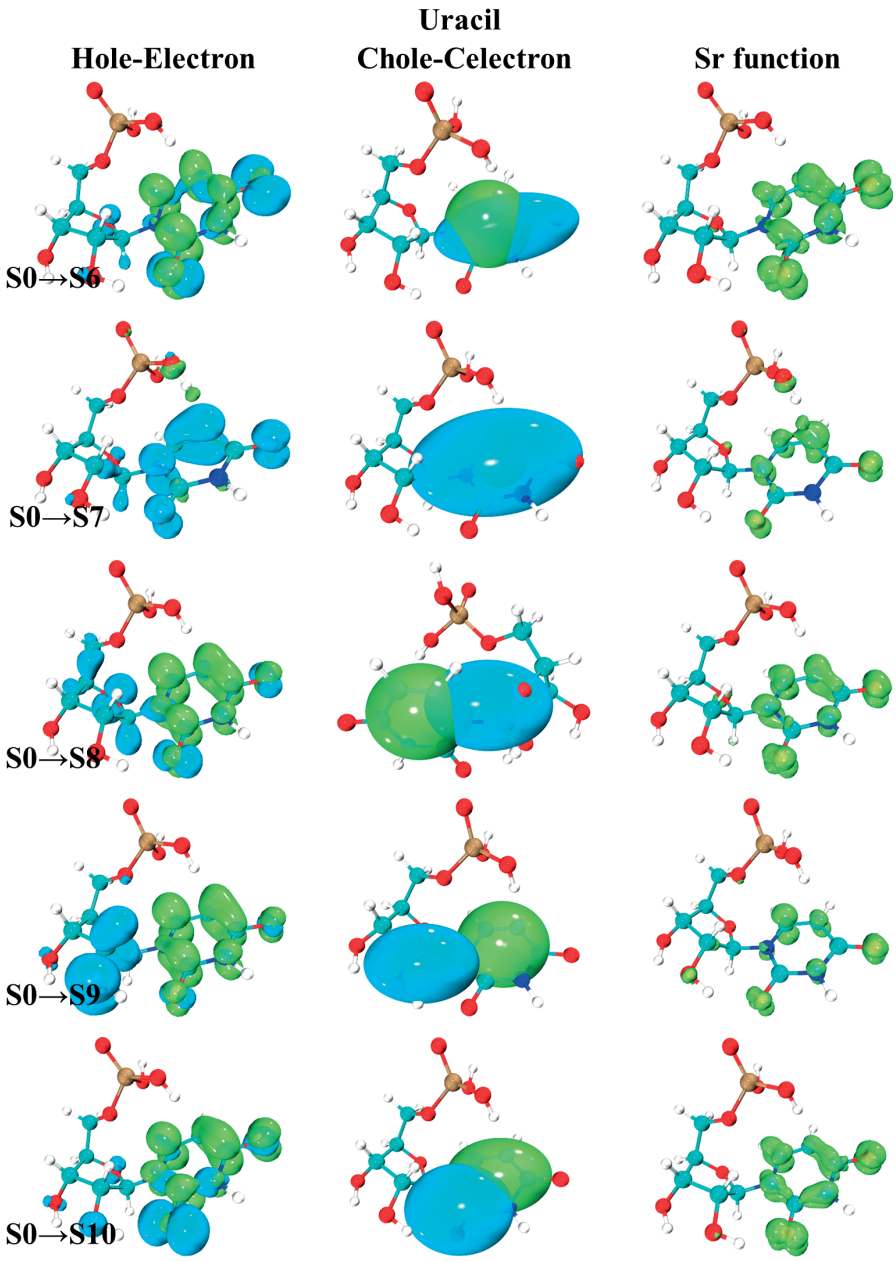


Figure 4.21: The illustration of hole-electron, Chole-Celectron, and Sr function for S6 to S10 of uracil. The isovalues for the hole and electron distributions are 0.003 au for the hole-electron, while they are set to 0.002 au for the Chole-Celectron and Sr function. The electron and hole distributions are denoted by green and blue colors, respectively.

are the principal damage to DNA [74]–[76]. For instance, 50000 pyrimidine dimers per cell are produced upon the UV dose of 4.5 J/m^2 [77].

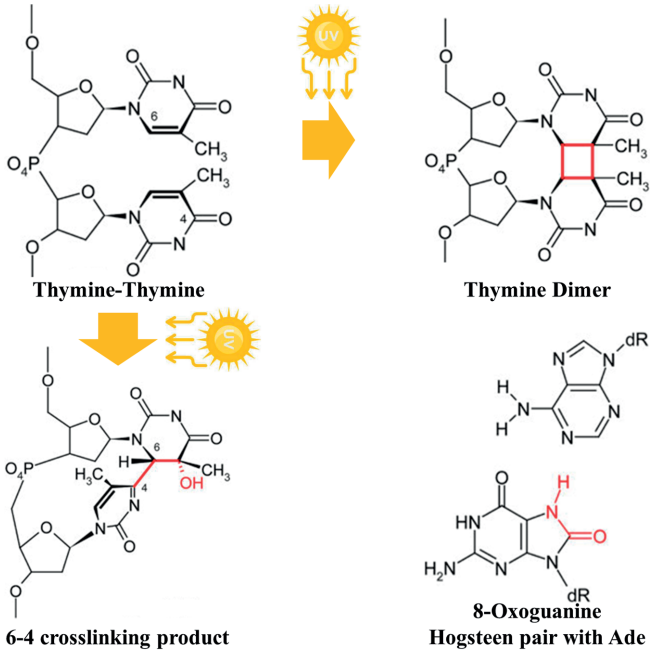


Figure 4.22: Several photochemical reaction products induced by UV light in DNA.

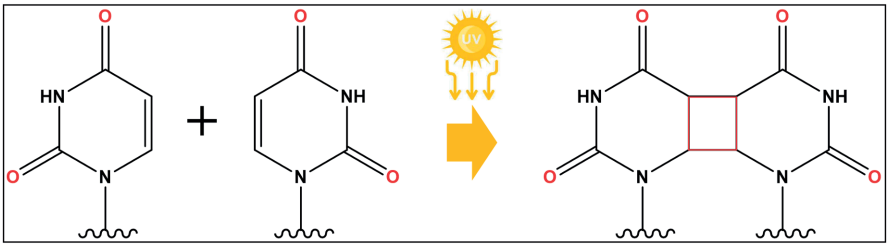


Figure 4.23: The cyclobutane dimerization product initiated by UV light in uracil bases.

Similarly, UV irradiation also induces the photochemical damage of nucleic acids in RNA, and pyrimidine photo-dimerization is the primary form of RNA photo-damage. Figure 4.23 displays the photochemical reaction of uracil dimers upon UV exposure. Photo-dimerization induced by UV damage dominantly occurs in adjacent pyrimidines (in order YY=UU, CU, UC, and UU) binding with cyclobutane-type linkages [78]. The cross-linking and photo-dimerization between uracil nucleotides are responsible for the inactivation of RNA viruses [79]. The long RT-qPCR genome analysis has clearly confirmed the presence of dimer sites in the SARS-CoV-2 genome after UVC treatment [80]. As plotted in Figure 4.24, the most UV-reactive dinucleotides are in the pyrimidine group,

such as UU, UC, CU, and CC, with the highest UV-reactivity being for UU dinucleotides, with the most extreme data even beyond the interquartile range. Additionally, non-YY sequences may not result in cyclobutane-type dimers, which may be due to transient contacts of base pairs [78]. In this study, the experimental virus is Influenza A, a single-stranded RNA virus, thus we only focus on the photochemical reaction process of uracil dimer to reveal the molecular mechanism of viral inactivation. It should be noted that the photo-dimerization process of nucleic acids mainly takes place in the base portion, not in the sugar-phosphate portion. Therefore, the sugar phosphate portion is not considered in the TS calculation of the uracil dimer.

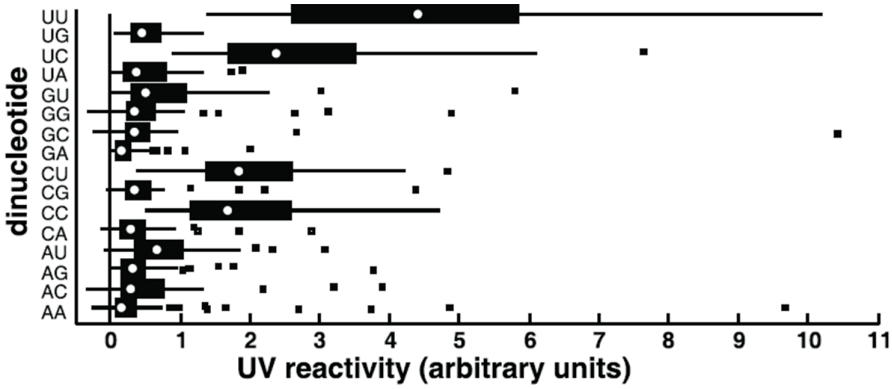


Figure 4.24: The box plot of reactivities across all dinucleotide types [78].

Utilizing the initial guess structures of the transition state of the uracil base reaction under the S0 and S1 to search the actual transition-state structures under these two states. As shown in Figure 4.25(a)-(d), it can be observed that the actual transition-state structures under the S0 and S1 are similar to their initial guess structures, which means that the initial guess structures are reasonable. The intrinsic reaction coordinate of the transition-state structures in S0 and S1 further confirms the rationality of the predicted transition-state structures. In Figure 4.25(e) and (f), it can be found that there is only one intermediate activated complex point during the photochemical reaction, which corresponds to the transition-state structure of dual-uracil with the highest total energy in the reaction process. Meanwhile, the transition state contributes to the decomposition of the activation complex, forming the cyclobutane uracil dimer. As listed in Table 4.12, we find that the C-C double bonds (C2=C4 and C14=C16) of uracil molecules are destroyed to form C-C single bonds (C2-C4 and C14-C16). Simultaneously, the unpaired electrons of C2 and C4 atoms prefer to bind to that of C14 and C16 atoms to form the cyclobutane ring of uracil dimer. Furthermore, we also observe that the length of the C2-C14 and C4-C16 bonds of the transition state in the S1 is smaller than that in the S0, and the total energy in the S1 is higher than that in the S0. Therefore, the reaction of uracil molecules in the excited state is more accessible than in the ground state. The length of C2-C4 and C14-C16 bonds in the S0 and S1 also further proves this result because the length of C2-C4 and C14-C16 bonds in the S0 is larger than that in the S1. This indicates that the binding strength of C2-C4 and C14-C16 bonds in the S0 is more robust than in the S1.

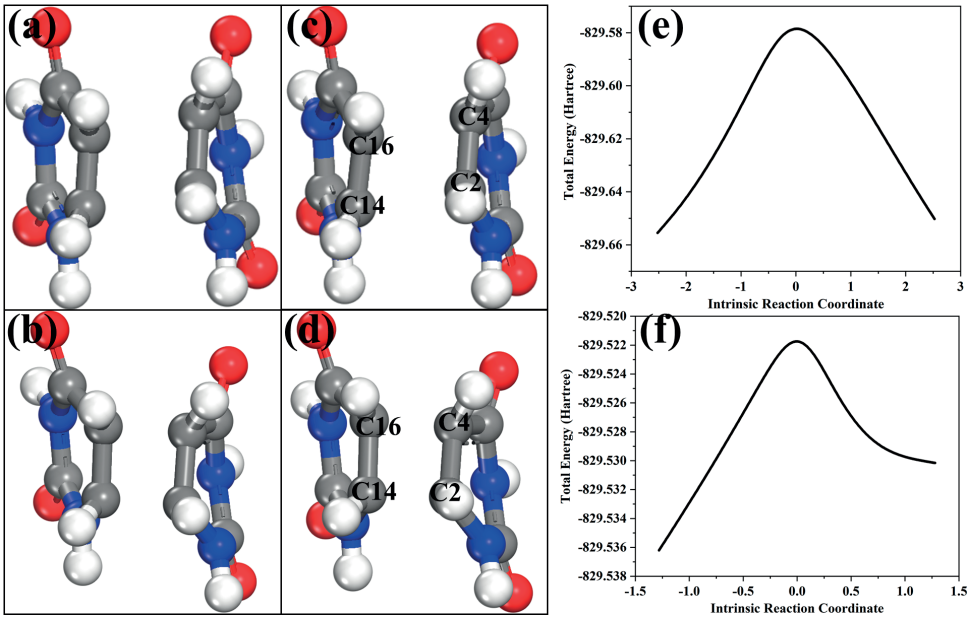


Figure 4.25: (a, b) Initial guess and (c, d) actual structures of the transition state for the uracil photochemical reaction under the ground and excited states, (e, f) along with their intrinsic reaction coordinates.

Table 4.12: Structural parameters of the transition state of uracil base reaction under the S0 and S1 states.

State	C2-C4 (Å)	C2-C14 (Å)	C4-C16 (Å)	C14-C16 (Å)	Energy (Hartree)
S0	1.462	2.145	2.116	1.398	-829.578
S1	1.529	1.687	1.726	1.502	-829.522

4.3.8. REACTION RATE CONSTANT OF DUAL URACIL MOLECULES

The reaction rate constant predicted by the transition state theory (TST) can theoretically characterize the speed of chemical reactions. Therefore, we can determine whether nucleotides are susceptible to reaction under S0 and S1 through this parameter. On the basis of the illustration of the above section, we only focus on the reaction rate constant of uracil molecules to confirm the photochemical reaction between adjacent nucleotides. Theoretically, the conventional TST rate can be expressed as

$$k_{TST}(T) = \sigma \frac{k_B}{h} \frac{Q_{TS}(T)}{\Phi_R(T)} exp[-V^{\ddagger}/k_B T] \tag{4.1}$$

where k_B, h, $V^{\ddagger}$, and T are Boltzmann's constant, Planck's constant, the classical barrier height, and the thermodynamic temperature, respectively [81]. Besides, $Q_{TS}(T)$ and $\Phi_R(T)$ are quantum mechanical transition state quasi-distribution and reactant distribution functions, respectively. According to thermodynamics theory, the TST formula

can be rewritten in an equivalent thermodynamic form

$$k_{TST}(T) = \sigma \frac{k_B}{h} (\frac{RT}{P_0})^{\triangle n} e^{-\triangle G^{0,\neq}/(k_B T)} \tag{4.2}$$

where $\triangle G^{(0,\neq)}(T)$=$G^0_{TS}(T)$-$G^0_{Reactant}(T)$ is the standard Gibbs energy of activation [82], [83], and $G^0_{TS}(T)$ does not consider the contribution of imaginary frequency. Moreover, $\triangle n$ is set as 1 for gas phase bimolecular, whereas it is zero for single molecule reaction. RT/P_0 is the reverse of molar concentration. It should be noted that δ would not be taken into account in the $k_{TST}(T)$ if the rotational symmetry is considered when calculating Gibbs' energy. The reaction path degeneracy σ can be calculated by the formula

$$\sigma = \frac{\sigma_{rot,Reactant}}{\sigma_{rot,TS}} \tag{4.3}$$

where $\delta_{(rot,Reactant)}$ and $\delta_{(rot,TS)}$ are rotational symmetry numbers of reactant and transition state, respectively. In our calculations, T, P, R, and δ are set to 298.15 K, 1 bar, 8.31 J/mol/K, and 1, respectively.

Table 4.13: Thermodynamic quantities with a thermal correction for single and dual uracil under the S0 and S1 states.

State	Thermodynamic Quantity	Single-Uracil (a.u.)	Dual-Uracil TS (a.u.)
S0	U	-414.751	-829.391
	H	-414.750	-829.391
	G	-414.788	-829.444
S1	U	-414.732	-829.488
	H	-414.731	-829.487
	G	-414.771	-829.536

In order to determine the reaction rate constant of uracil molecules under the S0 and S1, the corresponding thermodynamic quantities with thermal correction are calculated through Gibbs free energy. Table 4.13 clearly presents the thermodynamic quantities with thermal correction of uracil molecules with the S0 and S1, including internal energy (U), enthalpy (H), and Gibbs free energy (G). In particular, G is the most critical parameter for calculating the reaction rate constant. As listed in Table 4.13, for the S0, the G of single and dual uracil are -414.788 a.u. and -829.391 a.u., respectively. In contrast, they are -414.771 a.u. and -829.536 a.u. for the S1, respectively. Therefore, $\triangle G^{(0,\neq)}$ for the S0 and S1 is turned out to be 0.131 a.u. (344.651 kJ/mol) and 5.331×10^{-3} a.u. (13.997 kJ/mol), respectively. Eventually, the reaction rate constant of uracil molecules under the S0 is $6.419\times10^{-49} s^{-1}\cdot M^{-1}$, while that is $5.436\times10^{11} s^{-1}\cdot M^{-1}$ for the S1 [84]. For the chemical reaction at room temperature, k_{TST}=$3.33\times10^{-3} s^{-1}\cdot M^{-1}$ has been a criterion for determining the ease between molecules, derived from $t_{1/2} = 1/(k[A]_0)$. This half-life formula assumes $t_{1/2}$ and $[A]_0$ as five minutes and 1 M, respectively. When the reaction rate constant is larger than $3.33\times10^{-3} s^{-1}\cdot M^{-1}$, the reaction between molecules prefers to be easier and faster. Unsurprisingly, the reaction rate constant of uracil molecules under the S1 is much larger than $3.33\times10^{-3} s^{-1}\cdot M^{-1}$, which indicates that uracil molecules

are reacted easily to product uracil-uracil dimers under the excited states. By contrast, it is extremely difficult to react under the ground state due to the very low reaction rate constant. The calculated half-life further demonstrates this result. Depending on the half-life formula, the half-life of uracil under the S0 is 1.56×10^{48} s, which suggests the molecular reaction could barely occur. However, the half-life under the S1 is calculated to be 1.84×10^{-12} s (i.e., 1.84 ps), thus the transition of uracil molecules under the S1 is a transient reaction [85]. As a result, we can get a conclusion that photochemical reactions occur between nucleotides under UV light conditions. Besides, nucleotides' absorption of photon energies changes their molecular structures from the ground state to the excited state, lowering the reaction barrier and thus allowing the molecular reactions to occur more readily.

4.4. CONCLUSIONS

In summary, we systematically investigate the optimal wavelength recipe for inactivating Influenza A PR8 at the experimental level. At the same time, by means of the quantum chemical method, the underlying inactivation mechanism of UVC irradiation at the molecular level is theoretically revealed. Four primary nucleotides, forming the genetic materials of viruses, are chosen as the main studied objects. The inactivation result displays that 259 nm exhibits the best inactivation affection because of the largest logarithm reduction. Moreover, the dual-wavelength scheme does not have obvious advantage over the single-wavelength scheme. According to the calculated absorption spectrums, it is found that the strongest absorption peak is at 248.7 nm, 226.1 nm (second peak: 252.7 nm), 248.3 nm, and 205.8 nm (second peak: 249.2 nm) for adenine, cytosine, guanine, and uracil nucleotides, respectively. This is basically consistent with the measured data in the experiment. Besides, introducing an aqueous solution enhances the absorption spectrums of four nucleotides. A red- or blue-shifted behavior can also occur. Eventually, depending on the calculation of the transition state and reaction rate constant, we find that the molecular reaction for adjacent nucleotides is a photochemical process under UVC light. The reaction rate constants at the ground state are $6.419\times10^{-49}s^{-1}\cdot M^{-1}$, whereas, for the excited state, it is $5.436\times10^{11}s^{-1}\cdot M^{-1}$. Their corresponding half-life is 1.56×10^{48} and 1.84×10^{-12} s, respectively. Therefore, the reaction under UVC irradiation easily occurs; the opposite is tough.

REFERENCES

[1] J. M. Hughes, "Sars: An emerging global microbial threat.", *Transactions of the American Clinical and Climatological Association*, vol. 115, p. 361, 2004.

[2] C. T. Bauch and T. Oraby, "Assessing the pandemic potential of mers-cov", *The Lancet*, vol. 382, no. 9893, pp. 662–664, 2013.

[3] D. Malvy, A. K. McElroy, H. de Clerck, S. Günther, and J. van Griensven, "Ebola virus disease", *The Lancet*, vol. 393, no. 10174, pp. 936–948, 2019.

[4] G. Neumann, T. Noda, and Y. Kawaoka, "Emergence and pandemic potential of swine-origin h1n1 influenza virus", *Nature*, vol. 459, no. 7249, pp. 931–939, 2009.

[5] S. F. Pedersen, Y.-C. Ho, *et al.*, "Sars-cov-2: A storm is raging", *The Journal of clinical investigation*, vol. 130, no. 5, pp. 2202–2205, 2020.

[6] H. Štorkánová, S. Oreská, M. Špiritović, *et al.*, "Plasma hsp90 levels in patients with systemic sclerosis and relation to lung and skin involvement: A cross-sectional and longitudinal study", *Scientific Reports*, vol. 11, no. 1, p. 1, 2021.

[7] I. Zucker, Y. Lester, J. Alter, *et al.*, "Pseudoviruses for the assessment of coronavirus disinfection by ozone", *Environmental chemistry letters*, vol. 19, pp. 1779–1785, 2021.

[8] T. Pottage, C Richardson, S. Parks, J. Walker, and A. Bennett, "Evaluation of hydrogen peroxide gaseous disinfection systems to decontaminate viruses", *Journal of Hospital Infection*, vol. 74, no. 1, pp. 55–61, 2010.

[9] C. S. Heilingloh, U. W. Aufderhorst, L. Schipper, *et al.*, "Susceptibility of sars-cov-2 to uv irradiation", *American journal of infection control*, vol. 48, no. 10, pp. 1273–1275, 2020.

[10] N. Hatanaka, M. Yasugi, T. Sato, M. Mukamoto, and S. Yamasaki, "Hypochlorous acid solution is a potent antiviral agent against sars-cov-2", *Journal of Applied Microbiology*, vol. 132, no. 2, pp. 1496–1502, 2022.

[11] A. Sakudo, Y. Yagyu, and T. Onodera, "Disinfection and sterilization using plasma technology: Fundamentals and future perspectives for biological applications", *International journal of molecular sciences*, vol. 20, no. 20, p. 5216, 2019.

[12] T. Furukawa, T. Ueno, M. Matsumura, M. Amarasiri, and K. Sei, "Inactivation of antibiotic resistant bacteria and their resistance genes in sewage by applying pulsed electric fields", *Journal of Hazardous Materials*, vol. 424, p. 127 382, 2022.

[13] J. Hadi, M. Dunowska, S. Wu, and G. Brightwell, "Control measures for sars-cov-2: A review on light-based inactivation of single-stranded rna viruses", *Pathogens*, vol. 9, no. 9, p. 737, 2020.

[14] M. M. Delorme, J. T. Guimarães, N. M. Coutinho, *et al.*, "Ultraviolet radiation: An interesting technology to preserve quality and safety of milk and dairy foods", *Trends in food science & technology*, vol. 102, pp. 146–154, 2020.

[15] P. M. F. Maciel, N. d. M. N. Fava, A. W. Lamon, P. Fernandez-Ibañez, J. A. Byrne, and L. P. Sabogal-Paz, "Household water purification system comprising cartridge filtration, uvc disinfection and chlorination to treat turbid raw water", *Journal of Water Process Engineering*, vol. 43, p. 102 203, 2021.

[16] S. Li, R. Zhang, D. Lei, *et al.*, "Impact of ultrasound, microwaves and high-pressure processing on food components and their interactions", *Trends in Food Science & Technology*, vol. 109, pp. 1–15, 2021.

[17] S. K. Bhardwaj, H. Singh, A. Deep, *et al.*, "Uvc-based photoinactivation as an efficient tool to control the transmission of coronaviruses", *Science of The Total Environment*, vol. 792, p. 148 548, 2021.

[18] F. P. Sellera, C. P. Sabino, F. V. Cabral, and M. S. Ribeiro, "A systematic scoping review of ultraviolet c (uvc) light systems for sars-cov-2 inactivation", *Journal of Photochemistry and Photobiology*, vol. 8, p. 100 068, 2021.

[19] A. Rakita, N. Nikolić, M. Mildner, J. Matiasek, and A. Elbe-Bürger, "Re-epithelialization and immune cell behaviour in an ex vivo human skin model", *Scientific Reports*, vol. 10, no. 1, p. 1, 2020.

[20] K. Narita, K. Asano, Y. Morimoto, T. Igarashi, and A. Nakane, "Chronic irradiation with 222-nm uvc light induces neither dna damage nor epidermal lesions in mouse skin, even at high doses", *PloS one*, vol. 13, no. 7, e0201259, 2018.

[21] B. M. Tande, T. A. Pringle, W. A. Rutala, M. F. Gergen, and D. J. Weber, "Understanding the effect of ultraviolet light intensity on disinfection performance through the use of ultraviolet measurements and simulation", *Infection Control & Hospital Epidemiology*, vol. 39, no. 9, pp. 1122–1124, 2018.

[22] S Ali, S Yui, M Muzslay, and A. Wilson, "Comparison of two whole-room ultraviolet irradiation systems for enhanced disinfection of contaminated hospital patient rooms", *Journal of Hospital Infection*, vol. 97, no. 2, pp. 180–184, 2017.

[23] K. Song, F. Taghipour, and M. Mohseni, "Microorganisms inactivation by wavelength combinations of ultraviolet light-emitting diodes (uv-leds)", *Science of the Total Environment*, vol. 665, pp. 1103–1110, 2019.

[24] K. Oguma, K. Kanazawa, I. Kasuga, and S. Takizawa, "Effects of uv irradiation by light emitting diodes on heterotrophic bacteria in tap water", *Photochemistry and photobiology*, vol. 94, no. 3, pp. 570–576, 2018.

[25] M. Heßling, K. Hönes, P. Vatter, and C. Lingenfelder, "Ultraviolet irradiation doses for coronavirus inactivation–review and analysis of coronavirus photoinactivation studies", *GMS hygiene and infection control*, vol. 15, 2020.

[26] S.-J. Kim, D.-K. Kim, and D.-H. Kang, "Using uvc light-emitting diodes at wavelengths of 266 to 279 nanometers to inactivate foodborne pathogens and pasteurize sliced cheese", *Applied and environmental microbiology*, vol. 82, no. 1, pp. 11–17, 2016.

[27] K. Narita, K. Asano, K. Naito, *et al.*, "Ultraviolet c light with wavelength of 222 nm inactivates a wide spectrum of microbial pathogens", *Journal of Hospital Infection*, vol. 105, no. 3, pp. 459–467, 2020.

[28] K. Narita, K. Asano, Y. Morimoto, *et al.*, "Disinfection and healing effects of 222-nm uvc light on methicillin-resistant staphylococcus aureus infection in mouse wounds", *Journal of Photochemistry and Photobiology B: Biology*, vol. 178, pp. 10–18, 2018.

[29] M. B. Lore, B. K. Heimbuch, T. L. Brown, J. D. Wander, and S. H. Hinrichs, "Effectiveness of three decontamination treatments against influenza virus applied to filtering facepiece respirators", *Annals of occupational hygiene*, vol. 56, no. 1, pp. 92–101, 2012.

[30] S Pi, L. Seng-Libi, and D. Xao-Ping, "Stability of sars coronavirus in human specimens and environment and its sensitivity to heating and uv irradiation", *Biomed. Environ. Sci*, vol. 16, pp. 246–255, 2003.

[31] H. Inagaki, A. Saito, H. Sugiyama, T. Okabayashi, and S. Fujimoto, "Rapid inactivation of sars-cov-2 with deep-uv led irradiation", *Emerging Microbes & Infections*, vol. 9, no. 1, pp. 1744–1747, 2020.

[32] F. Bosshard, F. Armand, R. Hamelin, and T. Kohn, "Mechanisms of human adenovirus inactivation by sunlight and uvc light as examined by quantitative pcr and quantitative proteomics", *Applied and environmental microbiology*, vol. 79, no. 4, pp. 1325–1332, 2013.

[33] R. Nishisaka-Nonaka, K. Mawatari, T. Yamamoto, *et al.*, "Irradiation by ultraviolet light-emitting diodes inactivates influenza a viruses by inhibiting replication and transcription of viral rna in host cells", *Journal of Photochemistry and Photobiology B: Biology*, vol. 189, pp. 193–200, 2018.

[34] E. Araud, M. Fuzawa, J. L. Shisler, J. Li, and T. H. Nguyen, "Uv inactivation of rotavirus and tulane virus targets different components of the virions", *Applied and environmental microbiology*, vol. 86, no. 4, e02436–19, 2020.

[35] T. Tanaka, O. Nogariya, N. Shionoiri, Y. Maeda, and A. Arakaki, "Integrated molecular analysis of the inactivation of a non-enveloped virus, feline calicivirus, by uv-c radiation", *Journal of bioscience and bioengineering*, vol. 126, no. 1, pp. 63–68, 2018.

[36] D. Sano, R. M. Pinto, T. Omura, and A. Bosch, "Detection of oxidative damages on viral capsid protein for evaluating structural integrity and infectivity of human norovirus", *Environmental science & technology*, vol. 44, no. 2, pp. 808–812, 2010.

[37] K. Rule Wigginton, L. Menin, J. P. Montoya, and T. Kohn, "Oxidation of virus proteins during uv254 and singlet oxygen mediated inactivation", *Environmental science & technology*, vol. 44, no. 14, pp. 5437–5443, 2010.

[38] D. Park, H. M. Shahbaz, S.-H. Kim, *et al.*, "Inactivation efficiency and mechanism of uv-tio2 photocatalysis against murine norovirus using a solidified agar matrix", *International journal of food microbiology*, vol. 238, pp. 256–264, 2016.

[39] K. Wetz and K.-O. Habermehl, "Specific cross-linking of capsid proteins to virus rna by ultraviolet irradiation of poliovirus", *Journal of General Virology*, vol. 59, no. 2, pp. 397–401, 1982.

[40] Y. Nakaya, T. Fukuda, H. Ashiba, M. Yasuura, and M. Fujimaki, "Quick assessment of influenza a virus infectivity with a long-range reverse-transcription quantitative polymerase chain reaction assay", *BMC Infectious Diseases*, vol. 20, pp. 1–10, 2020.

[41] G. K. Madsen, "Functional form of the generalized gradient approximation for exchange: The pbe α functional", *Physical Review B*, vol. 75, no. 19, p. 195 108, 2007.

[42] N. Van Doremalen, T. Bushmaker, D. H. Morris, *et al.*, "Aerosol and surface stability of sars-cov-2 as compared with sars-cov-1", *New England journal of medicine*, vol. 382, no. 16, pp. 1564–1567, 2020.

[43] J. Bu, D.-D. Peng, H. Xiao, *et al.*, "Analysis of meteorological conditions and prediction of epidemic trend of 2019-ncov infection in 2020", *MedRxiv*, 2020.

[44] A. W. Chin, J. T. Chu, M. R. Perera, *et al.*, "Stability of sars-cov-2 in different environmental conditions", *The Lancet Microbe*, vol. 1, no. 1, e10, 2020.

[45] D Singh, K Joshi, A Samuel, J Patra, and N Mahindroo, "Alcohol-based hand sanitisers as first line of defence against sars-cov-2: A review of biology, chemistry and formulations", *Epidemiology & Infection*, vol. 148, 2020.

[46] V. Peuckert, "A new approximation method for electron systems", *Journal of Physics C: Solid State Physics*, vol. 11, no. 24, p. 4945, 1978.

[47] M. Cossi, V. Barone, R. Cammi, and J. Tomasi, "Ab initio study of solvated molecules: A new implementation of the polarizable continuum model", *Chemical Physics Letters*, vol. 255, no. 4-6, pp. 327–335, 1996.

[48] H. Eyring, "The activated complex and the absolute rate of chemical reactions.", *Chemical Reviews*, vol. 17, no. 1, pp. 65–77, 1935.

[49] J.-D. Chai and M. Head-Gordon, "Long-range corrected hybrid density functionals with damped atom–atom dispersion corrections", *Physical Chemistry Chemical Physics*, vol. 10, no. 44, pp. 6615–6620, 2008.

[50] J.-D. Chai and M. Head-Gordon, "Systematic optimization of long-range corrected hybrid density functionals", *The Journal of chemical physics*, vol. 128, no. 8, p. 084 106, 2008.

[51] R. D. Tosso, M. N. C. Zarycz, A. Schiel, *et al.*, "Evaluating the conformational space of the active site of d2 dopamine receptor. scope and limitations of the standard docking methods", *Journal of Computational Chemistry*, vol. 43, no. 19, pp. 1298–1312, 2022.

[52] X. Zou, X. Dai, K. Liu, H. Zhao, D. Song, and H. Su, "Photophysical and photochemical properties of 4-thiouracil: Time-resolved ir spectroscopy and dft studies", *The Journal of Physical Chemistry B*, vol. 118, no. 22, pp. 5864–5872, 2014.

[53] G. Scalmani and M. J. Frisch, "Continuous surface charge polarizable continuum models of solvation. i. general formalism", *The Journal of chemical physics*, vol. 132, no. 11, p. 114 110, 2010.

[54] T. Lu and F. Chen, "Multiwfn: A multifunctional wavefunction analyzer", *Journal of computational chemistry*, vol. 33, no. 5, pp. 580–592, 2012.

[55] W. Humphrey, A. Dalke, and K. Schulten, "Vmd: Visual molecular dynamics", *Journal of molecular graphics*, vol. 14, no. 1, pp. 33–38, 1996.

[56] T. Lu and Q. Chen, "Shermo: A general code for calculating molecular thermochemistry properties", *Computational and Theoretical Chemistry*, vol. 1200, p. 113 249, 2021.

[57] B Ishak, "Spectra of atoms and molecules , by peter f. bernath", *Contemporary Physics*, vol. 58, no. 2, pp. 201–202, 2017.

[58] G. D. Harris, V. D. Adams, D. L. Sorensen, and M. S. Curtis, "Ultraviolet inactivation of selected bacteria and viruses with photoreactivation of the bacteria", *Water Research*, vol. 21, no. 6, pp. 687–692, 1987.

[59] T. D. Cutler and J. J. Zimmerman, "Ultraviolet irradiation and the mechanisms underlying its inactivation of infectious agents", *Animal Health Research Reviews*, vol. 12, no. 1, pp. 15–23, 2011.

[60] D. Battigelli, M. Sobsey, and D. Lobe, "The inactivation of hepatitis a virus and other model viruses by uv irradiation", *Water Science and Technology*, vol. 27, no. 3-4, pp. 339–342, 1993.

[61] R. B. Setlow, "Cyclobutane-type pyrimidine dimers in polynucleotides: Ultraviolet radiation forms dimers that have distinctive properties and affect biological systems.", *Science*, vol. 153, no. 3734, pp. 379–386, 1966.

[62] P. K. Samanta, A. K. Manna, and S. K. Pati, "Thieno analogues of rna nucleosides: A detailed theoretical study", *The Journal of Physical Chemistry B*, vol. 116, no. 26, pp. 7618–7626, 2012.

[63] X. Wang, Z. Liu, X. Yan, *et al.*, "Photophysical properties and optical nonlinearity of cyclo [18] carbon (c 18) precursors, c 18–(co) n (n= 2, 4, and 6): Focusing on the effect of the carbonyl groups", *Physical Chemistry Chemical Physics*, vol. 24, no. 12, pp. 7466–7473, 2022.

[64] S. Chen, N. Ullah, and R. Zhang, "Exciton self-trapping in sp2 carbon nanostructures induced by edge ether groups", *The Journal of Physical Chemistry Letters*, vol. 9, no. 17, pp. 4857–4864, 2018.

[65] X. Tang, L.-S. Cui, H.-C. Li, *et al.*, "Highly efficient luminescence from space-confined charge-transfer emitters", *Nature Materials*, vol. 19, no. 12, pp. 1332–1338, 2020.

[66] Y. Jiao, J. Zhu, Y. Guo, W. He, and Z. Guo, "Synergetic effect between spin crossover and luminescence in the [fe (bpp) 2][bf4] 2 (bpp= 2, 6-bis (pyrazol-1-yl) pyridine) complex", *Journal of Materials Chemistry C*, vol. 5, no. 21, pp. 5214–5222, 2017.

[67] R. E. Rycyna and J. L. Alderfer, "Ultraviolet irradiation of nucleic acids: Formation, purification, and solution conformational analyses of the cis-syn and trans-syn photodimers of upu", *Biochemistry*, vol. 27, no. 9, pp. 3142–3151, 1988.

[68] R. Beukers, A. P. Eker, and P. H. Lohman, "50 years thymine dimer", *dna repair*, vol. 7, no. 3, pp. 530–543, 2008.

[69] J. Cadet, E. Sage, and T. Douki, "Ultraviolet radiation-mediated damage to cellular dna", *Mutation Research/Fundamental and Molecular Mechanisms of Mutagenesis*, vol. 571, no. 1-2, pp. 3–17, 2005.

[70] S. Mouret, C. Baudouin, M. Charveron, A. Favier, J. Cadet, and T. Douki, "Cyclobutane pyrimidine dimers are predominant dna lesions in whole human skin exposed to uva radiation", *Proceedings of the National Academy of Sciences*, vol. 103, no. 37, pp. 13 765–13 770, 2006.

[71] P. H. Clingen, C. F. Arlett, L. Roza, T. Mori, O. Nikaido, and M. H. Green, "Induction of cyclobutane pyrimidine dimers, pyrimidine (6-4) pyrimidone photoproducts, and dewar valence isomers by natural sunlight in normal human mononuclear cells", *Cancer research*, vol. 55, no. 11, pp. 2245–2248, 1995.

[72] J. Cadet, J.-L. Ravanat, G. R. Martinez, M. H. Medeiros, and P. D. Mascio, "Singlet oxygen oxidation of isolated and cellular dna: Product formation and mechanistic insights", *Photochemistry and photobiology*, vol. 82, no. 5, pp. 1219–1225, 2006.

[73] J. Cadet, T. Douki, J.-L. Ravanat, and P. Di Mascio, "Sensitized formation of oxidatively generated damage to cellular dna by uva radiation", *Photochemical & Photobiological Sciences*, vol. 8, no. 7, pp. 903–911, 2009.

[74] A. Kuzminov, "Pyrimidine dimers", in *Brenner's Encyclopedia of Genetics: Second Edition*, Elsevier Inc., 2013, pp. 538–539.

[75] M Protić-Sabljić, N Tuteja, P. Munson, J Hauser, K. Kraemer, and K. Dixon, "Uv light-induced cyclobutane pyrimidine dimers are mutagenic in mammalian cells", *Molecular and cellular biology*, vol. 6, no. 10, pp. 3349–3356, 1986.

[76] R. Tyrrell, "Induction of pyrimidine dimers in bacterial dna by 365 nm radiation.", Argonne National Lab., IL, Tech. Rep., 1973.

[77] R. Rothman and R. Setlow, "An action spectrum for cell killing and pyrimidine dimer formation in chinese hamster v-79 cells", *Photochemistry and Photobiology*, vol. 29, no. 1, pp. 57–61, 1979.

[78] W. Kladwang, J. Hum, and R. Das, "Ultraviolet shadowing of rna can cause significant chemical damage in seconds", *Scientific reports*, vol. 2, no. 1, pp. 1–7, 2012.

[79] R. L. Miller and P. G. Plagemann, "Effect of ultraviolet light on mengovirus: Formation of uracil dimers, instability and degradation of capsid, and covalent linkage of protein to viral rna", *Journal of virology*, vol. 13, no. 3, pp. 729–739, 1974.

[80] C.-W. Lo, R. Matsuura, K. Iimura, *et al.*, "Uvc disinfects sars-cov-2 by induction of viral genome damage without apparent effects on viral morphology and proteins", *Scientific reports*, vol. 11, no. 1, p. 13 804, 2021.

[81] A. Fernández-Ramos, B. A. Ellingson, R. Meana-Pañeda, J. Marques, and D. G. Truhlar, "Symmetry numbers and chemical reaction rates", *Theoretical Chemistry Accounts*, vol. 118, no. 4, pp. 813–826, 2007.

[82] A. Fernandez-Ramos, B. A. Ellingson, B. C. Garrett, and D. G. Truhlar, "Variational transition state theory with multidimensional tunneling", *Reviews in computational chemistry*, vol. 23, p. 125, 2007.

[83] P. Ptáček, F. Šoukal, and T. Opravil, "Introduction to the transition state theory", *Introducing the Effective Mass of Activated Complex and the Discussion on the Wave Function of this Instanton*, vol. 27, 2018.

[84] T. Lu, "Tstcalculator", *http://sobereva.com/310 (accessed 08, 21, 2021)*,

[85] T. Lu, "Bi-molecular reactions", *http://sobereva.com/506 (accessed 08, 21, 2021)*,

5

INACTIVATION OF PATHOGENS USING ELECTRIC FIELDS ON A MICROCHIP PLATFORM: AN EXPERIMENTAL AND COMPUTATIONAL STUDY

Electric field treatment is the most common means of non-thermal technologies in food processing. Microelectrodes on microchips might open the door to an integrated system for concentrating, sampling, and inactivating viruses. In this study, three microelectrodes are designed and fabricated, and their ability to inactivate viruses is explored. Among these microelectrodes, the out-of-phase castellated structure shows the best inactivation ability due to its highest titer reduction. An AC voltage with a high frequency reduces the titer more than a low-frequency AC or a DC voltage. Moreover, the reduction in viral titer depends strongly on the medium and virus concentration of the samples. Attractive forces are at play during an electric field treatment. The results in E. coli suggest that the inactivation effectiveness is strongly dependent on AC voltage and AC frequency. The morphological analysis of E. coli demonstrates that the disruption of the lipid envelope caused by electric fields is one of the major causes of pathogen death. In order to reveal the effect of electric fields on viruses, the dynamics of the bilayer membrane are investigated by adopting the MD method. The structural information demonstrates that electric fields less than the threshold field (250 mV/nm) do not lead to the disruption of the bilayer structure even after 200 ns, but when 250 mV/nm is reached, the bilayer collapses instantaneously. Those findings not only confirm the feasibility of microelectrode inactivation against viruses but also provide a molecular-level perspective for uncovering the effect of electric fields on the bilayer membrane of virions.

5.1. INTRODUCTION

OVER the past few decades, several pathogens including Ebola [1], influenza viruses [2], and human CoVs [3]–[5], have hugely impacted public health and the economic outlook worldwide. The emergence of these viruses also continuously brings the available viral inactivation approaches into the spotlight. For sterilization, a number of disinfection methods, e.g., chemical [6], optical [7], thermal [8], and electrical approaches [9], have been explored to inactivate lethal pathogens from contaminated surfaces or in confined spaces. As a non-thermal technology, electric-field treatment has been widely used to inactivate microorganisms and enzymes in food processing because of its virucidal feature, even at low temperatures [10]–[12]. Field strengths <100 V/cm belong to low-intensity electric fields, whereas 0.1-1 kV/cm are moderate, and >5 kV/cm are high-intensity electric fields [13]. The available scientific literature shows that field strengths of 20-50 kV/cm are required for effective microbial inactivation in food processing [14]. However, it has been reported that the critical electric field for inactivating Ent. faecal is 18 kV/cm, and bacteria E. coli is 1 kV/cm [15]. A previous study suggests that cell membranes are slightly broken down at a critical field of 150-200 V/cm, while 400-800 V/cm fields lead to significant membrane breakdown [16]. Besides, another study confirms that a breakdown phenomenon in the plasma membrane occurs at a field of >67 V/cm, while the tonoplast membrane requires one >133 V/cm [13]. These studies intensely highlight the feasibility of electric-field treatment in disinfection, and for bacteria and single-celled organisms in particular. Nevertheless, the mechanism of action of high electric fields on microorganisms is still debatable. It is commonly understood that the mechanism of high electric-field inactivation on microorganisms causes irreversible biomembrane damage rather than electrolysis or increased temperatures [17], [18]. This damage induces the loss of crucial membrane functions, thus leading to the death of the microorganisms. To uncover the inactivation mechanism of electric-field treatment, considerable efforts have led to substantial achievements [13], [16], [19]–[21]. Three possible mechanisms have been reported to be responsible for electric-field treatment against microorganisms, namely transmembrane potential effect, electric breakdown, and molecular reorientation [20], [21].

Transmembrane potential effect. A cell membrane can be modeled as a capacitor filled with a dielectric which dielectric constant is low relative to the intracellular and surrounding materials [20]. The cell membrane is a major target of high pulsed electric fields in microorganisms. The transmembrane potential of the cell membrane reaches 170 mV within around 10-20 ns when microorganisms are exposed to pulsed electric fields. Macromolecules in microorganisms suffer from strong electric fields, resulting in irreversible conformational changes, which lead to changes in their functions. As shown in Figure 5.1, micro-pores are formed in the cell membrane in the presence of low pulsed electric-fields, which are reversible and can repair themselves. However, the destruction of cell membranes is irreversible at high pulsed electric fields. This irreversible breakdown causes the loss of membrane functions. The transmembrane potential along the electric-field direction caused by a pulsed electric-field can be described by:

$$V_d = 1.5 r E \cos\theta \tag{5.1}$$

where V_d, r, E, and θ are the transmembrane potential, the cell radius, the electric field

strength, and the angle between cell position and electric-field direction, respectively.

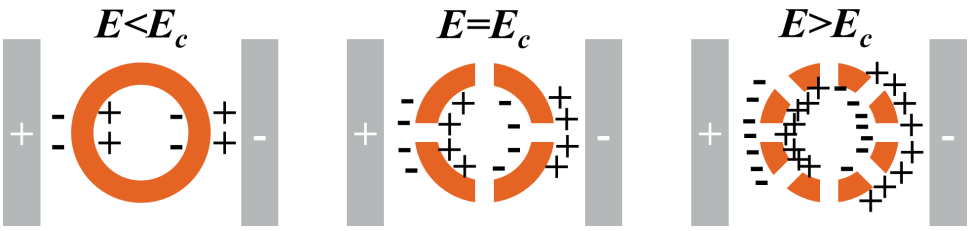


Figure 5.1: Electroporation of the cell membrane following pulsed electric-fields treatment. E and E_c are the applied and critical electric-field strengths, respectively.

Electrical breakdown. As microorganisms are exposed to an external electric field, the transmembrane potential increases due to the accumulation of additional free-charges on the inner and outer surfaces of their cell membrane. These charges are of opposite polarity and attract each other, resulting in compression of the membrane and a reduction in its thickness. On the other hand, the viscoelastic force in turn hinders the compression of the cell membrane. However, the electrical compression force is larger than the viscoelastic force of the cell membrane when the transmembrane potential is up to 1.0 V, as presented in Figure 5.2. The number and size of the pores in the cell membrane depend on the electric-field strength and treatment time. The critical electric-field is defined as that field strength at which the destruction of the cell membrane occurs. When the field strength is close to the critical value or the treatment time becomes shorter, only a few pores are generated with a small size. In this case, the permeabilization of the cell membrane is reversible. It is attributed to the recovery of the membrane structure following the electric-field treatment. Unfortunately, the number and size of pores will increase in the presence of higher electric fields, inducing irreversible membrane breakdown or mechanical damage of the microorganisms [20].

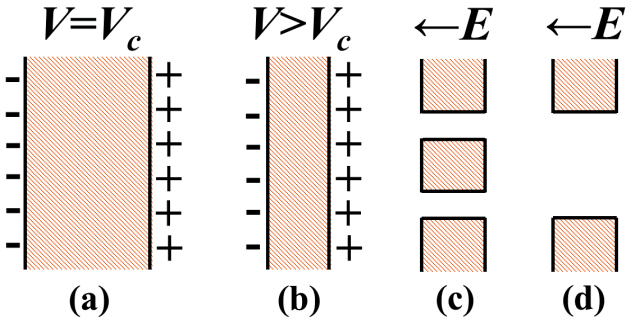


Figure 5.2: The mechanism of electric breakdown of microbial cells by pulsed electric-fields.

Molecular reorientation. The reorientation of the phospholipid dipole in two monolayers is responsible for the altered permeabilization of cell membranes. A previous study suggests that hydrophobic and hydrophilic pores will emerge in the lipid fraction under electric fields [21]. In particular, the hydrophilic pores will provide the elec-

tric current to generate the local thermal effect. An increase in temperature results in the thermal transfer from the gel structure to the lipid crystal structure, weakening the semi-permeable function of the cell membrane. In the cell membrane, there are protein channels, pores, and ion pumps, the functions of all of which depend on the transmembrane potential. Approximately 50 mV is required for opening or closing protein channels, which is less than the critical potential. Therefore, most protein channels are opened at high electric-fields. The generation of heat, the changes in other potentials, or the formation of pores can irreversibly denature protein channels.

These interactions clearly demonstrate that the lethal effect of electric-field treatment on microorganisms is caused by the instability of cell membranes. However, viruses are more difficult to manipulate because of their smaller size. They show resistance to inactivation using pulsed electric fields, even up to 29 kV/cm [22]. Therefore, it is still unclear whether those mechanisms happening in microorganisms will happen in viral inactivation. However, micro-nano processing effectively miniaturizes inactivation components and creates high electric-field regions between electrodes, even at moderate voltages. Electric methods of viral inactivation by utilizing microelectrodes fabricated on microchips might open the door to an all-in-one integrated system for concentrating, sampling, and inactivating viruses [23], [24]. Microelectrodes may enable the inactivation of individual virus particles, which is extremely difficult in macro-devices. Consequently, it is essential to understand the mechanisms of viral inactivation, such as SARS-CoV-2, in a practical setting.

5.2. ELECTRICAL INACTIVATION OF BACTERIOPHAGE PHI-6 ON MICROELECTRODES

5.2.1. DESIGN AND MODELING OF THREE MICROELECTRODES

Electric fields might be a promising method for integrating viral concentration and inactivation on microchips. A few studies have clearly suggested that the applied excitation potential, the electrical parameters of the particles, and the lipid itself strongly affect the distribution of electric-fields in the suspensions [25]–[27]. The determination of the parameters for the conductive medium is beneficial to effectively trap and inactivate viruses by positive dielectrophoresis (pDEP) between microelectrodes. In addition to those parameters, the structure of microelectrodes is also critical for the electric-field distribution. Therefore, in the design, those structures of microelectrodes where the ability in viral concentration and inactivation is maximum, should be considered. Here, three microelectrode structures (see Figure 5.3) are designed, namely the interdigitated, the castellated in-phase, and the castellated out-of-phase structures.

To gain insight into the electric-field distribution, the proposed structures are simulated within the framework of COMSOL Multiphysics. The input power is set to 30 V of DC voltage in the simulation. Besides, water is selected as the medium on the microelectrodes. The major parameters of the three microelectrode models are listed in Table D.1. The electric field distribution displays that the maximum electric field is located in the corners of the electrodes, regardless of the electrode structures, as shown in Figure D.1, D.3, and D.5. The maximum field strength for all electrode structures reaches 3×10^7 V/m or even higher, which contributes to virus inactivation. Moreover, it is found that

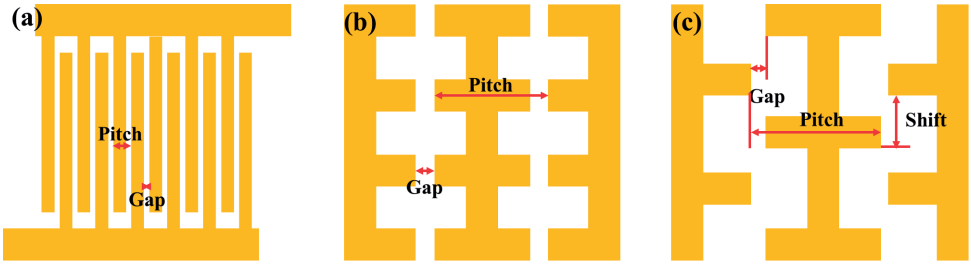


Figure 5.3: The geometries of the designed microelectrodes. (a) The interdigitated microelectrode, (b) castellated in phase, and (c) castellated out of phase.

Table 5.1: The maximum and minimum field strengths in the cross-section between microelectrodes. The field strength is in V/m. Note that *a* represents the maximum field strength in the microelectrode, whereas *b* is the minimum one.

Structure	0.0 μm	0.25 μm	0.5 μm	1.0 μm	1.5 μm	2.0 μm
Interdigitated	~	~	6.12×10^{7} ^{a}	2.90×10^{7}	1.77×10^{7}	1.23×10^{7}
	~	~	34.9 ^{b}	2.52	9.44	3.50
Castellated in phase	~	~	5.99×10^{7} ^{a}	2.71×10^{7}	1.61×10^{7}	1.10×10^{7}
	~	~	4.33×10^{3} ^{b}	7.97×10^{3}	1.32×10^{4}	2.01×10^{4}
Castellated out of phase	1.80×10^{8} ^{a}	5.24×10^{7}	3.24×10^{7}	1.82×10^{7}	1.23×10^{7}	9.25×10^{6}
	0 ^{b}	2.99×10^{3}	4.29×10^{3}	7.93×10^{3}	1.32×10^{4}	2.01×10^{4}

the electric field of the electrodes decreases with an increasing gap. In order to better understand the field strength at the centre of the two electrodes, the cross-section of the electric field along the cut line is taken. Similarly, the field strength between electrodes also significantly decreases with the gap, as presented in Figure D.2, D.4, and D.6. The maximum and minimum field strengths in the cross-sections are listed in Table 5.1. As we can see, the maximum field strength at the centre of the two electrodes for all structures comes up to 1×10^{7} V/m or even larger, except for the castellated out-of-phase structure with a gap of 2.0 μm. Surprisingly enough, the minimum field strength of the interdigitated structures is lower than 40 V/m, which is not conducive to attracting viruses that are far away from the microelectrodes. In comparison, the minimum field strength of the castellated structures could reach a magnitude of 10^{3} V/m. In this case, viruses is more readily attracted to microelectrodes. As a result, the inactivation ability of the castellated structures may be superior to the interdigitated structures. However, a published study has proven that the interdigitated electrodes can be used for the lysis of larger cells and bacteria (>1 μm) [28]. Furthermore, the electric field generated by all electrode structures is sufficient to induce the denaturation of S proteins in SARS-CoV-2 viruses [29]. It should be noted that there is a larger region of high electric-fields in the in-phase structures.

5.2.2. EXPERIMENTAL MATERIAL AND METHODS

PREPARATION OF VIRAL SUSPENSIONS

The bacteriophage phi-6 is selected as the surrogate of SARS-CoV-2 (a virus of bio-safety level 3, BSL-3) to evaluate the effect of electric fields generated by the designed devices on the viral viability. The bacteriophage phi-6 is a bacterial virus of BSL-1, thus it poses no risk to humans and does not require specialized bio-containment tools. The phi-6 is a double-stranded RNA-enveloped virus, and its S complex is structurally and morphologically similar to the s proteins of the CoVs [30], [31]. Therefore, the bacteriophage phi-6 has been an alternative to the CoVs in different experiments [30]–[32]. For instance, it is used as the surrogate to reveal the inactivation mechanisms of different methods (e.g., light irradiation, discharge, and electrostatic force) against CoVs [33]–[36]. The pseudomonas syringae is cultured to the early exponential phase and then infected with the phi-6 virus. We observed the phi-6 lesions daily and harvested the virus when the phi-6 lesions reached the expected value. The host strains are crushed to release the virus. Then, the virus samples are centrifuged as soon as possible, filter-sterilized with a polyetherosulfone membrane (0.2 μm, PES), and the supernatant containing the viral suspension is collected. The viral suspension is stored at 4 °C.

The viral suspension is mixed with distilled water to obtain the viral stock. The conductivity of the medium is a critical parameter and beneficial to determine the frequency of virus attraction using pDEP [23], [24]. The Lysogeny broth (LB) is commonly used as buffer solution for the bacteriophage phi-6, composed of peptone, yeast extract, and sodium chloride (NaCl). The presence of NaCl would enhance the conductivity of the medium. The conductivity of 10 mL of the LB solution containing 0.05 g NaCl is 1.02 S/m, which would be too high for pDEP. Thus, distilled water is chosen as the buffer solution because of its conductivity of 5×10^{-6} S/m, which may enable the designed microelectrodes to attract the virus in the range of 100 Hz to 10 MHz. However, the survival rate of the virus in distilled water is lower than in other saline solutions. Therefore, the initial concentration of the virus is set to 10^{11} pfu/ml to improve the viral stability and viability in the buffer solution. A previous study has demonstrated that higher initial concentrations of the phi-6 viruses could improve the stability and viability of the phage and protect it from environmental damage [37].

STATISTICS AND ANALYSIS

The viral titer is a measure of the total concentration of the virus without and with treatment. It is calculated by the following formula:

$$Viral concentration = \frac{N_p \times D}{V \times R} \tag{5.2}$$

where N_p, D, V, and R suggest the number of viral plaques, the dilution level at which the viral plaques are counted, the volume of the sample from the serial dilutions that are plated, and the dilution ratio of the sample that is treated, respectively. Here, the concentration unit is pfu/ml, and the dilution factor is 1/10 μL.

5.2.3. EXPERIMENTAL RESULTS AND DISCUSSION

In order to evaluate the inactivation effect of the DC and AC voltages against the virus, the viral samples are treated on all microelectrodes with a 30 V of DC and 40-45 V of

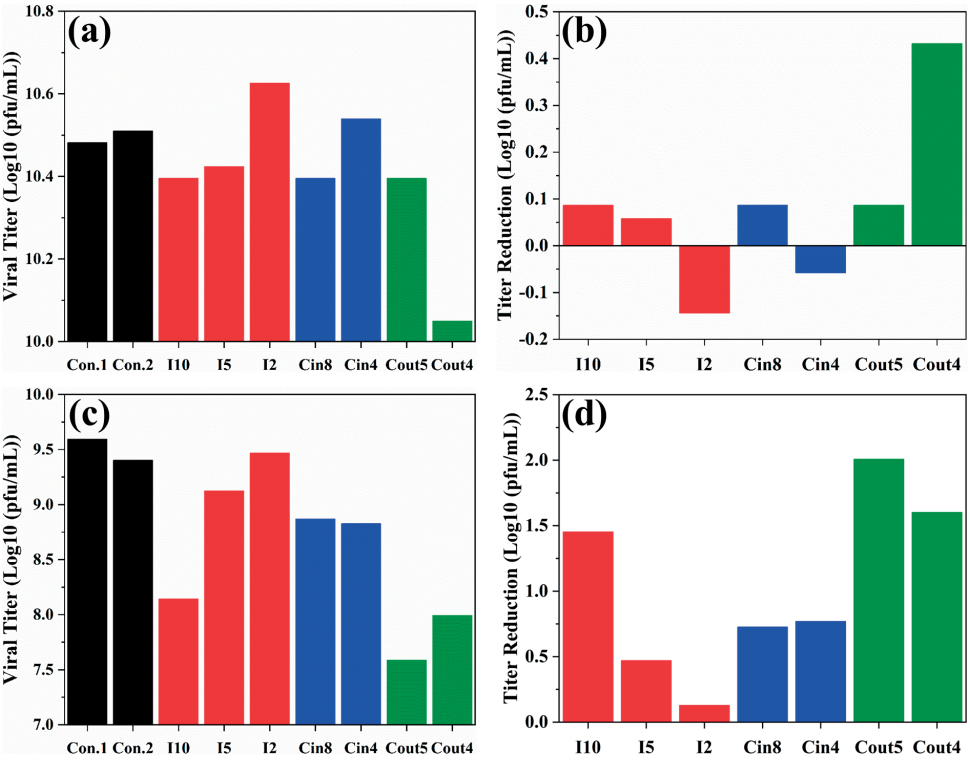


Figure 5.4: The viral titer and its reduction following DC (a-b) and AC (c-d) treatments of the viral samples.

AC (at 30 kHz) for 12 min. For comparison, two control groups are set, namely Con.1 and Con.2. Con.1 is that 10 μL of the viral sample is placed on the microelectrodes without the applied voltage, while Con.2 is the viral sample taken directly from the viral stock. The artificial factor-induced titer errors in the experimental process could be determined by the difference between two control groups. Figure 5.4 presents the viral titer and its reduction following the electric-field treatment. As shown in Figure 5.4(a), there are no the significant variations in the viral titers after the viral samples are treated with 30 V of DC voltage on the microelectrodes, regardless of the microelectrode geometries. In this case, the maximum titer reduction is observed in the Cout4 structure, but only by 0.43 $\log_{10}$ (see Figure 5.4(b)). Besides, the titer reductions in the I10, I5, Cin8, and Cout5 structures are less than 0.1 $\log_{10}$, being far from sufficient for viral inactivation. On the contrary, substantial variations in the viral titers can be observed following the AC treatment of the samples, as displayed in Figure 5.4(c). In Figure 5.4(d), it can be noted that the titer reductions for all structures are greater than 1.0 $\log_{10}$, except for the I5 and I2 structures. The maximum titer reduction occurs in the Cout5 structure, up to 2.01 $\log_{10}$, whereas the minimum reduction is 0.13 $\log_{10}$ for the I2 structure. Those results clearly show that the DC treatment for the viral samples on the microelectrodes does not lead to statistically significant inactivation, whereas the AC treatment does. The out-of-phase

castellated structures clearly exhibit optimal viral inactivation. In addition, we observe that the reduction in the viral titer increases with the pitch of the microelectrodes. This is inconsistent with the simulation result that the microelectrodes with a large pitch have low electric fields, which is not conducive to viral inactivation. The presence of more dead zones might be responsible for this phenomenon, which results in a smaller active area.

As mentioned above, the AC treatment of the viral samples results in a significant inactivation phenomenon. However, only 30 kHz of the AC frequency is considered. Here, 1 kHz of the AC frequency is also chosen to explore the effect of AC frequencies on viral inactivation. At the same time, the viral samples are treated on three electrode structures, i.e., I2, Cin4, and Cout5 structures, to further confirm the superiority of the out-of-phase castellated structures. As presented in Figure 5.5(a), the changes in the viral titers following the treatment with 30 kHz of an AC voltage is more significant than those with 1 kHz of an AC voltage, except for the I2 structure. This result is further proven by the data in Figure 5.5(b). Hence, high-frequency AC voltages might be better for effectively inactivating viruses. Besides, we observe that the titer reductions are greater than 0.5 $\log_{10}$ for the castellated structures, but less than 0.5 $\log_{10}$ for the interdigitated structures. Interestingly, there is no inactivation for the virus after the treatment with an AC voltage of 30 kHz on the I2 structure. The maximum titer reduction appears at the Cout5 structure at two frequencies, being 1.03 $\log_{10}$ at 1 kHz and 2.06 $\log_{10}$ at 30 kHz. Those findings is in agreement with the simulation result that the castellated structures are found to create more focused electric-field spots than the interdigitated structure. Consequently, the viral inactivation of the castellated structures, in particular the out-of-phase castellated one, is superior to the interdigitated structure.

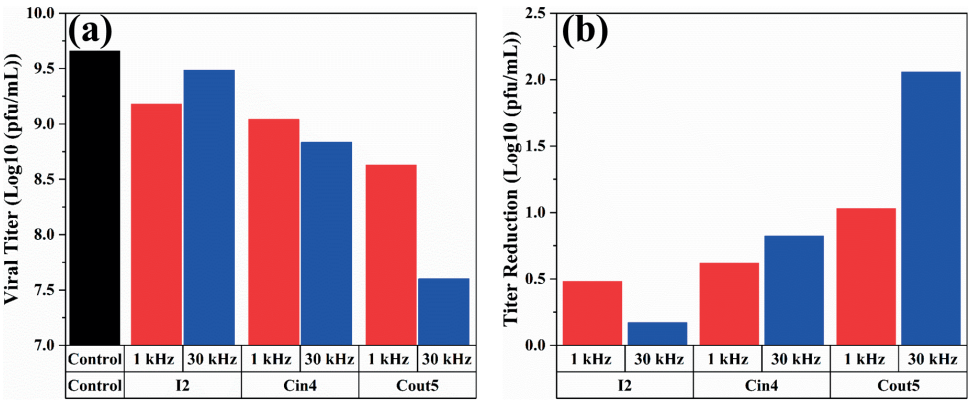


Figure 5.5: The effect of AC frequency on viral inactivation. The viral titer (a) and its reduction (b) following the AC treatment of the viral samples at 1 kHz and 30 kHz, respectively.

In the actual environment, virus particles are always dispersed, and their concentration is relatively low. This is a challenge for microelectrodes because of their small contact surface and the limited range of electric fields. Thus, to reveal the effect of viral dilutions on the inactivation. Diluted samples are obtained by adding 10 μL of distilled water to 10 μL of the viral stock. Figure 5.6 clearly shows the change in the viral titer

for the undiluted and diluted samples. Overall, the inactivation effectiveness of the microelectrodes for the undiluted samples is higher than for the diluted ones. The titer reductions caused by the I10 and Cout5 structures for the undiluted samples are larger than that for the diluted ones, as plotted in Figure 5.6(b). Even though the titer reduction induced by the Cin8 for the undiluted sample is smaller than that for the diluted one, their difference is merely 0.32 $\log_{10}$. The reductions in the viral titer are 1.28 and 1.86 $\log_{10}$ when the undiluted samples are treated on the I10 and Cout5 microelectrodes, respectively, whereas they only reach 0.01 and 1.05 $\log_{10}$ for the diluted ones. These results suggest that the increase in viral dilution reduces the inactivation ability of the microelectrodes against the virus. This might be attributed to the lower probability of the electric-field capturing of viral particles by the microelectrodes in the diluted samples. In addition, the diluted samples exhibit a relatively obvious change in the viral titer on the Cin8 and Cout5 electrodes, which means that more local spots of high electric-field could promote the viral capture of the microelectrodes.

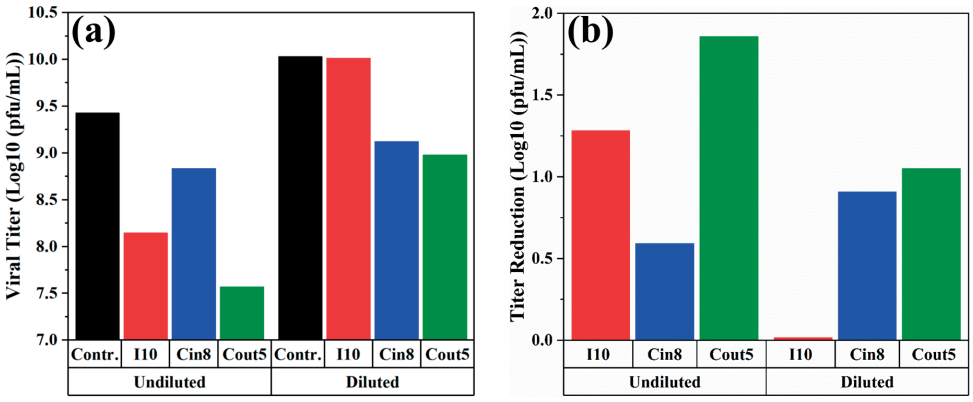


Figure 5.6: The effect of virus dilution on viral inactivation. The viral titer (a) and its reduction (b) following treatment with an AC voltage of 30 kHz.

The ability of electric-field capturing viruses highly depends on the conductivity of the medium [23], [24]. This directly leads to a difference in virus inactivation. Therefore, it is worth investigating the effect of different media on the inactivation of viruses by electric-field method. In section 5.2.2, it is described that the LB solution is a commonly used buffer for the phi-6 viruses, and its conductivity is 1.02 S/m if it contains 0.05 g NaCl. Thereby, the LB solution is selected as a high-conductivity medium for comparison with distilled water. As shown in Figure 5.7(a), it can be found that the change in the viral titer for the LB solution is smaller than that for distilled water from an overall perspective. The titer reductions in Figure 5.7(b) further provide powerful evidence for this result. According to the titer analysis, the reductions in viral titer for the viral samples with the DI water on the I10, Cin8, and Cout5 electrodes are 1.65 $\log_{10}$, 0.91 $\log_{10}$, and 2.21 $\log_{10}$, respectively, while being 0.32 $\log_{10}$, 1.62 $\log_{10}$, and 0.50 $\log_{10}$ for the ones with the LB solution. Those values clearly suggest that the electric-field captures the virus more easily in distilled water than in the LB solution for the same voltage. It might be attributed to the differences in the polarization of the virus by the electric-field in different

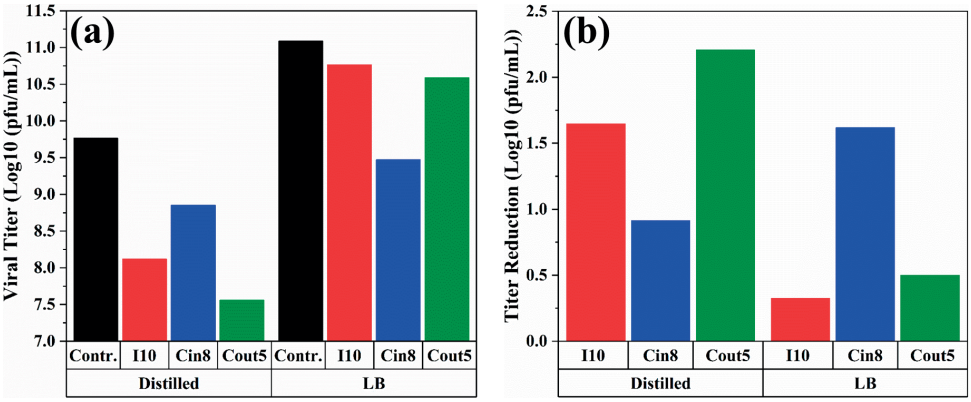


Figure 5.7: The effect of different media on viral inactivation . The viral titer (a) and its reduction (b) following treatment with an AC voltage of 30 kHz.

5

media. The virus is more easily polarised by the electric-field in low-conductivity ones, thus being readily captured to the electrodes. Besides, the simulation results also indicate that the increase in conductivity of the medium requires higher voltage frequencies to capture viruses so that viruses in the medium are more easily polarised by electric fields than the surrounding matter. As a result, a virus in the LB solution is difficult to capture in the high electric-field regions of the electrodes at a given same voltage.

As discussed above, AC voltages lead to a significant inactivation for the virus. With AC voltages, the virus also undergoes a dielectric force from the medium in addition to the electric-field force from the electrodes. The dielectric force might be also a major cause of the inactivation of the viruses, which has been confirmed in the published study [38]. Moreover, the virus is attached to the high electric-field areas of the microelectrodes at AC voltages, which could be primarily responsible for the obvious viral inactivation. In comparison, DC voltages only have a slight influence on the virus. However, this does not mean that DC voltages can not lead to significant viral inactivation. Previously, DC voltages were used for the lysis of larger organisms such as red-blood cells, hamster ovaries, and plant protoplasts [39]–[41]. Furthermore, the inactivation of smaller organisms requires higher DC voltages [42]. Consequently, very high electric-fields may be needed to inactivate viral particles, which are difficult to realize on our microelectrodes due to electrical breakdown.

Among the three microelectrode structures, the ability of the out-of-phase castellated structure in the viral inactivation is superior to the other ones. Studies suggest that castellated structures or structures with pointed tips are preferred for bacterial and viral inactivation [43], [44]. Compared to the interdigitated structures, the electric-fields in the castellated ones are higher, non-uniform, and more focused. Unexpectedly, there is a positive correlation between the viral inactivation rate and the pitch of the microelectrodes. This might be due to two reasons. One is that the microelectrodes with smaller pitches are more susceptible to electrical breakdown, and thus have less effective areas for capturing the virus than the ones with larger pitches. During the experiments, we observed no short circuit in the microelectrodes I10, Cin8, and Cin4, whereas it can be

in the I5, I2, Cout5, and Cout4. Another reason is that the microelectrodes with larger pitches are more efficient in concentrating the virus, being consistent with results focusing on the effect of electrode pitches on the concentration efficiency of viruses [45]. The concentration efficiency of the electrodes for the virus initially decreases with the pitch/height of the electrodes. It then obviously increases with a further increase in the pitch-height ratio of the electrodes. In the ideal case, the sample height above the microelectrode surface is 20 μm, but it might be more than 30-50 μm in reality. In this case, the microelectrode I10 with the largest pitch is the most efficient in concentrating the virus, which might explain the high inactivation rate in the I10 structure.

AC voltages with higher frequencies in viral inactivation are better than the ones with lower frequencies. The direction of the force on the particles depends on the Clausius Mossotti (CM) coefficient, which depends on the polarization of the suspending medium and the polarization of the particles [23], [24]. The CM coefficient is +0.1 at 30 kHz, leading to a weak pDEP force on the particles. However, this coefficient is very low compared to that of other more polarized bacteria and cells. For instance, the maximum CM coefficient for Escherichia coli is +1.0, resulting in a significant pDEP force even with higher conductivity of the suspending medium [46]. For the CoVs and the phi-6, their small size and the low conductivity of the membranes cause a very low attraction force, which might also explain the very low inactivation rate of the virus in the diluted samples. The electric field is the highest at the electrode surface, and decreases further away from the surface. Accordingly, the height of the inactivation area is set to 10 μm in this study. Viruses beyond this area need to be attracted to the microelectrodes in order to inactivate them. In the diluted samples, there are fewer viruses in the inactivation area, thus no obvious changes in the viral titer can be observed without the presence of a DEP force. The comparison of two ratios can prove the presence of DEP force in the viral samples, i.e., the height ratio of the inactivation area and the sample and the concentration ratio of viruses after and before treatment. When the height ratio is equal to the concentration ratio, it means that there are no attraction forces. The attraction forces are only at play as the concentration ratio is greater than the height ratio. For instance, in the microelectrode Cin8, the heights of the inactivation area and the sample are 10 and 100 μm respectively, thus the height ratio for the undiluted samples is 0.10. The viral concentrations after and before the treatment are 5.50×10^{9} and 7.15×10^{8} pfu/mL, respectively, with a concentration ratio of 0.13. Obviously, the height ratio is smaller than the concentration ratio, which indicates that weak DEP forces might attract the virus. For the diluted samples, the height ratio is 0.05 (10 μm/200 μm), and the concentration ratio is 0.12 (1.33×10^{9} pfu/mL /1.07×10^{10} pfu/mL). Thus, we can conclude that the attraction forces are also at play in the diluted samples.

5.3. ELECTRICAL INACTIVATION OF ESCHERICHIA COLI ON MICROELECTRODES

5.3.1. EXPERIMENTAL MATERIAL AND METHODS

EXPERIMENTAL MICROELECTRODE

Here, the microelectrode in Figure 5.8(a) is used to inactivate Escherichia coli (E. coli), which is different from those mentioned above. The gap between the two electrodes is

150 μm, and the width of the electrode is 180 μm. The electrode and substrate materials is gold (Au) and alumina ceramic, respectively. The thickness of the Au layer is 3~7 μm. The dimension of the entire electrode chip is 20×10×0.635 mm.

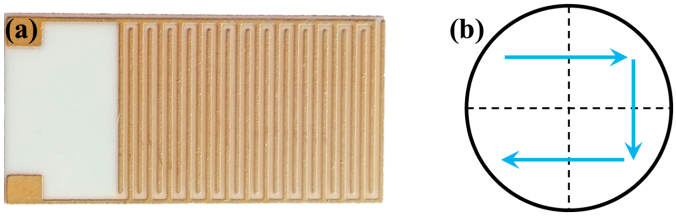


Figure 5.8: (a) The microelectrode used in the E. coli inactivation experiment. (b) The streak method used when E. coli is inoculated on solid medium.

PREPARATION OF E. COLI SAMPLES

We first thaw the frozen KANA-resistant E. coli (stored at -80 °C) in a 37 °C water bath. E. coli are then inoculated in an ultra-clean bench that must be pre-sterilized with UV light for 20 min. The streaking culture of E. coli placed in solid medium is performed in a CO_2 incubator at 37 °C for 12 h. The streak path is shown in Figure 5.8(b). Individual strains in the fourth zone of the plate are transferred to 10 mL centrifuge tubes containing 6 mL liquid media by adopting a 10 μL pipette aid. The centrifuge tubes containing E. coli are placed in a shaker at 37 °C and incubated for 8 h with shaking. Finally, the liquid media slowly becomes cloudy, and the target value for the optical density (OD) is 0.6-0.8.

EXPERIMENTAL DESIGN

60 μL E. coli samples are placed on the microelectrodes and treated by different AC voltages, treatment times, and AC frequencies. The E. coli samples after an electrical treatment are then transferred to testing tubes, and E. coli samples without an electrical treatment are set up as control groups. All experimental and control groups are incubated in the solid medium and the number of individual colonies on the plates is counted. AC voltage, AC frequency, and electric field treatment time are considered the influencing factors of the inactivation rate. Besides, DC electric fields are also taken into account. As listed in Table 5.2, three experimental groups are set up for each factor. For the DC field, the treatment time for all E. coli samples is 3 min. When the AC voltage is variable, the treatment time and frequency are 3 min and 60 kHz, respectively. For the treatment time, the AC voltage and frequency are set to 20 V and 60 kHz, respectively. Regarding the AC frequency, the AC voltage and treatment time are 20 V and 3 min, respectively.

STATISTICS AND ANALYSIS

The plate count method is the most commonly used to determine the number of living bacteria. Thus, the plate count method determines the total number of living E. coli before and after an electrical treatment. The inactivation rate is evaluated by the formula

$$\log S = \log\left(\frac{N}{N_0}\right) \tag{5.3}$$

Table 5.2: The set-up of experimental groups for each influencing factor.

Field type	Factor	No.1	No.2	No.3
DC	Voltage (V)	0.3	0.6	0.9
AC	Voltage (V)	10	20	30
	treatment time (min)	1	3	5
	Frequency (kHz)	30	60	90

where N_0 represents the initial concentration (CFU/mL) of E. coli before an electrical treatment, while N is the concentration of living E. coli after an electrical treatment. $\log S$ is the $\log_{10}$ value of the reduction in the concentration of E. coli after an electrical treatment.

PREPARATION OF E. COLI SAMPLE FOR MORPHOLOGICAL ANALYSIS

Scanning electron microscope (SEM) is a commonly used micro-morphological observation method. In order to better compare the surface morphology of E. coli before and after an electrical treatment, all samples are prepared with special treatments. The preparation process is mainly divided into six steps, namely, collection, fixing, dehydration, replacement, drying, and Au sputtering. First, the E. coli sample is centrifuged at 8000 rpm for 10 min, and the supernatant is then removed. Second, the collected E. coli suspension is fixed by adding 100 μL of 4% cell tissue fixative for 24 h. Third, the fixed E. coli suspension is dehydrated twice by adding 100 μL of 30% and 50% ethanol solution for 15 min each. Notably, it is essential to centrifuge the E. coli suspension and remove the supernatant after each dehydration. Fourth, the dehydrated E. coli is replaced twice by adding 100 μL of 50% and 99% isoamyl acetate solution for 5 min each. The centrifugation and removal of the supernatant are also two must-do steps after each replacement. Fifth, the E. coli suspension obtained in the previous step is mixed and transferred to the silver-plated silicon substrate, and then freeze-dried in a vacuum drying oven at -10 °C for 30 min. Finally, the E. coli sample is sprayed with an Au layer. The spraying time of the Au layer is 2 min.

5.3.2. EXPERIMENTAL RESULTS AND DISCUSSION

The results above on the inactivation of the DC voltage against the phi-6 virus clearly show that DC treatment cannot lead to a significant inactivation of the phi-6 virus. However, it is also worth investigating the effect of DC treatment on the inactivation of E. coli because of its much larger dimension. Therefore, the inactivation efficacy of microelectrodes against E. coli at DC voltages is evaluated. For DC treatment, voltage magnitude is an important variable influencing the inactivation of pathogens. The inactivation rates of E. coli at DC voltages of 0.3, 0.6, and 0.9 V is displayed in Figure 5.9. It can be seen that different DC voltages induce various the $\log_{10}$ reductions in E. coli colonies for the same treatment time. However, the inactivation efficacy is not in a positive or negative correlation with DC voltage. At a DC voltage of 0.3 V, the inactivation rate of E. coli is 0.19 $\log_{10}$. The inactivation rate of E. coli decreases to 0.09 $\log_{10}$ when the DC voltage reaches

0.6 V. As the DC voltage continues to increase to 0.9 V, the inactivation of E. coli is only 0.11 $\log_{10}$. This indicates that low DC voltages do not significantly inactivate E. coli.

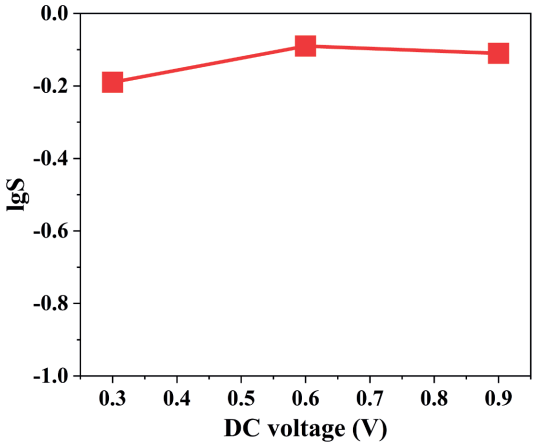


Figure 5.9: Effect of DC voltage on the inactivation efficacy of E. coli using electric fields from the microelectrode.

As discussed above, AC voltage has a better inactivation efficacy than DC one, thus AC voltage is considered to evaluate its effect on E. coli. For AC treatment, there are two major variables that affect inactivation, namely voltage magnitude and frequency. The inactivation rate of E. coli as a function of AC voltage and frequency is presented in Figure 5.10. As displayed in Figure 5.10(a), the inactivation of E. coli slowly increases with increasing AC voltage. The inactivation rate is 0.11 $\log_{10}$, 0.13 $\log_{10}$, and 0.19 $\log_{10}$ at an AC voltage of 10, 20, and 30 V respectively. These values show that the inactivation effect is positively correlated with the AC voltage. Figure 5.10(b) displays that the inactivation rate increases with the AC frequency. The inactivation rate is 0.14 $\log_{10}$, 0.18 $\log_{10}$, and 0.32 $\log_{10}$ for an AC frequency of 30, 60, and 90 kHz, respectively. In comparison, the AC frequency has a more significant impact on the efficacy of E. coli inactivation than the AC voltage.

Furthermore, the treatment time of pathogens in electric fields plays an essential role in the inactivation efficacy. Therefore, the inactivation effectiveness of E. coli is also studied for different treatment times. Figure 5.11 displays the inactivation rate of E. coli as a function of treatment time. In Figure 5.11, it can be noticed that the inactivation rate of E. coli first decreases and then increases slightly with increasing treatment time. However, there is little effect on the inactivation efficacy. At treatment times of 1, 3, and 5 min, the inactivation rates are 0.08 $\log_{10}$, 0.15 $\log_{10}$, and 0.11 $\log_{10}$, respectively. These values suggest that inactivating E. coli requires a sufficient treatment time, but for the electrical inactivation of microelectrodes, longer treatment times may not always be optimal.

In order to reveal the structure change of E. coli with an electrical treatment, the surface morphology of E. coli is analyzed by adopting SEM method. For comparison, E. coli without an electrical treatment are also used for the SEM analysis. As shown in Figure 5.12(a), without an electrical treatment, most E. coli are structurally complete and

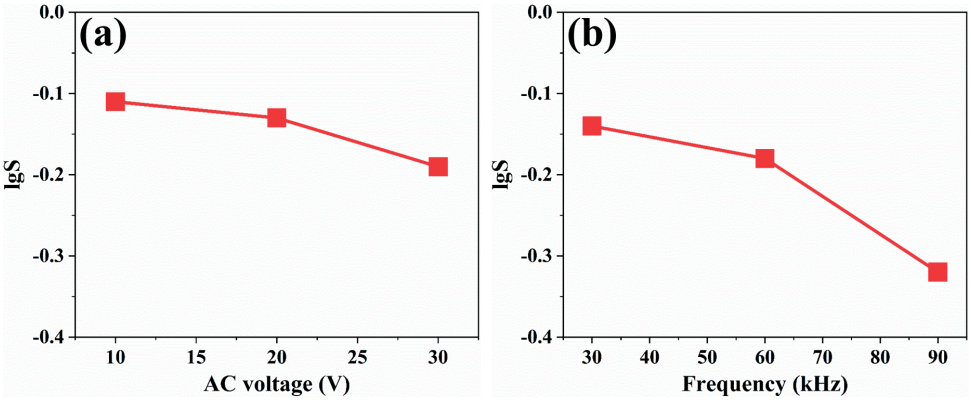


Figure 5.10: Effect of AC voltage on the inactivation efficacy of E. coli using electric fields from the microelectrode.

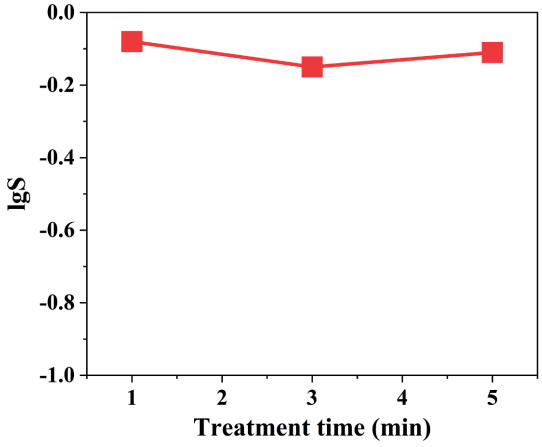


Figure 5.11: Effect of treatment time on the inactivation efficacy of E. coli using an AC voltage of 20 V and an AC frequency of 60 kHz.

full-bodied. The boundary between E. coli is clearly visible, and they are no fusion. Figure 5.12(b) displays the morphology of the entire E. coli in the absence of an electric field. As we can see, the entire E. coli is full-bodied, and its lipid envelope smooth. In comparison, the entire morphology of E. coli has an apparent change in the presence of an electric field. In Figure 5.12(c), a shriveled morphology of most E. coli is observed, suggesting damage to the envelope structure. This damage may result in the leakage of intracellular bacterial substances in E. coli. There is also no clear boundary between E. coli. Figure 5.12(d) further provides a more evident morphological structure of E. coli. It can be seen that the surface of E. coli is rougher than that without an electrical treatment; even some E. coli have severely collapsed and shriveled into flakes. These findings suggest that an electrical treatment of E. coli on microelectrodes can effectively disrupt its morphological structure, rendering it inactive and unable to carry out its normal life

activities [47].

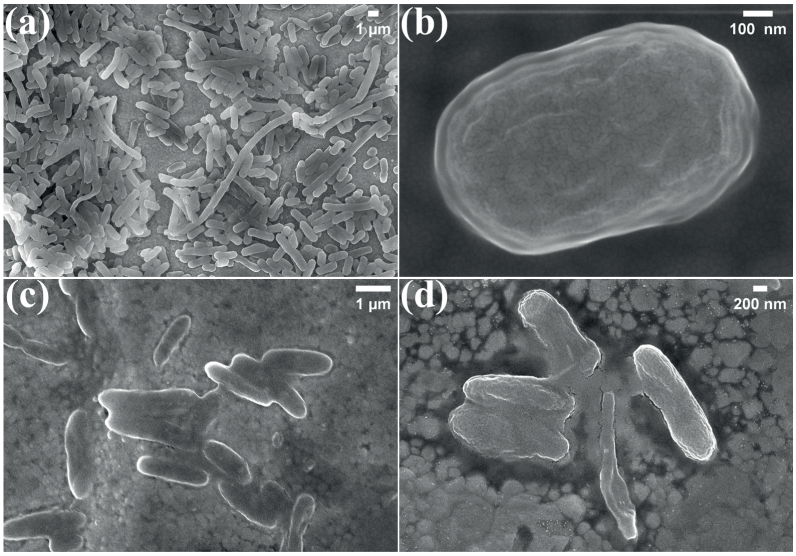


Figure 5.12: The SEM images of E. coli before (a-b) and after (c-d) electrical treatment.

In DC treatment, the inactivation of E. coli is independent on DC voltage. Surprisingly, a significantly lower DC voltage is sufficient to achieve similar inactivation in E. coli treatment, compared to 30 V DC needed for the phi-6 virus. This may be attributed to the large size of E. coli, enabling it be easily attracted to the microelectrodes by electric fields. During the experiments, it is noticed that the E. coli solution on the microelectrode will boil and bubble at a DC voltage above 1 V and a treatment time of 3 min. E. coli is a mesophilic bacterium capable of growing well from 21 °C to 49 °C [48], [49]. Therefore, in order to exclude the effect of temperature on the inactivation of E. coli, only DC voltages below 1 V are studied. In AC treatment, the inactivation of E. coli is positively correlated with both AC voltage and frequency, suggesting that higher AC voltages and frequencies are more effective in inactivating E. coli. The above findings are in agreement with the previously described results for the inactivation of the phi-6 virus at different AC frequencies. The findings indicate that there is no significant relationship between the treatment time and the inactivation of E. coli. Similar to the DC treatment, there is also a thermal concern with the AC treatment, where exceeding certain values of AC voltage, frequency, or treatment time can lead to a maximum temperature exceeding 70 °C. Accordingly, AC voltage, frequency, and treatment time are maintained within the threshold range to avoid the generation of high temperatures. Observations from the SEM images demonstrate that applying electric fields induces a morphological alteration in E. coli, characterized by the collapsing and shrinking of its lipid envelope, ultimately leading to the loss of its biological function [47]. A previous study has demonstrated that the application of electric fields results in significant surface damage to vegetative bacteria, particularly to its plasma membrane and cell wall [50]. Meanwhile, the presence of cell-debris was found near the vegetative bacteria. Another ESEM (environmental elec-

tron microscopy) study displayed that the cytoplasmic membrane of E. coli treated with electric fields appears to be torn by the formation of disordered pores [51]. The complete alteration of the cell wall and cytoplasmic membrane results in an evacuation of the cytoplasmic content to the outside of the cell, which causes the loss of the biological activity of E. coli. Therefore, the lipid envelope is one of the major targets for the inactivation of enveloped pathogens by electric fields.

5.4. DYNAMICS OF VIRAL LIPID BILAYER INDUCED BY ELECTRIC FIELDS

5.4.1. MODELING AND COMPUTATIONAL METHODS

The viral membranous envelope is antigenic, its major function is to aid the entry of the viruses into the host cells and maintain the structural integrity of the virions. Besides, it is speculated that the viral lipid envelope is not affected by viral mutations, unlike S proteins, so it would be a well-defined target [52]. Thereby, it is worth revealing the dynamic behavior of the viral lipid membrane under electric fields. Lipids are the defining components of the bilayer membranes, containing a hydrophilic, polar head group and a hydrophobic, non-polar tail. They are assembled into a bilayer with the head facing outwards, forming a barrier that separates the genetic material from the extra-membrane medium. Although the phi-6 virus has commonly been used as a surrogate for CoVs in different experiments, the bilayer membranes of various viruses are different in the type and content of the phospholipid molecules. The purpose of this study is to uncover the probability of electric-field treatment against SARS-CoV-2. Hence, the bilayer membrane of SARS-CoV-2 is chosen as the target of electric-fields. A previous study has shown that the lipid composition of the CoV membrane mainly includes POPC, POPE, POPI, POPS, PSM, and cholesterol molecules [52], as listed Table 2.4. A recent study focusing on SARS-CoV-2 envelope confirms that the lipid envelope of SARS-CoV-2 virions is mainly composed of phospholipids (primarily PC, PE, and PI), with some cholesterol and sphingolipids, and the ratio between cholesterol and phospholipid is similar to lysosomes [53]. Thus, POPC, POPE, POPI, POPS, PSM, and cholesterol molecules are assembled into the bilayer membrane of SARS-CoV-2 virions in this study. It should be noted that the structural proteins embedded in the bilayer membrane will not be considered in order to better understand the dynamic behavior of the lipid membrane under electric fields. Here, the pure lipid membrane comprises 200 lipid molecules in total, with an approximate size of 8.8 nm by 8.8 nm in the xy plane, as shown in Figure 5.13. According to the phospholipid ratio (see Table 2.4), the molecular numbers are 130, 20, 18, 10, 8, and 14 for POPC, POPE, POPI, POPS, PSM, and cholesterol molecules, respectively.

All simulations are carried out with the GROMACS set of programs version 2019.6 [54]. Lipid parameters are derived from CHARMM36, with all-atom parameters updated in 2020 [55]. The water molecules of the bilayer system is described with the TIP3 model. The bilayer system is coupled to a temperature bath at 315 K and a pressure bath of 1 bar. The temperature coupling of the system is achieved using the V-rescale thermostat [56]. Berendsen pressure coupling is adopted with a constant time of 50 ns in the equilibration process. In the production run, the pressure of the system is controlled by a Parrinello–Rahman barostat with a constant time of 200 ns. The coupling times of

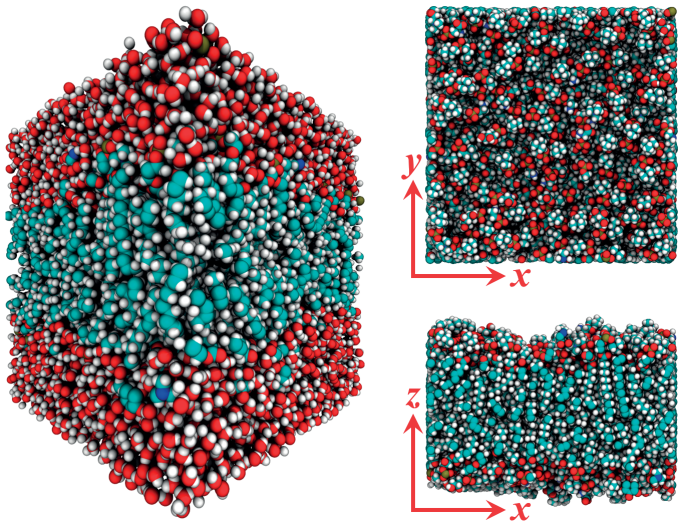


Figure 5.13: The 3D illustration for the lipid membrane of SARS-CoV-2 virions, including its top and side views without water and neutralising ions.

τ_T= 0.2 ps and τ_P= 2.0 ps are used for the thermostats and barostats, respectively, for all simulations. The pressure in the bilayer system is scaled semi-isotropically, with a compressibility of 4.5×10^{-5} bar^{-1} both in the membrane plane and perpendicular to the membrane. Long-range electrostatics are evaluated with the PME method. The vdW interaction is described using the cut-off method. A cut-off radius of 1.0 nm is set for long-range electrostatic and vdW interactions. In our study, the field strengths of 0, 50, 100, 150, 200, and 250 mV/nm are chosen to reveal the possible impact of electric fields on the bilayer membrane. The integration time step for our simulations is 0.001 ps. For visualization and analysis after the MD simulation, VMD 1.9.3 is used [57].

Furthermore, a pulsed and oscillating electric field can be expressed by the formula [58]

$$E(t) = E_0 \exp\left[-\frac{(t-t_0)^2}{2\sigma^2}\right] \cos\left[w\,(t-t_0)\right] \tag{5.4}$$

where E_0, $w = \frac{2\pi c}{\lambda}$, t_0, and σ are the field strength, the angular frequency, the time at of the peak in the field strength, and the width of the pulse, respectively. In order to approximately describe an AC source in the simulation, t_0, and σ are set to 0. In addition, E_0 is 1000 mV/nm to ensure that the strucutral change of the lipid membrane appears within the production time. w is set to 0.001, 0.01, 0.1, 1, and 100 ps^{-1} to explore the minimum time for the nanopore formation under different angular frequencies. The simulated oscillating field with the angular frequency of 1 ps^{-1} is shown in Figure D.11.

5.4.2. RESULTS AND DISCUSSION

Bilayer area and bilayer thickness. The APL can give informative about the structural and dynamic nature of the bilayer membrane. Thus, to observe the structural changes of the bilayer membrane at varying field strengths, the APL and membrane thickness are

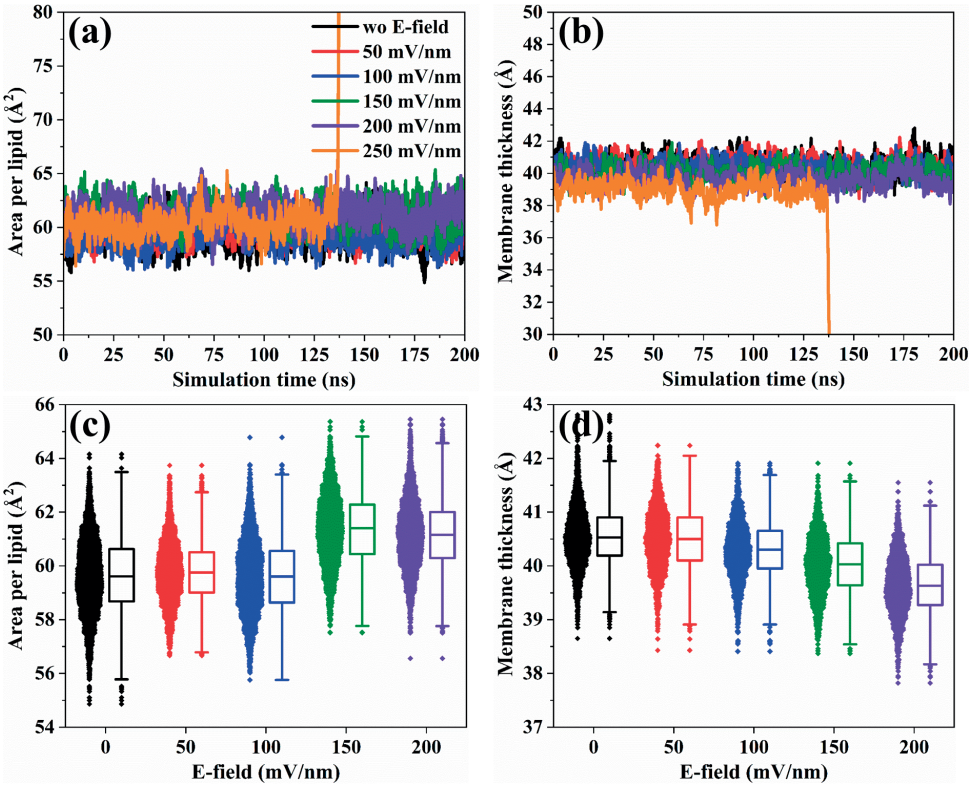


Figure 5.14: The total APL (a) and membrane thickness (b) of the multi-lipid bilayer structure as a function of electric field over 200 ns of simulation time. The box-chart analysis of the total APL (c) and membrane thickness (d) of the multi-lipid bilayer structure after 200 ns of simulation time.

first put in the spotlight. Figure 5.14 plots the APL and membrane thickness of the bilayer membrane as a function of electric fields. In Figure 5.14(a), it can be noted that the time-dependent APLs of the bilayer membrane almost overlap at a field from 0 to 200 mV/nm, which means that it is difficult to distinguish the structural difference caused by various field strengths. However, APL increases rapidly at 250 mV/nm after the simulation time reaches 137 ns, which clearly suggests that the membrane structure has been disrupted. At the same time, the statistical data in Figure 5.14(c) also give easily visible evidence of the change in APL at different electric fields. Note that the field of 250 mV/nm has not been plotted in Figure 5.14 to better observe the change of APL at fields less than 250 mV/nm. As we can see, there is a small change in the average total APL of the bilayer membrane at the fields of 0-100 mV/nm. Nonetheless, when the field strength increases further, a significant change in APL can be observed. Besides, it is also found that the fluctuation magnitude of APL first decreases and then increases when the field strength varies within the range of 0-100 mV/nm. The averaged total APLs at field strengths of 0, 50, 100, 150, 200, and 250 mV/nm are 59.63, 59.76, 59.62, 61.35, 61.16, and 172.09 Å^2, respectively. Those values directly confirm a small structural variation in the bilayer mem-

brane at fields of 0-100 mV/nm over 200 ns time. Similarly, the time-dependent membrane thickness undergoes a very slight change with the electric field, except for fields greater than 100 mV/nm. This is directly demonstrated by the data in Figure 5.14(b). In agreement with the total APL, when the field strength reaches 250 mV/nm, the membrane thickness decreases sharply near 137 ns. The membrane thickness at 250 mV/nm is significantly smaller than that at other field strengths. As shown in Figure 5.14(d), we find that the overall membrane thickness gradually decreases with the electric field, and the thickness difference between 0 and 50 mV/nm of fields is extremely small. The averaged membrane thickness is further calculated over 200 ns time. This turned out to be 40.56, 40.50, 40.29, 40.02, 39.64, and 30.21 Å at 0, 50, 100, 150, 200, and 250 mV/nm, respectively. These thickness values suggest that the bilayer membrane is compressed by the electric field perpendicular to the membrane, in particular at higher electric fields.

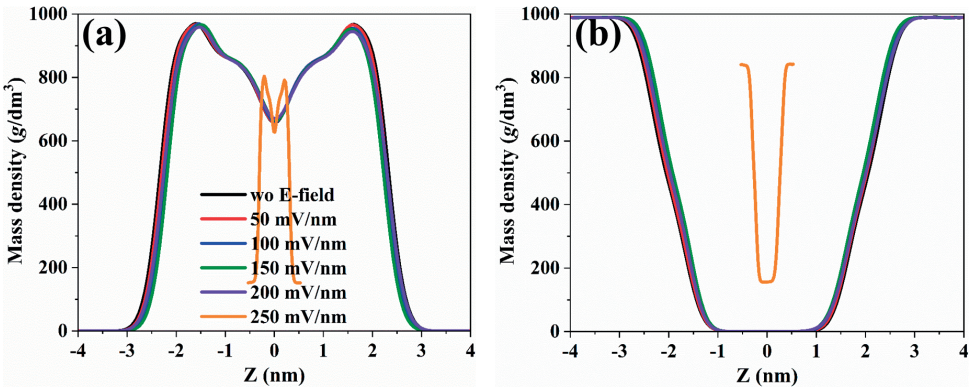


Figure 5.15: Mass density profiles of lipids and water molecules along the bilayer normal to the membrane at different electric fields over a simulation time of 200 ns.

Mass density of the lipids and water molecules. In order to uncover more visually the structural variation in the bilayer membrane caused by the electric field, the mass density profiles of lipids and water are discussed. As displayed in Figure 5.15(a), it can be observed that the mass density of the lipids is nearly unchanged at field strengths of 0-200 mV/nm, even at the head-groups of the lipids. However, there is a significant change in the mass density of the lipids as the field strength is raised up to 250 mV/nm. For fields less than 250 mV/nm, the density profile of the lipids is slightly scaled with the field strength, which is consistent with the change in the membrane thickness. In particular, when the field strength comes up to 250 mV/nm, the density profile of the lipids has shrunk severely and the mass density is not zero at the edge of the bilayer membrane. This indicates that the bilayer membrane is disrupted. In Figure 5.15(b), no significant changes can be seen in the mass density profiles of water molecules up to 250 mV/nm, which is the same as the change observed in the lipids. As we can see, at field strengths less than 250 mV/nm, the mass density of water molecules in the membrane interior remains still zero over 200 ns time, whereas it is not at 250 mV/nm. This suggests that a low electric field is insufficient for water to penetrate the membrane. An increase in the electric field could eliminate the unfavorable interaction with the alkyl lipid tails

and further promote membrane disruption.

Electron density profiles of the lipids. Compared to the total APL, the electron density profile is more informative about the fate of the bilayer structure. Figure 5.16 displays the electron density profiles of the lipids and the electron densities at their head-groups after 200 ns simulation time at different electric fields. As shown in Figure 5.16(a), there is no significant overall change in the electron density profile of the lipids at electric fields of 0-250 mV/nm. However, there is a significant change at the two head-groups of the lipids with field strength beyond the range of 0-250 mV/nm. Interestingly, the change in magnitude of the electron density between the two head-groups is very different, which might be attributed to the direction of the applied electric field. We find that the electron density of the head-group in the top leaflet increases gradually with the electric field, whereas for the bottom leaflet, it remains within a certain range. Furthermore, when the field strength reaches 250 mV/nm, the electron density profile of the lipids has shrunk severely towards the origin of the coordinate while the height of its two peaks also decreases sharply. At the same time, it should be noted that the electron density of the lipids between two peaks is not zero, suggesting that disruption of the bilayer occurs. Figure 5.16(b) further provides thoughts for these discussions. It can be found that the change of the electron density for the top leaflet is more regular than that for the bottom leaflet.

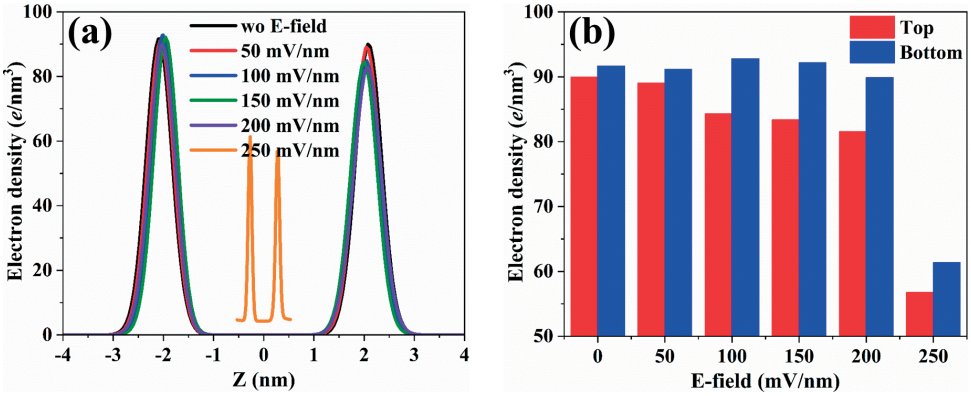


Figure 5.16: (a) Electron density profiles of the lipids along the bilayer normal for the multi-lipid bilayer at different electric fields over a simulation time of 200 ns. (b) The electron densities at the head-groups of the lipids for the top and bottom leaflets.

Lateral diffusion behavior of the lipids. Here, we evaluate the time-dependence dynamics of the lipids inside the membrane. It should be noted that the lateral diffusion behavior of the lipid molecules is only addressed. The MSD and LDC for the varying electric fields at 200 ns simulation time are plotted in Figure 5.17. As shown in Figure 5.17(a), we observe that the MSD almost overlaps within 150 ns as the field varies from 0 to 100 mV/nm, and then increases for fields from 150 to 200 mV/nm. However, the variation of the MSD is regarded as very small at fields less than 250 mV/nm. Unsurprisingly, there is a sharply increase in the MSD with time at a field strength of 250 mV/nm, suggesting that the diffusion of the lipid molecules diffuse becomes very active. These results are

further proven by the calculated LDC displayed in Figure 5.17(b). According to the fitting results within a 10-90% production time, the LDCs of the lipid molecules are (0.86±0.04), (0.85±0.04), (0.94±0.26), (0.91±0.15), (0.97±0.05) and (26.38±3.33)$\times 10^{-7}$ cm^2/s for field strengths of 0, 50, 100, 150, 200, and 250 mV/nm, respectively. As a result, electric fields lower than 250 mV/nm cannot lead to a significant increase in the LDC of the lipids. LDC shows a nearly exponential relationship with the electric field.

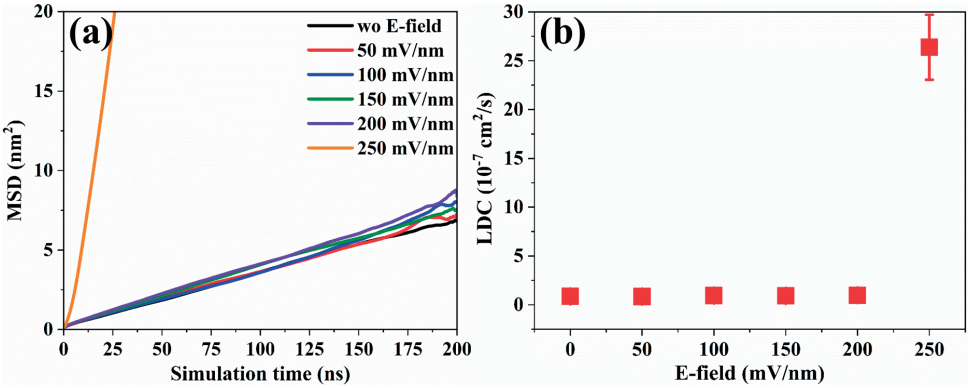


Figure 5.17: The MSD and LDC within the bilayer membrane plane at varying electric fields following a 200 ns simulation.

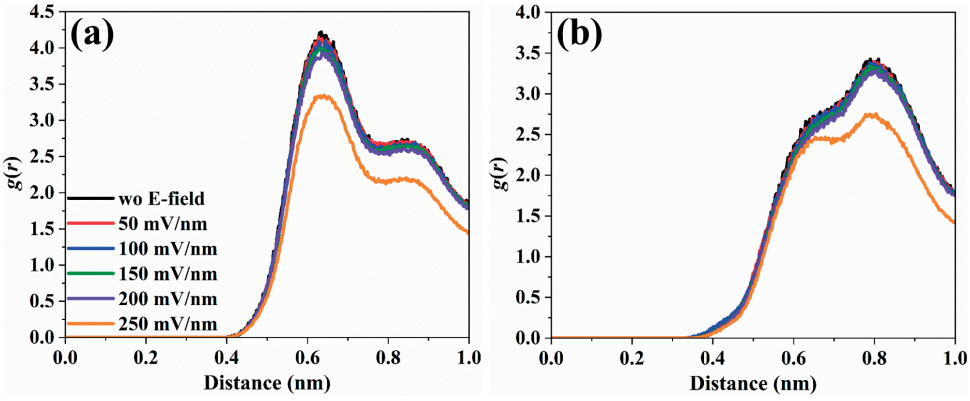


Figure 5.18: 2D RDFs $g(r)$ for atomic pairs of lipid molecules in the bilayer membrane at varying electric fields following a 200 ns simulation.

2D RDF of the bilayer system. Finally, the 2D RDFs of P-P and N-N pairs of the headgroups of the lipid molecules are discussed, as displayed in Figure 5.18. For the P-P pair, Figure 5.18(a) clearly shows that the P-P RDF has its first peak near 0.64 nm, followed by a second peak around 0.84 nm. The first peak is much higher than the second one, indicating that the probability of lipid molecules appearing at 0.64 nm is higher than at 0.84 nm. For an electric field with a field strength of less than 250 mV/nm, the P-P RDF slightly decreases, in particular at the two peaks. As the field increases to 250 mV/nm, the P-P

RDF shows a big drop, which suggests a very remarkable structural variation in the bilayer membrane. This is also demonstrated by the total APL of the lipid membrane at 250 mV/nm. Conversely, only a peak around 0.8 nm can be found in the N-N RDF, as plotted in Figure 5.18(b). Similarly, the N-N RDF changes slightly when the field strength is less than 250 mV/nm. Nonetheless, a large drop appears in the N-N RDF at 250 mV/nm. These results suggest that 250 mV/nm is sufficient to result in a significant structural alteration of the bilayer membrane over 200 ns time; below this value the bilayer will not undergo such a change or will require more time. To further demonstrate this result, two electric fields lower than 250 mV/nm, i.e., 150 and 200 mV/nm field strengths, are chosen to study the dynamics of the lipid membrane over longer lasting time. The production time of the membrane system is increased to 2000 ns. As presented in Figure 5.19, no significant structural change is found in the membrane system. Meanwhile, there are almost no water molecules in the centre of the membrane, which indicates that the spacing between lipid molecules is insufficient to allow water molecules to enter the interior of the membrane structure. This provides strong evidence for the result that electric fields lower than 250 mV/nm might require a much longer duration to disrupt the membrane structure.

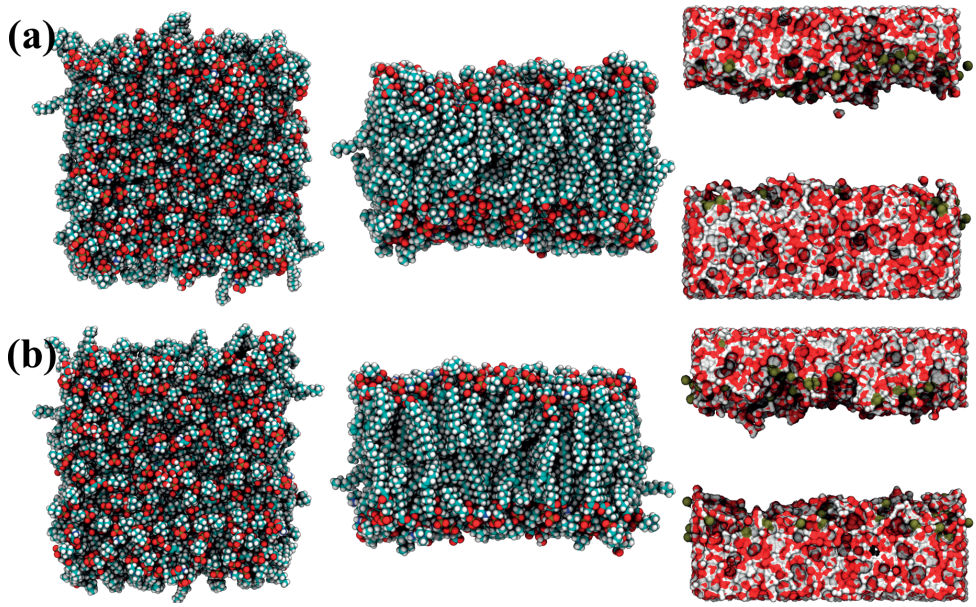


Figure 5.19: End snapshots of the membrane system at field strengths of (a) 150 and (b) 200 mV/nm with a production time of 2000 ns.

It is evident from the simulation that there is a significant difference in the molecular dynamics of the bilayer membrane at different field strengths. As plotted in Figure D.12, at electric fields below 250 mV/nm, there is no very obvious change in the membrane structure, but the membrane structure is completely destroyed when the field strength reaches 250 mV/nm. Furthermore, the simulation result for the 2000 ns running time



Figure 5.20: Nanoporation of the bilayer membrane for an electric field of 250 mV/nm, directed from bottom to top, with the positive electrode at the top.

suggests that the disruption of the membrane structure needs a much longer running time at electric fields below 250 mV/nm. Therefore, it is concluded that 250 mV/nm is the threshold field strength within 200 ns duration or even 2000 ns, above which the membrane structure is easily damaged in a short time (less than a few nanoseconds). A previous study confirms that a small decrease in electric fields that are lower

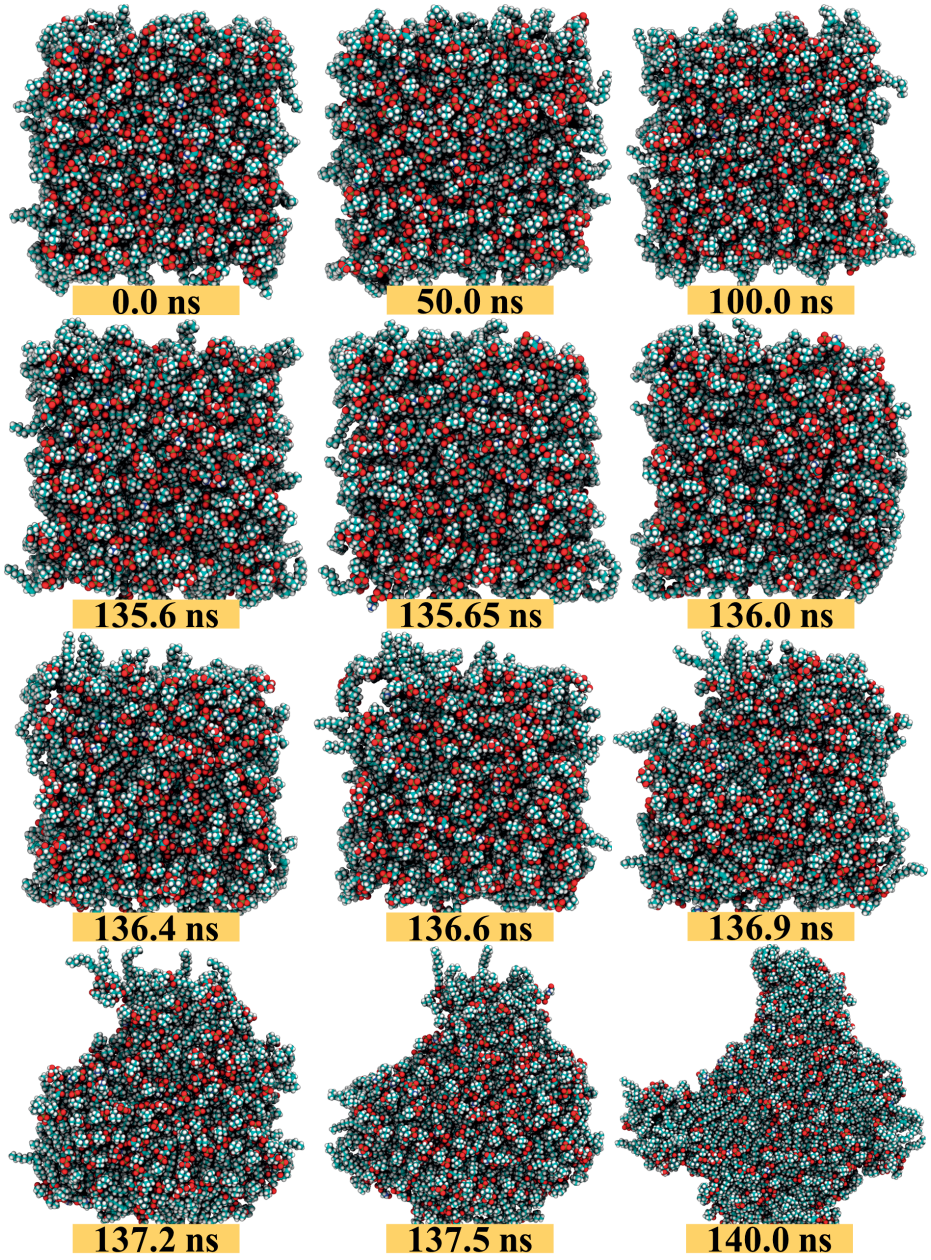


Figure 5.21: The variation in the bilayer membrane over time under an electric field of 250 mV/nm.

than the threshold field strength results in an exponential increase in average time to the nanopore formation [59]. This further proves the above conclusion. The change in the membrane structure should be attributed to the transmembrane potential in-

duced by different field strengths. Figure D.13(b) clearly displays that the potential of the lipid membrane is almost unchanged when an electric field is less than 250 mV/nm, while there is a noticeable difference at a field of 250 mv/nm. Its charge density also exhibits a similar change behavior (see Figure D.13(b)). Figure 5.20 and 5.21 visually present the nanoporation formation in the bilayer membrane at an electric field of 250 mV/nm. At the initial stage of nanoporation formation, several lipids with inward-facing head-group dipoles are formed. The position of their head-groups shifts closer to the membrane center than without the electric field. This contributes to the entry of water molecules into the bilayer membrane. As shown in Figure 5.20, water intrusion occurs at ~136 ns, from the cathode side of the lipid membrane. With further increases in time, the nanopore expands, becomes more cylindrical and forms a new, highly curved, quasi-stable lipid-water interface, resulting in a hydrophilic nanopore. The membrane structure is eventually disrupted when the electric field is maintained for a sufficiently long time. The time between the appearance of the nanoporation-forming dimple and the formation of the hydrophobic portion is roughly 0.4 ns, which exceeds that (typically less than 0.2 ns) published in a previous study [59]. In this time gap, the lipids and water molecules move into the interior of the bilayer membrane, forming a cone of the lipid head-groups surrounding water molecules. Furthermore, another MD study has demonstrated that the radius of the nanoporation remains constant and the head-group dipoles remain in the same orientation as the electric field when the field strength is reduced to half that of the applied electric field during the hydrophilic nanopore stage [60]. Reducing the electric field to zero leads to a randomization of the head-group dipole angles and the reduction of the hydrophilic nanoporations. Eventually, the nanopores will disappear and the lipid membrane will be repaired. The time for the disappearance of the nanoporations is larger than for the formation of the nanopores, which is generally more than 0.1 ns [59].

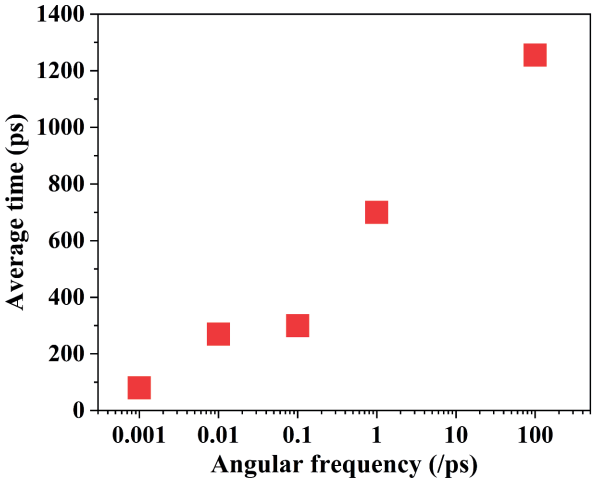


Figure 5.22: The average time to nanopore formation as a function of angular frequency.

As the experimental results suggest, the AC treatment has a higher inactivation rate

at the same conditions than the DC treatment. Furthermore, different frequencies of AC input also show an obvious effect on the virus inactivation. Therefore, it is meaningful to study the dynamics of the lipid membrane under different w values. Figure 5.22 shows the relationship between w and the average time to the nanopore formation. As we can see, the average time has a nearly linear relationship with the $\log_{10}$ of w values. With the w increases, the average time to nanopore formation linearly increases. This means that higher w values take a longer average time to form nanopores in the lipid membrane. Here, the average time to nanopore formation is 80, 270, 300, 700, and 1255 ps for 0.001, 0.01, 0.1, 1, and 100 ps^{-1}, respectively. At the same field strength (i.e., 1000 mV/nm), the average time to nanopore formation is 100 ps for the static field and the formation process of the nanopores is displayed in Figure D.16 and D.17. In comparison, the AC field with 0.001 ps^{-1} requires less time to form nanopores in the membrane. Therefore, this might interpret the low inactivation rate of the DC treatment. The nanoporation in the lipid membrane at different w values is shown in Figure D.18.

5.5. CONCLUSIONS

In summary, three microelectrodes are designed and fabricated to explore their probability of inactivating viruses, and SARS-CoV-2 in particular. We also investigate the dynamic behavior of the bilayer membrane at varying electric fields using molecular dynamics simulations. The experimental results clearly indicate that the out-of-phase castellated microelectrode has the highest inactivation rate for the phi-6 viruses compared to the interdigitated and the in-phase castellated microelectrodes. The DC treatment at 30 V shows no obvious reduction in the viral titer, while there clearly is one in the AC treatment at 40-45 V. Besides, an AC voltage with a high frequency gives a higher inactivation than a low-frequency one. The titer reduction of the virus depends strongly on the medium suspending the virus, and there are weak DEP forces to attract the virus. The inactivation of E. coli displays that the inactivation effectiveness strongly depends to AC voltage and AC frequency. The morphological analysis of E. coli clearly shows that electric fields will damage the lipid envelope, which is one of the major causes of pathogen death. The simulation results disclose that electric fields less than the threshold field (250 mV/nm) do not lead to the disruption of the bilayer structure even after 200 ns, while 250 mV/nm results in the instantaneous collapse of the bilayer. This is supported by the structural information, including total APL, membrane thickness, mass density, electron density, and radial distribution function. Those findings not only confirm the feasibility of microelectrode inactivation against viruses, but also provide the molecular-level perspective for uncovering the effect of electric fields on the bilayer membrane of virions.

REFERENCES

[1] D. Malvy, A. K. McElroy, H. de Clerck, S. Günther, and J. van Griensven, "Ebola virus disease", *The Lancet*, vol. 393, no. 10174, pp. 936–948, 2019.

[2] G. Neumann, T. Noda, and Y. Kawaoka, "Emergence and pandemic potential of swine-origin h1n1 influenza virus", *Nature*, vol. 459, no. 7249, pp. 931–939, 2009.

[3] J. M. Hughes, "Sars: An emerging global microbial threat.", *Transactions of the American Clinical and Climatological Association*, vol. 115, p. 361, 2004.

[4] C. T. Bauch and T. Oraby, "Assessing the pandemic potential of mers-cov", *The Lancet*, vol. 382, no. 9893, pp. 662–664, 2013.

[5] S. F. Pedersen, Y.-C. Ho, *et al.*, "Sars-cov-2: A storm is raging", *The Journal of clinical investigation*, vol. 130, no. 5, pp. 2202–2205, 2020.

[6] G. Xiling, C. Yin, W. Ling, *et al.*, "In vitro inactivation of sars-cov-2 by commonly used disinfection products and methods", *Scientific Reports*, vol. 11, no. 1, pp. 1–9, 2021.

[7] S. Boegel, M Gabriel, M Sasges, *et al.*, "Robust evaluation of ultraviolet-c sensitivity for sars-cov-2 and surrogate coronaviruses", *Microbiology Spectrum*, vol. 9, no. 2, e00537–21, 2021.

[8] J. Burton, H. Love, K. Richards, *et al.*, "The effect of heat-treatment on sars-cov-2 viability and detection", *Journal of virological methods*, vol. 290, p. 114 087, 2021.

[9] A. Ruiz-Fernández, M Rosemblatt, and T Perez-Acle, "Nanosecond pulsed electric field (nspef) and vaccines: A novel technique for the inactivation of sars-cov-2 and other viruses?", *Annals of Medicine*, vol. 54, no. 1, pp. 1749–1756, 2022.

[10] J. Riener, F. Noci, D. A. Cronin, D. J. Morgan, and J. G. Lyng, "Combined effect of temperature and pulsed electric fields on pectin methyl esterase inactivation in red grapefruit juice (citrus paradisi)", *European Food Research and Technology*, vol. 228, no. 3, pp. 373–379, 2009.

[11] G Saldana, E Puertolas, S Monfort, J Raso, and I Alvarez, "Defining treatment conditions for pulsed electric field pasteurization of apple juice", *International Journal of Food Microbiology*, vol. 151, no. 1, pp. 29–35, 2011.

[12] M Amiali, M. Ngadi, J. Smith, and G. Raghavan, "Synergistic effect of temperature and pulsed electric field on inactivation of escherichia coli o157: H7 and salmonella enteritidis in liquid egg yolk", *Journal of Food Engineering*, vol. 79, no. 2, pp. 689–694, 2007.

[13] S. Asavasanti, S. Ersus, W. Ristenpart, P. Stroeve, and D. M. Barrett, "Critical electric field strengths of onion tissues treated by pulsed electric fields", *Journal of food science*, vol. 75, no. 7, E433–E443, 2010.

[14] S Toepfl, V Heinz, and D Knorr, "High intensity pulsed electric fields applied for food preservation", *Chemical engineering and processing: Process intensification*, vol. 46, no. 6, pp. 537–546, 2007.

[15] X. Liu, T. Lendormi, and J.-L. Lanoisellé, "Conventional and innovative hygienization of feedstock for biogas production: Resistance of indicator bacteria to thermal pasteurization, pulsed electric field treatment, and anaerobic digestion", *Energies*, vol. 14, no. 7, p. 1938, 2021.

[16] A. Angersbach, V. Heinz, and D. Knorr, "Effects of pulsed electric fields on cell membranes in real food systems", *Innovative Food Science & Emerging Technologies*, vol. 1, no. 2, pp. 135–149, 2000.

[17] A. Sale and W. Hamilton, "Effects of high electric fields on microorganisms: I. killing of bacteria and yeasts", *Biochimica et Biophysica Acta (BBA)-General Subjects*, vol. 148, no. 3, pp. 781–788, 1967.

[18] W. Hamilton and A. Sale, "Effects of high electric fields on microorganisms: Ii. mechanism of action of the lethal effect", *Biochimica et Biophysica Acta (BBA)-General Subjects*, vol. 148, no. 3, pp. 789–800, 1967.

[19] G. Barbosa-Cánovas, D. Sepúlveda, *et al.*, "Present status and the future of pef technology", *Novel food processing technologies*, pp. 1–44, 2005.

[20] U. Zimmermann, "Electrical breakdown, electropermeabilization and electrofusion", *Reviews of Physiology, Biochemistry and Pharmacology, Volume 105*, pp. 175–256, 1986.

[21] T. Y. Tsong, "On electroporation of cell membranes and some related phenomena", *Journal of electroanalytical chemistry and interfacial electrochemistry*, vol. 299, no. 3, pp. 271–295, 1990.

[22] M. Khadre and A. Yousef, "Susceptibility of human rotavirus to ozone, high pressure, and pulsed electric field", *Journal of food protection*, vol. 65, no. 9, pp. 1441–1446, 2002.

[23] D. Mantri, "Concentrating and inactivating the surrogate of sars cov-2 using electric fields on micro-chip platforms", 2022.

[24] D. Mantri, L. Wymenga, J. van Turnhout, H. van Zeijl, and G. Zhang, "Manipulation, sampling and inactivation of the sars-cov-2 virus using nonuniform electric fields on micro-fabricated platforms: A review", *Micromachines*, vol. 14, no. 2, p. 345, 2023.

[25] M. P. Hughes, H. Morgan, F. J. Rixon, J. P. Burt, and R. Pethig, "Manipulation of herpes simplex virus type 1 by dielectrophoresis", *Biochimica et Biophysica Acta (BBA)-General Subjects*, vol. 1425, no. 1, pp. 119–126, 1998.

[26] I. Ermolina, J. Milner, and H. Morgan, "Dielectrophoretic investigation of plant virus particles: Cow pea mosaic virus and tobacco mosaic virus", *Electrophoresis*, vol. 27, no. 20, pp. 3939–3948, 2006.

[27] J. Ding, R. M. Lawrence, P. V. Jones, B. G. Hogue, and M. A. Hayes, "Concentration of sindbis virus with optimized gradient insulator-based dielectrophoresis", *Analyst*, vol. 141, no. 6, pp. 1997–2008, 2016.

[28] B. I. Morshed, M. Shams, and T. Mussivand, "Investigation of low-voltage pulse parameters on electroporation and electrical lysis using a microfluidic device with interdigitated electrodes", *IEEE Transactions on biomedical engineering*, vol. 61, no. 3, pp. 871–882, 2013.

[29] C. R. Arbeitman, P. Rojas, P. Ojeda-May, and M. E. Garcia, "The sars-cov-2 spike protein is vulnerable to moderate electric fields", *Nature communications*, vol. 12, no. 1, pp. 1–13, 2021.

[30] Á. Serrano-Aroca, "Antiviral characterization of advanced materials: Use of bacteriophage phi 6 as surrogate of enveloped viruses such as sars-cov-2", *International Journal of Molecular Sciences*, vol. 23, no. 10, p. 5335, 2022.

[31] M. Ferraz, F. M. Monteiro, and J. Barros, "Bacteriophage phi 6 as surrogate and human-harmless viruses to study anti-sars-cov-2 approaches", 2021.

[32] A. Fedorenko, M. Grinberg, T. Orevi, and N. Kashtan, "Survival of the enveloped bacteriophage phi6 (a surrogate for sars-cov-2) in evaporated saliva microdroplets deposited on glass surfaces", *Scientific reports*, vol. 10, no. 1, pp. 1–10, 2020.

[33] B. Ma, P. M. Gundy, C. P. Gerba, M. D. Sobsey, and K. G. Linden, "Uv inactivation of sars-cov-2 across the uvc spectrum: Krcl* excimer, mercury-vapor, and light-emitting-diode (led) sources", *Applied and environmental microbiology*, vol. 87, no. 22, e01532–21, 2021.

[34] C. Lytle, A. Budacz, E Keville, S. Miller, and K. Prodouz, "Differential inactivation of surrogate viruses with merocyanine 540", *Photochemistry and photobiology*, vol. 54, no. 3, pp. 489–493, 1991.

[35] S. B. Jeong, J. H. Shin, S. W. Kim, S. C. Seo, and J. H. Jung, "Design and performance evaluation of an electrostatic precipitator for viral aerosol control using a surrogate for sars-cov-2", *Available at SSRN 4166515*,

[36] P. Vatter, K. Hoenes, and M. Hessling, "Photoinactivation of the coronavirus surrogate phi6 by visible light", *Photochemistry and Photobiology*, vol. 97, no. 1, pp. 122–125, 2021.

[37] R. Bangiyev, M. Chudaev, D. W. Schaffner, and E. Goldman, "Higher concentrations of bacterial enveloped virus phi6 can protect the virus from environmental decay", *Applied and environmental microbiology*, vol. 87, no. 21, e01371–21, 2021.

[38] S.-W. Lee and Y.-C. Tai, "A micro cell lysis device", *Sensors and Actuators A: Physical*, vol. 73, no. 1-2, pp. 74–79, 1999.

[39] D. W. Lee and Y.-H. Cho, "A continuous electrical cell lysis device using a low dc voltage for a cell transport and rupture", *Sensors and Actuators B: Chemical*, vol. 124, no. 1, pp. 84–89, 2007.

[40] M. Fox, D. Esveld, A Valero, *et al.*, "Electroporation of cells in microfluidic devices: A review", *Analytical and bioanalytical chemistry*, vol. 385, no. 3, pp. 474–485, 2006.

[41] V. F. Veiga, L. Nimrichter, C. A. Teixeira, *et al.*, "Exposure of human leukemic cells to direct electric current", *Cell Biochemistry and Biophysics*, vol. 42, no. 1, pp. 61–74, 2005.

[42] Y. Zhou, Y. Wang, and Q. Lin, "A microfluidic device for continuous-flow magnetically controlled capture and isolation of microparticles", *Journal of Microelectromechanical Systems*, vol. 19, no. 4, pp. 743–751, 2010.

[43] K. Park, D. Akin, and R. Bashir, "Electrical capture and lysis of vaccinia virus particles using silicon nano-scale probe array", *Biomedical microdevices*, vol. 9, no. 6, pp. 877–883, 2007.

[44] H. Lu, M. A. Schmidt, and K. F. Jensen, "A microfluidic electroporation device for cell lysis", *Lab on a Chip*, vol. 5, no. 1, pp. 23–29, 2005.

[45] H. Sadeghian, Y. Hojjat, and M. Soleimani, "Interdigitated electrode design and optimization for dielectrophoresis cell separation actuators", *Journal of Electrostatics*, vol. 86, pp. 41–49, 2017.

[46] M Castellarnau, A Errachid, C Madrid, A Juarez, and J Samitier, "Dielectrophoresis as a tool to characterize and differentiate isogenic mutants of escherichia coli", *Biophysical journal*, vol. 91, no. 10, pp. 3937–3945, 2006.

[47] S. Shen, T. Zhang, Y. Yuan, S. Lin, J. Xu, and H. Ye, "Effects of cinnamaldehyde on escherichia coli and staphylococcus aureus membrane", *Food control*, vol. 47, pp. 196–202, 2015.

[48] M. Ferrer, T. N. Chernikova, M. M. Yakimov, P. N. Golyshin, and K. N. Timmis, "Chaperonins govern growth of escherichia coli at low temperatures", *Nature biotechnology*, vol. 21, no. 11, pp. 1266–1267, 2003.

[49] P. Kumar and A. Libchaber, "Pressure and temperature dependence of growth and morphology of escherichia coli: Experiments and stochastic model", *Biophysical journal*, vol. 105, no. 3, pp. 783–793, 2013.

[50] F. Pillet, C. Formosa-Dague, H. Baaziz, E. Dague, and M.-P. Rols, "Cell wall as a target for bacteria inactivation by pulsed electric fields", *Scientific reports*, vol. 6, no. 1, p. 19 778, 2016.

[51] N Boudjema, M Kherat, N Drouiche, and N Mameri, "Investigation of the mechanisms of escherichia coli cells sterilization by the application of an electric field", *International Journal of Environmental Science and Technology*, vol. 16, pp. 6259–6266, 2019.

[52] C. Liu, P. Elvati, and A. Violi, "On drug-membrane permeability of antivirals for sars-cov-2", *The journal of physical chemistry letters*, vol. 12, no. 5, pp. 1384–1389, 2021.

[53] Z. Saud, V. J. Tyrrell, A. Zaragkoulias, *et al.*, "The sars-cov2 envelope differs from host cells, exposes pro-coagulant lipids, and is disrupted in vivo by oral rinses", *Journal of lipid research*, p. 100 208, 2022.

[54] M. J. Abraham, T. Murtola, R. Schulz, *et al.*, "Gromacs: High performance molecular simulations through multi-level parallelism from laptops to supercomputers", *SoftwareX*, vol. 1, pp. 19–25, 2015.

[55] J. B. Klauda, R. M. Venable, J. A. Freites, *et al.*, "Update of the charmm all-atom additive force field for lipids: Validation on six lipid types", *The journal of physical chemistry B*, vol. 114, no. 23, pp. 7830–7843, 2010.

[56] R. S. Dondapati, "Overview of gromacs", *Molecular Dynamics Simulation of Nanocomposites using BIOVIA Materials Studio, Lammps and Gromacs*, p. 70, 2019.

[57] W. Humphrey, A. Dalke, and K. Schulten, "Vmd: Visual molecular dynamics", *Journal of molecular graphics*, vol. 14, no. 1, pp. 33–38, 1996.

[58] S. S. Jain, A. Suresh, and E. Pirogova, "Effects of oscillating electric fields on conotoxin peptide conformation: A molecular dynamic simulation study", *Journal of Molecular Graphics and Modelling*, vol. 103, p. 107 799, 2021.

[59] M. J. Ziegler and P. T. Vernier, "Interface water dynamics and porating electric fields for phospholipid bilayers", *The Journal of Physical Chemistry B*, vol. 112, no. 43, pp. 13 588–13 596, 2008.

[60] P. T. Vernier and M. J. Ziegler, "Nanosecond field alignment of head group and water dipoles in electroporating phospholipid bilayers", *The Journal of Physical Chemistry B*, vol. 111, no. 45, pp. 12 993–12 996, 2007.

6

CONCLUSION AND FUTURE PERSPECTIVE

In this chapter, all research works in the above-mentioned would be summarized, and some suggestions for future related research are figured out for discussion.

6.1. CONCLUSIONS

Up to now, COVID-19 pandemics associated with SARS-CoV-2 remain endemic worldwide. Its presence poses a considerable threat to the development of human society and life health. Because of the infectious, lethal, and mutagenic natures of SARS-CoV-2, the effective inactivation of SARS-CoV-2 has become important issue in the scientific field. Although there are various available methods for inactivating SARS-CoV-2, their efficiency and usefulness are variable. Therefore, it is urgent to explore more effective disinfection methods for human CoVs, and multi UVC-LEDs and the electric fields generated by microelectrodes in particular. Furthermore, massive efforts have been performed on the antiviral activity of chemical and physical methods against bacteria and some viruses at the experimental and theoretical levels. However, their theoretical and molecular-level understanding of the inactivation mechanisms of viruses is still unclear and debated, especially SARS-CoV-2. Consequently, deciphering molecular mechanisms of chemical and physical approaches for inactivating SARS-CoV-2 is worth investigating to provide a theoretical perspective in depth for the actual treatment and prevention. This thesis aims to reveal the molecular-level mechanism of chemical and physical approaches for inactivating SARS-CoV-2 using DFT and MD simulations in-depth, explore the optimal recipe of UVC irradiation and the feasibility of electric fields generated by microelectrodes on microchips for inactivating SARS-CoV-2. In order to achieve those purposes, the central research for this thesis focuses on the following.

Study on the inactivation mechanism of high temperature. Utilizing the MD method, the possible impact of high temperature on the lipid membrane of SARS-CoV-2 is theoretically investigated. It is found that the total APL of the bilayer membrane is positively correlated with temperature, whereas the membrane thickness gradually decreases with increasing temperature. However, there is no water in the interior of the bilayer membrane, regardless of temperature. This result means that the spacing between lipid molecules is insufficient to enable water molecules to penetrate the interior of the lipid membrane. Therefore, high temperatures do not destroy the bilayer structure, which is consistent with the experimental result that the disruption of the viral envelope is rare. Besides, the mass and electron density profiles suggest that the head-groups of the lipid molecules are sensitive to temperatures compared to the fatty acid tail. Upon heating, the lipid membrane transitions into the liquid-disordered phase in which lipid molecules intensely diffuse in the membrane plane, and their fatty acid tails are considerably flexed and bent. The end snapshots of the bilayer membrane further confirm this phenomenon. In 2D RDFs of P-P and N-N atomic pairs, we find that the height at the peak decreases as the temperature increases, which may be attributed to the lateral expansion of the lipid membrane.

Study on the inactivation mechanism of chemical disinfectants. The interaction mechanism of chemical agents with 3CL hydrolase and phospholipid membrane of SARS-CoV-2 is investigated by adopting the MD or combining the DFT method. For the case of 3CL hydrolase, it is found that ethanol and hypochlorite molecules are more sensitive to the GLU and ASP residues of 3CL hydrolase than other residues. In contrast, silver ion is readily bonded to THR and PHE residues. The RDF results suggest that the unsaturated oxygen atoms of GLU, ASP, THR, and PHE residues play a crucial role in the interaction process of those three biocidal ingredients. The increase in ethanol concen-

tration results in the strengthening of the interaction between ethanol molecules and 3CL hydrolase. However, there is a critical value for concentration, and larger than this value, the probability of acting molecules appearing within a specific region is reduced. This result confirms that the concentration of acting molecules determines the disinfection efficiency. Furthermore, the DFT results clearly show that the hydrogen bonds are responsible for the interaction of ethanol and hypochlorite with residues, while the silver ion-PHE residues constraint can be attributed to the pseudo-covalent bond. For the case of a bilayer membrane, we find that the presence of chemical agents (i.e., ethanol and HClO) causes the structural alteration of the bilayer membrane, such as lateral expansion and a reduction of membrane thickness. Moreover, at the same concentration, the account of HClO molecules in the hydrophobic portion of the bilayer is more than ethanol molecules. Ethanol and HClO molecules mainly accumulate in the lipid-water interface. Gradual thinning of thickness, lateral expansion, and accumulation of hydrophilic substances eventually accelerate the decomposition of the virus membrane.

Study on the inactivation recipe and mechanism of UVC irradiation. By designing and constructing the inactivation platform with a UVC-LED array, the inactivation experiments for Influenza A PR8 are conducted. In the meantime, the molecular-level mechanism of UVC irradiation for inactivating the selected virus is clarified at the theoretical level by applying quantum chemical calculation. In the theoretical calculations, four nucleotides are chosen as the investigated objects. The results indicate that the dual-wavelength irradiation has no obvious advantage over the single-wavelength irradiation. The wavelength of 259 nm has the best inactivation affection due to its most considerable logarithm reduction. The calculated absorption spectra visually display that the strongest absorption peak is at 248.7 nm, 226.1 nm (252.7 nm), 248.3 nm, and 205.8 nm (249.2 nm) for adenine, cytosine, guanine, and uracil nucleotides, respectively. These wavelengths are close to the obtained data at the inactivation experiments. Furthermore, the introduction of an aqueous solution would strengthen the absorption spectra of the investigated nucleotides, and a red- or blue-shifted phenomenon can be found. According to the results of the transition state and reaction rate constant, it can be found that the molecular reaction between adjacent nucleotides is a photochemical process in the presence of UVC light. The reaction rate constants for the ground and excited states turned out to be 6.419×10^{-49} and 5.436×10^{11} $s^{-1}\cdot M^{-1}$, respectively. The corresponding half-life is 1.56×10^{48} and 1.84×10^{-12} s, respectively. As a result, the reactions for adjacent nucleotides in the presence of UVC light easily occur and vice versa with extreme difficulty.

Study on the viral inactivation and mechanism of electric fields generated by microelectrodes. By designing and fabricating three microelectrodes on microchips, the inactivation experiments for viruses are performed. At the same time, the inactivation mechanism of electric field treatment against viruses is uncovered at the molecular level using the MD method. In the experiments, the phi-6 is selected as an alternative to SARS-CoV-2 because of its low bio-safety level requirements. In the simulations, the lipid membrane is chosen as the target of the electric field. The experimental results show that the out-of-phase castellated microelectrode is superior to other microelectrodes due to its highest titer reduction. In contrast to DC treatment, AC treatment contributes to a high inactivation rate. The AC frequency also plays a vital role in titer reduction. Furthermore,

the reduction in viral titer highly depends on samples' medium and virus concentration. Weak DEP forces attract the viruses to the surface of microelectrodes. The inactivation of E. coli on microelectrodes is also studied. The results confirms that the inactivation efficacy is strongly dependent on the AC voltage and frequency. Electric fields will damage the lipid envelop of enveloped pathogens, which is supported by the morphological analysis of E. coli. According to the MD results, it is found that 250 mV/nm can result in the disruption of the lipid membrane in 200 ns production time, and there is an instantaneous collapse of the bilayer around 140 ns. Meanwhile, the nanopore of the membrane begins to occur at 135 ns. Nevertheless, electric fields less than 250 mV/nm do not significantly change in the lipid membrane even after running 200 ns production time.

6.2. FUTURE PERSPECTIVE

The efforts to seek new methods of pathogen inactivation have never been interrupted, with more in-depth theoretical mechanism and phenomenon in particular. The current research works theoretically clarify the molecular-level mechanism of viral inactivation in the presence of high temperature, chemical disinfectants, UVC light, and electric field. Meanwhile, based on the UVC inactivation experiment, the optimal inactivation recipe for the target virus is determined. Furthermore, from the perspective of miniaturization of inactivation components, three microelectrodes fabricated on microchips for electric field inactivation of viruses are studied, suggesting that those microelectrodes have very high viability for viral inactivation. These researches have obtained some achievements. However, there are still some things that could be improved for the current research works, such as the absence of four major structural proteins in the constructed bilayer membrane of SARS-CoV-2 and only choosing the affection of UVC light on genetic materials. In the meantime, theoretical calculation methods still have some limitations at present. Therefore, the main works for the next step are as follows:

For the inactivation mechanism of conventional chemical and physical methods, only 3CL hydrolase and the bilayer membrane of SARS-CoV-2 are considered here. In fact, as the crucial key to unlocking the host cells, the S protein's biological denaturation is also critical to the inactivation of SARS-CoV-2. Therefore, the action mechanism of chemical agents on S protein should be investigated in depth. Meanwhile, chemical agents should be selected according to their chemical properties. Furthermore, the affection of high temperature on S proteins is also one of the main research contents. The absence of structural proteins in the bilayer membrane could reduce interaction factors between the simulation model and acting molecules. Thus, a complete bilayer membrane containing structural proteins, especially S protein, is essential to obtain more comprehensive simulation results.

In the inactivation experiment of UVC irradiation, only UVC-LEDs with wavelengths larger than 250 nm are taken into account. The inactivation efficiency and reduction rate for wavelengths smaller than 250 nm are still unknown. Therefore, to figure out the most optimal recipe, the irradiation wavelengths should be extended below 250 nm. Besides, there is no significant advantage in the dual-wavelength experiment groups compared to the single-wavelength groups. This result is supported by a 1-log manual experiment variance. Nevertheless, the dual-wavelength scheme is still worth exploring when we have UVC-LEDs with wavelengths smaller than 250 nm and the related experimental

equipment. Furthermore, the variety of viruses in the experiment can be more homogeneous. All calculations for the inactivation mechanism of UVC irradiation are based on the hypothesis that RNA absorbance is the leading cause of the dominant genome damage. The fact is that proteins in viruses can also be denatured during UVC irradiation, leading to genetic or viral inactivation. Therefore, the influence of proteins in viral inactivation should be studied in the next step. In the simulation, the models are more idealistic. Thus, there is still some error with experimental results.

In the inactivation experiment of electric fields, the obtained results are insufficient to deduce the virus's inactivation mechanism. Notably, the studied virus is not SARS-CoV-2. Thus, the experiments on SARS-CoV-2 virions should be repeated to better evaluate the feasibility of microelectrodes in viral inactivation. Meanwhile, the micro-analysis of the virus before and after electric field treatment also should be carried out to clarify the structural variations of the virus-induced by electric fields. A better electrode design and fabrication should be performed to obtain more stable experimental data, such as the probability reduction of short circuits in the electrodes and the construction of microchannel around the electrodes to minimize evaporation and contamination of the sample. Furthermore, the movement of virus particles on the electrodes needs to be observed with a fluorescence microscope. The labeling of viruses with fluorescent modules may provide additional insights into the electrophoretic behavior and inactivation mechanisms of coronaviruses to support the claims made in this study. Eventually, the dynamics of the lipid membrane with structural proteins at varying electric fields need to be studied.

The limitations of the calculation methods limit the breadth, depth, and usefulness of our current research works. Currently, many advanced algorithms have been introduced into theoretical simulations, such as artificial intelligence and machine learning. These advanced algorithms compensate for the shortcomings of existing simulation methods and promote the development of simulation techniques. Therefore, utilizing these advanced algorithms to support our subsequent research works is essential.

ACKNOWLEDGEMENTS

It has been such a long journey, and after enduring hard times, I have finally presented this doctoral dissertation here. During my Ph.D. period, I sincerely appreciate my family, colleagues, and friends because of their support and kindness. In beginning, I am very grateful to my supervisor Prof. Guoqi Zhang, who gave me the opportunity for this Ph.D. candidate position, the essential suggestions in my research works, and the research resources. Meanwhile, I also express my great gratitude to my daily supervisor Prof. Huaiyu Ye, who always provided me with all the research resources he could be found. Most importantly, Prof. Guoqi Zhang and Prof. Huaiyu Ye always gave me enough patience and confidence during my Ph.D. research. Therefore, my Ph.D. project can be fully developed and entirely smooth.

It is my pleasure to receive help from ECTM. I am deeply grateful to Xinyu Xu and Tianyi Jin for their outstanding contributions to the UVC-LEDs platform and inactivation experiments. They share their experimental data on the UVC inactivation of the Influenza virus on a multifunctional UVC-LED platform. Their experiment results make my thesis more rich and completion. In particular, I had a lot of discussions with Xinyu Xu about the experimental design and analysis, as well as the inactivation mechanism of UVC irradiation, and came to an agreed collaboration, thanks to her patience and kindness. Besides, I would also like to be extremely grateful to Mark from Erasmus MC for providing virus samples and performing several inactivation experiments and analyses in the BSL2 laboratory. More information about the multifunctional UVC-LED platform is shown in "Multifunctional UV-C LED Virus Inactivation Experimental Platform (Xinyu Xu, MSc thesis, TU-Delft, Sep. 2021)".

I am deeply grateful to Devashish Mantri, who contributed his effort to the design and fabrication of microelectrodes, and the viral inactivation experiments. He shares his experimental data on the electrical inactivation of the phi-6 phage on the micro-chip platform. Besides, he also supported me in the viral inactivation at different electric fields and exposure times. With his experimental data and support, the study on electric-field inactivation would have a completion. At the same time, discussing with Devashish always gave me some inspiring ideas for the simulations of the inactivation mechanism. I would also like to thank Luutzen Wymenga for providing his DC setup and helping to solve the problems we encountered during the experiments. Furthermore, I would also like to thank and show my heartfelt gratitude to Dr. S. Brouns (Fac. Applied Sciences, TU-Delft) and his co-workers for conducting the phi-6 virus titers and for providing the virus stock solution, especially Ana Rita Costa and Jelger Esser who provided helpful guidance and support in the inactivation experiment. The related information about the electrical inactivation of the phi-6 phage on the micro-chip platform is shown in "Concentrating and inactivating the surrogate of SARS CoV-2 using electric fields on micro-chip platforms and Manipulation, sampling (Devashish Mantri, MSc thesis, TU-Delft, Oct. 2022)".

Similarly, it is also my pleasure to receive help from Group Ye. All the group members are very patient and kind. They have always done their best to help me solve problems and provided the resources they have available to speed up my research, including Shaogang, Shizhen, Wucheng, Ke Liu, Junfeng, Xu Liu, and Huirui. At the same time, they always stood by me all through my difficult time. In particular, Shaogang and Ke Liu gave me huge support in the inactivation experiments of E. coli, including experimental preparation, pre-experiments, experimental design, and SEM operation. We also had many discussions about the problems we encountered during the experiments. Besides, I would also like to thank and show my heartfelt gratitude to Prof. Yi Li (Fac. microelectronics, SUSTECH) and his co-workers and students for conducting the E. coli count and for providing the E. coli stock solution and related experimental equipment, especially Jing Dai who gave helpful guidance and support in the inactivation experiment.

In addition, I truly appreciate the valuable inputs and interests of Dr. Henk van Zeijl, Prof. Jan van Turnhout, and Dr. Sander Herfst for my Ph.D. project. Last but not least, I would like to express my heartfelt gratitude to all family members who kept me sane and in good spirits throughout my Ph.D. period. With their support, I was able to finish my Ph.D. study and this thesis.

Everything in the past is a preface, and all the future is to be looked forward to.

A

SUPPORTING INFORMATION CHAPTER 2

A.1. ANALYTICAL DETAILS OF THE BILAYER MEMBRANE

The area per lipid, thickness, and deformation of the bilayer membrane is analyzed using MEMBPLUGIN, a membrane analysis tool for molecular-dynamics simulations [1]. For the calculation of area per lipid, selecting one critical atom (i.e., sterols) or a triad of atoms (i.e., phospho- or sphingolipids) is essential. Therefore, the P atom of POPC, POPE, POPI, POPS and PSM molecules is selected, while the O13 atom of cholesterol molecules is selected. The membrane thickness per frame is calculated on the basis of the projected mass distributions for the selected atoms (usually P atom). The mass projections form two mass peaks, and their distance is the membrane thickness. The first and second central moments of the mass distributions along the Z direction can be expressed as follows

$$z_0 = \sum_i m_i z_i / M \tag{A.1}$$

$$w^2 = 4 \sum_i m_i (z_i - z_0)^2 / M \tag{A.2}$$

where z_i is the coordinate along the membrane normal of the i-th atom considered, m_i is its mass, and $M = \sum_i m_i$ is the total mass. According to the structural information of the lipid molecules, the overall length of POPC, POPE, POPI, POPS, and PSM molecules is longer than that of cholesterol molecules. Thus, in order to better characterize the bilayer thickness, the P atom is chosen for the thickness computation.

A.2. DEFORMATION OF THE BILAYER MEMBRANE

Deformation is defined as the head-groups' interpolated location after translating the chosen leaflet's center at Z=0. Therefore, deformation takes on both negative and positive values. Notably, irrespective of a leaflet, deformation is positive when it expands the membrane and negative otherwise. FigureA.1 clearly shows that the deformation

caused by the varying temperatures is significantly different. According to the end snapshots' membrane structures, it is found that the phospholipid membrane has different degrees of depression (see red region) at different temperatures.

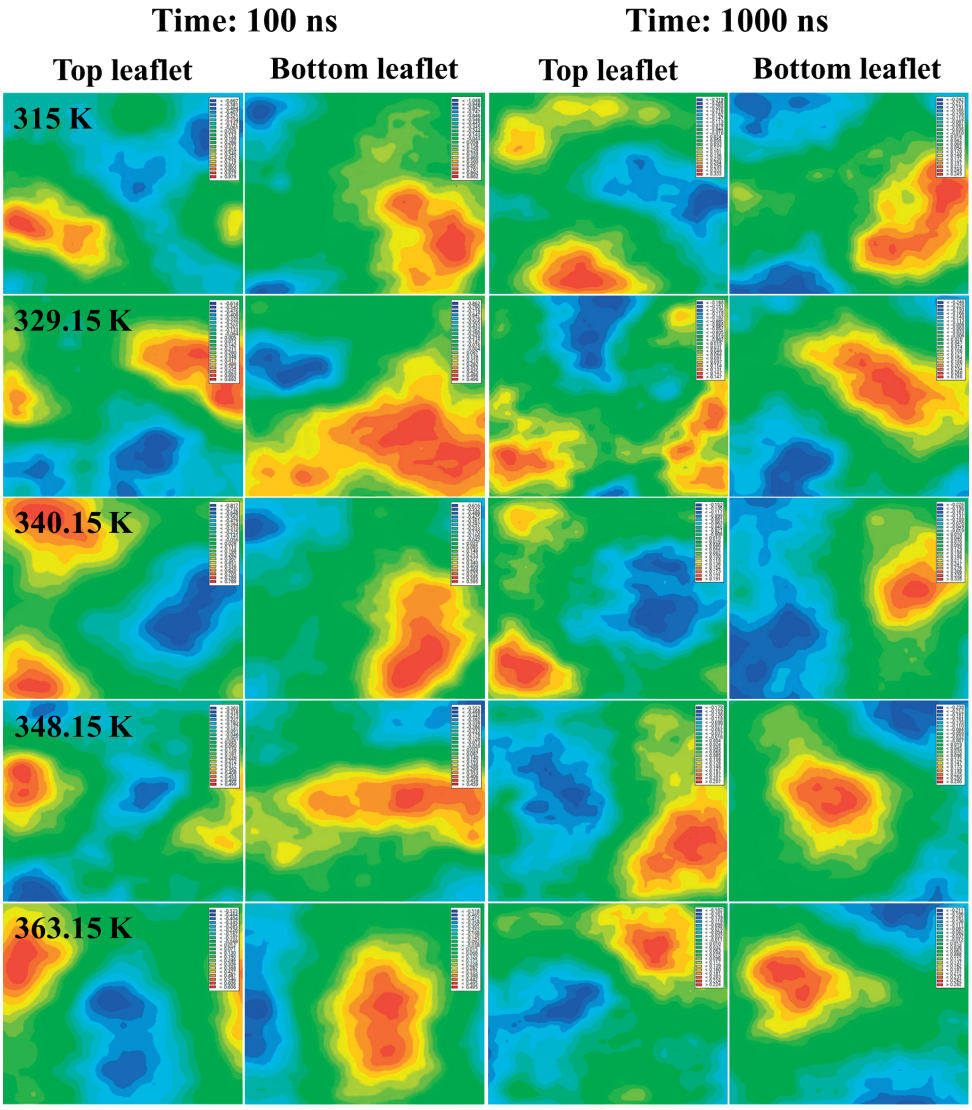


Figure A.1: Deformation in the top and bottom leaflets of the lipid membrane over 100 ns and 1000 ns production times. Note that red and blue represent positive and negative values, respectively.

REFERENCES

[1] R. Guixà-González, I. Rodriguez-Espigares, J. M. Ramírez-Anguita, *et al.*, "Membplugin: Studying membrane complexity in vmd", *Bioinformatics*, vol. 30, no. 10, pp. 1478–1480, 2014.

B

SUPPORTING INFORMATION CHAPTER 3

B.1. THE STRUCTURE OF SPIKE PROTEIN AND THE PROTEIN-ETHANOL SYSTEM

The S envelope glycoprotein, as the mediating fusion of viruses and cellular membranes, plays a vital role in the infection of SARS-CoV-2 [1], [2]. In order to make a thorough understanding of the inactivation mechanism of SARS-CoV-2, the interaction mechanism between S protein and ethanol molecules is investigated using the MD method. The structure of the S protein and the S protein-ethanol (75%) system is shown in Figure B.1.

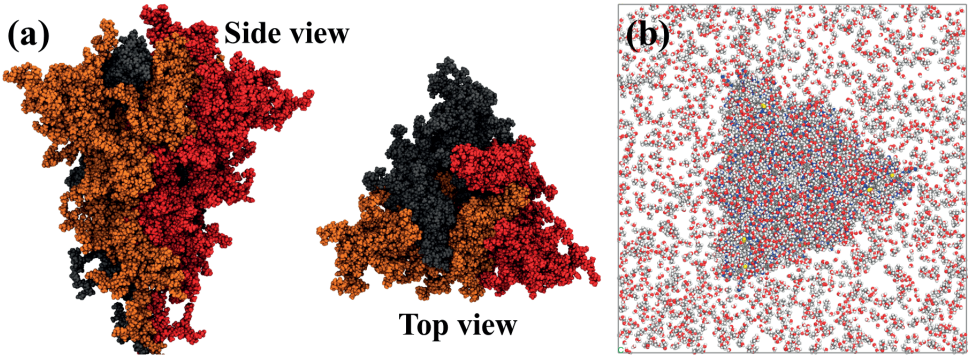


Figure B.1: The structures of (a) the S protein and (b) the S protein-ethanol (75%) system.

B.2. RADIAL DISTRIBUTION FUNCTION

Using the steepest descent and conjugate gradient algorithm, the geometric structure of the S protein-ethanol system is fully relaxed. The optimized system clearly states

that ethanol molecules are mainly concentrated near glutamate acids (GLU) and N-acetylglucosamine (NAG) residues of the S protein. Although ethanol molecules also are observed near other amino acid residues, such as aspartic acid (ASP), glutamine acid (GLN), and histidine acid (HIS) residues, the number of adsorbed molecules by them is relatively small compared with that by GLU and NAG residues. The S protein-ethanol system's radial distribution function (RDF) is analyzed based on the MD simulation trajectories. As illustrated in Figure B.2, the first peak of $g(r)_{O-O}$ of O(GLU residues)-/O(NAG residues)-O(ethanol) pairs appear around 2.0 Å and 2.5 Å, respectively, indicating the bond interactions between ethanol molecules and these two residues. Interestingly, their second peaks are depicted in the vicinity of 3.0 Å and 4.0 Å, respectively. For N(GLU residues)-/N(NAG residues)-O(ethanol) pairs, it can be found that the first peak is located within the range of 9.0-10.0 Å. Therefore, the constraint between GLU/NAG residues and ethanol molecules is contributed by the non-bond interactions, which indicates that the O atoms of GLU/NAG residues have stronger interactions with ethanol molecules than with their N atoms. This conclusion is in agreement with the calculated results of 3CL hydrolase.

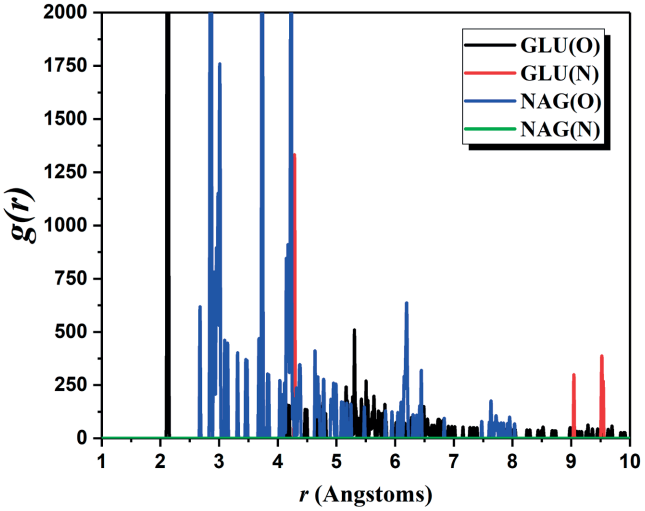


Figure B.2: Pair correlation function g(r) of the S protein with ethanol molecules.

B.3. DEFORMATION OF THE BILAYER MEMBRANE

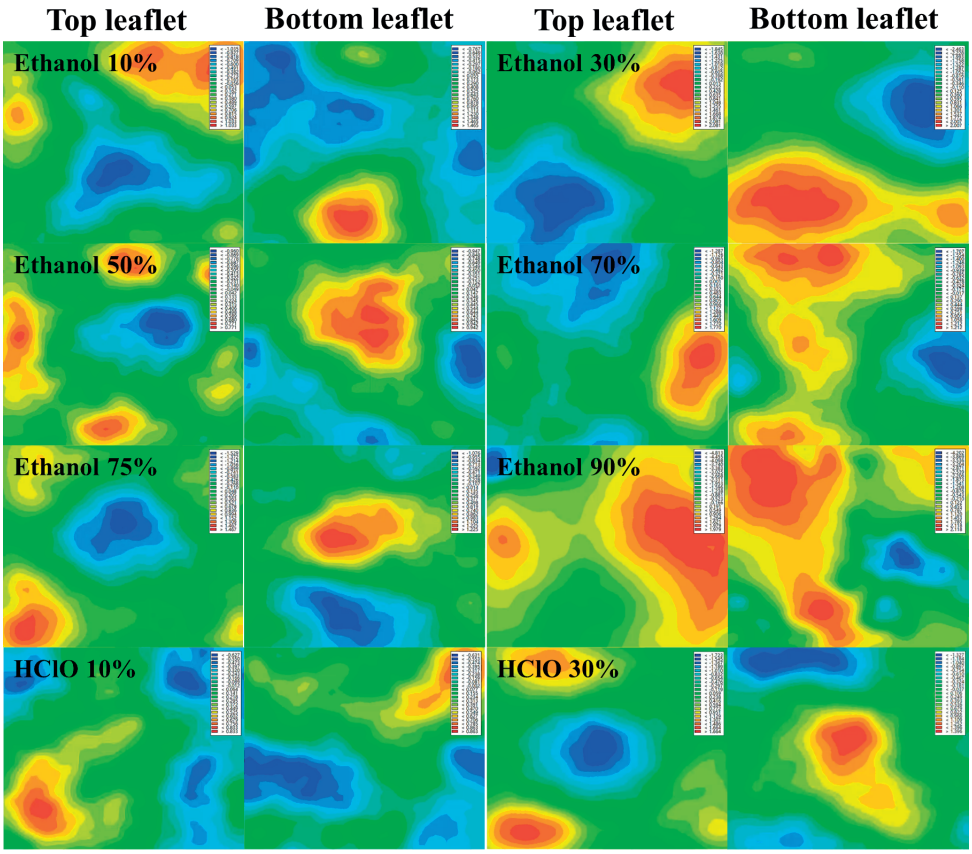


Figure B.3: Deformation in the top and bottom leaflets of the lipid membrane in the presence of ethanol and HClO. Note that red and blue represent positive and negative values, respectively.

REFERENCES

[1] C. Peng, Z. Zhu, Y. Shi, *et al.*, "Exploring the binding mechanism and accessible angle of sars-cov-2 spike and ace2 by molecular dynamics simulation and free energy calculation", 2021.

[2] J. A. Jaimes, N. M. André, J. K. Millet, and G. R. Whittaker, "Structural modeling of 2019-novel coronavirus (ncov) spike protein reveals a proteolytically-sensitive activation loop as a distinguishing feature compared to sars-cov and related sars-like coronaviruses", *arXiv preprint arXiv:2002.06196*, 2020.

C

Supporting Information Chapter 4

C.1. UVC-LED platform design for virus inactivation

C.1.1. Irradiance modeling

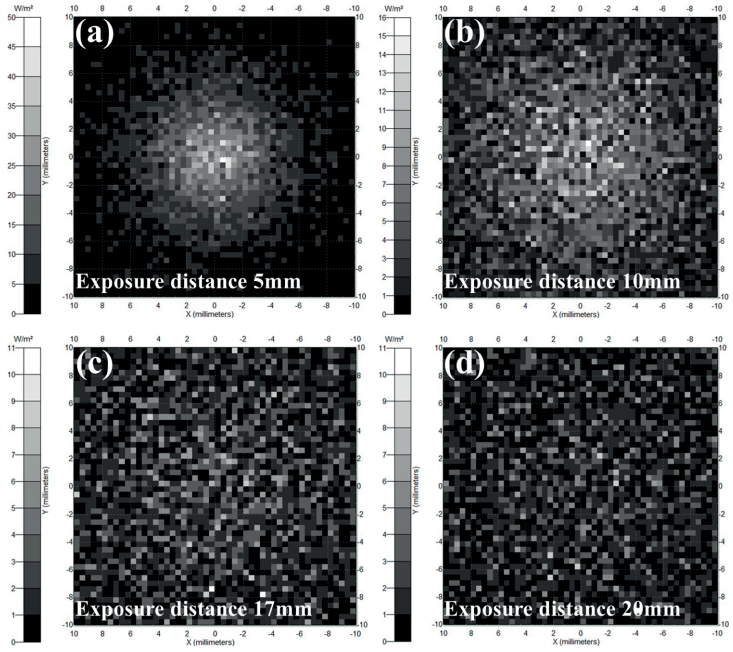


Figure C.1: Simulation of the irradiance for a single UV-LED at various exposure distances.

The exposure time for each well depends on the irradiance, i.e., the amount of ra-

diation flux emitted, reflected, transmitted, or received per unit projected surface area. Therefore, the irradiance simulation of a single UV LED is conducted at varying exposure distances. Here, four exposure distances, i.e., 5 mm, 10 mm, 17 mm, and 20 mm, are considered in this simulation. The irradiance maps at different distances are shown in Figure C.1. According to the simulation results, the average irradiance is 5.63, 3.52, 1.87, and 1.46 W/m^2 for 5, 10, 17, and 20 mm, respectively. This result suggests that the irradiance decreases with increasing exposure distance. However, it should be noted that the illumination area becomes more prominent as the exposure distance increases. Hence, selecting the exposure distance and relevant illumination area is crucial in the inactivation experiment.

C.1.2. REQUIREMENT AND DESIGN OF UVC-LED PLATFORM

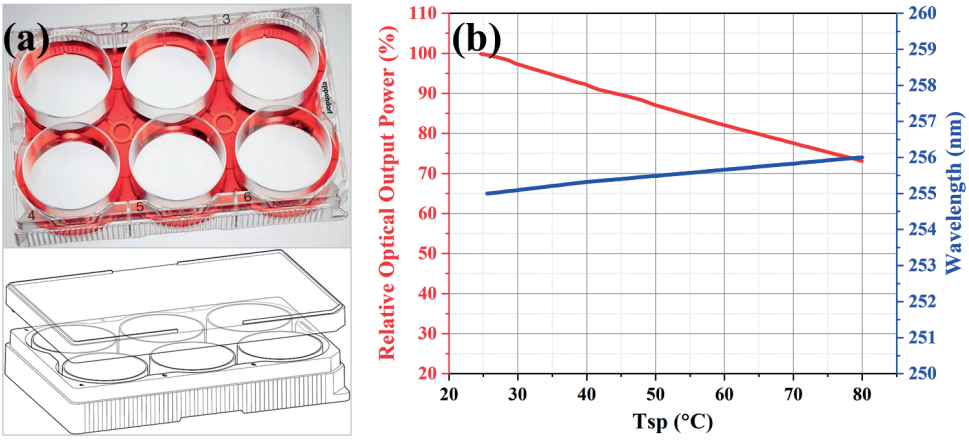


Figure C.2: (a) A commercial-grade Eppendorf cell culture plate featuring six clear, flat-bottom wells. (b) The relationship between temperature and the UCV-LED platform's optical output power and peak wavelength. Note that the Tsp represents the solder point temperature and IF is set to 100 mA.

In order to better meet the requirements of the standard virology experiments, the UVC-LED array must be designed to fit the standard virology laboratory apparatus. The UVC inactivation experiments are carried out in the Erasmus medical center because of the risk of the target virus, and commercial Eppendorf 6-well cell culture plates (see Figure C.2(a)) are adopted as the carrier plate of the target virus. In the inactivation experiment, the dried target virus has to be placed in each well. Therefore, the designed UVC-LED array contains six groups of LEDs, each directly exposes above each well of the cell culture plate at a specific exposure dose and exposure distance. Due to the widespread use of cell culture plates in standard biology research, the designed UVC-LED platform has become a consistent tool in viral inactivation studies. Notably, all the UVC-LED groups are controlled through the same driver module. Additionally, considering the effect of high temperature on the performance of UVC-LEDs, the cooling module is introduced to maintain the performance stability of the designed platform. Figure C.2(b) clearly shows that the optical output power of the UVC-LED platform decreases linearly with the increase of temperature from 25 °C to 80 °C under the 100 mA of forward current

(IF). In contrast, the peak wavelength exhibits a linearly increasing relationship with the temperature under the same IF condition. Thus, the cooling module is an essential part of the inactivation platform.

As plotted in Figure C.3, the complete inactivation experimental system comprises three main parts: UVC-LED array, driver module, and cooling module. The driver module plays a critical role in the platform. On the one hand, it can deal with the interactive signals from a personal computer, keyboard, and LCD (liquid crystal display) monitor. On the other hand, it can also provide real-time driving signals for each UVC-LED. Furthermore, the power management and communication ports are available in the driver module. Flat flexible cable connectors would carry the temperature and driving signals on the UVC-LED arrays. In order to monitor the real-time onboard temperature, temperature sensors are embedded in the center of each UVC-LED group. At the same time, the performance of the cooling module is evaluated through the temperature monitor. The datasheet for UVC LEDs generally includes the peak wavelength and a half-width of less than 10 nm. Due to the inconsistency of UVC-LED chips and the effect of relative experimental temperature, the peak wavelength and optical power between UVC-LED chips can be different. Therefore, optical characterization is required to assess the performance of UVC-LED chips quantitatively. Besides, it can also be used to compute the UVC dose for each well on the 6-well cell culture plate. Considering the effective inactivation probability of single or dual wavelength, the UVC-LED arrangement in the same well is designed for both approaches. As presented in Figure C.3, the UVC-LED chips with different wavelengths are adjacently installed, and that of the same wavelengths are diagonally placed.

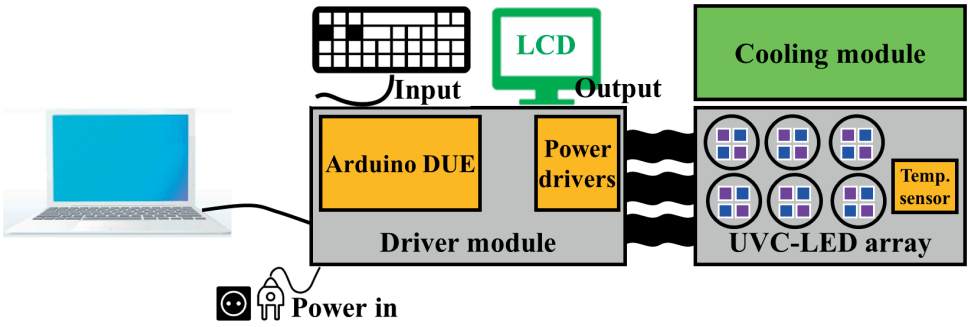


Figure C.3: An illustration of the UVC-LED viral inactivation experimental platform system.

Cooling module design. In our platform, there are two cooling schemes, namely air and liquid cooling solutions. In comparison, liquid cooling is more effective than air cooling using heat-transfer fluids in the cooling blocks because of its higher thermal capacity and thermal conductivity. To increase the total cooling surface for faster heat dissipation, a heat sink is adhered to the object's surface by means of a thermally conductive grease. It should be noted that liquid leakage from the liquid cooling module can cause damage to electronic components. Thus, it must be paid attention to the connect operation. As displayed in Figure C.4, the two liquid blocks are installed on the back of the aluminum substrate with the UVC-LED array, and the water pump is used as the

power source of liquid circulation. There are two connectors in the water pump, one for liquid input and the other for liquid output. In addition, thermally conductive grease is applied to the aluminum substrate as a thermal contact material for the liquid cooling block.

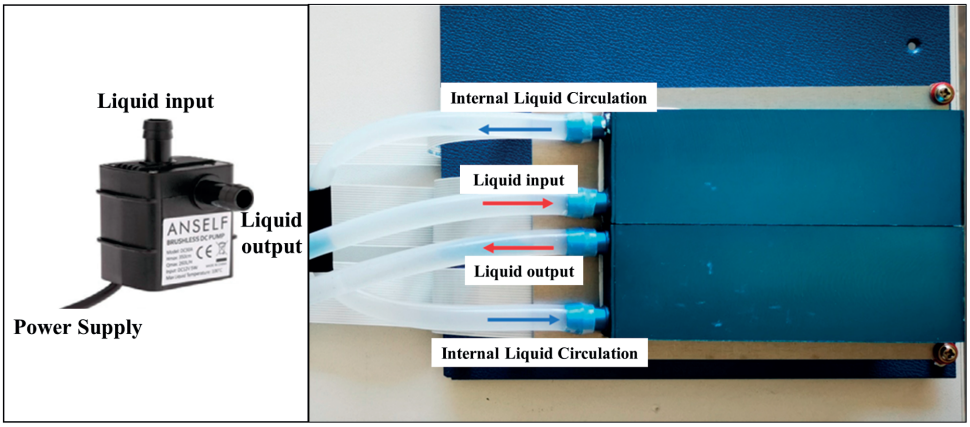


Figure C.4: A diagram demonstrating the water circulation in the liquid cooling module.

Driver module design. Figure C.5 clearly shows that the driver module consists of power management, a pulse width modulated (PWM) generator, an input/output port, an LED controller, a communication port, and Arduino DUE as an MCU. This portion mainly introduces the PWM generator, LED controller, and port design. As a power source, the PWM generator provides the power signals for UVC-LEDs, and its programmable frequency is from 24 Hz to 1526 Hz. Each PWM LED output signal has a 12-bit resolution (i.e., 4096 power steps) and a single UVC-LED brightness control with a programmable 0%-100% duty cycle. In addition to the PWM generator, a constant current LED driver with PWM control is also adopted for the UVC-LED controller. The constant current source is constructed using PWM power control, as presented in Figure C.6. The output current of UVC-LED is dependent on the current sense resistor when the PWM signal enables the current source. This relationship can be described as the formula $R_s(\Omega) = (0.2(V))/(I_{UVC-LED}(A))$, where 0.2 V is the reference voltage of the amplifier. The selected driver has an output current ranging from 20 mA to 300 mA, and its output current accuracy achieves 1.5%. The output ports aim to transmit the UVC-LED control signal to the UVC-LED array, and communication ports serve external devices, including PC, keypads, LCDs, and temperature sensors. The irradiation parameters (e.g., exposure power and exposure time) typed in the PC would be sent to each UVC-LED via communication ports. Meanwhile, the keypad is adopted to transmit input signals, and LCD shows real-time operation.

UVC-LED array design. The UVC-LED array comprises six UVC-LED groups, and its PCB schematic is shown in Figure C.7. Each UVC-LED group has four UVC-LEDs, aligning with one well in the 6-well cell culture plate. There are two causes for equipping with four UVC-LEDs in each group. One is to identify the most influential single- or dual-wavelength inactivation ingredient. Thus, four UVC-LEDs with the same wavelength or

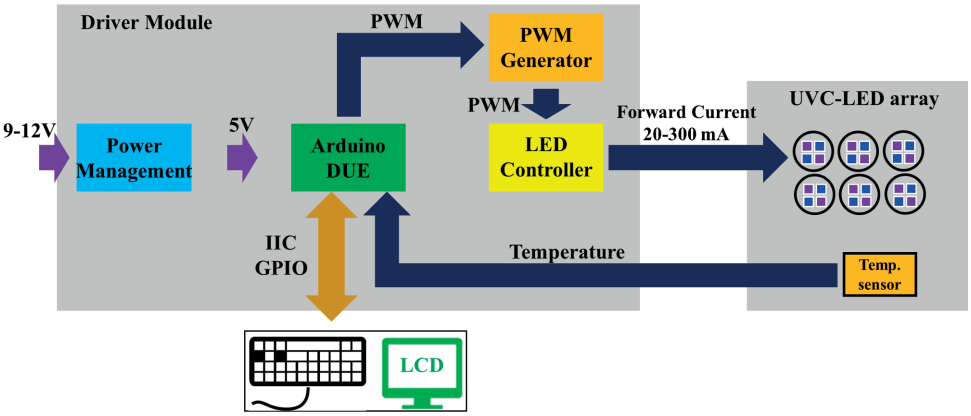


Figure C.5: A diagram of the driver module's components.

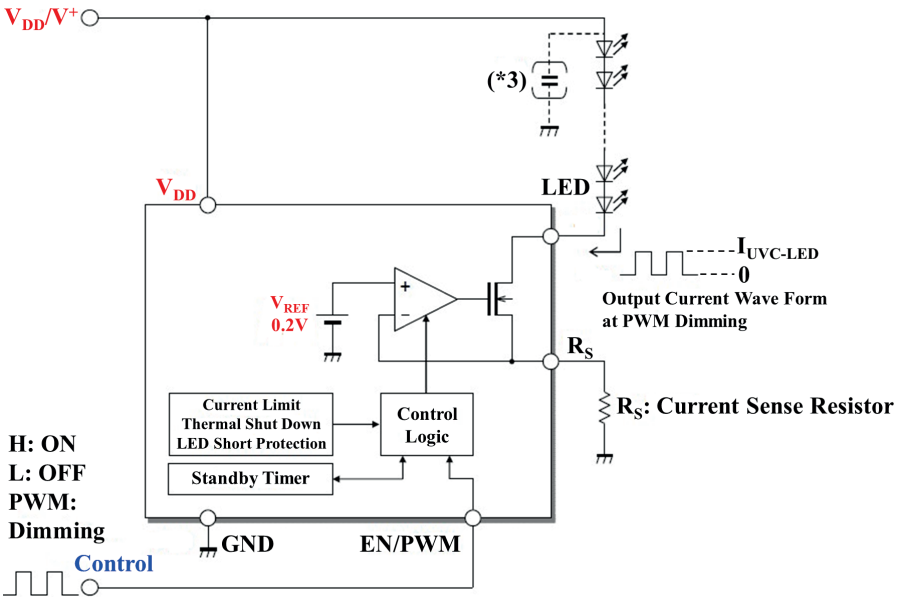


Figure C.6: A schematic of the constant current source.

with two different wavelengths are designed in the same single UVC-LED group. The other is to increase the exposure power and reduce the inactivation time. According to the simulated result of the TracePro irradiation, it would cost nearly one minute for a single UVC-LED to reach 110 J/m^2, which inactivates Ebola viruses. When the number of UVC-LED exposed in each well is changed from one to four, the inactivation time would be considerably shorter, and the exposure power is higher. Depending on the designed irradiation dose, the number of UVC-LEDs for each group can be flexibly equipped. In order to monitor the temperature of each UVC-LED group in real-time, a thermistor is

installed in the centre of each UVC-LED group. These sensors would convert the signals and transmit them to the MCU. Besides, introducing a DC into these temperature sensors to collect their data signals. The flexible cable connectors on the right edge of the UCV-LED array are applied to carry the driving current of UVC-LEDs and the collected signals of temperature sensors.

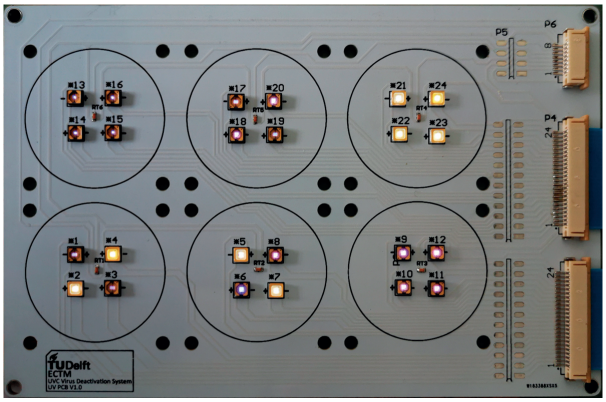


Figure C.7: The UVC-LED array's layout on the PCB.

C.1.3. CHARACTERIZATION OF UVC-LEDS

The UVC-LED light characterization aims to identify the exposure power and peak wavelength of each UVC-LED because there may be differences in peak wavelength and radiance between the datasheet and the measured results. Note that the exposure dose designed for the inactivation experiments is based on the measured results. Table C.1 lists the original parameters of each UVC-LED provided by various manufacturers. The peak wavelength and optical power output of UVC-LEDs from different manufacturers are measured under the preset forward current. In fact, due to the differences in experimental equipment and human operation, the actual forward current of UVC-LED may differ from the datasheet's value. Furthermore, the chip inconsistency caused by the fabrication process also leads to variations between UVC-LEDs. Therefore, these parameters in the datasheet should not be used as the reference in the inactivation experiments. In the characterization, the peak wavelength and optical power are obtained under the stepped driving current, and the relationship of UVC-LED radiance with the stepped driving current is also determined.

The characterization experiment is carried out in the Signify platform, as shown in Figure C.8. We can observe that the UVC-LED array is equipped in the testing platform and the distance between the detector and the UVC-LEDs is 6.5 cm. The UVC-LEDs are aligned to the center of the detector for each test. The driving current of the UVC-LED array is divided into the power value of 25%, 50%, 75%, and 100% to obtain the radiant power and peak wavelength under different power steps.

Five UVC-LEDs are characterized, and the characterized peak wavelengths are 259.4 nm, 260.3 nm, 269.1 nm, 273.9 nm, and 283.8 nm for 255 nm UVC-LED with maximum

Table C.1: Light parameters of UVC-LEDs from different manufacturers.

Peak Wavelength	Optical Power Output	Spectrum Half Width	Manufacturer
255 nm @ 100 mA	3.5 mW @ 100 mA	11	SeoulViosys
255 nm @ 20 mA	0.5 mW @ 20 mA	11	SeoulViosys
265 nm @ 500 mA	60 mW @ 500 mA	11.2	UVSIS Technology
278 nm @ 100 mA	15 mW @ 100 mA	10	Vishay Semiconductors
285 nm @ 100 mA	10 mW @ 100 mA	11	SeoulViosys

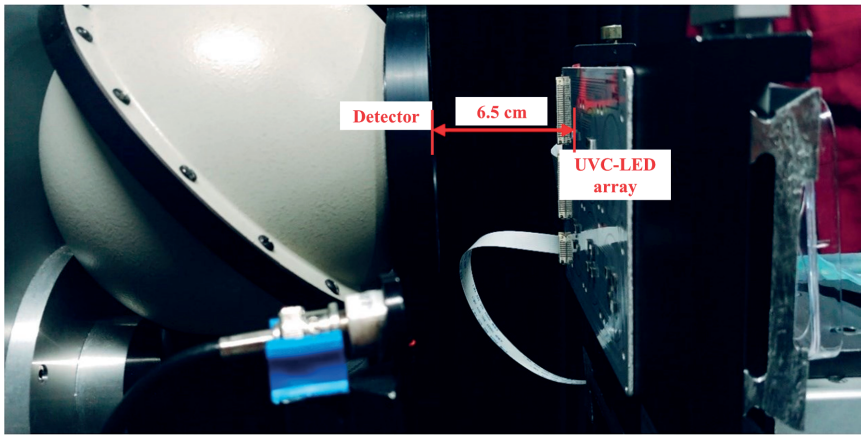


Figure C.8: The UVC-LED array's characterization platform.

current 200 mA, 255 nm UVC-LED with maximum current 20 mA, 265 nm UVC-LED, 278 nm UVC-LED, 285 nm UVC-LED, respectively. This result reveals that the peak wavelength of each UVC-LED has a shift compared to the nominal values in the datasheet. Considering 255 nm UVC-LEDs as an example, the radiation powers and peak wavelengths of five UVC-LEDs are tested at the maximum power duty cycle. As plotted in Figure C.9(a), their peak wavelengths exhibit a shifting behavior. The peak wavelengths for most 255 nm UVC-LEDs are close to 259 nm, and one of the UVC-LEDs shifts to over 260 nm. Ideally, there is a linear relationship between radiation power and the stepped driving current, which is also expected in characterization. All radiation power points can be deduced through this linear relationship, not to characterize them. Figure C.9(b) shows that the radiance increases linearly with increasing of the power step, regardless of the variation of radiation power. Notably, as the alignment of each UVC-LED is manual, there are slight fluctuations or uneven radiation power. Therefore, the experimental radiation power parameters can be directly derived from the linear relationship by reasonably characterizing the radiance curve. As listed in Table C.2, the characterized radiation power is measured in four power steps of 1000, 2000, 3000, and 4096, i.e., four preset duty cycles of 25%, 50%, 75%, and 100%. The characterized peak wavelength is the average value of the peak wavelengths of four power steps. In the subsequent experiments, the

100% of power step acts as the calculation-reference of radiation power.

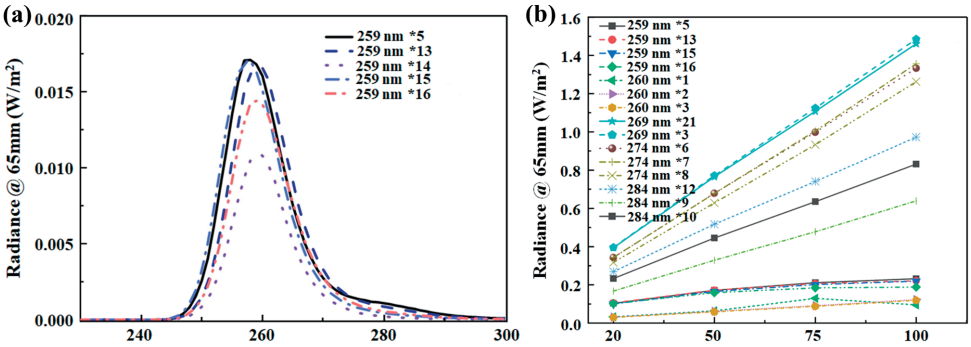


Figure C.9: (a) The variation in the radiation power and peak wavelength for a 255 nm UVC-LED. (b) The relationship between radiance and power step.

Table C.2: The characterization of radiance power and peak wavelength for UVC-LEDs.

Datasheet Peak Wavelength (nm)	Power Step	Characterized Radiance Power (W/m^2)	Characterized Peak Wavelength (nm)
255 (200 mA)	1000	0.1206	259.4
	2000	0.2035	
	3000	0.2546	
	4096	1.4228	
255 (30 mA)	1000	0.0306	260.3
	2000	0.0602	
	3000	0.0895	
	4096	0.1210	
265	1000	0.3957	269.1
	2000	0.7715	
	3000	1.1247	
	4096	1.4851	
278	1000	0.3432	273.9
	2000	0.6785	
	3000	1.0017	
	4096	1.3448	
285	1000	0.2002	283.8
	2000	0.3869	
	3000	0.5564	
	4096	0.7354	

C.2. THE ATOM-TO-ATOM CHARGE TRANSFER MATRIX OF FOUR RNA NUCLEOTIDES.

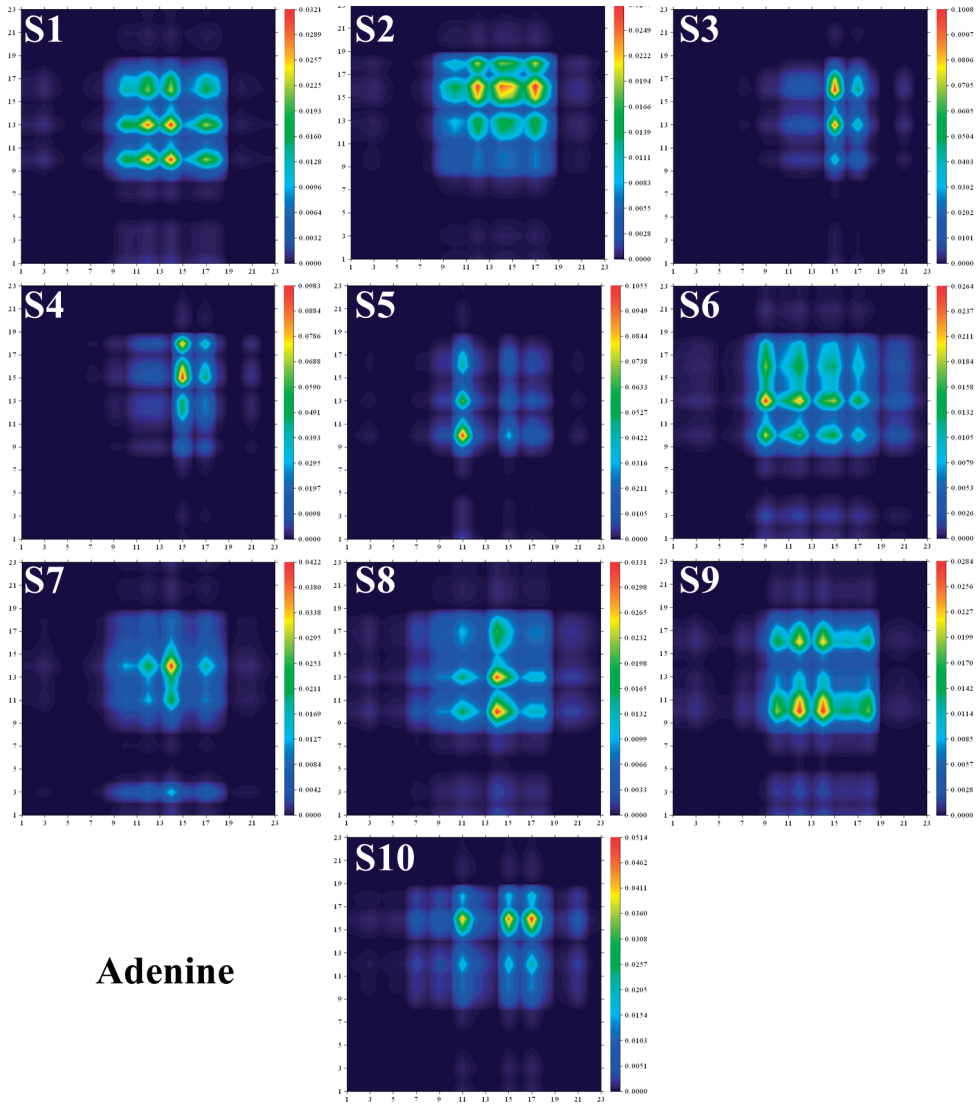


Figure C.10: The atom-to-atom charge transfer matrix of an adenine molecule in various excited states.

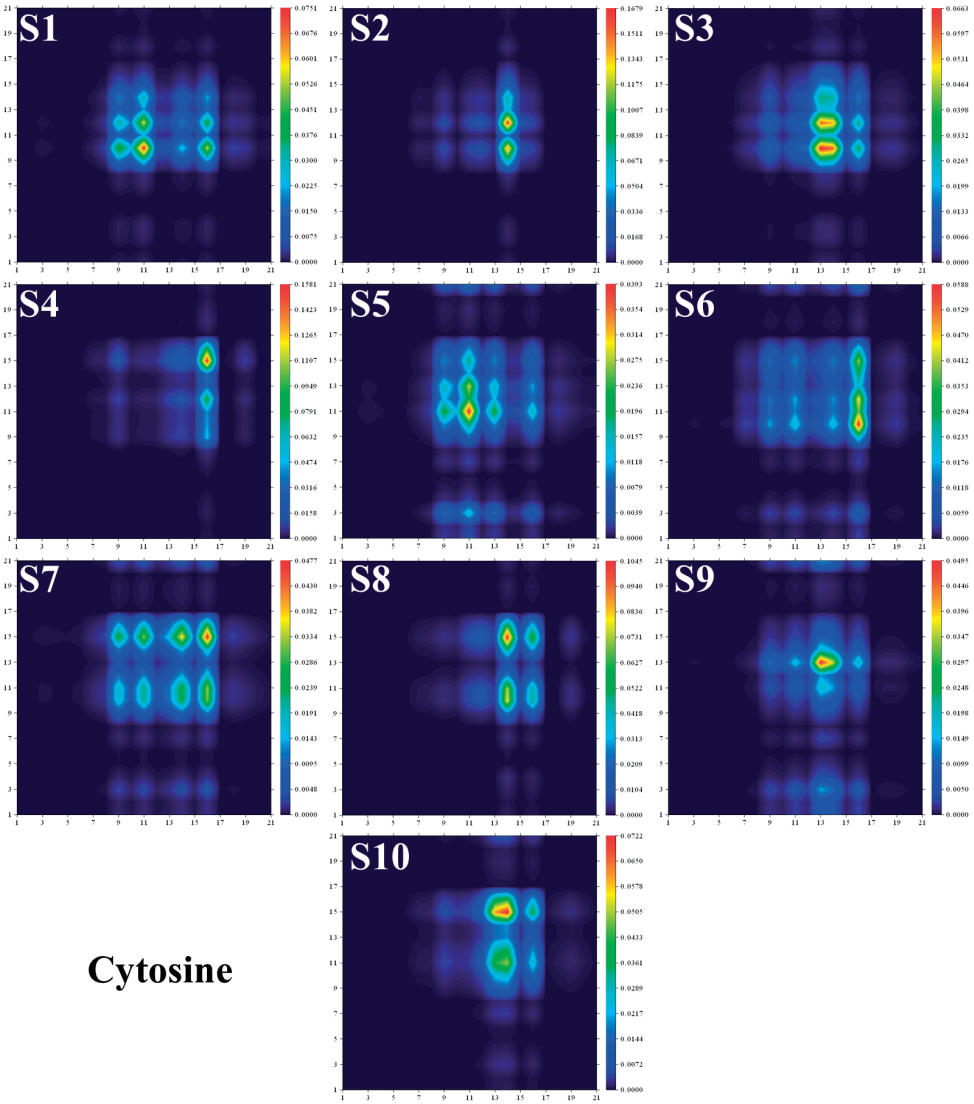


Figure C.11: The atom-to-atom charge transfer matrix of a cytosine molecule in various excited states.

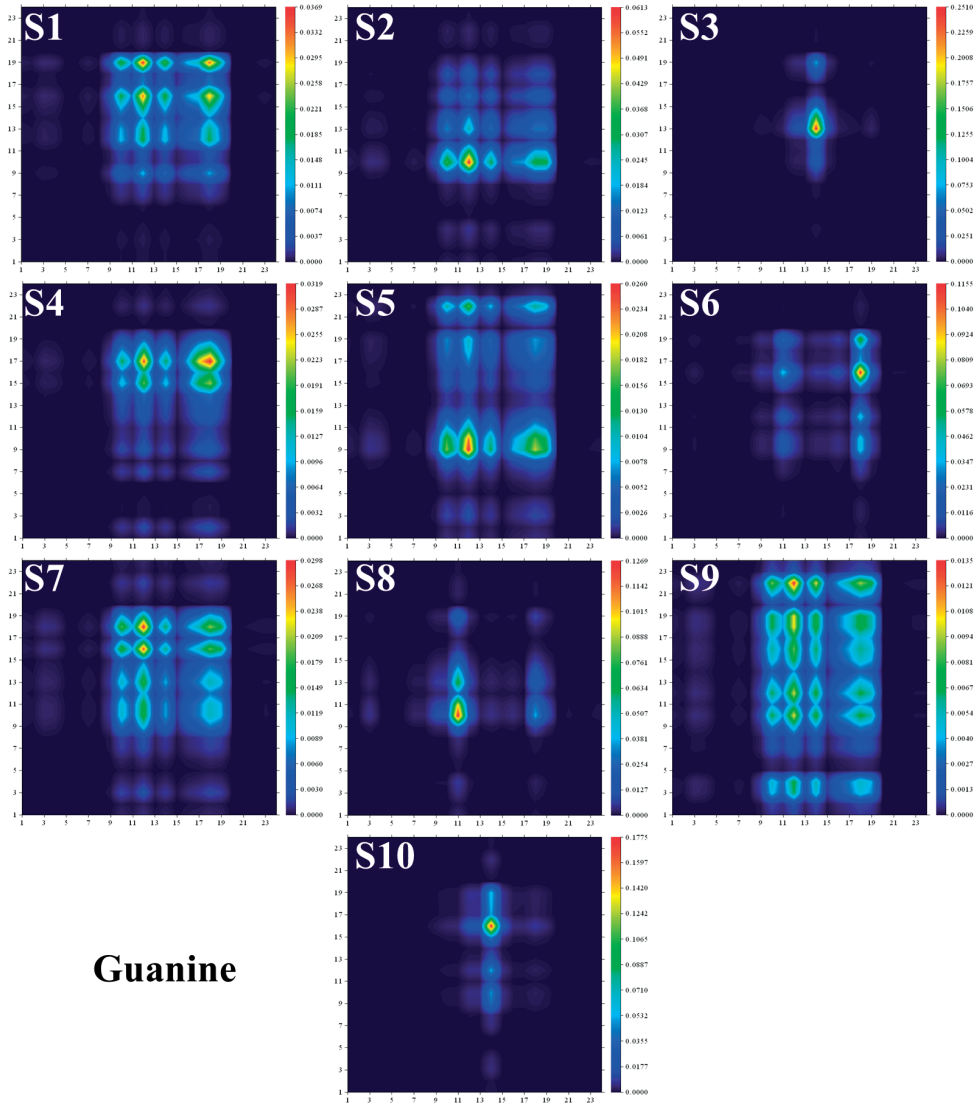


Figure C.12: The atom-to-atom charge transfer matrix of of a guanine molecule in various excited states.

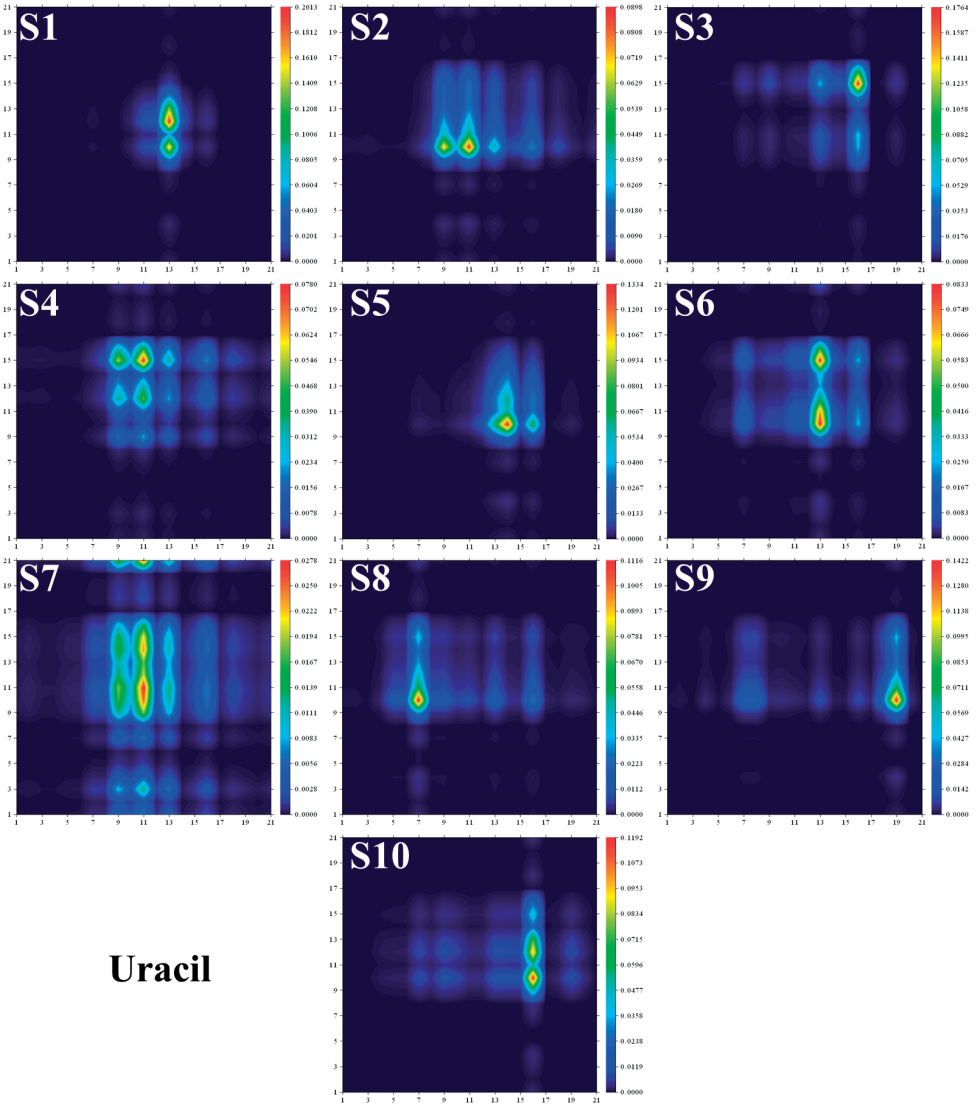


Figure C.13: The atom-to-atom charge transfer matrix of a uracil molecule in various excited states.

D

SUPPORTING INFORMATION CHAPTER 5

D.1. MATERIAL PARAMETERS FOR MICROELETRODE MODELS.

Table D.1: Material parameters for the microeletrode models.

Material	Relative Permittivity	Conductivity (S/m)
Water	75	5.5×10^{-6}
Aluminum	1.6	3.56×10^{7}
Quartz	4.2	1×10^{-14}

D.2. STRUCTURAL PARAMETERS FOR THREE MICROELETRODES

Table D.2: Structural parameters for the designed microelectrodes. Note that the width is the width of the electrode digit.

Microelectrode	Structure	Pitch (μm)	Width (μm)	Gap (μm)
Interdigitated	I2	2	1	1
	I5	5	1	4
	I10	10	1	9
Castellated (in-phase)	Cin4	4	1	1
	Cin8	8	1	5
Castellated (out-of-phase)	Cout4	4	1	0.5
	Cout5	5	1	1.5

D.3. ELECTRIC FIELD DISTRIBUTION OF MICROELECTRODES

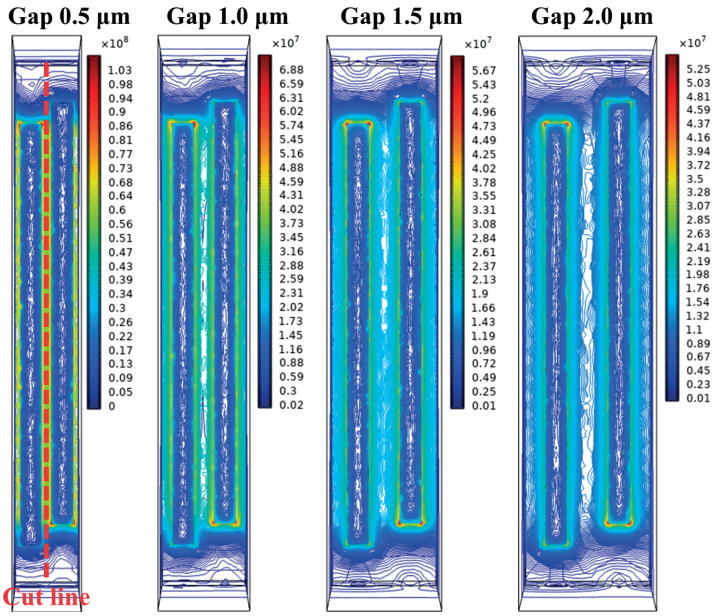


Figure D.1: Electric field distribution of interdigitated structures with varying gaps.

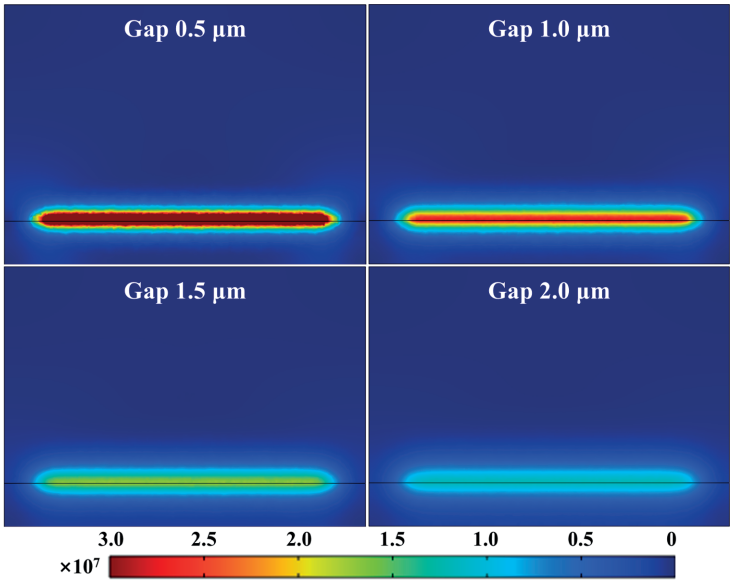


Figure D.2: Electric field distribution of the cross-section for interdigitated structures with varying gaps.

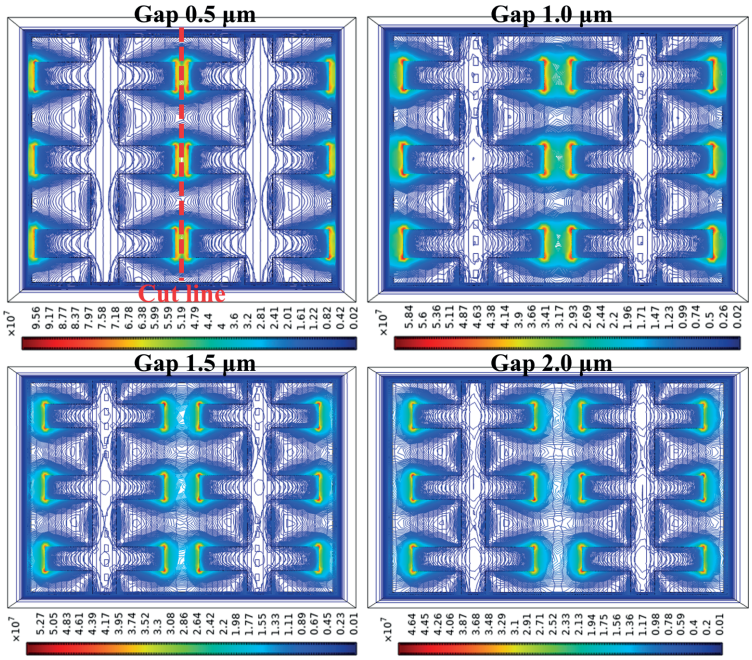


Figure D.3: Electric field distribution of in-phase castellated structures with varying gaps.

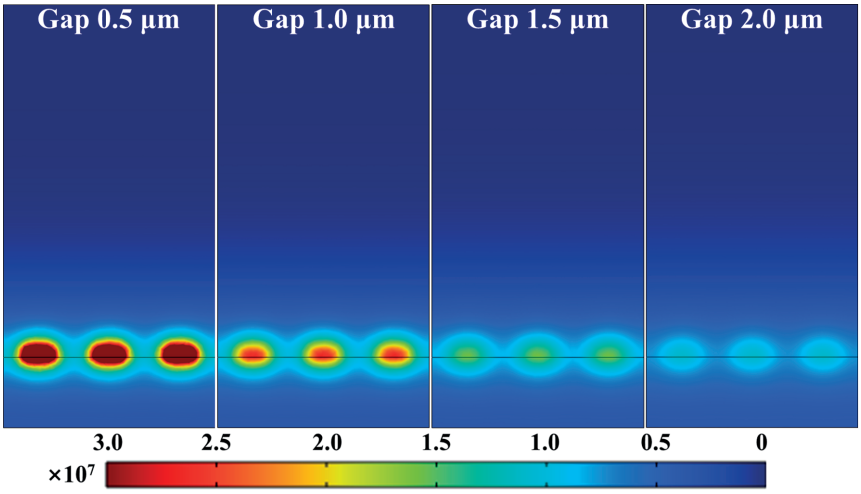


Figure D.4: Electric field distribution of the cross-section for in-phase castellated structures with different gaps.

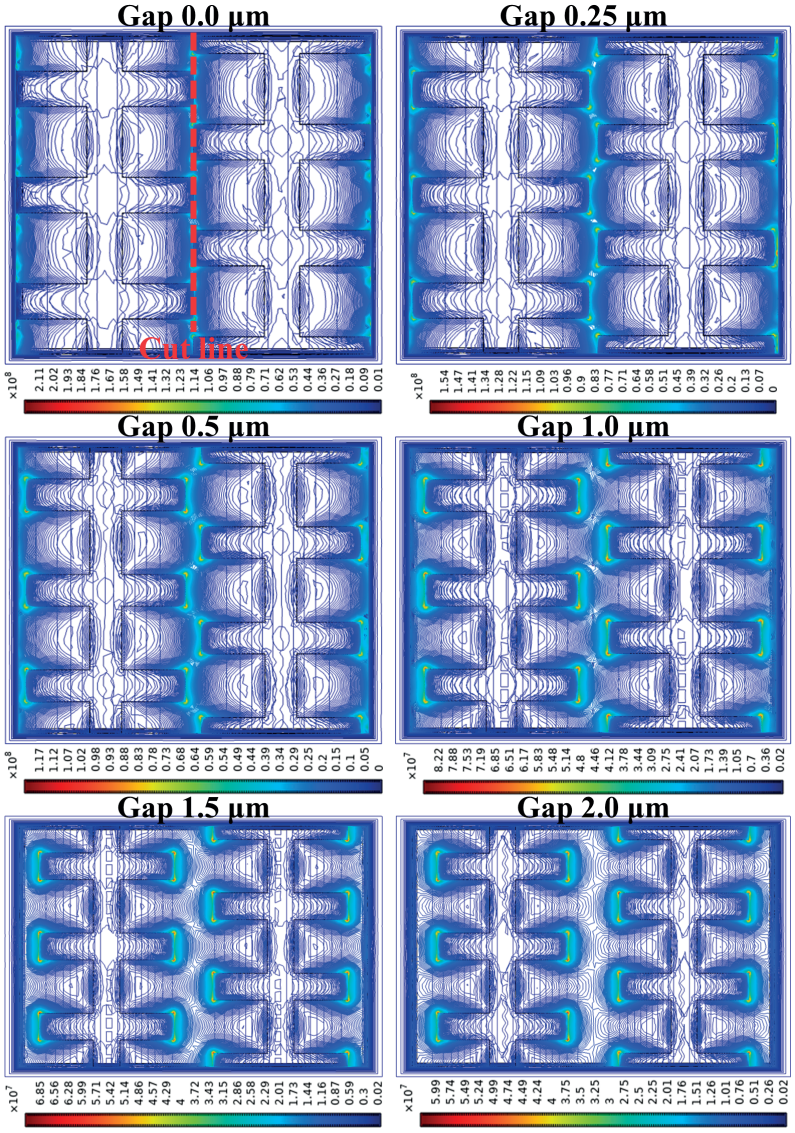


Figure D.5: Electric field distribution of out-of-phase castellated structures with varying gaps.

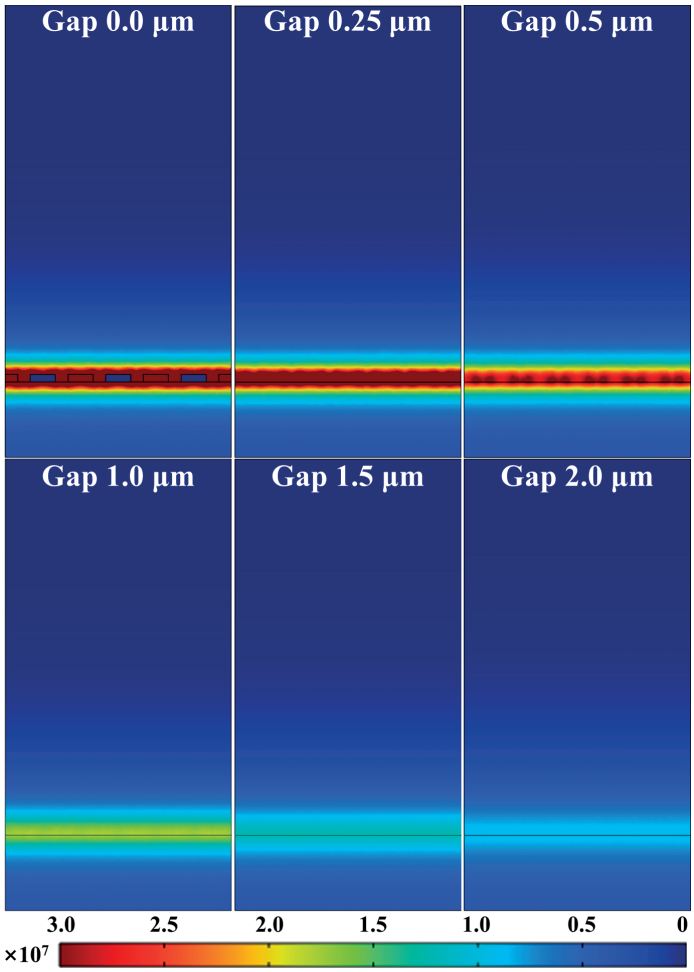


Figure D.6: Electric field distribution of the cross-section for out-of-phase castellated structures with varying gaps.

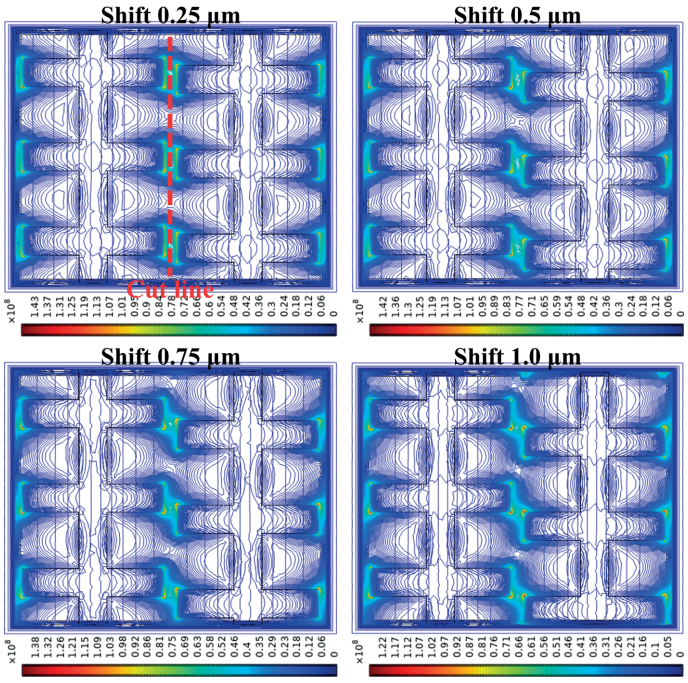


Figure D.7: Electric field distribution of castellated structures with various shifts. The gap is 0.5 μm.

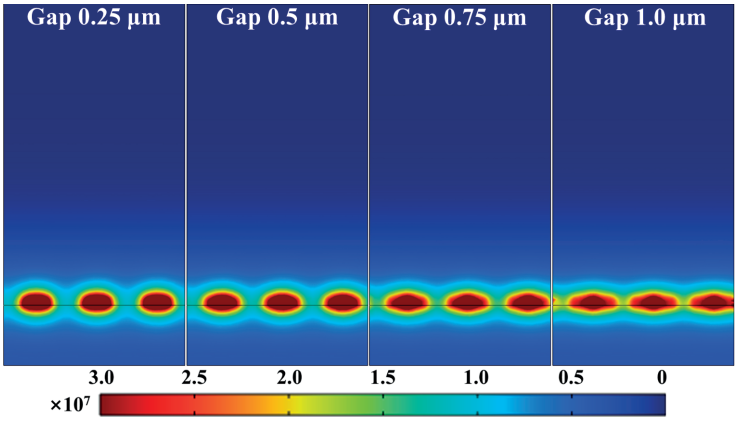


Figure D.8: Electric field distribution of the cross-section for castellated structures with various shifts. The gap is 0.5 μm.

D.4. FABRICATION OF THE MICROELECTRODES

All microelectrodes are fabricated at the Else Kooi Lab at TU Delft. Here, a glass wafer with a thickness of 525 μm and a diameter of 100 mm is used as the substrate of the microelectrodes because electric fields generated by metal insulation are superior to those by silicon materials. A 300 nm thick layer of aluminum is sputtered on the front and back sides of the glass wafer to be better aligned and handled by laser-assisted equipment. The current density for the deposited aluminum layer could reach a magnitude of 1×10^{10} A/m^2. The interdigitated structure will generate 0.016 W of Joule heating upon the short circuit. Exposure energies greater than 150 kJ/cm^2 will lead to around 0.8 μm of the electrode width. Based on PECVD (plasma enhanced chemical vapor deposition) process, a 150 nm thick TEOS (silicon oxide Tetraethyl Orthosilicate) is deposited on the electrodes to enhance the surface hydrophilic. The TEOS layer not only enables virus particles to distribute uniformly on the electrode surface but also prevents the electrolysis of the medium containing viruses. However, the deposition of the TEOS layer will weaken the electric field between the electrodes or reduce the divergence of the electric field. Hence, in the TEOS deposition, the pressure, HF power, temperature, and deposition time were 2.2 Torr, 1 kW, 400 °C, and 3.2 s, respectively. Finally, a 25-μm micro-frame on the electrode's edge is fabricated using a photoresist. Note that the penetration of the electric field reduces after the initial 20 μm. SU-8 is selected to construct the micro-frame because of its covalent solid bonds upon exposure. In this process, a soft bake for 10 min at 65 °C and a hard bake for 25 min at 95 °C are required. Figure D.9 displays the wafer with different electrode structures and the zoom-out views of all electrodes.

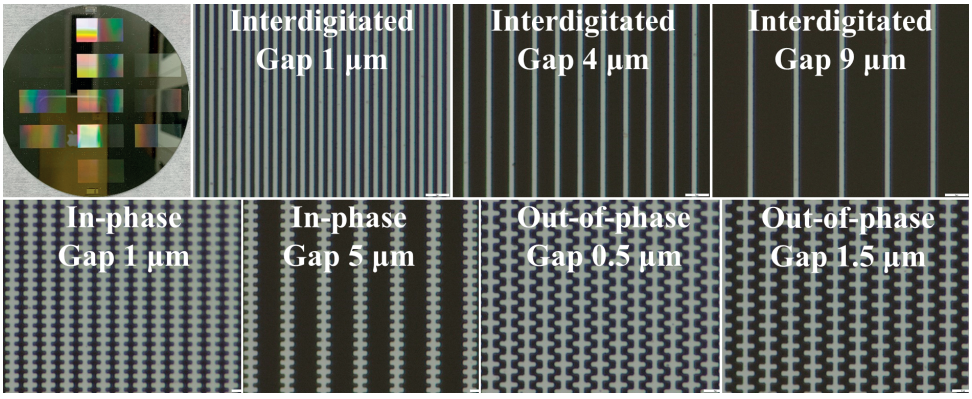


Figure D.9: A wafer with various electrode structures and an overview of all electrodes at a zoomed-out scale.

The wafer is diced, and the bare dies are then assembled on the PCBs using a non-conductive gel. The dies are interconnected to the metallic pads on the PCB by a gold wire bonding process. Eventually, the leaded bonding portion is encapsulated with a non-conductive gel and cured under UV light for 20 min. The bare dies and the assembled electrode samples are shown in Figure D.10.

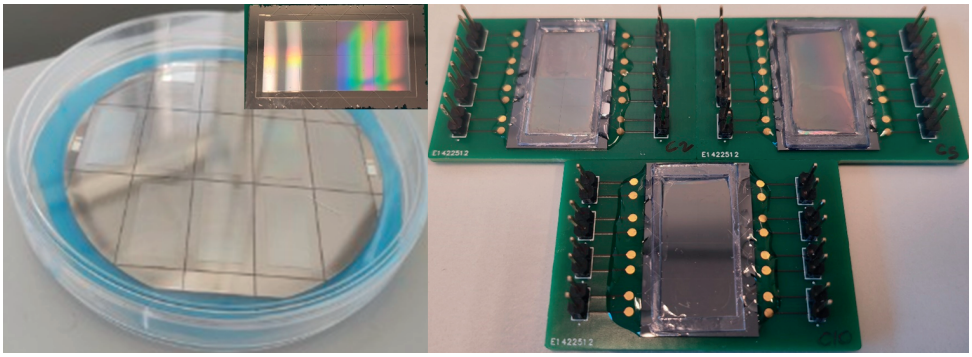


Figure D.10: The bare dies and the assembled electrode samples.

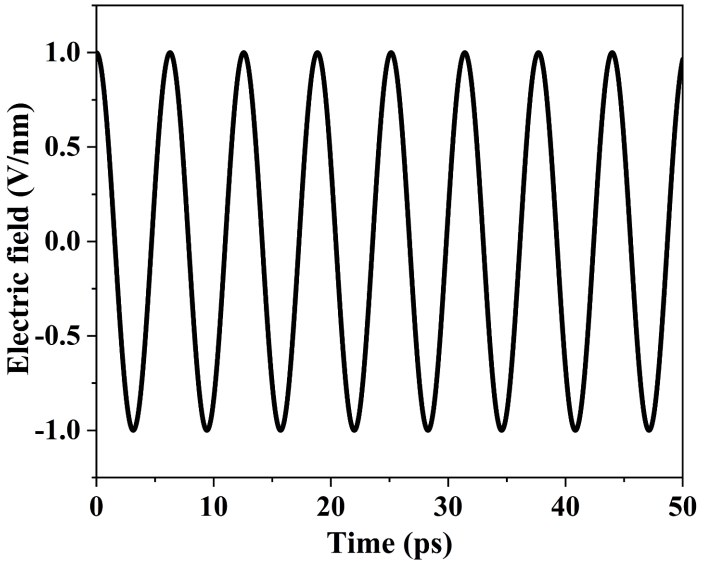


Figure D.11: The simulated oscillating field with an angular frequency of 1 /ps.

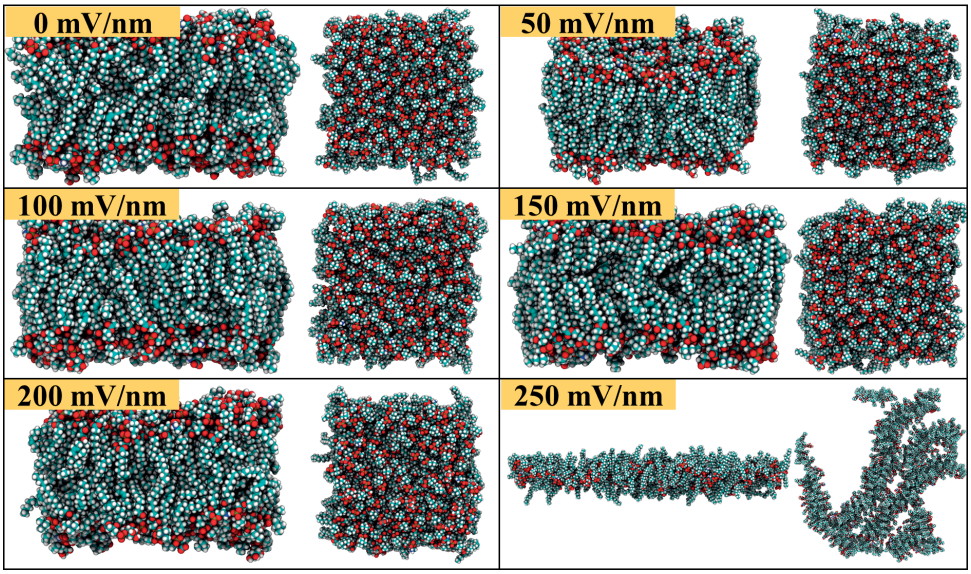


Figure D.12: End snapshots of the membrane structure following a 200 ns simulation at varying field strengths.

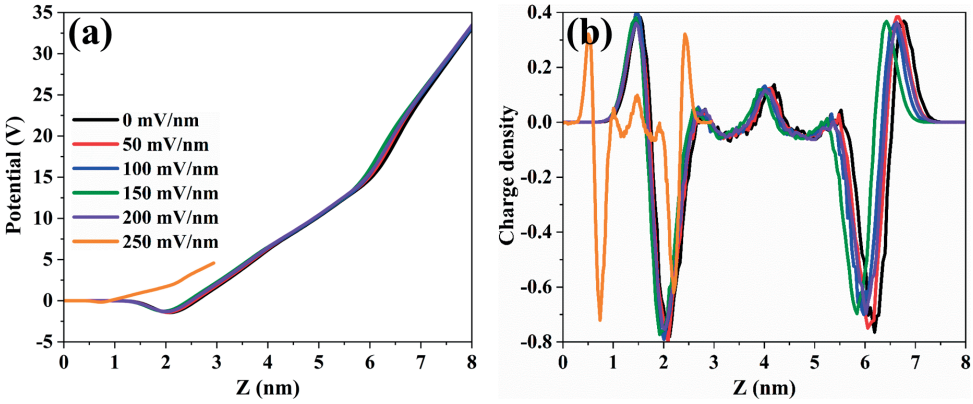


Figure D.13: The potential (a) and charge density (b) of the membrane structure.

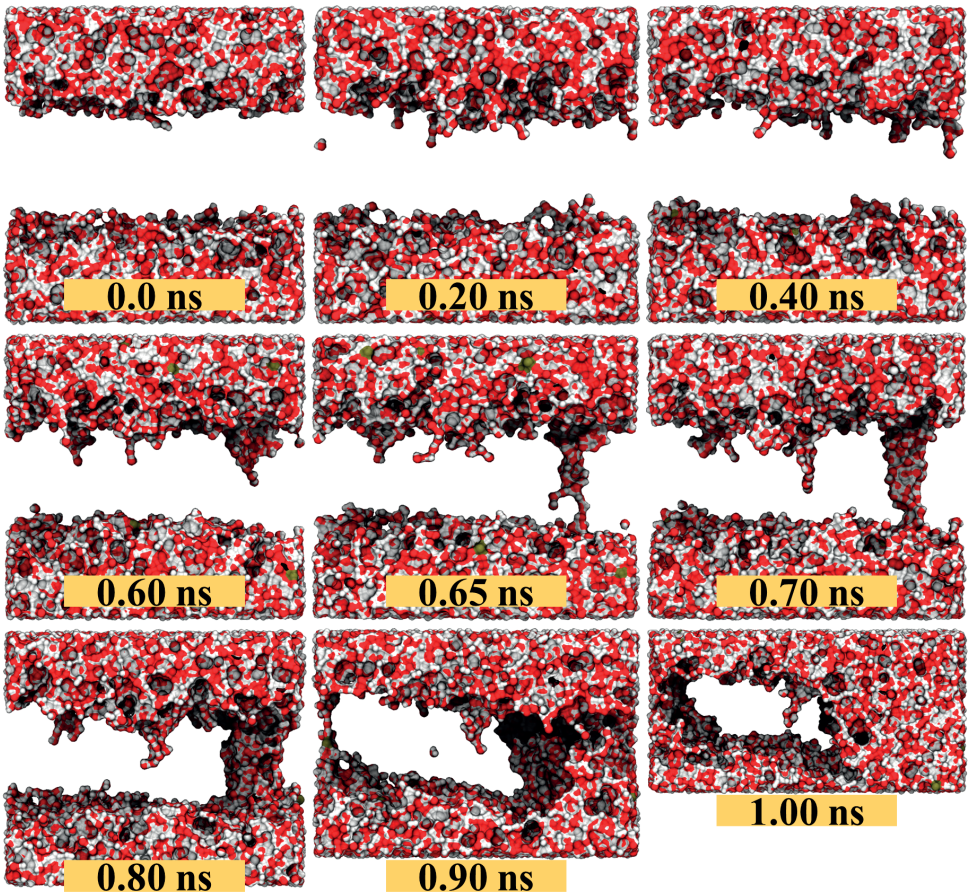


Figure D.14: Nanoporation in the bilayer membrane under an electric field of 500 mV/nm.

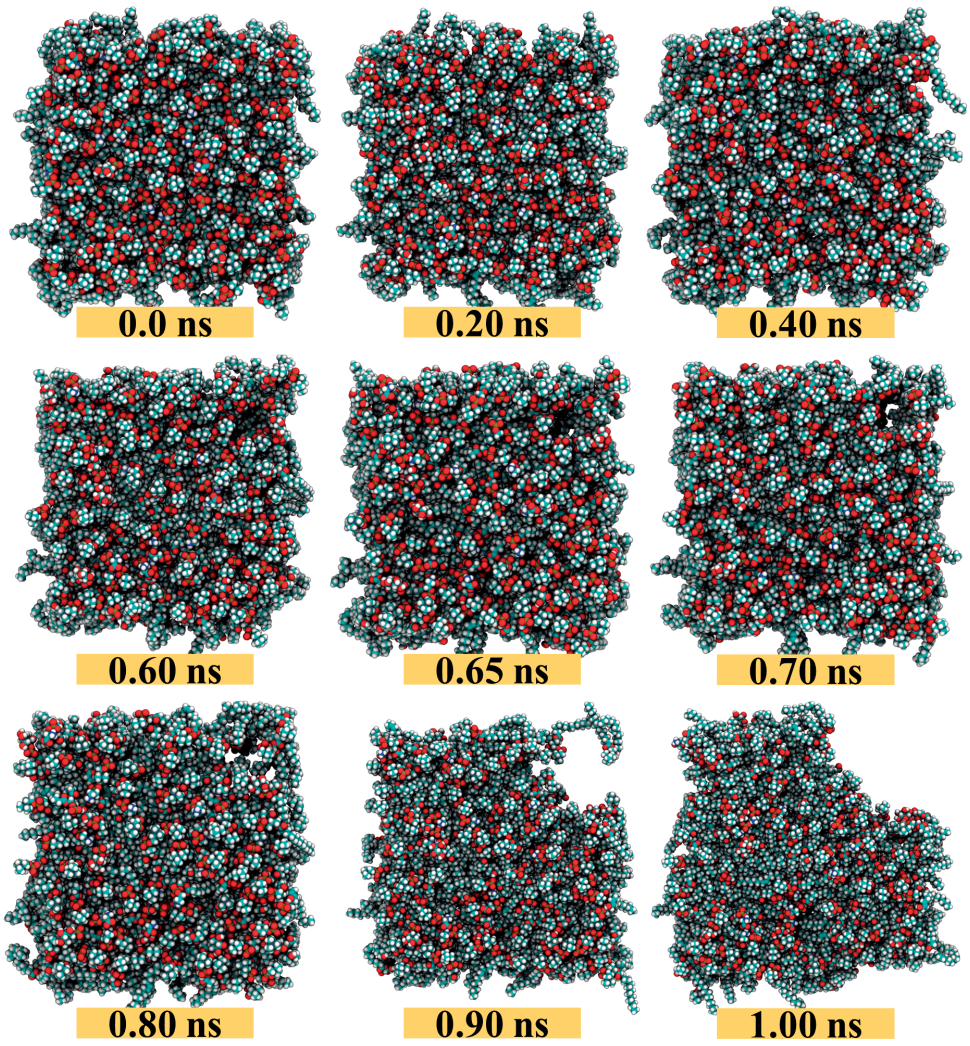


Figure D.15: The variation in the bilayer membrane with running time under an electric field of 500 mV/nm.

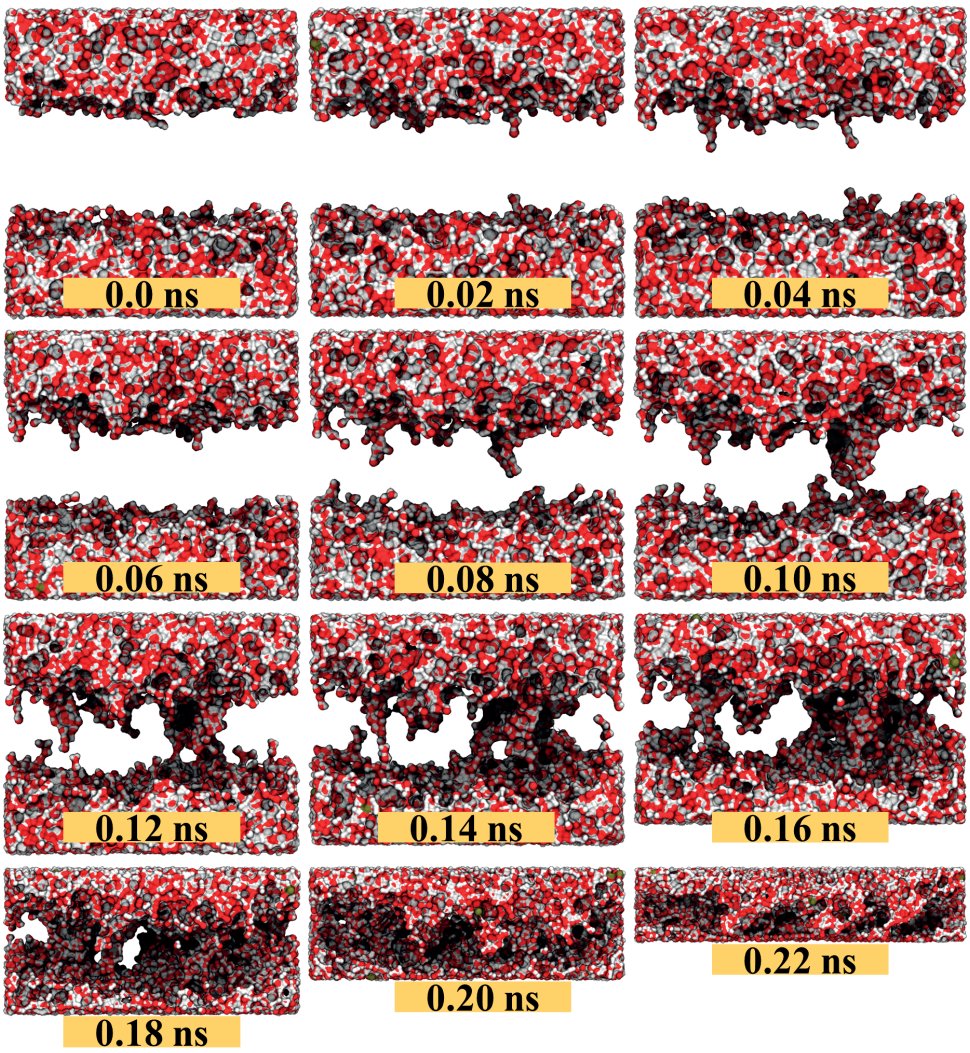


Figure D.16: Nanoporation in the bilayer membrane under an electric field of 1000 mV/nm.

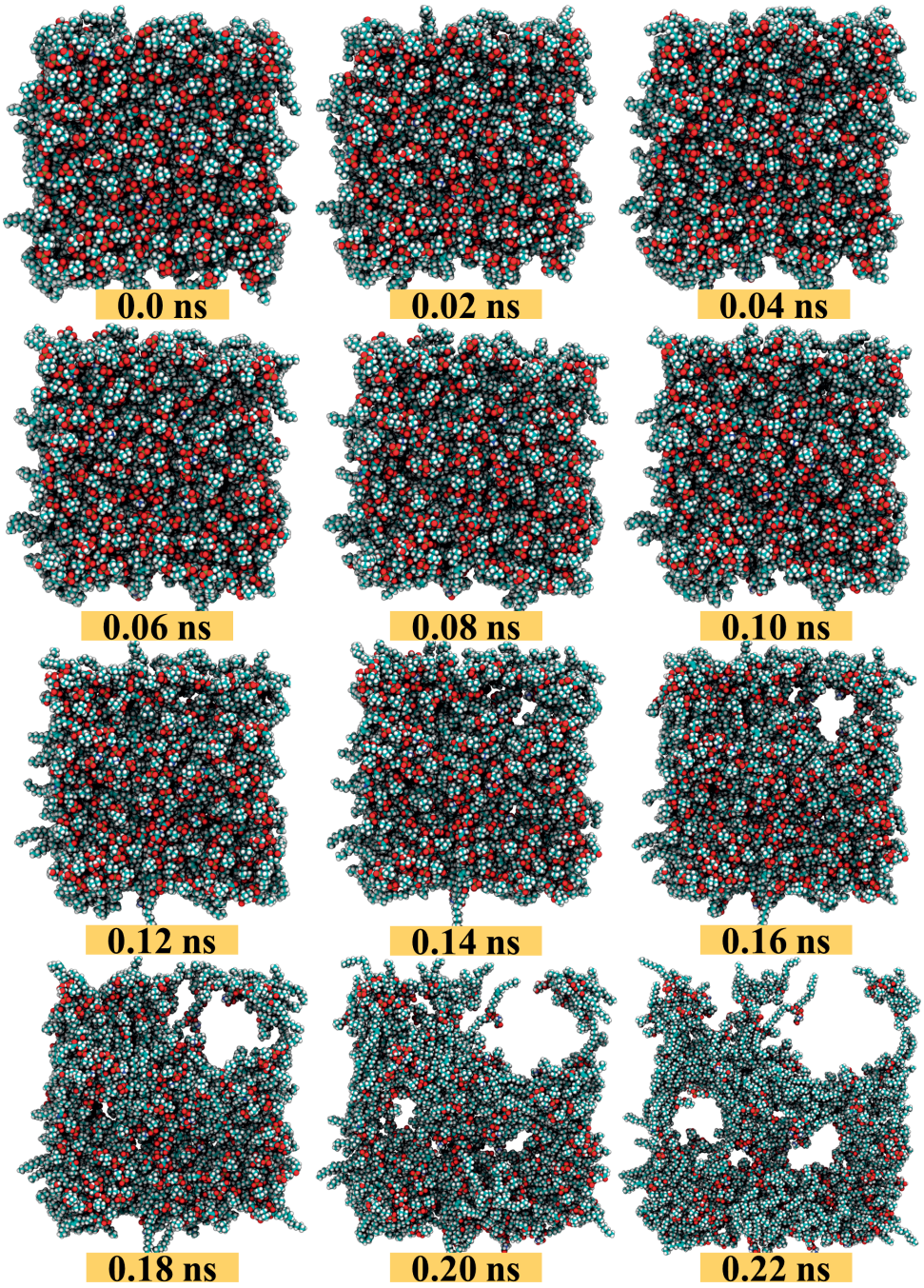


Figure D.17: The variation in the bilayer membrane with running time under an electric field of 1000 mV/nm.

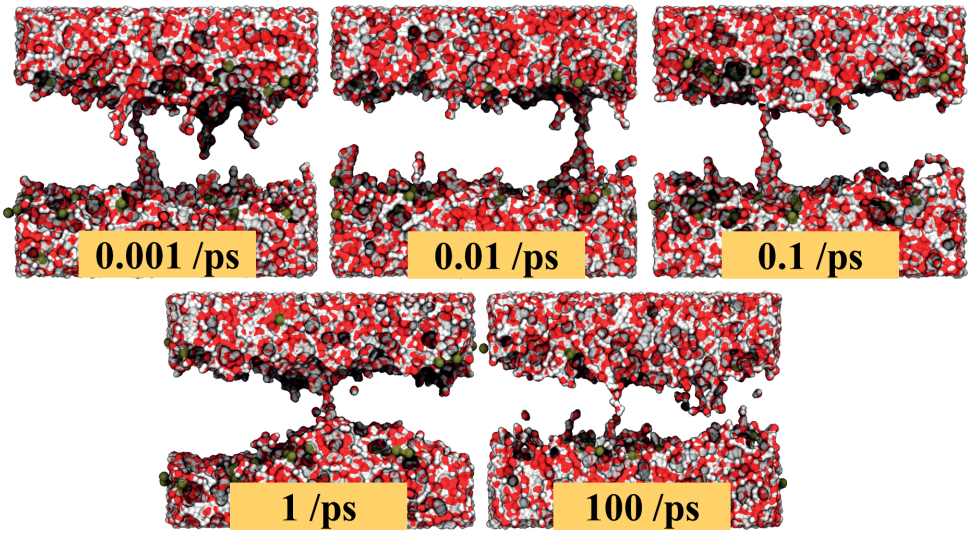


Figure D.18: Snapshots showing the membrane structure as a nanopore first begins to form at varying angular frequencies.

CURRICULUM VITÆ

Chunjian TAN

15-11-1990 Born in Guangxi, China.

EDUCATION

2011–2015 Bachelor in Microelectronic Engineering
Guilin University of Electronic Technology
Guangxi, China

2015–2018 Master in Mechanical Engineering
Guilin University of Electronic Technology
Guangxi, China

2018 PhD. in ECTM
Technische Universiteit Delft
Thesis: Understanding the Fundament of Virus Inactivation Via Modeling
Promotor: Prof. dr. G. Q. Zhang

LIST OF PUBLICATIONS

18. **C. J. Tan, S. G. Wang, J. Dai, K. Liu, Y. Li, H. Y. Ye*, G. Q. Zhang***, *Inactivation of pathogens using electric fields on a microchip platform: Virucidal performance and mechanism*, Preparing.

17. **C. J. Tan, S. G. Wang, H. Y. Ye*, G. Q. Zhang***, *A computational study on the inactivation mechanism of SARS-CoV-2: Unrevealing the possible impact of high temperature on phospholipid membranes*, Preparing.

16. **C. J. Tan, S. G. Wang, H. Y. Ye*, G. Q. Zhang***, *The disinfection mechanism of SARS-CoV-2: effect of virucidal agents on phospholipid membranes*, Preparing.

15. **C. J. Tan, S. G. Wang, H. R. Yang, Q. M. Huang, S. Z. Li, X. Liu, H. Y. Ye*, G. Q. Zhang***, *Design and numerical simulation of a CHANEL-shaped THz-resonant metamaterial blood analyzer for COVID-19 prompt tests*, Optics Communications , Under Review.

14. **C. J. Tan, S. G. Wang, H. R. Yang, Q. M. Huang, S. Z. Li, X. Liu, H. Y. Ye*, G. Q. Zhang***, *Understanding the interaction of nucleotides with UVC light: An insight from quantum chemical calculation-based findings*, Physical Chemistry Chemical Physics , Accepted.

13. **C. J. Tan, S. G. Wang, H. R. Yang, Q. M. Huang, S. Z. Li, X. Liu, H. Y. Ye*, G. Q. Zhang***, *Hydrogenated Boron Phosphide THz-Metamaterial-Based Biosensor for Diagnosing COVID-19: A DFT Coupled FEM Study*, Nanomaterials **12**, 22 (2022).

12. **C. J. Tan, S. G. Wang, S. Z. Li, X. Liu, J. Wei, G. Q. Zhang, H. Y. Ye***, *Cancer Diagnosis Using Terahertz-Graphene-Metasurface-Based Biosensor with Dual-Resonance Response*, Nanomaterials **12**, 21 (2022).

11. **C. J. Tan, Q. Zhou, X. Liu, G. Q. Zhang, H. Y. Ye*, Q. B. Wu***, *Hydrogenated boron phosphide with the excellent tunability of electronic properties and Current-Voltage responses*, Applied Surface Science **15**, 572 (2022).

10. **C. J. Tan, C. S. Gao, Q. Zhou, W. V. Driel, H. Y. Ye, G. Q. Zhang**, *The inactivation mechanism of chemical disinfection against SARS-CoV-2: From MD and DFT perspectives*, RSC Advances **10**, 40480-40488 (2020).

9. **J. Jiang, S. G. Wang, X. Liu, J. H. Liu, J. Li, D. X. Zhou, G. Q. Zhang*, H. Y. Ye, C. J. Tan***, *Electron-Irradiation-Induced Degradation of Transfer Characteristics in Super-Junction VD-MOSFET*, Electronics **11**, 13 (2022).

8. **X. Liu, S. Z. Li, C. J. Tan, C. S. Gao, Y. Liu, H. Y. Ye*, G. Q. Zhang**, *Coalescence kinetics and microstructure evolution of Cu nanoparticles sintering on substrates: a molecular dynamics study*, Journal of Materials Research and Technology **17**, 1132-1145 (2022).

7. **H. R. Yang, J. F. Li, Z. Y. Shao, C. J. Tan, C. S. Gao, H. Y. Cui, X. S. Tang, Y. F. Liu, H. Y. Ye*, G. Q. Zhang**, *Strain-engineered S-HfSe2 monolayer as a promising gas sensor for detecting NH3: A first-principles study*, Surfaces and Interfaces **34**, 102317 (2022).

6. **H. Y. Tang, C. J. Tan, H. R. Yang, K. Zheng, Y. T. Li, H. Y. Ye, X. P. Chen, X. J. Fan, T. L. Ren, G. Q. Zhang**, *Tunable electronic and optical properties of the WS2/IGZO heterostructure via an external electric field and stra in: a theoretical study*, Physical Chemistry Chemical Physics **21**, 14713-14721 (2019).

5. **H. C. Luo, L. M. Wang, S. G. Wang, C. J. Tan, K. Zheng, G. Q. Zhang, L. Q. Tao, X. P. Chen**, *Investigations of SiC VDMOSFET with Floating Island Structure Based on TCAD*, IEEE Transactions on Electron Devices **66**, 5 (2019).

4. **C. J. Tan, S. G. Wang, X. Liu, J. Jiang, G. Q. Zhang, H. Y. Ye***, *High-Voltage and High-Current IGBT Press-pack Module for Power Grid*, 23rd International Conference on Thermal, Mechanical and Multi-Physics Simulation and Experiments in Microelectronics and Microsystems (EuroSimE) **,** (2022).

3. **S. Z. Li, X. Liu, J. Jiang, C. J. Tan, C. S. Gao, Y. Liu, H. Y. Ye, G. Q. Zhang***, *Effects of shell thickness on the thermal stability of Cu-Ag core-shell nanoparticles: a molecular dynamics study*, 23rd International Conference on Thermal, Mechanical and Multi-Physics Simulation and Experiments in Microelectronics and Microsystems (EuroSimE) **,** (2022).

2. **K. Liu, W. C. Yuan, S. G. Wang, C. J. Tan, H. Y. Ye***, *Study on Reverse Recovery Characteristics of P-pillar Tunable Super-Junction MOSFET*, 23rd International Conference on Electronic Packaging Technology (ICEPT) **,** (2022).

1. **W. C. Yuan, K. Liu, S. G. Wang, C. J. Tan, H. Y. Ye***, *A TCAD simulation study on the short-circuit performance of 650V super-junction MOSFET*, 23rd International Conference on Electronic Packaging Technology (ICEPT) **,** (2022).

TU Delft Delft University of Technology



